Homogeneous quantum gases: strongly interacting fermions and rotating bosonic condensates

by

Biswaroop Mukherjee

B. A., University of California, Berkeley (2013)

Submitted to the Department of Physics
in partial fulfillment of the requirements for the degree of

Doctor of Philosophy in Physics

at the

MASSACHUSETTS INSTITUTE OF TECHNOLOGY

February 2022

Author. . . . .
Department of Physics
December 10, 2021

Certified by. . . . .
Martin W. Zwierlein
Thomas A. Frank (1977) Professor of Physics
Thesis Supervisor

Accepted by. . . . .
Deepto Chakrabarty
Associate Department Head of Physics

Homogeneous quantum gases: strongly interacting fermions and rotating bosonic condensates

by

Biswaroop Mukherjee

Submitted to the Department of Physics
on December 10, 2021, in partial fulfillment of the
requirements for the degree of
Doctor of Philosophy in Physics

Abstract

Quantum gases are an ideal platform for studying problems in many-body physics. Highly tunable and reconfigurable, these systems work as quantum simulators for a range of other quantum mechanical systems, ranging from neutron stars, to superconductors, to quantum Hall systems. A crucial degree of freedom is the external geometry of the trapping potential. In this thesis, we describe experiments on creating homogeneous quantum gases and performing measurements using them.

The first section of the thesis focuses on homogeneous Fermi gases, where we use tailored optical potentials to trap ^{6}Li atoms in a homogeneous box potential. We observe uniform fermionic superfluids and measure the temperature dependence of the noninteracting Fermi surface. Radiofrequency (rf) spectroscopy offers unique insights into the spectral properties of Fermi gases. We exploit the high signal to noise ratio of rf spectroscopy of uniform Fermi gases to obtain precise measurements of the thermodynamic contact. We observe a dramatic change in the contact at the superfluid transition.

The second section of this thesis concerns uniform rotating bosonic condensates. We discuss a new experimental apparatus and outline how geometric squeezing can be used to prepare systems of quantum gases in the lowest Landau level, a long sought-after goal. Lastly, we show a surprising spontaneous crystallization of these quantum Hall systems, and find that it is driven by interactions.

Thesis Supervisor: Martin W. Zwierlein
Title: Thomas A. Frank (1977) Professor of Physics

To my parents and teachers

Acknowledgments

I have been very fortunate to work alongside and learn from so many incredible people. From my first day at MIT, my research advisor Martin Zwierlein has been a light in the darkness. His infectious enthusiasm and absolute fearlessness keeps us engaged as we explore the unknown. When we inevitably encounter technical challenges in the lab, he provides both the encouragement and the key insight needed to break through them. When we enter into our spirals of solving lab problems, he helps us focus on the main goal: doing real science and taking interesting measurements. And when we think our observations are trivial (because we are saturated with cutting-edge science), he helps us step back and realize how far we have pushed the boundaries of our field without realizing it. On a personal level, Martin has been a wonderful source of guidance in life, and I thank him for his endless patience when I struggled to find my path through a PhD (and when I replaced the legendary BEC1 MOT tweaking mirror with a camera).

I have learned something unique from every person I have worked with. I thank the members of BEC1 who helped me find my footing in the chaotic jumble of wires, fibers and lasers that is BEC1. Tarik Yefsah, Wenjie Ji, and Mark Ku were there to show me how it's done. Elmer Guardado-Sanchez was also great companion during those early days, especially as we struggled with a new lithium laser system. I thank Tarik especially for engaging discussions, and showing me how to do physics cowboy-style. Julian Struck on the other hand, showed us how to do physics professional-style, and I have enjoyed many wonderful discussions with him geeking out about photography equipment.

Soon, Parth Patel and Zhenjie Yan joined BEC1, and much of the work presented in this thesis would be impossible without their incredible drive and companionship. Both had such deep questions that I realized many of the ideas I thought I understood were actually a lot more mysterious than I thought. Together, we plumbed, coded, whiteboarded, argued, and plotted. It is my absolute honor to have worked with

5

them.

I was fortunate to have been given the opportunity to run the historical machine that is BEC1, use it to reveal new physics, and construct a completely new lab from scratch. It was beyond my wildest imagination that we would reveal even more new physics with the new lab. I must thank the incredible effort and guidance of Richard Fletcher, who joined as a Pappalardo postdoc, and became an MIT professor towards the end of my time here. Richard's ability to succinctly write down a page of math to explain something we all struggled with is legendary. He is gifted at distilling science into clear words. Many times, I have waited for Richard to ask a seminar question so that I can understand the speaker better. Together with Airlia Shaffer and Cedric Wilson, we constructed Fermi3, and learned ultrahigh vacuum the hard way. Airlia and Cedric have been incredible friends to work with and learn from. Fermi3 is in excellent hands.

I also thank the other members of the research group, without whom life would have been far more dull. Cycling trips with Zoe, Richard, Parth, Yiqi, and Lee Liu were major highlights of my time here. Improving at triathlons with Zoe likely means I added a few years to my lifespan. I would like to thank the members of the MIT cycling club for an amazing time racing around the east coast. In Fermi2, Matt and Lawrence have been great friends, and I thank them for endless shenanigans.

Tim Savas and Jim Daley at the NSL have been instrumental to producing the masks that were so crucial to the results from BEC1. I appreciate their efforts in allowing a complete beginner at fabrication to build a new process and plod around their cleanroom looking for o-rings.

I would like to thank my partner Katie for her patience while I spent long hours in the lab. Lastly, but most importantly I would like to thank my parents for their guidance and care in raising me to follow in their footsteps. My mother has been my greatest inspiration and role model. Her honest approach to science, fearless attitude towards programming and math, and endless love have made me who I am. Without

her, I would not be.

Contents

11

List of Figures

List of Tables

Chapter 1

Introduction

Quantum mechanics in three dimensions restricts particles to fall into one of two categories: fermions and bosons. Theoretically demonstrated in 1924 by Bose and Einstein and 1926 by Fermi and Dirac [9, 37, 44, 32], the quantum statistics of a gas of particles determines their thermodynamics and evolution. Fermions obey the Pauli exclusion principle, where no two particles can occupy the same quantum state. Bosons on the other hand, have no such restriction. Since then, perhaps every single experiment in quantum physics has in one way or another, demonstrated the consequences of these fundamental statistical principles.

Simulating quantum systems is a computationally challenging problem on classical computers. The number of states in a Hilbert space grows exponentially in the number of particles: thus, even the best classical computers of today would struggle to contain the full Hilbert space of just 50 fermions. In 1982, Feynman suggested that in order to efficiently model a quantum system, we should consider building another quantum system that follows the same physical laws [49]. Over the past few decades, ultracold gases of atoms have emerged as a highly controllable platform for exactly this task: quantum simulation [70, 56, 153, 122, 156]. Although all atoms are composed of fermionic fundamental particles, the statistics of composite particles is determined by the total spin, and as a result, composite bosons can be produced us-

ing neutral atoms. This, in combination with laser trapping, laser cooling [121] and evaporative cooling [30], enabled the first Bose-Einstein condensation of a dilute gas of bosonic atoms [4, 29]. The quantum statistics of the constituent atoms resulted in macroscopic consequences: the condensate was observed to behave as a macroscopic wavefunction, with a well-defined phase. The observation of Abrikosov vortex lattices [91, 62, 1] strikingly demonstrated superfluidity: a phenomenon where a system flows without dissipation. Soon after the observation of BEC, fermionic atoms were cooled to quantum degeneracy [31, 145, 110, 61]. Although Pauli blocking prevents s-wave interactions between fermions in the same internal quantum state, a spin-mixture of fermions can experience interparticle interactions through a magnetic-field controlled resonance between a molecular bound state and an open channel. First studied by Hermann Feshbach in 1958 [46], these Feshbach resonances were realized as a method for controlling interactions in ultracold gases [143, 71]. In a Feshbach resonance, fermions were observed to form bosonic pairs and molecules which condensed at sufficiently high phase space densities [60, 157, 73, 155, 123]. Much like a BEC consisting of atomic bosons, these pair condensates exhibited superfluidity, directly demonstrated with the appearance of Abrikosov lattices in rotating fermionic pair condensates [154].

The simplest confinement for a gas of particles is a box. The uniform density inside a box allows for large signal for precision many-body thermodynamics, and a translationally invariant system for studying propagating waves. Ultracold atoms have historically been trapped in harmonic potentials. However, recent developments have shown the power of uniform Bose-Einstein condensates for measuring critical phenomena and turbulence, among others [55, 106, 108]. In this thesis, we cover our efforts to produce uniformly trapped ultracold fermions [102]. Since then, we have used the box to measure the contact of spin-balanced and polarized Fermi gases [150, 100] and measure both first and second sound in a fermionic superfluid [114].

Uniform systems are ideal for studying emergent phenomena. The presence of

translational symmetry allows for spontaneous modes to grow without being driven by an external trapping potential. This makes them ideal for studying supersolidity for instance. In supersolids, translational symmetry is spontaneously broken, but the system retains superfluidity [13, 119, 129]. There has been much recent interest in studying supersolids in stripe phases of BECs, as well as dipolar quantum gases [89, 88, 21, 10, 92]. Here, we study the spontaneous crystallization of a uniform gas under rotation. The only ingredients required are an artificial gauge field, and interparticle interactions. We find a regime where the crystallization growth rate is entirely set by interactions, and demonstrate that an interacting Landau gauge wavefunction is unstable towards forming a droplet array. These observations connect to the lowest Landau level, and pave a path forward towards more exotic states of matter that lie at even higher vortex densities [25].

1.1   Thesis outline

This thesis is organized as follows:

The second chapter of this thesis begins with an introduction to the theory behind Fermi gases in bulk. We cover the properties of ideal Fermi gases, and provide a brief overview on our use of Feshbach resonances to tune the interparticle scattering length. Finally, we provide intuition for a thermodynamic quantity known as the contact.

In Chapter 3, we discuss the second quantization of the rotating 2D harmonic oscillator, and discuss the ground state wavefunctions for a quantum gas under rotation.

In Chapter 4, we outline technical details on the homogeneous box for fermions. We discuss our optically tailored potentials, as well as our efforts to characterize the homogeneity of our trap.

In Chapter 5 , we finally arrive at the main scientific results with fermions. We present our measurements of the temperature dependence of the Fermi surface of

non-interacting fermions, and outline a momentum focusing method that allows us to effectively image in infinite time-of-flight. Then, we discuss thermometry as well as a method to calibrate our thermometers from the onset of the superfluid transition. We outline our measurements of the Joule-Thomson coefficient. Lastly, we discuss rf spectroscopy of the unitary Fermi gas. We outline how the contact varies with temperature, and show a clear effect of the onset of pairing on the contact.

In Chapter 6, we discuss our results on rotating quantum gases. We offer technical details on the construction of our newest experiment. Turning to the scientific results, we show how a saddle potential in the rotating frame enacts geometric squeezing and prepares Landau gauge wavefunctions in the lowest Landau level. Finally we discuss the spontaneous crystallization of interacting quantum Hall systems.

In Chapter 7, we provide an outlook for the two branches of experiments discussed in this thesis.

Chapter 2

Ultracold Fermi gases

In this chapter, we briefly present the background theory for Chapters 4 and 5, which concern ultracold Fermi gases.

2.1   Ideal Fermi gases

Fermi gases are characterized by Pauli blocking. Indistinguishable fermions occupy one quantum state, and prevent other fermions from occupying the same state. This is crucially different to bosons, which owing to the spin-statistics theorem, can occupy the same quantum state. Consider a system of two indistinguishable single particle states $|a\rangle$ and $|b\rangle$. Since they are identical, an exchange operation must preserve the wavefunction up to a global phase factor. In 3D, there are only two choices: a symmetric state where particle exchange results in a phase factor of $+1$, and an antisymmetric state, where the phase is -1. Fermions choose to be antisymmetric, with a general state given by the singlet

$$|\Psi\rangle \sim |a\rangle|b\rangle - |b\rangle|a\rangle \tag{2.1}$$

If the two quantum states are identical, $|a\rangle = |b\rangle$, and Ψ is identically zero. This

is forbidden, and is known as Pauli blocking.

We first consider ideal Fermi gases, which are unable to form superfluids due to a lack of interactions. At zero temperature, non-interacting fermions occupy each momentum state up to the Fermi momentum

$$k_F = (6\pi^2 n)^{1/3} \tag{2.2}$$

in 3D, where n is the density of particles. The corresponding energy is the Fermi energy $E_F = \hbar^2 k_F^2 / 2m$. The total number of particles is given by

$$N = \frac{V}{(2\pi)^3} \int d^3k \; n_k \tag{2.3}$$

where the momentum distribution of fermions is the Fermi-Dirac distribution

$$n_k = \frac{1}{e^{(\varepsilon_k - \mu)/k_B T} + 1}. \tag{2.4}$$

Here, T is the temperature, μ is the chemical potential, and $\varepsilon_k = \hbar^2 k^2 / 2m$. At high temperatures, this distribution smoothly transforms into the Maxwell-Boltzmann distribution

$$n_k = \frac{1}{e^{(\varepsilon - \mu)/k_B T}} \tag{2.5}$$

The transition between the two happens at

$$(\varepsilon - \mu) \sim k_B T \tag{2.6}$$

For the ideal Fermi gas, we can identify the chemical potential with the Fermi energy. So in other words, the gas behaves like a quantum gas when $T \leq T_F$, where $T_F = E_F / k_B$ is the Fermi temperature. It is worth noting here that the ideal Fermi gas has only two energy scales - the Fermi energy and the temperature, and only two lengthscales - the interparticle distance, set by the Fermi wavevector, and the

thermal de Broglie wavelength

$$\lambda_T = \frac{h}{\sqrt{2mk_BT}} \tag{2.7}$$

2.2   Tunable interactions

Fermi gases exhibit a rich phase diagram when interactions are turned on. Interactions allow fermions to correlate their motion, forming pairs, molecules, and more exotic strongly-correlated superfluids.
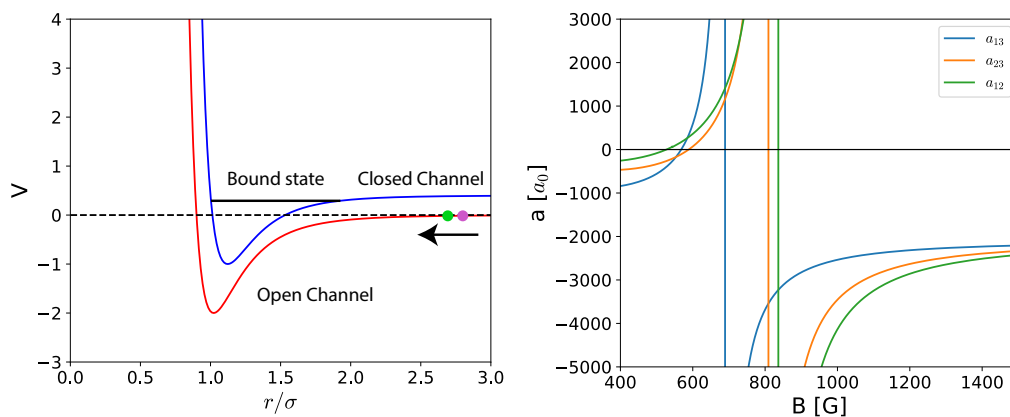
Figure 2-1: Feshbach resonances of ^{6}Li.   Left: the two-channel model of a Feshbach resonance. Here, two atoms approach each other through an open channel. This collision process can be resonant to a bound state of a closed channel. The energy of this bound state can be tuned using a magnetic field, to form wide Feshbach resonances (right).

In Figure 2-1, we show the mechanism for tuning interparticle interactions. Two free atoms of opposite spin states approach each other, interacting through a short-range contact interaction, typically characterized by a Lennard-Jones potential [87]:

$$V(r) = \epsilon \left[(\sigma/r)^{12} - (\sigma/r)^6 \right] \tag{2.8}$$

where σ and ϵ are the length and energy scales of the potential. In 3D, quantum

scattering can be written as

$$\psi(\mathbf{r}) = \psi_0(\mathbf{r}) + f(k,\theta)\frac{e^{ikr}}{r} \tag{2.9}$$

where an incoming wavefunction ψ_0 interacts and scatters into an outgoing component given by the second term. For fermions scattering at low temperatures, s-wave scattering dominates, and the scattering amplitude can be written as a function of k, independent of angle, an a phase shift δ satisfying the equation

$$k \cot \delta = -\frac{1}{a} + \frac{1}{2}r_e k^2 \tag{2.10}$$

where a is the scattering length and r_e is the effective range. If we only consider the r^{-6} term in the Lennard-Jones potential, the effective range can be written as

$$r_e = \left(\frac{mC_6}{\hbar^2}\right)^{1/4} \tag{2.11}$$

where in the notation of Equation 2.8, the coefficient $C_6 = \sigma^6 \epsilon$. For weakly-interacting Fermi gases, the two atoms barely interact with each other, and escape along the open channel. In these cases, a is small (on the order of $100a_0$). Note that since the effective range $r_e \approx 62a_0$ for ^{6}Li [151], the contribution from r_e can be ignored for low-k scattering if $a > r_e$. Scattering processes at much higher energies (e.g. in particle physics) involve high momenta. Those events can resolve r_e and generally, the structure of the contact interaction.

To vary the scattering length, a magnetic field bias can be used to tune the binding energy of a molecular state

$$E_b = \frac{\hbar^2}{ma^2} \tag{2.12}$$

where we assume $a > r_e$. This allows us to tune the scattering length through a

26

Feshbach resonance where the scattering length is given by

$$a = a_{bg} \left(1 + \frac{\Delta B}{B - B_0} \right) \tag{2.13}$$

located at B_0, characterized by a width ΔB and a background scattering length a_{bg}. Fortunately, ^{6}Li has a set of three wide Feshbach resonances at 690G (between states $|1\rangle - |3\rangle$), 809G ($|2\rangle - |3\rangle$), and 832G ($|1\rangle - |2\rangle$).

For positive scattering lengths, the system forms a condensate of Feshbach molecules at low temperatures. For negative scattering lengths, fermions form Cooper pairs that are loosely bound, and whose size is much larger than the interparticle distance. In between this BEC-BCS crossover, at the resonance, is a strongly-correlated system where the pair size is the same lengthscale as the interparticle distance [117, 77]. Here, much like the noninteracting system, there are only two energy scales, set by the Fermi energy, and the temperature. Due to the diverging scattering length, interactions are as strong as allowed by unitarity.

2.3   The contact

Fermions interacting through a short-range interaction in the s-wave channel are characterized by a thermodynamic quantity known as the contact [141, 139, 140]. In nuclear physics, the contact reveals information about short-range correlations [148] and momentum distributions within the nucleus [41]. Insensitive to the details of the interaction potential, the contact is a universal quantity, and measurements in ultracold gases can have direct implications on nuclear physics.

It can be shown that there is a universal relation between the tails of the momentum distribution of the system and the change of the total energy with respect

to the inverse scattering length:

$$\frac{\hbar^2 C}{4\pi m} = \frac{1}{V}\left.\frac{\partial E}{\partial(-1/a)}\right|_{S,N,V} \tag{2.14}$$

$$C = \lim_{k\to\infty} k^4 n_k \tag{2.15}$$

This holds whenever the effective range of the interaction is much smaller than the interparticle distance, or other lengthscales. Here, E is the total energy of the system, and C is the contact coefficient. The high-k tails of the momentum distribution are closely connected to the short-range behavior in real space. Along these lines, it can be shown that the pair correlation function at short distances is also set by the contact:

$$\chi_{nn}(r) = \lim_{r\to 0}\langle n_1(\mathbf{r_0} + \mathbf{r}/2)n_2(\mathbf{r_0} - \mathbf{r}/2)\rangle = \frac{C}{(4\pi r)^2} \tag{2.16}$$
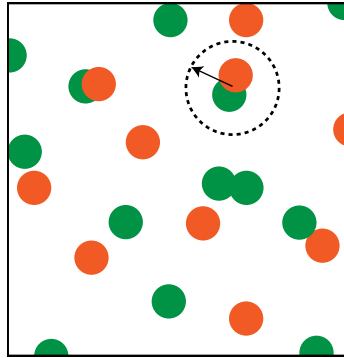
Figure 2-2: Short-range pair correlations. The contact measures the short-range pair correlations of an interacting system. In this cartoon, fermions of opposite spin states are labeled green and orange. The dotted circle denotes a candidate region over which the number of pairs are to be counted. On average, the contact for this system is likely to be on the order of 2.

Integrating over r, we find the number of pairs of opposite spin within a ball of

radius s is set by the contact.

$$N_p(s) = \int_0^s dr \, \chi_{nn}(r) \tag{2.17}$$

This provides an intuition for the contact - it quantifies short-range pair correlations (see Figure 2-2). Since the contact sets the weight of the momentum distribution at large momenta, it is mostly insensitive to temperature, which typically affects the Fermi surface. However it has been predicted that near the superfluid transition, the contact is sensitive to the pairing gap $\tilde{C} \sim (\Delta/E_F)^2$ [65, 116]. An observation of changes in the contact for temperatures above the superfluid temperature T_c could suggest the existence of a pseudogap, where pairing exists without superfluidity. As we show in chapter 5, the superfluid transition marks a sharp rise in the two-body contact. We leave further discussion on the contact and its relation to rf spectroscopy to those chapters.

Chapter 3

Rotating quantum gases

In this chapter, we provide theoretical background for a rotating system of ultracold atoms. We start with an intuitive physical picture for working in the rotating frame: the Foucault pendulum, and then introduce language from quantum Hall physics to understand noninteracting quantum particles in a rotating frame. We provide examples of ground state wavefunctions in the lowest Landau level, and discuss gauge choices for rotating quantum systems. Finally, we discuss turbulence in the context of quantum fluids, and present results from a numerical simulation of a condensate filled with vortices.

3.1   The Foucault pendulum

Foucault pendulums are oscillators in rotating frames. In 1851, Leon Foucault suspended a large pendulum from the dome of the Pantheon in Paris to measure the rotation of the Earth. Since the pendulum oscillates independently of the Earth's motion, to first degree, its precession in the rotating frame must inform us of the Earth's rotation. The motion of the pendulum can be expressed as epicycles, where the bob traces out arcs of a circular path. This is most evident when the pendulum oscillates at the same frequency as the frame rotation. Then, the bob undergoes
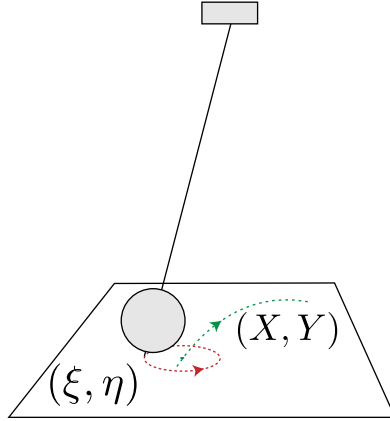
Figure 3-1: A Foucault pendulum.. A Foucault pendulum measures the rotation of a reference frame. Here, we place the pendulum oscillating at frequency ω in a frame rotating at a frequency Ω. The motion can be decomposed into a cylotron orbit (ξ, η) and a guiding center (X, Y). In much of this thesis, we will consider the case where $\omega = \Omega$, and non-driven guiding centers are effectively frozen. The (X, Y) space of guiding centers can be counter-intuitive: the spatial variables do not commute, and forces cause perpendicular displacement, not acceleration.

a fast cyclotron orbit with a stationary center. For every Foucault pendulum, the actual orbit can be decomposed into a slow guiding center oscillating at $\omega - \Omega$, and a fast cyclotron motion oscillating at $\omega + \Omega$. In Figure 3-1, we show a diagram of a Foucault pendulum oscillating for the case $\omega = \Omega$.

3.2   1D Harmonic Oscillator

We start without rotation or interactions, in one dimension. Although this is fairly trivial, it allows us to define a number of useful quantities. A quadratic Hamiltonian for a particle in a harmonic trap is:

$$H = \frac{p^2}{2m} + \frac{m}{2}\omega^2 x^2$$

where p is the momentum, ω is the trapping frequency, and x is position along the single dimension. To quantize this Hamiltonian, we construct a length scale using

these quantities and $\hbar$: the harmonic oscillator length:

$$d = \sqrt{\frac{\hbar}{m\omega}}$$

and a set of ladder operators

$$a = \frac{1}{\sqrt{2}} \left(\frac{x}{d} + \frac{ipd}{\hbar} \right) \tag{3.1}$$

$$a^\dagger = \frac{1}{\sqrt{2}} \left(\frac{x}{d} - \frac{ipd}{\hbar} \right) \tag{3.2}$$

Here, the commutation relation $[x, p] = \hbar$ implies $[a, a^\dagger] = 1$. Simple algebra will show that

$$x = \frac{d}{\sqrt{2}}(a^\dagger + a) \tag{3.3}$$

$$p = \frac{i\hbar}{d\sqrt{2}}(a^\dagger - a) \tag{3.4}$$

Writing the Hamiltonian in terms of the ladder operators:

$$H = \frac{p^2}{2m} + \frac{m}{2}\omega^2 x^2 \tag{3.5}$$

$$= \frac{-\hbar^2}{4md^2} \left(a^\dagger a^\dagger - a^\dagger a - aa^\dagger + aa \right) \tag{3.6}$$

$$+ \frac{md^2\omega^2}{4} \left(a^\dagger a^\dagger + a^\dagger a + aa^\dagger + aa \right) \tag{3.7}$$

$$= \frac{-\hbar^2}{4m} \frac{m\omega}{\hbar} \left(a^\dagger a^\dagger + aa - 2a^\dagger a - 1 \right) \tag{3.8}$$

$$+ \frac{m\omega^2}{4} \frac{\hbar}{m\omega} \left(a^\dagger a^\dagger + aa + 2a^\dagger a + 1 \right) \tag{3.9}$$

$$= \hbar\omega \left(a^\dagger a + \frac{1}{2} \right) \tag{3.10}$$

where in the middle we use the commutation relation and the definition of the harmonic oscillator length. This is the familiar quantum harmonic oscillator. Recogniz-

33

ing that $a^\dagger a$ is the number operator, the energy eigenstates are:

$$E_n = \hbar\omega \left(n + \frac{1}{2} \right)$$

3.3 2D Harmonic Oscillator with rotation

Now let's look at the 2D harmonic oscillator, initially without any rotation. Again, the Hamiltonian is:

$$H_0 = \frac{p_x^2 + p_y^2}{2m} + \frac{m}{2}\omega^2(x^2 + y^2)$$

Defining two annihilation operators like before, along x and y:

$$a_x = \frac{1}{\sqrt{2}} \left(\frac{x}{d} + \frac{ip_x d}{\hbar} \right) \tag{3.11}$$

$$a_y = \frac{1}{\sqrt{2}} \left(\frac{y}{d} + \frac{ip_y d}{\hbar} \right) \tag{3.12}$$

with creation operators defined as the adjoints of these two. Since the Hamiltonian is separable, we can use the same analysis as the last section to write:

$$H_0 = \hbar\omega(a_x^\dagger a_x + a_y^\dagger a_y + 1)$$

We can also define two new annihilation operators, that are the right-circular and left-circular polarized combinations of the previous operators (the meaning of this will become clearer when we bring in angular momentum):

$$a = \frac{a_x + ia_y}{\sqrt{2}} \tag{3.13}$$

$$b = \frac{a_x - ia_y}{\sqrt{2}} \tag{3.14}$$

This corresponds to choosing a symmetric gauge $\mathbf{A} = 2\Omega(-y, x, 0)$. We can write the Hamiltonian again in terms of these operators, and nothing much changes, since

all we've done is rotated the operators in the complex plane:

$$H_0 = \hbar\omega(a^\dagger a + b^\dagger b + 1)$$

Now let's turn on rotation. The Hamiltonian becomes:

$$H = H_0 - \mathbf{\Omega} \cdot \mathbf{L} \tag{3.15}$$

$$= H_0 - \Omega L_z \tag{3.16}$$

where we define our coordinate system so that $\mathbf{\Omega} = (0, 0, \Omega) = \Omega\,\mathbf{e}_z$. Now we can write the angular momentum operator in terms of our new ladder operators:

$$L_z = \hat{\mathbf{z}} \cdot (\mathbf{r} \times \mathbf{p}) = xp_y - yp_x \tag{3.17}$$

$$= \frac{1}{2}i\hbar\left((a_x^\dagger + a_x)(a_y^\dagger - a_y) - (a_y^\dagger + a_y)(a_x^\dagger - a_x)\right) \tag{3.18}$$

$$= \frac{i\hbar}{4}(a_x^\dagger a_y^\dagger + a_x a_y^\dagger - a_x^\dagger a_y - a_x a_y \tag{3.19}$$

$$- a_y^\dagger a_x^\dagger - a_y a_x^\dagger + a_y^\dagger a_x + a_y a_x) \tag{3.20}$$

$$= \frac{i\hbar}{2}(a_x a_y^\dagger - a_x^\dagger a_y) \tag{3.21}$$

$$= \frac{\hbar}{2}\left((b + a)(b^\dagger - a^\dagger) - (b^\dagger + a^\dagger)(a - b)\right) \tag{3.22}$$

$$= \frac{\hbar}{2}(bb^\dagger - ba^\dagger + ab^\dagger - aa^\dagger - (b^\dagger a - b^\dagger b + a^\dagger a - a^\dagger b)) \tag{3.23}$$

$$= \frac{\hbar}{2}(bb^\dagger - aa^\dagger + b^\dagger b - a^\dagger a) \tag{3.24}$$

$$= \hbar(b^\dagger b - a^\dagger a) \tag{3.25}$$

The two terms in the last line are the two number operators that are constructed from the ladder operators a and b. This gives us another physical insight: a and b are clearly operators that change angular momentum in opposite directions, since one number operator increases L_z and the other decreases it. So we can now write

35
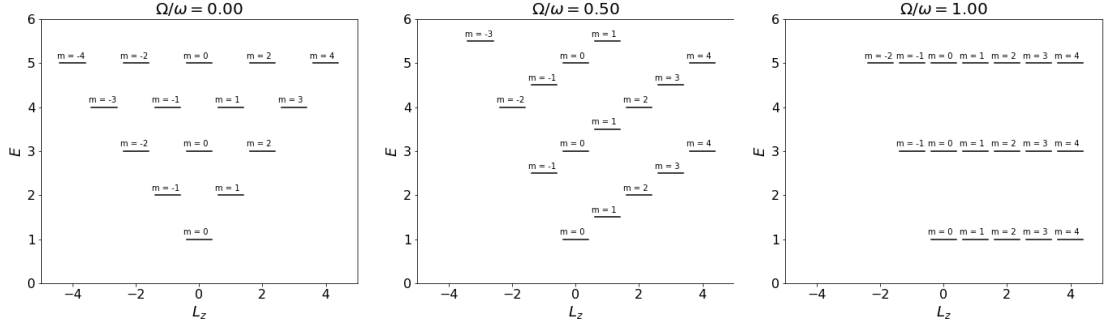
Figure 3-2: **Rotation and Landau levels.** As the rotation frequency Ω increases, the energy levels of the harmonic oscillator move from a symmetric fan shape to a set of degenerate flat bands known as Landau levels.

our full rotating 2D Hamiltonian in terms of the ladder operators:

$$H = \hbar\omega(a^\dagger a + b^\dagger b + 1) - \hbar\Omega(b^\dagger b - a^\dagger a) \tag{3.26}$$

$$= \hbar\omega + \hbar(\omega - \Omega)b^\dagger b + \hbar(\omega + \Omega)a^\dagger a \tag{3.27}$$

The energy eigenvalues are:

$$\varepsilon(n_a, n_b) = \hbar\omega + \hbar(\omega - \Omega)n_b + \hbar(\omega + \Omega)n_a \tag{3.28}$$

where the quantum numbers $n_{a,b} \in \mathbb{Z}^{\geq 0}$ correspond to the number operators $a^\dagger a$ and $b^\dagger b$. We can also define a new set of quantum numbers

$$n = n_a + n_b \tag{3.29}$$

$$m = n_a - n_b \tag{3.30}$$

so that the energy eigenvalues are

$$\varepsilon(n, m) = n\hbar\omega - m\hbar\Omega \tag{3.31}$$

36

and the eigenvalues of the angular momentum operator are $\hbar m$. In Figure 3-2, we show the change in energy levels as Ω increases. At $\Omega = \omega$, the energy landscape comprises of highly degenerate Landau levels separated by the cyclotron energy $2\hbar\omega$. Individual states in each Landau level are degenerate, and physically correspond to translations of the guiding centers. At $\Omega = \omega$, it costs no energy to move a cyclotron guiding center in the plane. Intuitively, this can be understood from the fact that there is no confining potential now, in the rotating frame.

3.4   Wavefunctions in the LLL

Let us consider the groundstate wavefunctions of the Hamiltonian in Equation 3.27. In the lowest Landau level (LLL), the wavefunctions $|\Psi_{LLL}\rangle$ satisfy

$$a|\Psi_{LLL}\rangle = 0 \tag{3.32}$$

We want to rewrite the annihilation operator a as a differential operator in real space.

$$a = \frac{a_x + ia_y}{\sqrt{2}} = \frac{1}{2}\left[\left(\frac{x}{d} + \frac{ip_x d}{\hbar}\right) + i\left(\frac{y}{d} + \frac{ip_y d}{\hbar}\right)\right] \tag{3.33}$$

$$= \frac{1}{2}\left[\left(\frac{x + iy}{d}\right) + i\left(\frac{d(p_x + ip_y)}{\hbar}\right)\right] \tag{3.34}$$

We can map $\mathbb{R}^2$ to $\mathbb{C}$ by making the complex variable and a corresponding differential operator

$$z = \frac{x + iy}{d} \tag{3.35}$$

$$\partial = \frac{p_x - ip_i y}{\hbar} \tag{3.36}$$

37
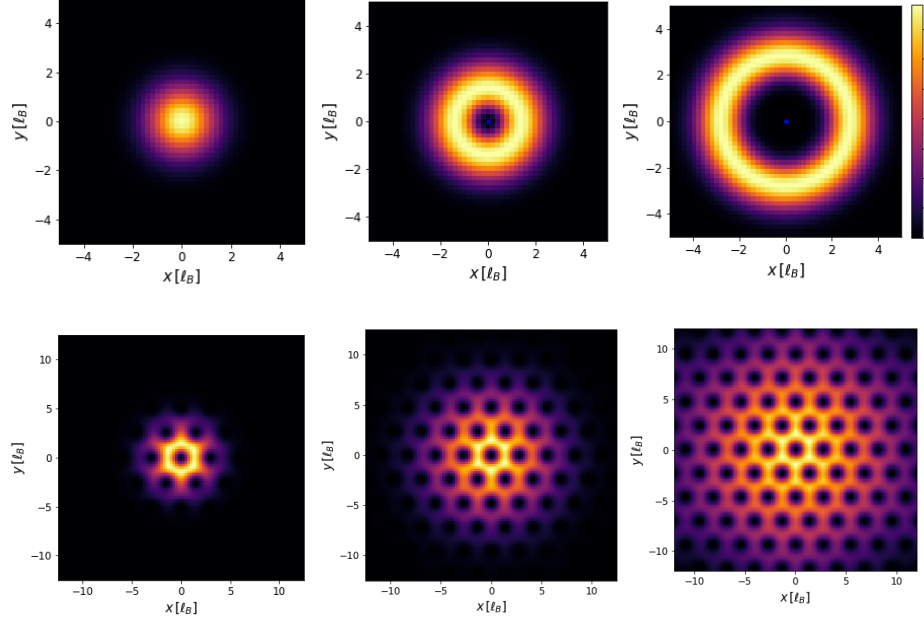
Figure 3-3: Ground state wavefunctions in the LLL. Using Equation 3.38, we display a set of possible wavefunctions to illustrate the behavior of the polynomial as the zeros are moved. In the upper row, zeros are added to the center of the system, left to right: none, one, and four. In the lower row, we place vortices on a triangular lattice, with the lattice constant being from left to right in units of the magnetic length ℓ_B: 3.00, 2.77, and 2.72, defined in the next section. As the vortex density grows, so does the edge of the cloud.

So, $a = \frac{1}{\sqrt{2}}(z + \bar{\partial})$, and

$$(z + \bar{\partial})|\Psi_{LLL}\rangle = 0 \tag{3.37}$$

$$|\Psi_{LLL}\rangle \propto f(z)e^{-z\bar{z}/4} \tag{3.38}$$

where $f(z)$ is any holomorphic (complex-differentiable) function. From complex analysis, all holomorphic functions are analytic, so it can be expressed as a polynomial of degree n. By the fundamental theorem of algebra, these can be factored into a product of zeros z_i

$$f(z) = \prod_i^n (z - z_i) \tag{3.39}$$

Here, the roots ξ_n correspond to the positions of zeros that can be freely translated

38

without changing the energy of the ground state. Indeed, the ground state of a rotating quantum gas in the LLL realizes random polynomials [16]. For illustration, we show in Figure 3-3 a set of polynomials that resemble common quantum gas systems. The first three are rotationally symmetric, while the lower three show an Abrikosov lattice. Interestingly, it is possible to reconstruct a Thomas-Fermi profile by optimizing the positions of the vortices [2].

3.5   Gauge freedom

There is a direct correspondence between systems of neutral atoms under rotation and systems of charged particles in a magnetic field. This connection underlies a major motivation for studying rotating quantum gases. Here we provide an outline for this correspondence. We begin by simply drawing an analogy through classical mechanics. Compare the Coriolis force on a neutral particle of mass M in a rotating frame with the Lorentz force on a particle of charge q in a magnetic field $\mathbf{B}$. With each particle moving with velocity $\mathbf{v}$,

$$\mathbf{F}_{\text{Coriolis}} = 2M\mathbf{v} \times \mathbf{\Omega} \tag{3.40}$$

$$\mathbf{F}_{\text{Lorentz}} = q\mathbf{v} \times \mathbf{B} \tag{3.41}$$

The equivalent magnetic field for a system of neutral atoms under rotation is $\mathbf{B} = \frac{2M}{q}\mathbf{\Omega}$. We know from classical electromagnetism that a magnetic field can be alternatively expressed as a vector potential so that $\mathbf{B} = \nabla \times \mathbf{A}$. The Lagrangian can be written using the vector potential

$$L = \frac{1}{2}m\dot{\mathbf{r}}^2 + q\dot{\mathbf{r}} \cdot \mathbf{A} \tag{3.42}$$

The Euler-Lagrange equations using this Lagrangian result in the equation of motion $\mathbf{F}_{\text{Lorentz}} = m\ddot{\mathbf{r}}$. These equations are invariant under the gauge transformation
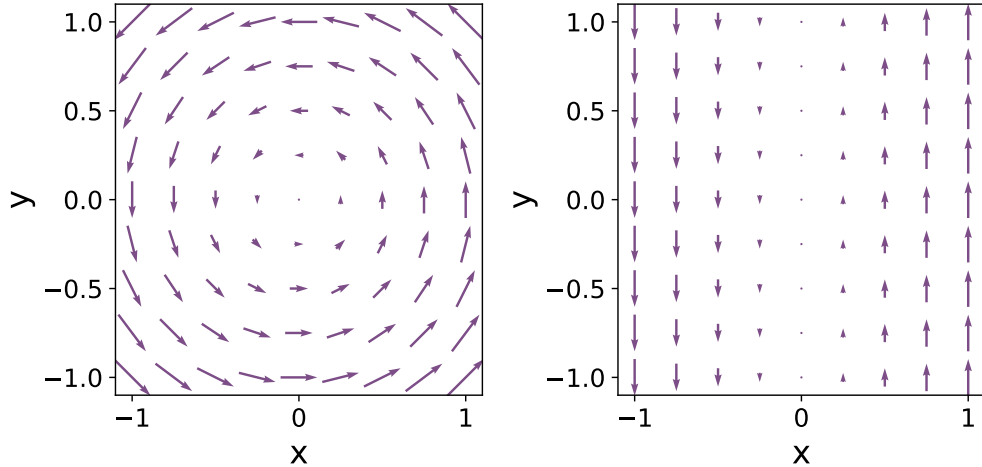
Figure 3-4: Gauge choices. Here we illustrate two common choices for the vector potential **A**. The symmetric gauge (left) preserves rotational symmetry, while the Landau gauge (right) preserves translational symmetry along y.

$\mathbf{A} \to \mathbf{A} + \nabla\phi$, where ϕ is a scalar field. This is readily verified by noting the vector identity $\nabla \times \nabla\phi = 0$. The Hamiltonian is

$$H = \mathbf{p} \cdot \dot{\mathbf{r}} - L \tag{3.43}$$

$$= \frac{1}{2}m(\mathbf{p} - q\mathbf{A})^2 \tag{3.44}$$

where $\mathbf{p} = \partial L/\partial\dot{\mathbf{r}}$ is the canonical momentum. Note that while **A** is gauge-dependent, so is the canonical momentum **p**, and the Hamiltonian – a physical observable – is gauge-invariant. The Landau level energy structure exists regardless of the gauge choice. In Figure 3-4, we show two options for the vector potential. One is in the symmetric gauge, $\mathbf{A} = \frac{1}{2}B\langle -y, x, 0\rangle$. The Hamiltonian using the symmetric gauge is the one we have considered so far in the rotating system, and results in the set of ground state wavefunctions described in Equation 3.38. This choice of gauge preserves rotational symmetry, and is an ideal choice when the underlying geometry of the system (e.g. any scalar potentials) is rotationally symmetric. Another choice of

40

gauge is the Landau gauge $\mathbf{A} = B\langle 0, x, 0\rangle$, resulting in the Hamiltonian

$$H = \frac{1}{2m}(p_x^2 + (p_y - qBy)^2) \tag{3.45}$$

$$= \frac{p_x^2}{2m} + \frac{1}{2m}(p_y - 2\Omega x)^2 \tag{3.46}$$

$$= \frac{\hbar^2 k_x^2}{2m} + \frac{1}{2}m\omega_c^2(x - k_y\ell_B^2)^2 \tag{3.47}$$

where we have returned to the language of rotating neutral particles. Here, $\omega_c = 2\Omega$ is the cyclotron frequency and

$$\ell_B = \sqrt{\frac{\hbar}{m\omega_c}} \tag{3.48}$$

is the magnetic length. Since $[H, p_y] = 0$, the quantum eigenstates of H are plane waves in y. In the x direction, the Hamiltonian is a displaced harmonic oscillator, so the eigenstates in x are the product of Hermite polynomials H_n and a gaussian function:

$$\psi(x, y) \sim \exp(iky)H_n(x + k\ell_B^2)\exp\left[-\frac{1}{2\ell_B^2}\left(x + k\ell_B^2\right)^2\right] \tag{3.49}$$

For the lowest Landau level, $n = 0$ and $H_0(x + k\ell_B^2) = 1$. Notably, the gauge field couples momentum in y with position in x. This effect will feature heavily in chapter 6, where interactions create an interference pattern between displaced momentum components of a wavefunction.

So which gauge should one choose? From a symmetry argument, the Landau gauge is an appropriate choice when the system breaks rotational symmetry but is translationally invariant along one direction. A classic example where the Landau gauge is an appropriate choice is the story of the quantum Hall effect. For further reading on the quantum Hall effect, we refer the reader to the excellent review in [144]. In chapter 6, we will consider the effect of a rotating anisotropic potential $V(x, y) = \frac{1}{2}m(\omega^2 - \Omega^2)(x^2 + y^2) + \frac{1}{2}m\epsilon\omega^2(x^2 - y^2)$. When $\omega = \Omega$, the first term is identically zero and scalar potential is a saddle in the rotating frame. Particles placed in this saddle

potential drift along a zero equipotential - extending diagonally outwards from the center. As we will see, the resulting system is translationally invariant along the diagonal, and the Landau gauge wavefunctions are a good basis for the system. This is seen by rotating the coordinates of the saddle potential $V(x, y) \sim m\Omega(x^2 - y^2)$ by $\pi/4$ to obtain the potential $V(\tilde{x}, \tilde{y}) \sim m\Omega\tilde{x}\tilde{y}$, where the equipotentials are aligned with the (x, y) coordinate space of the Landau gauge. We can now construct a gauge transformation from a phase shift given by the scalar saddle potential: $U = e^{im\Omega xy/\hbar}$. Applying this transformation to the symmetric gauge Hamiltonian $H_s = H_0 - \Omega L_z$ recovers the Landau gauge Hamiltonian $H_L = UH_SU^\dagger$ in Equation 3.47. Thus, by breaking the rotational symmetry, the saddle potential acts as a gauge transformation from the symmetric gauge to the Landau gauge.

3.6   Turbulence

We now discuss a numerical study of quantum turbulence. The motivation for this study lies in the turbulence we observe in the long time evolution of a Bose-Einstein condensate under rotation in an anisotropic harmonic trap (see Figure 6-12). Turbulence is ubiquitous in nature but challenging to describe. Unlike laminar flow, where the fluid velocity is predictable and uniform, turbulent flow is characterized by chaos and the appearance of self-similar structures in fluids. Due to its chaotic nature, turbulence lends itself to statistical analysis. The resulting insights we obtain are often universal – they do not depend on the kind of fluid, its temperature, or the scale of its turbulent structures. Thus, insights obtained for one fluid are readily transferred to a vast range of physical phenomena.

One of these insights was discovered in 1941, when Kolmogorov predicted that the velocity field of an incompressible turbulent fluid should be self-similar over a large range of scales [79]. This self similarity comes from a cascade of energy from one lengthscale to another. From the cascade, it can be shown that energy spectrum
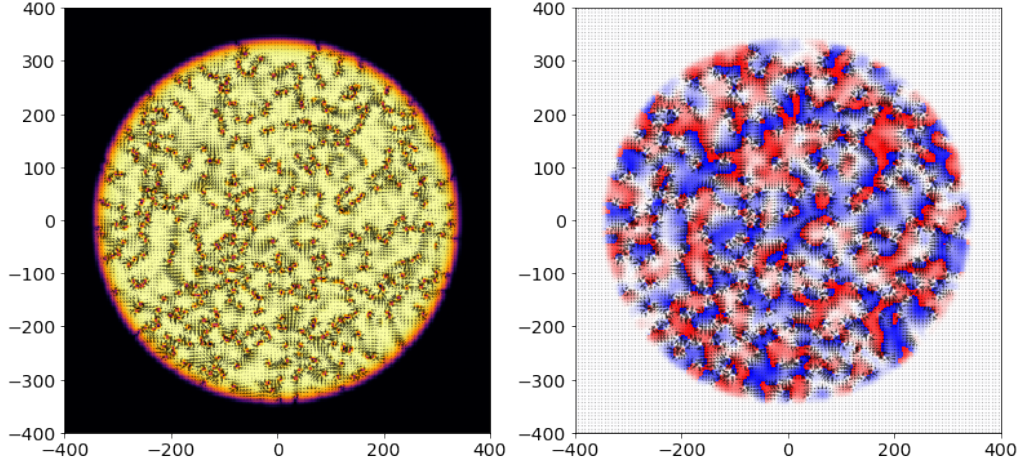
Figure 3-5: Simulated 2D quantum turbulence. Here we display the density (left) and phase (right) of a simulated wavefunction. The fluid flow profile is overlaid on each as a vector field. Here the units of the x and y axes are in microns.

follows a power law:

$$E(k) \sim k^{-5/3} \tag{3.50}$$

Turbulent flow is a well-known solution to the Navier-Stokes equation. While the Kolmogorov scaling law can be rigorously derived from the Navier-Stokes equation, a proof of the existence and smoothness of the solutions remains elusive [42]. For quantum fluids, turbulent cascades and their associated power laws have been observed in liquid helium [34], as well as 2D [74] and 3D [108] Bose-Einstein condensates. Here, we present the energy spectrum of a turbulent uniform Bose-Einstein condensate, simulated using the Gross-Pitaevskii equation. For more on the simulation, see Equation 6.6 and Appendix A. We begin by initializing a condensate within a uniform 2D disk trap, and nucleating vortices at random positions. The resulting vortex tangle is shown in Figure 3-5. To obtain the energy spectrum, we need the velocity of the incompressible component of the fluid flow. The total flow field is given by the gradient of the phase:

$$\mathbf{v}(\mathbf{r}) = (\hbar/m)|\psi(\mathbf{r})|\nabla\phi \tag{3.51}$$

The gradient of the phase can be obtained from the following differentiation

$$\nabla e^{i\phi(\mathbf{r})} = ie^{i\phi(\mathbf{r})}\nabla\phi \tag{3.52}$$

$$\nabla\phi = -ie^{i\phi(\mathbf{r})}\nabla e^{i\phi(\mathbf{r})} \tag{3.53}$$

The gradient of the exponential can be numerically obtained from the wavefunction $\psi = \sqrt{\rho}e^{i\phi(\mathbf{r})}$. Note that this can also be understood as obtaining the probability flux $\mathbf{j}$

$$\mathbf{j} = \frac{1}{2}(\psi^*\nabla\psi - (\nabla\psi)^*\psi) \tag{3.54}$$

We now want to separate the flow into a compressible component and an incompressible component. The incompressible component has no divergence:

$$\nabla \cdot \mathbf{v}_{ic} = 0 \tag{3.55}$$

To separate $\mathbf{v}$ into its components, we take a Fourier transform:

$$\nabla \cdot \mathbf{v}_{ic} = \int \mathbf{k} \cdot \widetilde{\mathbf{v}}e^{i\mathbf{k}\cdot\mathbf{r}}d\mathbf{r} \tag{3.56}$$

Since both sides must be identically zero, the incompressible component of the flow is perpendicular to $\mathbf{k}$ in momentum space: $\mathbf{k} \cdot \widetilde{\mathbf{v}}_{ic} = 0$. So, we can project the flow into parallel and orthogonal components: $\mathbf{v} = \mathbf{v}_c + \mathbf{v}_{ic}$ where in Fourier space, the parallel (to $\mathbf{k}$) component is :

$$\widetilde{\mathbf{v}}_c = \frac{\mathbf{k} \cdot \mathbf{v}}{k^2}\mathbf{k} \tag{3.57}$$

and the orthogonal component is:

$$\widetilde{\mathbf{v}}_{ic} = \widetilde{\mathbf{v}} - \widetilde{\mathbf{v}}_c \tag{3.58}$$
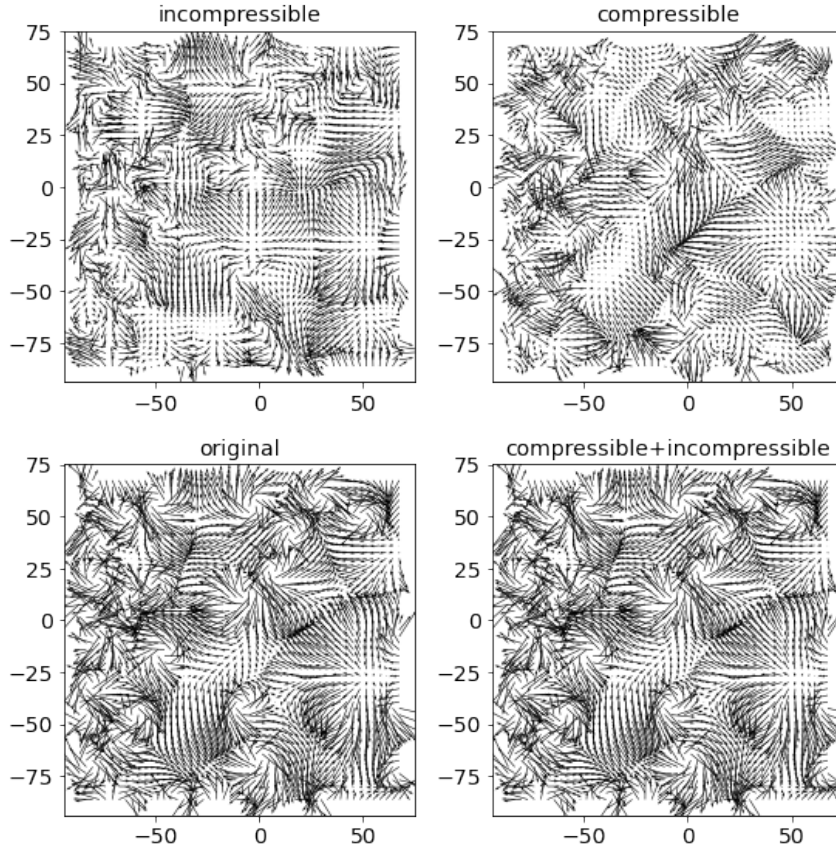
Figure 3-6: Compressible and incompressible flow. The compressible and incompressible components of the flow can be separated in momentum space. Here we show vector fields of both components for a turbulent 2D condensate.

In Figure 3-6, we show the compressible and incompressible components of the flow. Now, from the incompressible flow in momentum space, we can obtain the incompressible energy spectrum

$$E_{ic} = 2\pi \mathbf{k} |\widetilde{\mathbf{v}}_{ic}|^2 \tag{3.59}$$

In Figure 3-7 we show the evolution of the energy spectrum in time, and compare it to scaling laws observed in a vast range of turbulent media. We observe a scaling that is consistent with Kolmogorov's prediction: 1.65 ± 0.06.

45
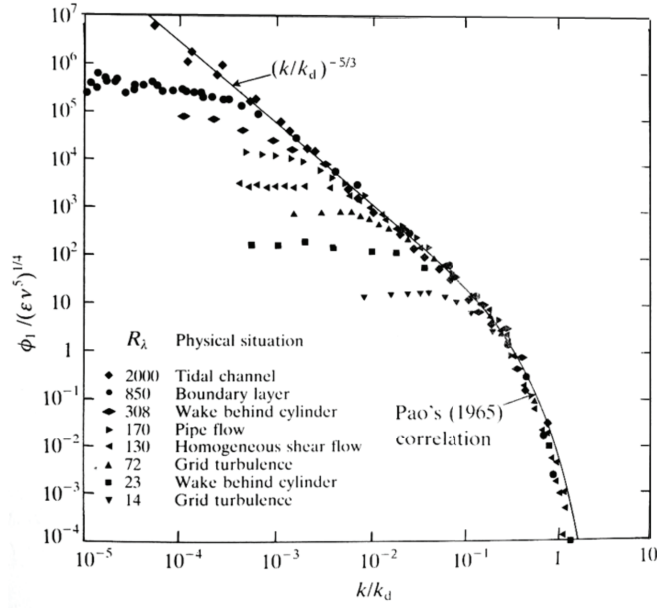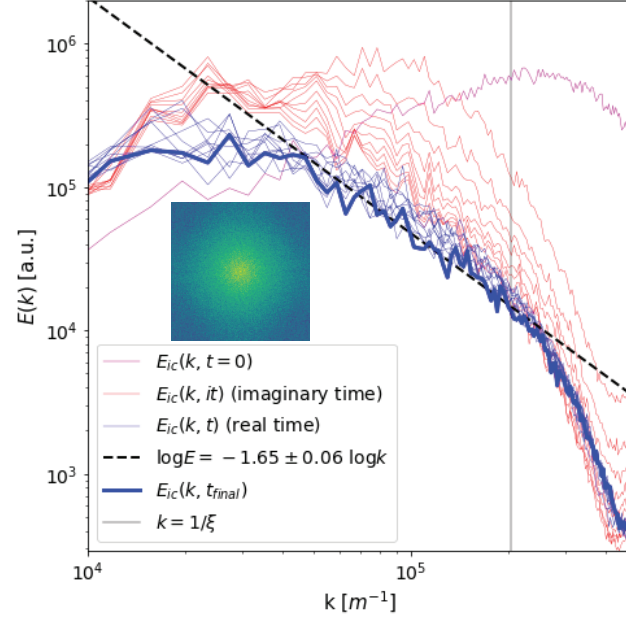
Figure 3-7: Energy spectrum of turbulent systems. Here we show the incompressible energy spectrum of a 2D quantum turbulent system (upper plot), and compare with a the energy spectra from a range of turbulent media (lower plot reproduced from [94]). In an inset, we show the 2D Fourier transform of the incompressible flow $|\widetilde{\mathbf{v}}(k)|$. The apparent four-fold pattern is an aliasing from the window size: we are only concerned with the region near the center. The time evolution of the energy spectrum shows a convergence to a Kolmogorov-like scaling law, over about a decade of energy scales. Here, the vertical line shows the healing length $\xi = \frac{\hbar}{\sqrt{2mgn}}$.

Chapter 4

Tailored potentials

In this chapter we discuss the tailored potentials that produce homogeneous atomic Fermi gases.

4.1   Optically tailored potentials

We generate potentials by shaping light. These work by employing the AC Stark effect. Atoms are polarizable - the electric field of light can induce a small dipole that experiences a potential in the beam of light. In the dressed atom picture, a light field changes the energies of the quantum states of the atom. This can be seen by writing out the time evolution of a wavefunction $|\psi\rangle = c1|1\rangle + c2|2\rangle$ in a two level system:

$$i\frac{d}{dt}\begin{pmatrix} c1 \\ c2 \end{pmatrix} = \frac{1}{2}\begin{pmatrix} \delta & \Omega \\ \Omega & -\delta \end{pmatrix}\begin{pmatrix} c1 \\ c2 \end{pmatrix} \tag{4.1}$$

where Ω is the Rabi frequency of the light. The eigenvalues to this differential equation are $\lambda = \pm\frac{1}{2}\sqrt{\delta^2 + \Omega^2}$. For large detunings, $|\delta| \gg \Omega$, and the eigenvalues

are shifted from their original values of $\delta/2$ by the following quantity:

$$\Delta U = \frac{\hbar \Omega^2}{4\delta} \quad (4.2)$$

For $\delta < 0$, the light is red detuned, and the potential is attractive. For $\delta > 0$, it is repulsive. For a homogeneous trap, a repulsive potential is ideal since it is dark within the bulk of the trap. In dark traps, the majority of the inhomogeneity comes from the edges, which have a finite resolution. So, the ideal box potential is a set of sharp confining walls.
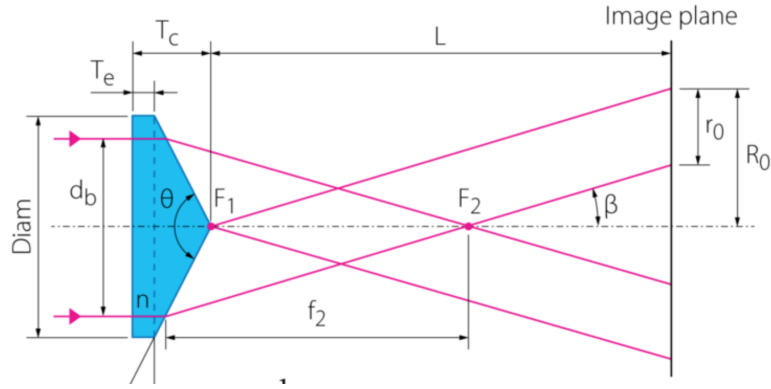
Figure 4-1: In the far field, an axicon generates a ring beam. Figure from [3]

We started with a set of requirements: the trap height needed to be taller than 10kHz, the edge sharpness needed to be limited by our optical resolution, and the setup needed to be stable enough to avoid large mechanical vibrations during experiments. Although directly masking a large gaussian beam in the center would work, a large portion of the power (both inside the dark region as well as far in the gaussian tails) would be dumped, instead of focused around the edges. Axicons provide an ideal solution. Used for industrial hole-cutting, the axicon is simply a conical element [95]. In the far field at distance L, it generates a ring with a radius
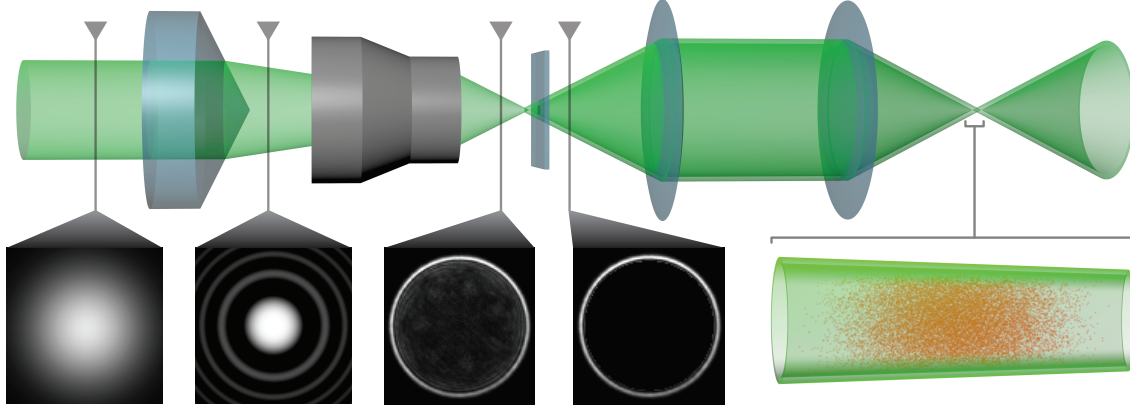
Figure 4-2: Axicon for a dark trap.   Top: the axicon setup focuses 532nm light into a ring pattern. However, the ring radius varies with distance along z, so the effective shape is a cone. We use a silver mask to block light from the center from reaching the atoms.

given by

$$R = L \tan[(n-1)\alpha] \tag{4.3}$$

where n is the refractive index of the material, $\alpha = 180° - \theta$ is the cone angle of the axicon (see Figure 4-2).

The thickness of the ring is simply the gaussian waist w_0 of the incoming beam. However, this limits us to fairly thick rings ($w_0 \sim$mm), whereas we would like to focus the beam down to tens of microns. In the near field, axicons generate a Bessel beam with the following electric field profile:

$$E(r,z) = E_0 \sqrt{\frac{2\pi k z w_0 \sin \beta}{z_{max}}} e^{-\frac{z^2}{z_{max}^2}} J_0(kr \sin \beta) \tag{4.4}$$

Here, β is as shown in the figure; J_0 is the zeroth order Bessel function of the first kind; $z_{max} = w_0/\tan \beta$ is called the Bessel range - the range over which the beam does not diffract. Although this is not a ring potential, its Fourier transform is a ring. This may be obvious from the fact that far field light propagation (Fraunhofer) effects a Fourier transform. More precisely, the 2D Fourier operator in polar coordinates is
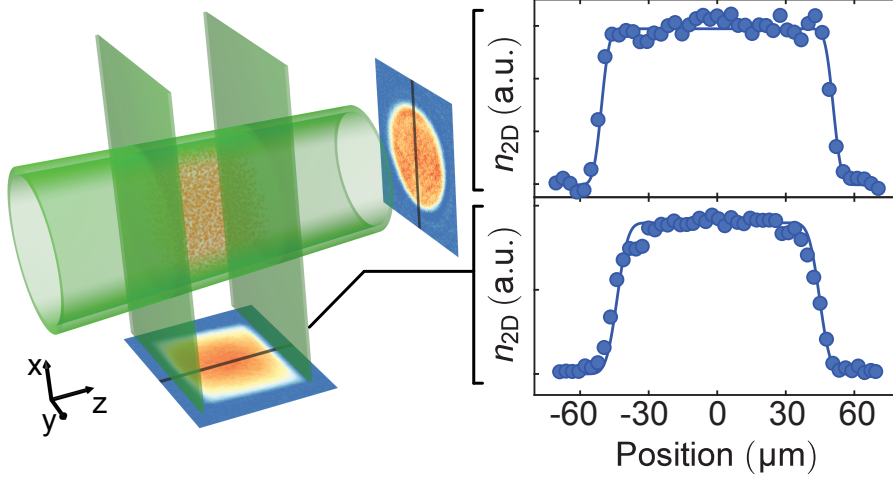
Figure 4-3: A uniform box potential for fermions. We overlap 532nm hollow beams to trap ^{6}Li atoms in a dark homogeneous trapping potential. Right: column-integrated atomic density profiles in the uniform box trap.

as follows:

$$E(r') = \int dr\, E(r) J_0\left(\frac{rr'}{f}\right) r \tag{4.5}$$

Using the orthogonality of Bessel functions,

$$\int dr\, J_0(R_o r) J_0\left(\frac{rr'}{f}\right) r = \frac{\delta(r' - R_0)}{R_0} \tag{4.6}$$

This is a delta function ring, which is exactly what we want. In practice, the profile is convolved with the propagated gaussian waist of the input beam. To generate this beam profile without having to propagate to the far field, we use a lens (see Figure 4-2). This also achieves a narrow wall thickness since instead of a diverging gaussian beam, the wall thickness is set by the focal length of the lens. Now, the ring size is given by

$$R = (n-1)\alpha f \tag{4.7}$$

where f is the focal length of the lens. We use a 10mm microscope objective to

50

generate a ring of radius $R = 60\mu$m and a thickness of 3μm before the vacuum chamber. We send this beam into the chamber with a 1:1 telescope configuration, and combine the beam with a set of perpendicular sheet beams that act as endcaps to the cylinder. To ensure that the inside of the box is dark, we use a mask. We detail the mask preparation steps in Appendix B. The resulting light profile is shown in Figure 4-3.

While the mask suited us well in the densely packed environment of the old lab, we implemented a more configurable option using a digital micromirror device in the new lab (see Figure 4-4). We use a cube to multiplex a stirring beam, which is then sent to both a monitor camera as well as the atoms after the objective. The ring is 4mm at the DMD device, and 100μm at the objective.
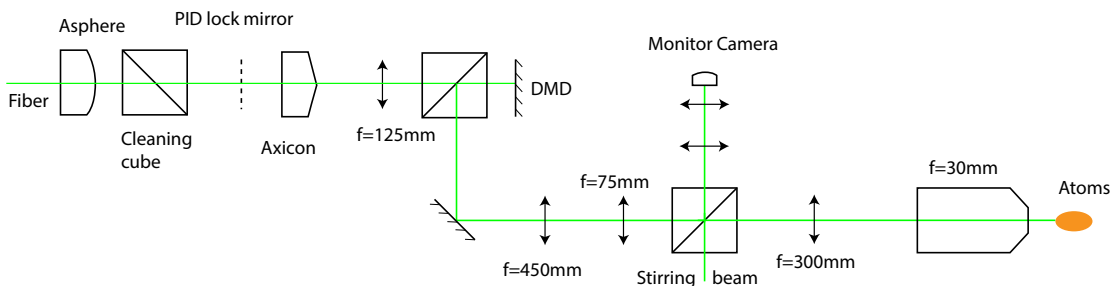
Figure 4-4: Tailored potential optical setup. We use an axicon to send a 4mm diameter ring beam on the DMD. The DMD masks the central part of the beam to ensure it is as dark as possible.

4.2   Trap characterization

In this section, we outline two methods we use to characterize the homogeneity of our trap. The first method measures the sharpness of the walls. Modeling the walls as a power law, we plot the measured cloud radius as a function of Fermi energy. For an ideal box, the Thomas Fermi radius is independent of the Fermi energy. For finite wall sharpness, the gas 'recedes' into the box as the number of atoms decreases. We find that our implementation of the box is equivalent to $V(r) \sim r^{16.2\pm1.6}$.

Another measure of the trap homogeneity, one that includes the nonuniformity at the center of the box, is the probability of finding an atom at a particular density. For a perfectly homogeneous cloud, this is a delta function: all atoms are likely to be found at the constant density. However, for a harmonic trap, this function is almost uniform [102]. We find that for our homogeneous trapped gas, the probability is sharply peaked around the central density.
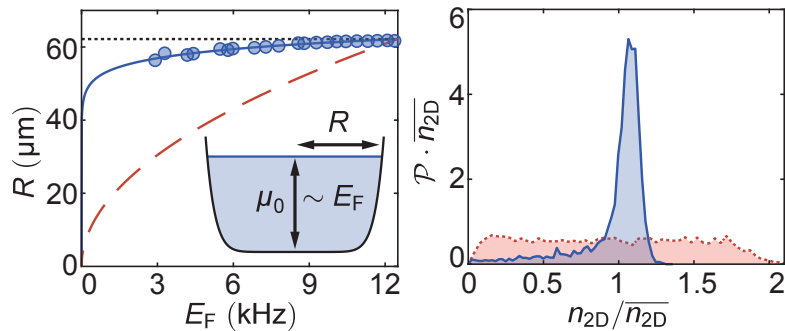
Figure 4-5: Box homogeneity characterization. Left: Compared to a harmonic trap (red dashed line), the Thomas-Fermi radius of our box is closer to a perfect box (black dashed line), as a function of the Fermi energy. The blue line is a power law fit to $V(r) \sim r^{16}$. Right: A comparison of the probability of finding a particle at a given density, between the uniform trap (blue) and the harmonic trap (red).

Chapter 5

Thermodynamics of Fermi gases

In this chapter, we present the first science results with homogeneous Fermi gases. We start the chapter with momentum distributions of Fermi gases, discussing both the ideal noninteracting Fermi gas, and the spin-balanced unitary superfluid. The next section covers thermometry, and outlines a number of methods we have used to extract global temperatures in our gases. We provide a discussion of the Joule-Thomson coefficient, and present measurements using the local density approximation.

The remainder of the chapter is dedicated to the measurement of the spectral response of a balanced Fermi gas at unitarity. We provide details on radiofrequency (rf) spectroscopy methods in the box and the hybrid potential, and discuss how we enzsure that we remain in linear response. Diffusion is a significant obstacle when it comes to measuring spectra in the hybrid trap, and we will provide measurements that place bounds on the resolution of rf spectroscopy in inhomogeneous trapping potentials. Spectroscopy measurements in the box do not suffer from diffusion, so the subsequent measurements were all performed in the box. We chart the evolution of rf spectral response and discuss the shape of the high frequency tails. These tails are influenced by both the interactions in the final state after the rf transfer as well as the contact. We present our measurement of the temperature dependence of the contact, and compare with theoretical predictions. Finally, we show how

the temperature dependence of the spectral response can be used to perform insitu thermal imaging and measure second sound.

The research presented in this chapter has resulted in the following publications:

B. Mukherjee, Z. Yan, P. B. Patel, T. Yefsah, J. Struck, M. W. Zwierlein, "Homogeneous Atomic Fermi Gases," Phys. Rev. Lett. 118, 123401 (2017)[102]

B. Mukherjee, P. B. Patel, Z. Yan, R. J. Fletcher, J. Struck, M. W. Zwierlein, "Spectral Response and Contact of the Unitary Fermi Gas," Phys. Rev. Lett. 122, 203402 (2019)[100]

5.1 Momentum distributions

As a direct consequence of Pauli blocking, degenerate fermions fill up low energy states, forming what is known as the Fermi sea. Many phenomena, from transport to superfluidity, are a result of physics near the surface of that sea, at the Fermi surface.

5.1.1 Previous experimental work

Two prominent methods for measuring the Fermi surface in solid state systems connect directly with topics discussed in this thesis. The first involves a technique that exploits the quantum Hall effect. Following the discussion in Section 3.4, an applied magnetic field causes oscillations in the conductivity of the sample. It was shown by Onsager that the frequency of these oscillations is directly related to the cross sectional area of the Fermi surface:

$$A_\perp = \frac{2\pi e \Delta H}{\hbar c} \tag{5.1}$$

By changing the direction of the B-field, it is possible to map out the shape of the Fermi surface. Although the method does not provide the entire momentum distribution, in solid state systems, the relevant quantity is often the Fermi surface.

The second method is similar in principle to the method described in this chapter. Angle-resolved photo-emission spectroscopy (ARPES) is a technique used to map the entire spectral function of a solid state system [26]. The technique works on the principle of photoemission spectroscopy, where a photon that impacts a surface at energy $E = h\nu$ can release an electron at an angle θ to the surface normal with energy $E_k = h\nu - E_b$ where E_b is the binding energy of the electron. This constrains the magnitude of the total momentum, $p = \sqrt{2mE_k}$. The angle provides another piece of information: the component of the momentum parallel to the crystal lattice: $\mathbf{p}_\parallel = p \sin\theta$. Both the energy and the angle of the emitted electrons can be measured with a tool known as an electron spectrometer. In the spectrometer, electrons with different kinetic energies are separated with a hemispherical electrode, and analyzed on a multichannel plate. The resulting data provide a map of the spectral weight at a point in momentum and energy. A simple example is a free electron: an ARPES measurement would result in a parabolic spectral map, representing the free particle dispersion relation. With interactions, the picture changes, and details of the electronic band structure can be obtained from an ARPES measurement. As a byproduct of obtaining the full spectrum of excitations, ARPES also provides the shape of the Fermi surface. The Fermi surface is simply a slice of the energy-momentum map at a constant Fermi energy E_F. Note that since ARPES is a surface measurement, it is best suited for two dimensional solid state systems.

In typical cold atom experiments, the atoms are trapped in nonuniform harmonic potentials. These inhomogeneous traps result in a broadening of the Fermi surface. Since the density is typically distributed over a large range of k_F (see section 4.2), each shell in an inhomogeneous cloud contributes to a Fermi surface at a different k_F. In addition, the density in the trap varies so the size of each shell also depends on the
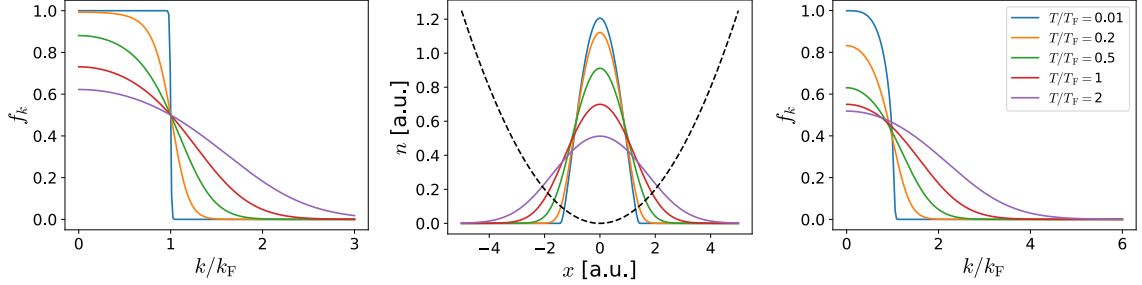
Figure 5-1: Trap averaged Fermi-Dirac momentum distributions. The familiar Fermi-Dirac distributions f_k are shown in (a) for homogeneous ideal Fermi gases at a range of temperatures ($T/T_F = 0.01, 0.2, 0.5, 1$, and 2). The insitu density distributions for 1D harmonically-trapped ideal Fermi gases are shown in (b), and the corresponding trap-averaged momentum distributions are shown in (c). Even for very low temperatures, the apparent Fermi surface is no longer sharp at $k = k_F$.

global temperature of the gas. Typically, the trap-averaged momentum distribution of a degenerate cold Fermi gas looks unlike a Fermi-Dirac distribution (see Fig. 5-1). Thus, a simple time of flight measurement from a trapped gas would not reveal a clear Fermi surface.

This obstacle can be partly overcome by selecting a subset of the trapped gas that is roughly at a constant density. Selection can be performed using hollow beams of pumping light that transfer atoms into an optically dark state just before the time-of-flight imaging. This technique, pioneered at JILA, has resulted in measurements of the Fermi surface, the contact, and the spectral function [35, 126, 125]. However, many of these measurements remained sensitive to the fraction of the atoms probed. Since a smaller fraction probed meant a more homogeneous measurement, there was a tradeoff between signal to noise and homogeneity. Ideally, those two concerns should be decoupled, and the gas should be as homogeneous as possible. Furthermore, the temperature dependence of the contact remained mysterious, and in conflict with most theories, with no resolution even after half a decade [33].

5.1.2 Momentum focusing

Having motivated the need for a homogeneous trap for fermions, we now turn to our method of measuring the momentum distribution. A popular method for measuring the temperature of a thermal gas is to release it from the trap and allow for a free ballistic expansion [76] Faster atoms travel further; as a result, the resulting atomic density profile reveals the temperature T of the Maxwell-Boltzmann distribution in the initial gas:

$$T = \lim_{t \to \infty} \frac{m}{2k_B} \frac{\sigma^2}{t^2} \tag{5.2}$$

Here σ is the width of the cloud after expansion, t is the duration of expansion and m is the mass of each atom. Note that the direct relationship between the width of the cloud in time-of-flight and the temperature is only true in the limit of infinitely long expansion. After a finite expansion time t, the position of an atom with initial momentum $p(0)$ is $r(t) = r(t = 0) + p(0)t/m$. Thus for shorter times, the width of the cloud is convolved with the initial density profile and obtaining the initial momentum distribution can be challenging. Furthermore, the iconic bimodal profiles that represent the onset of BEC reveal another important obstacle in time-of-flight measurements: hydrodynamic flow. For sufficiently large densities, the interatomic interactions are relatively strong. While thermal atoms quickly expand, decreasing the interaction strength to negligible values, the condensate remains at a high density. Thus, the profile of a condensate after a time-of-flight expansion is a hydrodynamic expansion from a trapped gas, whose profile is strongly influenced by both the insitu density profile as well as hydrodynamic expansion. This expansion has been used to obtain properties of strongly-interacting gases, from the viscosity of the unitary Fermi gas [14] to properties of normal Bose gases [52].

We now consider the two important ingredients for time-of-flight measurements: long expansion times, and low interactions during expansion. We achieve the first

through a technique called momentum-space focusing [136, 146, 103]. From observing local phase fluctuations in 1D Bose gases, to pinpointing the emergence of the presuperfluid regime in 2D Bose gases, condensate focusing has been successfully used to perform pioneering momentum-space measurements. As the name suggests, the method takes inspiration from optics. In optical systems, phase gradients in the near-field determine intensity patterns at far-field. Thus, far-field propagation can be thought of as a Fourier transform, mapping momentum-space to real-space. As in cold atom systems, far-field propagation (or long-time expansion) can be inconvenient, so we use lenses to perform the same transform.

The kinetic equivalent of an optical lens is a harmonic potential. We will now overview how momentum focusing works, and provide details that are specific to momentum focusing strongly-interacting homogenous Fermi gases. Let us first consider ideal noninteracting particles of mass m moving freely in a 1D harmonic trap of frequency ω. The Hamiltonian is:

$$H = \frac{p^2}{2m} + \frac{m\omega^2 x^2}{2} \tag{5.3}$$

Hamiltonian time evolution under H is given by oscillatory motion, which can be written as a rotation in phase space:

$$\begin{bmatrix} \bar{x}(t) \\ p(t) \end{bmatrix} = \begin{bmatrix} \cos(\omega t) & \sin(\omega t) \\ -\sin(\omega t) & \cos(\omega t) \end{bmatrix} \begin{bmatrix} \bar{x}(0) \\ p(0) \end{bmatrix} \tag{5.4}$$

Here $\bar{x} = m\omega x$ is a rescaled position coordinate. After a time of $t = T/4 = \pi/(2 * \omega)$, the coordinates are rotated by $\pi/4$ in phase space. Finally, the position of the particle reads out the initial momentum:

$$x(T/4) = \frac{1}{m\omega}\bar{x}(T/4) \tag{5.5}$$

$$= \frac{p(0)}{m\omega} \tag{5.6}$$
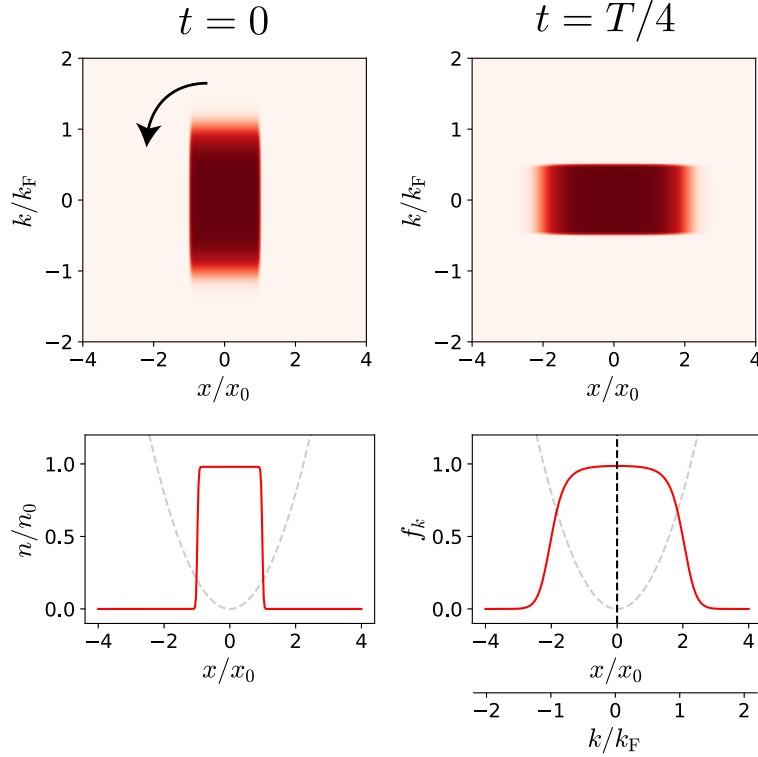
Figure 5-2: Momentum focusing of an ideal Fermi gas. (a) A 1D Fermi gas in phase space occupies a rectangle, with edges that are softened by the temperature $T/T_{\mathrm{F}} = 0.2$ along the momentum axis, and the box wall rounding along the position axis. (b) After a time $t = \pi/(2*\omega)$, the phase space is rotated by 90°, transforming the initial uniform density profile (c) into the familiar Fermi-Dirac distribution, duplicated along the rescaled x-axis (d).

It can be shown that for both bosonic and fermionic field operators, time evolution under the same Hamiltonian is a Fourier transform of the initial operators [103]. Thus for ideal Fermi gases, momentum focusing provides an ideal method to read out the Fermi-Dirac distribution of a homogeneously trapped gas. For illustration, we show in Fig. 5-2 a 1D non-interacting Fermi gas released from a uniform trapping potential into a harmonic trap. The density profile expands, and at $t = T/4$, the profile along the position axis displays the familiar Fermi-Dirac distribution. Note that conveniently, the distribution is duplicated on either side of the harmonic trap, allowing an experimentalist to double the signal for each experimental run. Further-

more, releasing from a >1D homogeneous trap into a 1D harmonic trap allows for averaging along the uniform axes, significantly improving the signal. An important point to note here is the timescale and lengthscale set by the focusing trap frequency ω. For large ω, the gas is contained within a small field of view, and the higher optical density can improve the signal-to-noise ratio. However, the momentum-space magnification is also lower, and therefore, for a finite optical resolution, the momentum space resolution is also smaller. Efforts that attempt to resolve fine structures in momentum space must consider the finite resolution imposed by both the optics as well as the harmonic trap.

Our box of atoms lives inside not only hollow light beams, but also a deep, smooth magnetic potential. The magnetic potential is anti-confining in the x-y plane (including gravity), and provides levitation. Along the z-axis, the potential is confining: we set the current in the curvature coil to form an $\omega = 23$Hz trapping potential. We now briefly consider the effective momentum resolution obtained by condensate focusing into the confining magnetic trap. For this experiment, the z-axis harmonic trap frequency was set to $\omega_z = 23$Hz. At the camera, the digital resolution is $\delta x = 1.39\mu$m per pixel. This is comparable to the optical resolution limited by the first imaging lens, an $f = 90$mm focal length Special Optics objective with a diameter of $D = 50.8$mm. The Rayleigh criterion for lithium imaging is therefore

$$d = 0.61\lambda\frac{2f}{D} \tag{5.7}$$

$$\approx 1.45\mu\text{m}. \tag{5.8}$$

If we consider an ideal Fermi gas with a generous 10kHz Fermi energy, then $k_\text{F} = \sqrt{2mE_\text{F}}\hbar = 3.44\times10^6$ m^{-1}. The momentum focused cloud will span $2*\hbar k_\text{F}/(m\omega_z) = 3.2$ mm. The momentum resolution is $\delta k = m\omega_z\delta x/\hbar = 3.0 \times 10^3$ m^{-1}. Comparing this to the Fermi momentum, we can fit $\delta k/k_\text{F} \sim 10^3$ momentum-resolved bins in the Fermi sea.

(a)

(b)
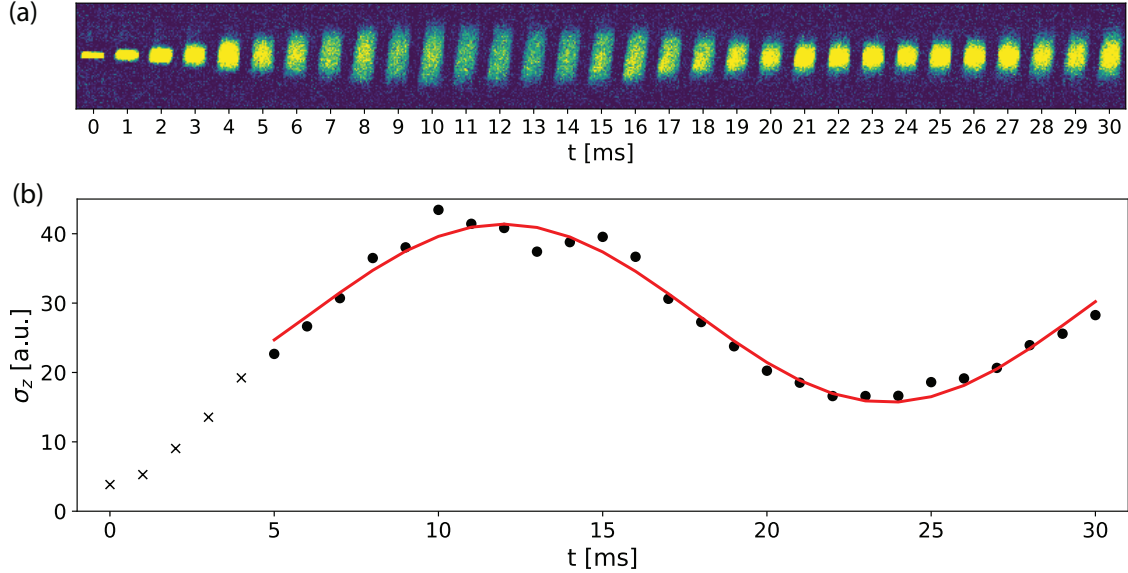
Figure 5-3: Momentum focusing in the axicon. (a) A sequence of images starting with a spin-imbalanced (95-5) box of fermions in $|1\rangle - |2\rangle$ at unitarity. At t=0, the endcaps are switched off, and the subsequent evolution is shown in steps of 1 ms. (b) A gaussian fit produces a width σ_z in arbitrary units. The time evolution of the width can be fit to a sin function to find the point in time that corresponds to $T/4$.

As noted above, the magnetic potential along the x-y direction is anti-confining at an imaginary frequency $\omega_r = 23i/\sqrt{2}$. This results in an radial expansion of the cloud during the axial focusing. In order to avoid this expansion, we might consider keeping the cylindrical trap on during the focusing process. The experimental sequence involves preparing the box, and then switching off the axially confining endcap beams. After a variable focusing time t, the cloud is imaged from the top, integrating along the y direction. The expected $T/4$ time is $1/(4*23 \text{ Hz}) = 10.8$ ms.

In Fig. 5-3, we show a sequence of images that show momentum focusing in the cylindrical axicon. Here, we prepare a 95/5 spin mixture of $|1\rangle - |2\rangle$ at unitarity. The small admixture of the interacting minority enables thermalization during preparation, and importantly, allows us to reach a temperature low enough to both load efficiently into the box, and potentially measure a clear Fermi surface. From the

61

Spin imbalance	T_{max}	$\sigma_z(T/2)/\sigma_z(0)$
50-50	12.3	1.3
80-20	12.0	2.9
95-5	11.4	3.7

Table 5.1: Interactions during expansion in the axicon. For each level of spin imbalance, we image time-resolved sequences of momentum focusing into a 23 Hz harmonic trap from an $L = 30\mu$m box. We compare T_{max}, the time taken to reach the largest axial extent of the cloud with $T/4 \sim 10.8$ ms. We also compare the width $\sigma_z(T/2)$ after half a period to the initial width $\sigma_z(0)$. For an ideal focusing, ballistic expansion implies that $T_{max} = T/4$ and $\sigma_z(T/2)/\sigma_z(0) = 1$. We attribute the observed deviations to interactions during focusing.

sequence, a few things are apparent. The first is the profile of the gas after $T/2$ is no longer the same as the initial box profile. Assuming a perfect ballistic evolution under a harmonic potential, the density profile should have returned to the initial profile after $T/2$. Furthermore, the apparent point at which the gas reaches its maximum extent is measurably late: 12.2 ms, instead of 10.8. In order to characterize effects of interactions during the expansion in the axicon, we vary the spin-imbalance and find that both the width after $T/2$ and the time taken to reach the maximum σ_z vary considerably with the spin imbalance (see Table 5.1). We attribute both deviations to interactions during the expansion, and we will return to this effect.

When momentum focusing a 3D box along a 1D harmonic trap, we benefit from integrating along the two nonfocused axes. We provide an overview on how to obtain the momentum distribution $f(\mathbf{k})$ from the measured 1D density distribution $n_{1D}(z)$. As discussed earlier, a quarter period in the harmonic trap applies a rescaling transformation between position and momentum $\hbar k_z = m\omega_z z$. We can use this to relate the density distribution with the integrated momentum distribution $f_{1D}(k_z)$:

$$n_{1D}(z) = Af_{1D}(k_z) \tag{5.9}$$

$$= \frac{A}{4\pi^2} \iint dk_x dk_y \ f(k_x, k_y, k_z) \tag{5.10}$$

Now, all we need is to solve this equation for $f(\mathbf{k})$, and find the appropriate proportionality constant A. We can convert to cylindrical coordinates k_ρ, k_z and apply a change of variables using the energy $\epsilon = \hbar^2(k_\rho^2 + k_z^2)/2m$:

$$f_{1D}(k_z) = \frac{1}{2\pi} \int_0^\infty dk_\rho k_\rho \ f(k_\rho, k_z) \tag{5.11}$$

$$= \frac{m}{2\pi\hbar^2} \int_{\hbar^2 k_z^2/2m}^\infty d\epsilon \ f(\epsilon, k_z) \tag{5.12}$$

This equation can be inverted through differentiation:

$$\frac{df_{1D}(k_z)}{d\epsilon} = \frac{m}{2\pi\hbar^2} \left(f(\epsilon = \infty, k_z) - f\left(\epsilon = \frac{\hbar^2 k_z^2}{2m}, k_z\right) \right) \tag{5.13}$$

We know that $\lim_{\epsilon \to \infty} f_k = 0$, so that leaves us with only the second term:

$$\frac{df_{1D}(k_z)}{dk_z^2} = -\frac{1}{4\pi} f(k) \tag{5.14}$$

where we have substituted $\epsilon = \hbar^2(k_\rho^2 + k_z^2)/2m$. We also make use of the assumption that the momentum distribution is spherically symmetric and $f(\mathbf{k}) = f(k)$. Now, all that's left is to find the proportionality constant. We know that the total atom number is

$$N = \frac{V}{2\pi} \int_{-\infty}^{+\infty} dk_z \ f_{1D} k_z \tag{5.15}$$

$$= \frac{V}{2\pi A} \int_{-\infty}^{+\infty} \frac{dk_z}{dz} dz n_{1D}(z) \tag{5.16}$$

$$= \frac{V m \omega_z}{2\pi \hbar A} \int_{-\infty}^{+\infty} dz \ n_{1D}(z) \tag{5.17}$$

$$= \frac{V m \omega_z}{2\pi \hbar A} N \tag{5.18}$$

Solving for the proportionality constant A, and substituting into Equation 5.10,

we finally arrive at a formula for the momentum distribution f_k:

$$f_k = -\frac{8\pi^2\hbar^3}{Vm^3\omega_z^3}\frac{dn_{1D}(z)}{dz^2} \tag{5.19}$$

In order to identify whether the shape of the axicon has an effect on the momentum focusing procedure, we show results from a simple classical Monte Carlo simulation with atoms moving in two dimensions. Along one axis, they are confined by configurable hard walls, and along the other, they are confined in a box for $t < 0$. We initialize the box with $N = 2000$ atoms, with momenta sampled from a $T = 0$ Fermi-Dirac distribution (a.k.a, a uniform distribution up to a finite k_F). At $t = 0$, the simulated atoms are released along the z-axis into a harmonic trap. The particles undergo elastic collisions with the walls, and do not interact with each other. Time evolution is implemented using the forward Euler method. When a particle reaches a hard wall, its velocity is reflected about a normal vector at the nearest wall:

$$\mathbf{r}(t + \delta t) = \mathbf{r}(t) + \mathbf{v}(t) \times \delta t \tag{5.20}$$

$$\mathbf{v}(t + \delta t) = \begin{cases} \mathbf{v}(t) & x \in \Omega \\ \mathbf{v}(t) - 2[\mathbf{v}(t) \cdot \mathbf{n}(\mathbf{r})] \ \mathbf{n}(\mathbf{r}) & x \in \delta\Omega \end{cases} \tag{5.21}$$

where Ω is the region inside the box, $\mathbf{r}(t)$ and $\mathbf{v}(t)$ are the position and velocity respectively, and $\mathbf{n}(\mathbf{r})$ is the normal vector at the wall near the particle. The results, shown in Figure 5-4, demonstrate that tilted hard walls alter the z component of the momentum during focusing, and distort the symmetry of the measured momentum distribution. Since as shown earlier, the single axicon produces a conical trapping potential for our fermions, it must be switched off during the ballistic expansion required for momentum focusing. The code for this simulation is available at [99]

We now return to the effects of interactions during the focusing. Turning off the axicon from the focusing process allows the atoms to freely explore the magnetic potential. For a spin-balanced superfluid at unitarity, interactions are as strong as
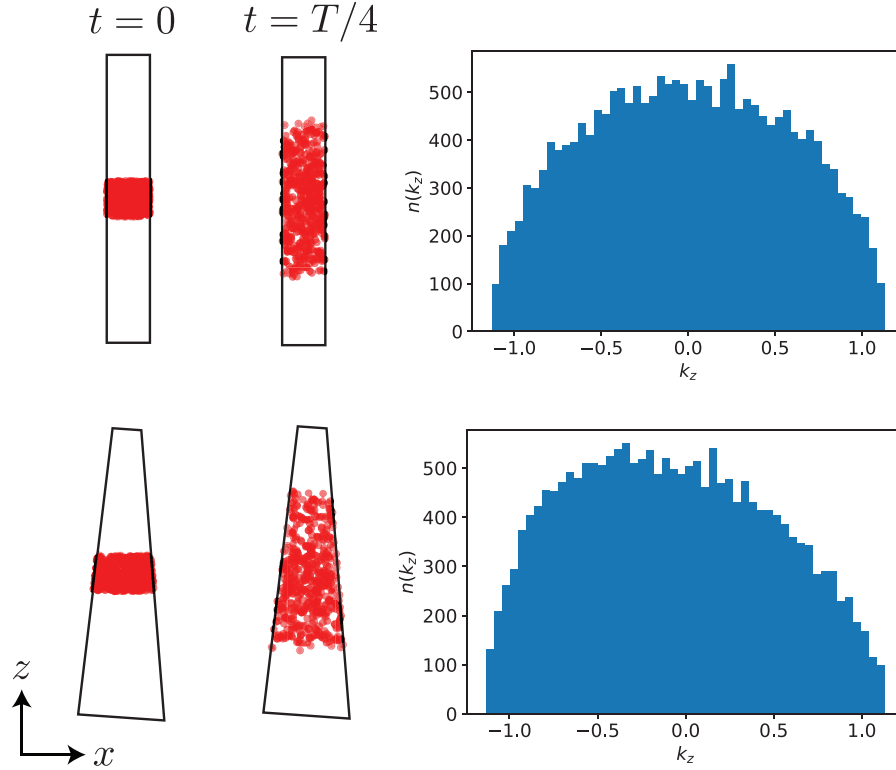
Figure 5-4: Single particle simulations of momentum focusing. A single particle simulation of noninteracting fermions at T=0 shows a dependence on the shape of the radial confinement. Top row: hard walls in x parallel to the z-axis. Bottom row: a wedge-shaped trap with walls at an angle. Boundary collisions are fully elastic. After $t = T/4$, the extents of the clouds are similar. However, the 1D density profile (right) shows a large asymmetry in the case of the wedge-shaped trap.

allowed by quantum mechanics. The expansion of the gas is hydrodynamic, not ballistic. In Figure 5-5, we show absorption images of a fermionic superfluid released into a harmonic trap. In the first few milliseconds, the box shape is inverted, and a diamond shape appears. This is the analog of the characteristic aspect ratio inversion when a BEC is released from an anisotropic harmonic trap. For a box, the expansion is fastest at the points on the surface where the curvature is minimal, as this allows for a coherent fast-moving wavefront to propagate outwards. This effect has been previously observed in uniform box-trapped BECs [58].

Measuring the momentum distribution of an ideal Fermi gas is challenging with-
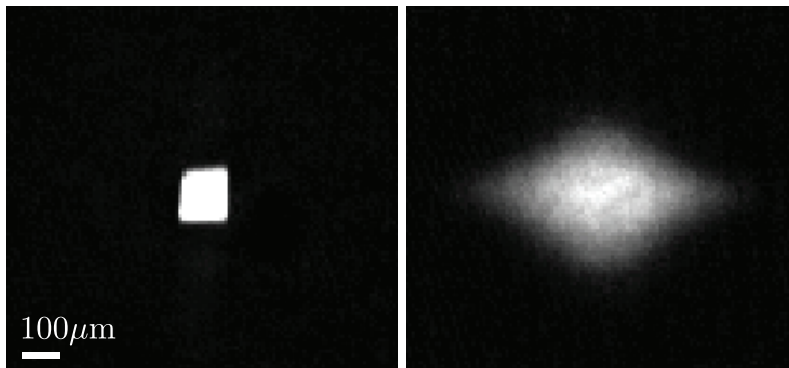
Figure 5-5: Expansion of a uniform superfluid. A spin-balanced superfluid trapped in a box (left) is released from the box into a weak harmonic trap with a characteristic period $T = 43.2$ ms. Within 6ms, the cloud develops a diamond shape (right) due to hydrodynamic flow during free expansion.

out interactions. This is because interactions allow the gas to re-thermalize once its momentum distribution has been changed. So for instance, if we started with an ideal Fermi gas at a given temperature in the dipole trap, after loading into the box, its momentum distribution may be completely different from a Fermi-Dirac distribution with a well-defined temperature. So in our measurements, we keep a small amount of a strongly-interacting second spin state, $|2\rangle$, typically below 5% of the total atom number. However, the momentum focusing method requires ballistic expansion. In order to measure the effects of interactions, we plot in Figure 5-6 the integrated 1D momentum distribution f_{1D} as a function of k_z^2. For finite temperatures $\widetilde{T} = T/T_F$,

$$f_{1D}((k_z/k_F)^2) = -\frac{1}{4\pi} \int_{k_z^2}^{\infty} dk^2 \frac{1}{1 + \exp\left[\left(\frac{k^2}{k_F^2} - 1\right)/\widetilde{T}\right]} \tag{5.22}$$

$$= \frac{k_F^2}{4\pi} \log\left[1 + \exp\left[\left(1 - \frac{k^2}{k_F^2}\right)/\widetilde{T}\right]\right] \tag{5.23}$$

Note that tor a zero temperature Fermi-Dirac distribution $\widetilde{T} \to 0$, the function $f_{1D} \cdot 4\pi/k_F^2$ is a straight line with a slope of -1. This line is shown in comparison with the measured f_{1D}.

In order to completely remove interactions during the expansion, we apply an
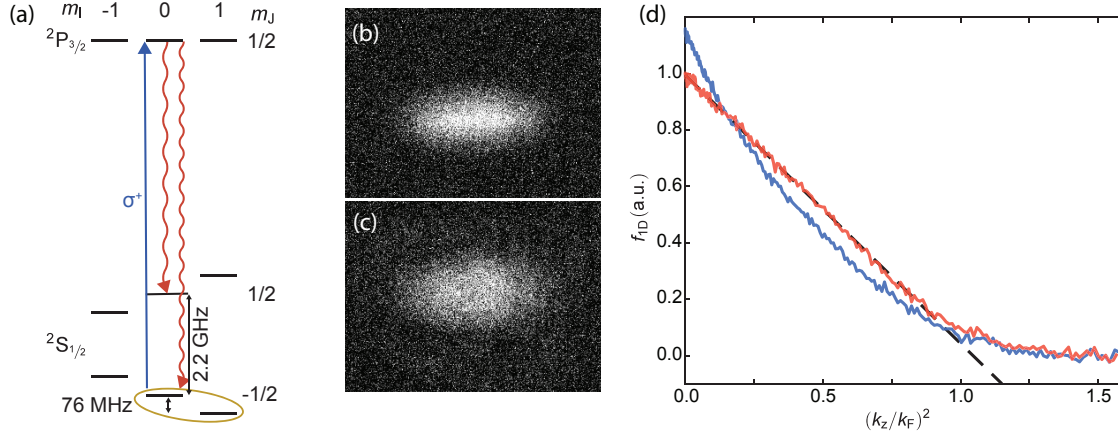
Figure 5-6: Optical pumping for ballistic expansion. (a) Level diagram show-
ing the pumping light (blue straight arrow) and the spontaneous decay to the other
states (wavy red arrows). On average, 1.5 photons are required to pump the atom
into $|5\rangle$. After $t = T/4$, the cloud looks clearly modified when the pumping beam is
turned off (b) as opposed to flashed on before the expansion (c). The effect is clear
in the integrated momentum distribution f_{1D}, where the blue curve is without the
pumping beam, and the red is with it flashed on.

optical pumping beam for 5μs that pumps atoms in $|2\rangle$ into a weakly interacting $|5\rangle$.
The impact of this is clear in f_{1D}, where interactions otherwise lead to a distorted
profile. A qualitative explanation for the specific shape of the distorted profile is that
the small amount of $|2\rangle$ lives within a smaller Fermi sea in momentum space. Atoms
in $|1\rangle$ at low momenta expand slower in the harmonic trap, and have more time to
interact with the smaller Fermi sea of $|2\rangle$ atoms. The mean-field attraction between
$|1\rangle$ and $|2\rangle$ at unitarity results in a greater apparent weight at lower momenta, and
a peaked f_{1D} profile. Another method to remove interactions during the expansion
is to rapidly ramp the Feshbach field to 532 G, a zero-crossing in the scattering
length for states $|1\rangle$ and $|2\rangle$. In our experiment, the ramp takes 25 μs to drop to
500G, and then another 50-100 μs for a full ringdown. Since this timescale is three
orders of magnitude smaller than the trap period, it has little effect on the measured
momentum distribution. The resulting momentum distribution measurements are
identical to those obtained by optically pumping away the minority population. This
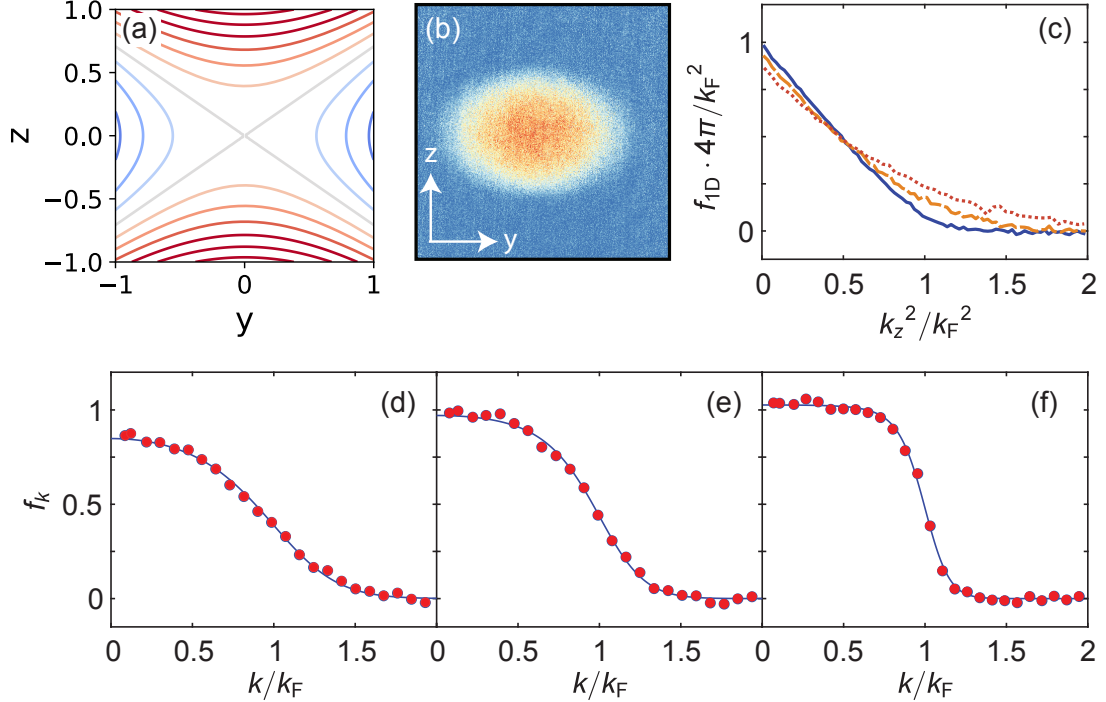
Figure 5-7: Measuring the Fermi-Dirac distribution. (a) The magnetic field results in a saddle-like potential in the y-z plane. Along z, the trap is confining, and along y, it is anti-confining. The resulting equations of motion describe oscillatory motion in z and hyperbolic expansion in y. This is reflected in the cloud profile (b) after $t = \pi/2\omega_z$, where the z-extent is given by k_F, and the y-extent is the expansion into the anti-confinement. From the integrated profiles f_{1D} shown in (c), we obtain the momentum distributions f_k, and fit the Fermi-Dirac distribution with a free temperature (d)-(f). The temperatures are from left to right $T/T_F = 0.49(2)$, $0.32(1)$, and $0.16(1)$.

is a viable solution if a separate offset-locked slicing laser is unavailable.

We finally turn to the main result of this study: the measured Fermi-Dirac distribution as a function of temperature. We vary the temperature by oscillating the intensity of the compensating dipole trap at a resonance of the box (approximately 200 Hz). The duration of this oscillation allows us to control the amount of heat delivered to the box of fermions. We plot the resulting momentum distributions in Figure 5-7, along with their corresponding f_{1D} profiles. The measured f_k are obtained by differentiating f_{1D} profiles with a Savitsky-Golay filter to mitigate noise [128]. Finally, the data is fit to Fermi-Dirac functions with a free temperature.
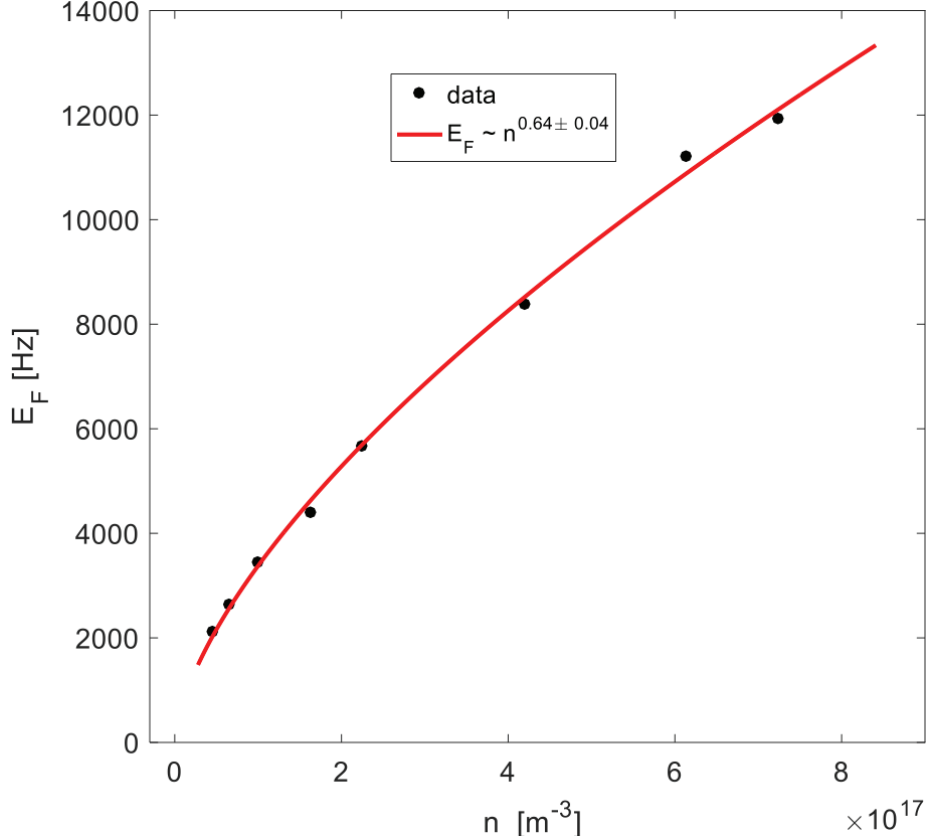
Figure 5-8: Fermi energy scaling. We vary the total atom number in the box, and measure the Fermi surface momentum through focusing. From k_F, we obtain E_F, shown in the y-axis, and from absorption imaging, we count the total number of atoms in the box n.

We observe the saturation of momentum space occupation for momenta below k_f. Only one particle is allowed per momentum space cell, reflecting the Pauli blocking inherent in fermions. Note that the absolute atom number calibrations are verified with a comparison to the ideal Fermi gas compressibility in the hybrid trap, which will be describe in the next subsection. It is reassuring to compare the Fermi energy obtained from the edge of the Fermi sea, with a total atom number count from the imaging. Ideally, $E_\mathrm{F} = \hbar^2 k_\mathrm{F}^2 / 2m \sim n^{2/3}$. In Figure 5-8, we show the results of this measurement. The exponent is observed to be 0.64 ± 0.04, consistent with $2/3$.

69

5.2 Thermometry

We now turn to the topic of thermometry of homogeneous atomic Fermi gases. Temperature is an important control in the toolkit for undestanding many-body physics in ultracold gases. Historically, thermometry in ultracold Fermi gases have used the low-density tails in trapped gases [70]. Here we outline how this is possible using a hybrid trap, and how we have used the equation of state of the ideal Fermi gas to verify our atom number calibrations. For experiments that require complete homogeneity, the box offers no low-density wings for temperature calibrations. One method, suitable for ideal Fermi gases, was outlined in the previous section. Through momentum focusing and fitting the momentum distribution with a finite temperature, we have demonstrated the preparation of nearly spin-polarized gases at temperatures below $T/T_{\mathrm{F}} = 0.17$. For spin-balanced gases, momentum focusing offers fewer advantages. In order to remove interactions, the optical pumping process would likely inject a large amount of kinetic energy into both spin states, in a momentum-dependent fashion. In addition, the true interacting momentum distribution as a function of temperature at unitarity remains a matter of active research [33]. By combining the momentum focusing technique with a rapid ramp of the interaction strength, we are able to image the pair momentum distribution, and pin point the superfluid transition. Nevertheless, this does not provide a reliable measure of the temperature, especially for $\widetilde{T} \ll T_c$. In this section, we outline how we measure the total energy per particle of a homogeneous Fermi gas, and use an equation of state to obtain the global temperature. In a subsequent section, we discuss a novel method to perform direct insitu thermometry, and use it to observe temperature waves in the homogeneous Fermi gas.

5.2.1 Hybrid trap thermometry

When the local density approximation (LDA) is valid, each shell of an inhomogeneous trapped gas represents a larger system in equilibrium at the same density, temperature and pressure. This has resulted in a precision measurement of the equation of state for fermions at unitarity [105, 81], and state of the art spectroscopic measurements [134, 130]. Since the density varies across the trap, a single absorption image of the gas scans through the phase diagram. This is a significant advantage over a gas at a single density, as the inhomogeneous trap effectively parallelizes a thermodynamic measurement. However, measurements on individual shells at constant density requires tomographic techniques such as the inverse Abel transform that exploit the cylindrical symmetry of the harmonic trap. Typically, such transforms decrease the signal-to-noise ratio. An ideal solution would appear to combine a uniform density along the line-of-sight with a spatial variation along an orthogonal axis. This is typically trivial in 2D systems, but in 3D, it requires some potential engineering. Here, we present the hybrid trap, and our efforts to use it for thermodynamic measurements.

Evaporation in the hybrid involves ramping down the laser power in the green cylinder. As the height of the radial trap decreases, atoms with a higher kinetic energy pass through and escape due to the radial anticonfinement from the magnetic trap. Typically, evaporation ramps that are on the order of seconds allow the gas to rethermalize into new states. Practically, this requires a good PID control over the power sent through the axicon. Since electronic noise is typically on the scale of tens of mV, we set the lowest powers to be controlled at 10mV, and the highest powers controlled at a set point of a few volts.

In Figure 5-9, we show absorption images of a unitary Fermi gas being cooled in the hybrid trap. Perhaps most strikingly, the Thomas-Fermi radius only decreases along one axis, and remains constant along the uniform axis. This reflects the sharpness of the cylinder walls in comparison to the harmonic trap, and is in stark contrast
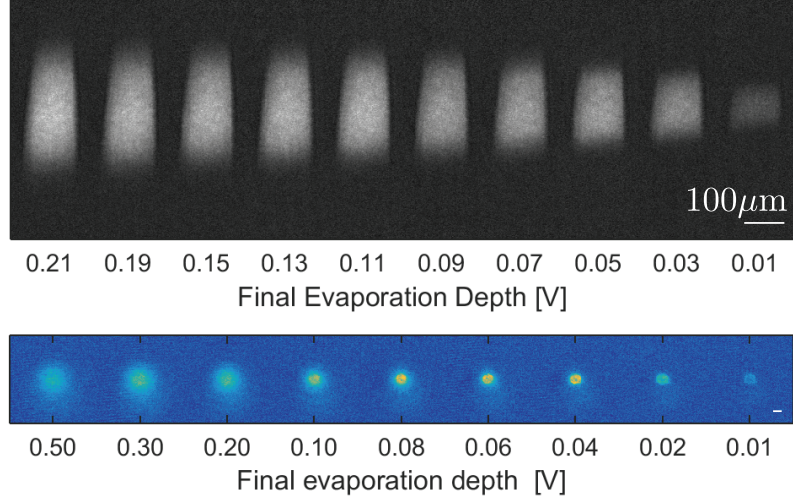
Figure 5-9: Evaporation in the hybrid trap. A series of absorption images taken from the top (a) show the evolution of the cloud profile in the z-x plane as the gas is cooled in the hybrid trap. After a rapid ramp that preserves the pair center-of-mass momentum and a free expansion that allows thermal atoms to expand, the condensate can be clearly seen once the gas is sufficiently cold (b). As expected, the Thomas-Fermi radius along the harmonic trap axis changes dramatically once most of the gas is a superfluid. This is because the width of the thermal gas is set by the temperature, while the width of the superfluid is set by the chemical potential.

to what one might expect from a 3D harmonic trapped gas. By applying a rapid ramp of the Feshbach field to 690G during time of flight, we can separate the thermal atoms from the condensate. The appearance of the condensate in the rapid ramp is interpreted as the point at which the temperature at the center of the gas drops below $T_c = 0.167 T_{\mathrm{F}}$, the superfluid transition temperature. By performing an azimuthal average through the rapid ramp images, we can see the emergence of the condensate (see Figure 5-10).

For a quick calibration of the relevant Fermi energies that can be reached, we find the Thomas-Fermi radius along the z-axis. The radius across the classical and the degenerate regimes as a function of temperature is [70]:

$$R = \sqrt{\frac{2k_{\mathrm{B}}T}{m\omega_z^2} f(e^{\mu\beta})} \qquad (5.24)$$
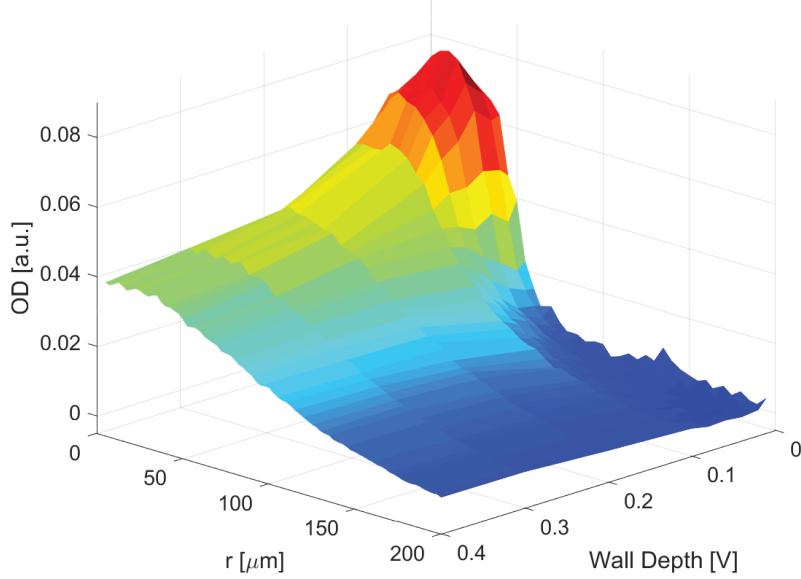
Figure 5-10: Evaporation in the hybrid trap. A surface plot showing the appearance of the condensate in the hybrid trap. Azimuthal averages are taken from the rapid ramp images in Figure 5-9(b) and stacked. Note that while the wall depth is in the very experimental units of PID setpoint voltage, we show the calibration of the wall depth in units of Fermi energy in the next figure.

where μ is the chemical potential, $\beta = 1/k_\mathrm{B}T$ and

$$f(x) = \frac{1+x}{x} \ln(1+x) \tag{5.25}$$

Note that in the zero temperature limit, this reduces to the familiar relation $E_\mathrm{F} = \frac{1}{2}m\omega_z^2 R^2$. By finding the Thomas-Fermi radii of the clouds in Figure 5-10, we can calibrate the Fermi energies in our experiment. We observe E_F in the range of 500 Hz to over 12 kHz, spanning a large dynamic range in the phase diagram.

In order to quantitatively obtain the temperature of the gas, we need to extract accurate 1D profiles. We correct for the varying cross-sectional area along the hybrid by integrating along the homogeneous axes and dividing by the cross-sectional area. This provides the true 1D number density $n(z)$. We compare the number densities imaged from both spin states in Figure 5-11, and discuss the thermodynamics of both spin-imbalanced and spin-balanced gases. The 1D number density provides access

to the isothermal compressibility

$$\kappa = -\frac{1}{n^2}\left(\frac{\partial n}{\partial V}\right)_T \tag{5.26}$$

It is convenient to compare the isothermal compressibility to that of the ideal gas: $\widetilde{\kappa} = \kappa/\kappa_0$ where the ideal gas compressibility at $T = 0$ is $\kappa_0 = \frac{3}{2}\frac{1}{nE_{\mathrm{F}}}$. In terms of the Fermi energy E_{F} and the external potential U,

$$\widetilde{\kappa} = -\left(\frac{\partial E_{\mathrm{F}}}{\partial U}\right)_T \tag{5.27}$$

This derivative is numerically performed using a Savitsky-Golay filter, and the signal to noise is sufficient to extract the isothermal compressibility from an average of just 6 images. This is a significant advantage over the harmonic trap, which requires more than 100 images for an accurate equation of state measurement [81]. We observe an isothermal compressibility that saturates to the ideal gas value in a spin-polarized gas, reflecting the Pauli blocking in the system. However, interactions enable the gas to compress further, and in the spin-balanced gas, the compressibility rises to nearly $3\kappa_0$ at T_c before settling at $\kappa = \kappa_0/\xi$ where $\xi = 0.37$ is the Bertsch parameter. The chemical potential in a spin-balanced gas at unitarity is directly connected to the Fermi energy through the Bertsch parameter: $\mu = \xi E_{\mathrm{F}}$ [56].

We now briefly focus on the compressibility of the majority component of the spin-imbalanced cloud. The ideal gas equation of state provides the following relation between density $n(z)$ and potential energy $U(z)$ [70]:

$$n(z) = -\frac{1}{\lambda_{\mathrm{dB}}{}^3}\mathrm{Li}_{3/2}\left(-e^{\beta(\mu - U(z))}\right) \tag{5.28}$$

Here, $\lambda_{\mathrm{dB}} = \sqrt{\frac{2\pi\hbar^2}{mk_{\mathrm{B}}T}}$ is the de Broglie wavelength and $\mathrm{Li}_{3/2}$ is the 3/2 order poly-logarithm. We fit the majority density $n_\uparrow$, shown in Figure 5-12, with this function. The only free variables are the temperature $T = 1/k_{\mathrm{B}}\beta$ and the chemical potential
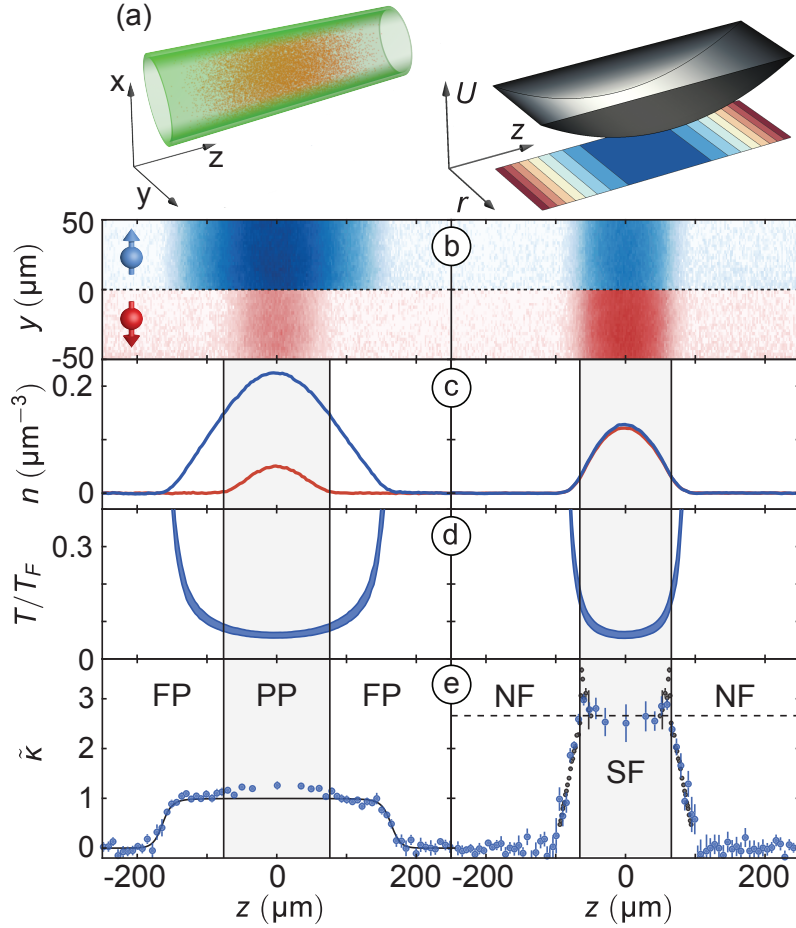
Figure 5-11: Unitary Fermi gases in the hybrid trap. (a) Fermions are loaded in to a hybrid trap, where the trapping potential varies as a quadratic function in the z-coordinate. By dividing absorption images by the local column depth, we can obtain column-corrected images (b) of spin-imbalanced (left) and spin-balanced clouds (right). The homogeneity in the transverse direction is evident, and allows us to integrate across the x-y plane, and obtain the number density n, shown in (c). From the number density and the known equation of state for ideal Fermi gases and the strongly-interacting spin-balanced Fermi gas, we can obtain the normalized temperature T/T_F as well as the normalized isothermal compressibility $\widetilde{\kappa} = -\frac{\partial E_F}{\partial V}$. The grey shaded region on the left demarcates the Thomas-Fermi radius of the minority cloud while on the right, it denotes the superfluid region. The solid line in the spin-imbalanced cloud in (e) represents the ideal Fermi gas compressibility while the dashed horizontal line in the spin-balanced (e) represents $1/\xi$. Yellow points are taken from the measured equation of state [81].

75
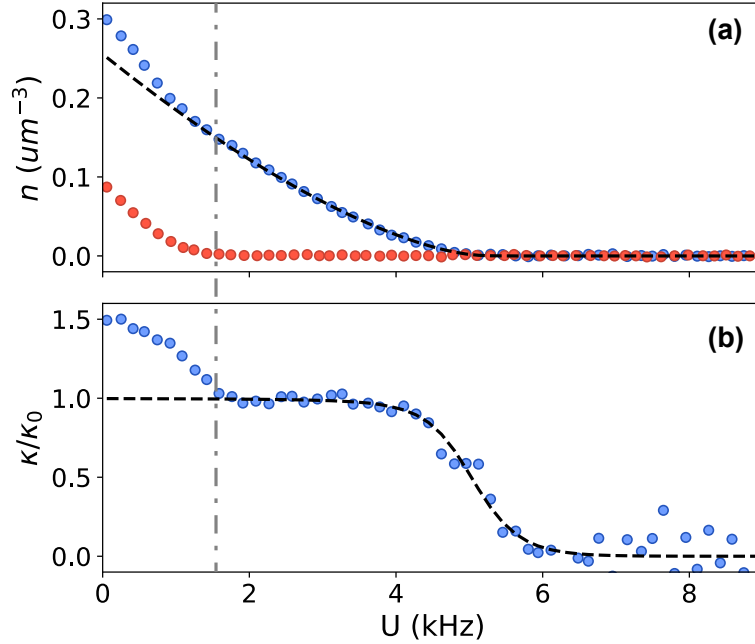
Figure 5-12: Spin-imbalanced compressibility. In (a) we show the density of the minority (red) and majority (blue) components of a spin-imbalanced gas. The isothermal compressibility of only the majority component is shown in (b). The extent of the minority component is demarcated with the vertical dot-dashed line, while the dashed line is a fit to Equation 5.28. The Fermi energy at the center of the trap is $E_F = 5.7(1)$ kHz, the imbalance is $N_\downarrow/N_\uparrow = 0.18$, and the temperature of the majority is $T/T_F = 0.05(1)$.

μ. The observation of a saturated compressibility of κ_0 in the spin-polarized wings is a testament to both the low temperatures achieved as well as the accuracy of the atom number calibrations in the experiment.

A clear feature in Figure 5-12 is the bump in the majority compressibility in the partially polarized region. Using a Fermi liquid ansatz, we can describe the gas as a mixture of noninteracting atoms and an ensemble of polarons [105, 107, 150]. The resulting majority and minority densities can be shown to be

$$n_\uparrow(\mu_\uparrow, \mu_\downarrow, T) = n_0(\mu_\uparrow, T) - An_\downarrow(\mu_\uparrow, \mu_\downarrow, T) \tag{5.29}$$

$$n_\downarrow(\mu_\uparrow, \mu_\downarrow, T) = (m^*/m)^{3/2} n_0(\mu_\downarrow - A\mu_\uparrow, T) \tag{5.30}$$

Our measurements are consistent with $A = -0.615$, which represents the average excess majority atoms surrounding each minority atom in the polaron [120]. From the compressibility of the minority gas, we determine $m^*/m = 1.25(1)$, which is the ratio of the effective mass of of the polaron with respect to the bare mass of the Lithium atom [150].

The Fermi liquid ansatz assumes low interactions between the quasiparticles, and therefore, a low spin-imbalance. For higher spin-imbalance, the phase diagram shows a transition from a partially polarized normal fluid to the paired superfluid. This is in direct analogy to the critical magnetic field at which superconductivity is broken in solid state systems, known as the Clogston-Chandrasekhar limit [22, 18]. Right in BEC1, this phase diagram was mapped using a harmonic trap [135]. In that study, a sufficiently cold spin-imbalanced Fermi gas was observed to phase separate, with a clear boundary demarcating a balanced superfluid from a partially-polarized normal fluid. This reflects a tricritical point in the phase diagram below which the system is unstable towards forming a balanced superfluid. As an outlook to this section, we briefly revisit this effect in the hybrid trap, and consider future avenues of research.

In Figure 5-13, we show a cold spin-imbalanced Fermi gas at unitarity in the hybrid trap. The minority component visually seems to have a boundary between a denser superfluid and fuzzy polarized wings. Plotting the spin-polarization as a function of the z coordinate confirms this, and shows that the polarization is virtually zero in the central portion. Although a dramatic phase separation is still elusive, we see a sudden increase in the spin polarization at the boundary of the superfluid. The isothermal compressibility of the minority $\kappa_\downarrow$ is interesting to consider here. In the spin-balanced superfluid, the compressibility is roughly the same as κ_0/ξ. However, as the Clogston-Chandrasekhar limit is approached, the compressibility rises until right at the phase transition, where it reaches a maximum of approximately $5.9\kappa_0$. This is over twice as high as in the phase transition in a globally spin-balanced gas.

Near the phase transition, we suspect that bubbles of balanced superfluid appear
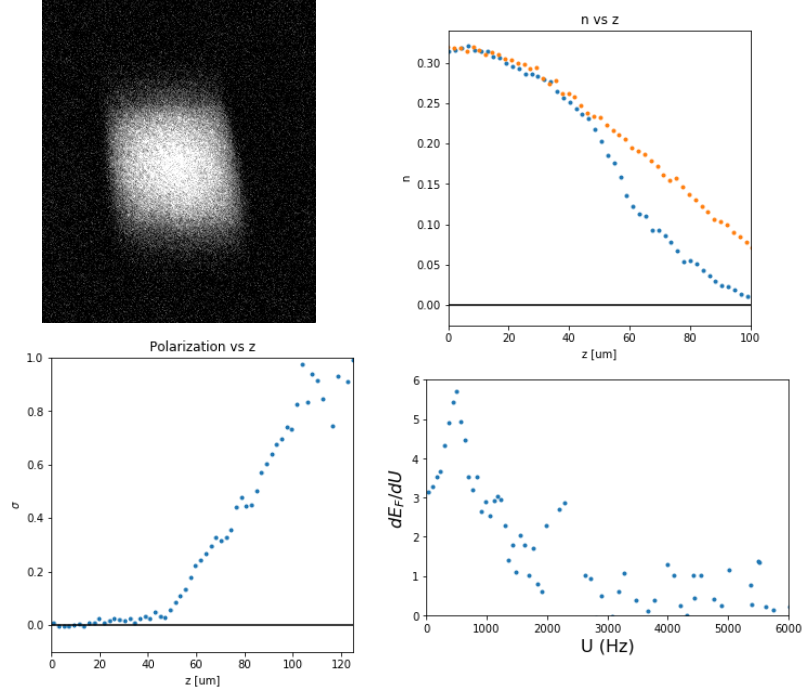
Figure 5-13: Phase separation in the hybrid trap. In (a) we show the density of the minority (red) and majority (blue) components of a spin-imbalanced gas. The isothermal compressibility of only the majority component is shown in (b). The extent of the minority component is demarcated with the vertical dot-dashed line, while the dashed line is a fit to Equation 5.28. The Fermi energy at the center of the trap is $E_{\mathrm{F}} = 5.5$ kHz, and the temperature of the majority is $T/T_{\mathrm{F}} = 0.07$.

within the partially-polarized gas. Minority atoms near these phase boundaries can now decide to pair up with majority atoms, and in a sense, 'escape' the Pauli pressure that keeps them apart. Near the transition, it costs no energy to create the bubbles, and as a result when a potential changes (i.e. a force is applied), the density is free to jump between the dense superfluid and the less dense normal fluid. This results in an effectively infinite compressibility of the minority gas at zero temperature. The contrast of phase separation is set by the temperature of the gas: above the tricritical point $T_{tc}/T_{F\uparrow} = 0.07$, there is no phase separation, while at $T = 0$, a perfect jump in the spin-polarization is expected [135]. We suspect that we are just barely below the tricritical point. The hybrid trap remains the coldest partially uniform system we have prepared in this experiment. Temperatures in the gas are likely limited by

the stability of the uniform trap; in our efforts to obtain transport coefficients by generating sound in the gas, we have found that it is exceedingly easy to generate heat by shaking the walls of the box. Since at low temperatures, most excitations are of the phononic kind, we hope that more stable implementations of the unitary Fermi box will be more stable and therefore colder.

5.2.2 Box trap thermometry

We now consider the thermometry of spin-balanced gases that are trapped in a 3D uniform potential. Details on our thermometry method are provided, as well as a novel method of measuring the condensate fraction in a 3D homogeneous interacting Fermi gas. As mentioned previously, a fully homogenous potential does not allow for a variation in the chemical potential, and the standard methods used in inhomogeneous traps described above cannot be used. Instead, we use an isoenergetic expansion from the box trap into the hybrid trap to find the total energy. Then, the equation of state is used to obtain the initial temperature of the gas prior to expansion. Below we provide a derivation of the total energy per particle measurement from the expanded profile, and offer some technical details that are specific to the experimental process.
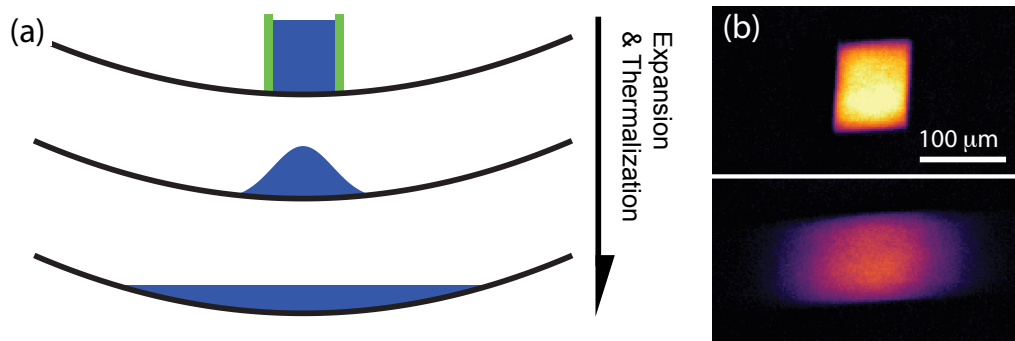
Figure 5-14: Isoenergetic expansion into a harmonic trap. (a) The gas is released from a box trap into an axial harmonic trap at $t = 0$. As the gas freely expands and thermalizes into the hybrid trap, the total energy is conserved. (b) The initial box-shaped profile of the gas evolves into a profile whose width reflects the energy and temperature of the system before the expansion.

In Figure 5-14, we show the process of isoenergetic expansion into a harmonic trap. The initially uniform gas is trapped in a cylindrical potential with endcaps. At $t = 0$, the endcap beams are suddenly turned off and the gas is free to expand along the z-direction. The magnetic field curvature results in the same $\omega_z = 2\pi \cdot 23$ Hz confinement potential as the one used for the hybrid trap and for momentum focusing. As the gas expands, the interatomic interactions scramble the momentum states, and the gas thermalizes into a well-defined profile that is constant in time. Since the removal of the endcap walls does no work on the gas, the total energy is conserved through this entire process.

The width of the cloud initially oscillates at a period close to the trapping period, before achieving a steady-state in approximately 2s (see Figure 5-15). Gradually over a timescale of seconds, the axicon trap heats the gas at a rate that is calibrated and corrected for. The total energy of the system is given by the sum of the internal energy $\epsilon(r)$ and the potential energy $U(r)$ weighted by the density $n(r)$:

$$E = E_{int} + E_{pot} \tag{5.31}$$

$$= \int d^3r \ (\epsilon(r) + n(r)U(r)) \tag{5.32}$$

Since the hybrid trap is uniform in the x-y plane, we can integrate along x and y, with a prefactor A representing the cross-sectional area of the hybrid trap:

$$E = A \int dz \ (\epsilon(z) + n(z)U(z)) \tag{5.33}$$

In the unitary Fermi gas, the internal energy is given by the pressure $\epsilon(z) = 3/2p(z)$ [66]. Furthermore, using the Gibbs-Duhem relation at constant scattering length and tem-
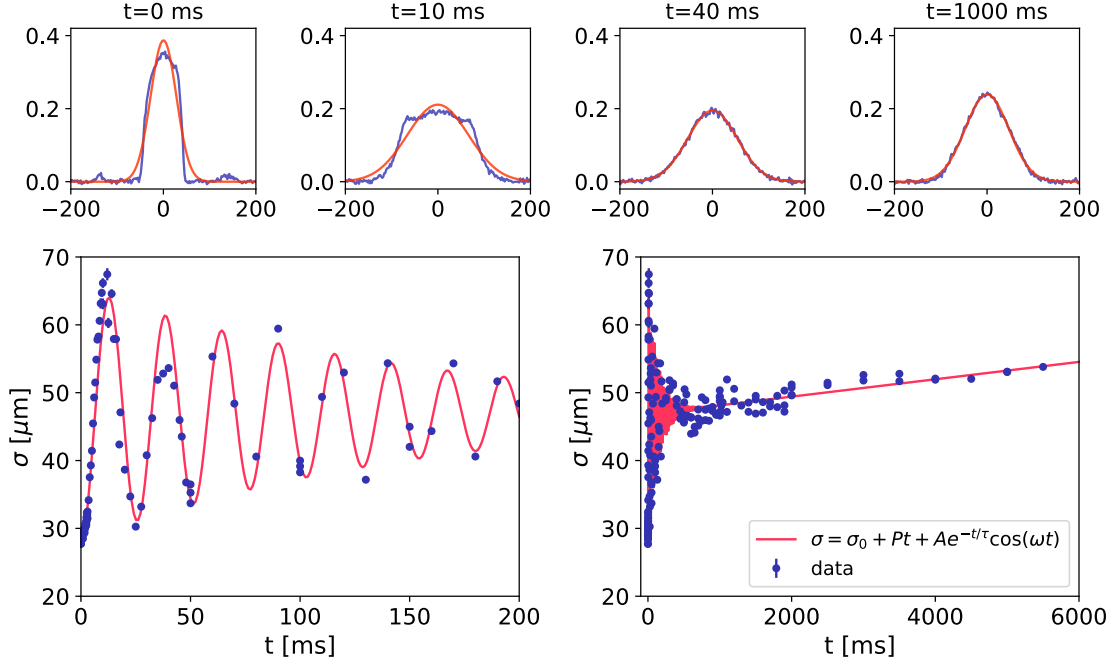
Figure 5-15: Oscillations and long-term heating during expansion thermometry. Top row: the axial profile of the cloud (shown in a blue line) expands from the box shape at $t = 0$ms into a gaussian-like profile. A gaussian fit to the profile provides an estimate of the rms width $\sigma \sim \sqrt{\langle z^2 \rangle}$. This is plotted in the lower row as a function of time from release. The initial hydrodynamic oscillations (shown on the right) are damped within 1000ms, after which a slow heating is visible.

perature, $\mathrm{d}P = n\mathrm{d}\mu = -n\mathrm{d}U$, results in:

$$z\frac{\mathrm{d}P}{\mathrm{d}z} = -nz\frac{\mathrm{d}U}{\mathrm{d}z} \tag{5.34}$$

$$= -2nU(z) \tag{5.35}$$

for the harmonic trap. We can now use integration by parts to rewrite the internal

energy as

$$E_{int} = \frac{3}{2} A \int P(z) \, dz \qquad (5.36)$$

$$= \frac{3A}{2} \left(zP(z=+\infty) - zP(z=-\infty) - \int z \frac{dP}{dz} dz \right) \qquad (5.37)$$

$$= 3A \int n(z)U(z) \, dz \qquad (5.38)$$

Combining the two terms, the total energy is now

$$E_{tot} = 4A \int n(z)U(z) dz \qquad (5.39)$$

$$= 2Am\omega_z^2 \int n(z)z^2 dz \qquad (5.40)$$

$$= 2Nm\omega_z^2 \langle z^2 \rangle \qquad (5.41)$$

This provides a very convenient formula for the energy per particle E/N, in terms of the width of the profile $\langle z^2 \rangle$. In practice, a gaussian fit to the profile provides the most robust method of estimating $\langle z^2 \rangle$. Numerically computing the second moment integral is much more sensitive to the low density noisy wings of the trap. Due to scale invariance for fermions at unitarity, $E_0 = \frac{3}{5} N E_F$, so

$$\frac{E}{E_0} = \frac{5}{3E_F} \frac{E}{N} \qquad (5.42)$$

From the measured equation of state, we can therefore obtain T/T_F from a measurement of E/N. Since the gas takes a few seconds to thermalize in the hybrid trap, there is a fair amount of residual heating that must be subtracted in order to obtain an accurate E/N measurement. Thus, we would ideally like to have an independent anchor for a known temperature.

The sharpest thermodynamic feature in strongly-interacting Fermi gases is the superfluid transition at $T_c = 0.167T_F$. Measuring the condensate fraction N_c/N is a good proxy for the superfluid fraction ρ_S/ρ, especially when pinpointing the
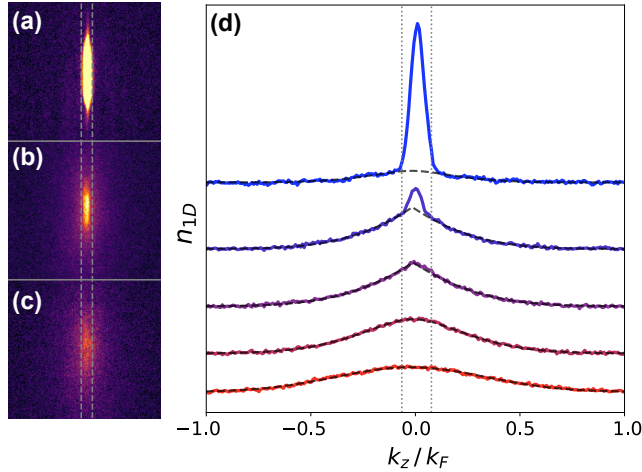
Figure 5-16: Momentum space measurements of the pair condensate. (a)-(c) Images after a rapid ramp of the unitary Fermi gas. (d) The 1D profiles show a good agreement with a thermal bose gas fit (black lines). Note that in all fits, the region delineated by the dashed vertical black lines are excluded from the fit as they contain the condensate.

superfluid transition temperature. In other words, the appearance of a pair condensate is coincident with the normal to superfluid phase transition. We obtain the condensate fraction by rapidly ramping the magnetic field to the BEC side of the Feshbach resonance [123, 155]. This process is rapid relative to the many-body timescale $\hbar/E_{\mathrm{F}} \sim 3$ μs, and slow relative to the two-body timescale $\hbar/g_0\sqrt{n} \sim 20$ ns. Thus, the pair center-of-mass momentum distribution is preserved as the pairs are converted into tightly bound molecules. These molecules are released from the trap, causing the faster thermal atoms to fly away and separate from a pair condensate. The magnetic field is finally ramped back up closer to the resonance in order to image the atoms with an acceptable scattering cross-section. Typically, in the limit of a long time of flight, the cloud profile appears bimodal, and the condensate fraction is estimated from the relative weight under the two modes.

Armed with the tools of momentum focusing from the previous section, we combine accurate momentum space measurement with the rapid ramp technique. Instead of a completely free expansion, we release the atoms into the magnetic curvature po-

tential right as the Feshbach field is rapidly ramped. After approximately a quarter period, the Feshbach field is ramped back, and an image is taken. The resulting images show an incredibly sharp line-like condensate embedded in a broad thermal cloud (see Figure 5-16). Note that since the curvature changes slightly as the Feshbach field is changed, the actual wait time in free expansion is not exactly $T/4$, but rather fine-tuned for the narrowest condensate. Since we expect the condensate to appear mostly at $k = 0$, with a width set by a residual mean-field repulsion during expansion, the condensate should be as sharp as possible after momentum focusing.

A simple gaussian fit for the thermal fraction no longer works well. Near T_c, bosonic pair correlations emerge before a true condensate forms. These correlations are reflected in a prominent sharp cusp at $k = 0$, as expected from a cold Bose gas [104]. Accordingly, we fit the wings of the axial momentum profiles with the momentum distribution for a thermal gas of noninteracting bosons:

$$n_{1D}(k_z) = \frac{1}{(2\pi k_B T)^{3/2}} g_{3/2}\left(e^{-|\hbar^2 k_z^2/2m - \mu|/k_B T}\right) \tag{5.43}$$

The condensate fraction is equivalent to the difference in area between the observed profile and a fit to the thermal wings. The condensate fraction obtained in this method is one of the most robust measures of the global temperature of the gas. In Figure 5-16, we vary the temperature of the trapped Fermi gas by oscillating the height of the walls at 200 Hz for a variable number of cycles. The condensate fraction appears to sharply vanish at a reproducible number of heating cycles, demonstrating the stability of both the heating method as well as our momentum space mapping technique. As we will see in the subsequent section on the spectroscopy in the unitary Fermi gas, this stability has allowed us to demonstrate a dramatic increase in the contact at the superfluid transition.

5.3 The Joule-Thomson effect

Classical ideal gases obey the law $PV = Nk_BT$. During an adiabatic expansion of an ideal gas, the product PV remains constant, and thus, the temperature is unchanged. However, if you let air rush out of a bicycle tube, you'll notice that the valve becomes cold to the touch. This effect was first investigated in a series of experiments by Joule and Thomson in 1852, where they observed that real gases do change in temperature once they undergo a rapid change in pressure [75]. Now known as the Joule-Thomson effect, this process is especially useful when applied to the production of liquid nitrogen and oxygen [78].

The physical origin of this effect lies in the interactions between the molecules of a real gas. The internal energy of a gas typically comprises of an internal kinetic energy due to the motion of the molecules, and an internal potential energy due to the intermolecular forces. During a Joule-Thomson expansion, the molecules can climb or roll down the intermolecular potential (such as the van der Waals potential), and that energy can be removed from, or converted into kinetic energy. In the subsequent derivation of the Joule-Thomson coefficient $\alpha = \left(\frac{\partial T}{\partial P}\right)_H$, we will discuss the thermodynamics behind this process in a more rigorous fashion.

Before the derivation, it is worth mentioning that unlike ideal classical gases, ideal quantum gases do have a nonzero Joule-Thomson coefficient. Predicted in 1937, the quantum statistics of bosons results in a cooling effect, while the Fermi-Dirac statistics of degenerate fermions is predicted to have a heating effect [80]. For fermions, this can be understood by thinking of Pauli pressure as an effective repulsive interaction between atoms. An expanding gas allows atoms to occupy a larger range of momentum states, which increases the internal kinetic energy. This quantum Joule-Thomson effect has been observed in a weakly-interacting quasihomogeneous BEC, where atom number losses from background collisions results in an isenthalpic cooling [131]. It is important to note that this quantum effect only appears for very weak interactions, and at very low temperatures. For our unitary Fermi gas, the

interactions are as strong as quantum mechanics allows, and the effects of interactions dominates over Pauli pressure. We leave a detailed evaluation of the Joule-Thomson effect as a function of interactions for a future study.

We take a brief moment to derive the Joule-Thomson (JT) coefficient, and show how it can be obtained as a by-product of measuring the equation of state of the unitary Fermi gas. To calculate the JT coefficient for the unitary Fermi gas:

$$\alpha = \left(\frac{\partial T}{\partial P}\right)_H \tag{5.44}$$

we make use of the relation $E = \frac{3}{2}PV$ to note that the enthalpy is $H = E + PV = \frac{5}{3}E$, so constant enthalpy is equivalent to constant E. The JT coefficient can now be calculated in terms of thermodynamical quantities using the cyclic identity:

$$\left(\frac{\partial T}{\partial P}\right)_E \left(\frac{\partial E}{\partial T}\right)_P \left(\frac{\partial P}{\partial E}\right)_T = -1 \tag{5.45}$$

Since the specific heat at constant pressure is

$$C_P = \left(\frac{\partial E}{\partial T}\right)_P \tag{5.46}$$

we can write the JT coefficient as:

$$\alpha = -\frac{1}{C_P}\left(\frac{\partial E}{\partial P}\right)_T \tag{5.47}$$

$$= -\frac{1}{C_P}\left(\frac{\partial}{\partial P}\left[\frac{3}{2}PV\right]\right)_T \tag{5.48}$$

$$= -\frac{3}{2C_P}\left(V + P\frac{\partial V}{\partial P}\right)_T \tag{5.49}$$

$$= -\frac{3}{2}\frac{V}{C_P}\left[1 + P\frac{1}{V}\left(\frac{\partial V}{\partial P}\right)_T\right] \tag{5.50}$$

The isothermal compressibility is

$$\kappa = -\frac{1}{V}\left(\frac{\partial V}{\partial P}\right)_T \tag{5.51}$$

so the Joule-Thomson coefficient can be rewritten in terms of the compressibility and the pressure as:

$$\alpha = \frac{3}{2}\frac{V}{C_P}(\kappa P - 1) \tag{5.52}$$

Now $C_P = \frac{5}{3}C_V\kappa P$, so

$$\alpha = \frac{9}{10}\frac{V}{C_V}\left(1 - \frac{1}{\kappa P}\right) \tag{5.53}$$

$$= \frac{9}{10}\frac{V}{C_V}\left(1 - \frac{1}{\tilde{\kappa}\tilde{p}\kappa_0 P_0}\right) \tag{5.54}$$

$$= \frac{9}{10}\frac{1}{\tilde{\kappa}\tilde{p}}\frac{V}{C_V}\left(\tilde{\kappa}\tilde{p} - \frac{5}{3}\right) \tag{5.55}$$

$$\tag{5.56}$$

We can rewrite

$$\frac{C_V}{V} = \frac{nC_V}{N} \tag{5.57}$$

$$= \frac{5}{2}\frac{nk_BT_F}{T}\left(\tilde{p} - \frac{1}{\tilde{\kappa}}\right) \tag{5.58}$$

$$= \frac{5}{2}\frac{nk_BT_F}{T}\left(\frac{1}{\tilde{\kappa}}\right)(\tilde{\kappa}\tilde{p} - 1) \tag{5.59}$$

Finally, the JT coefficient can be written as

$$\alpha = \frac{9}{10}\left(\frac{2}{5}\frac{T}{nk_BT_F\tilde{p}}\right)\frac{\tilde{\kappa}\tilde{p} - 5/3}{\tilde{\kappa}\tilde{p} - 1} \tag{5.60}$$
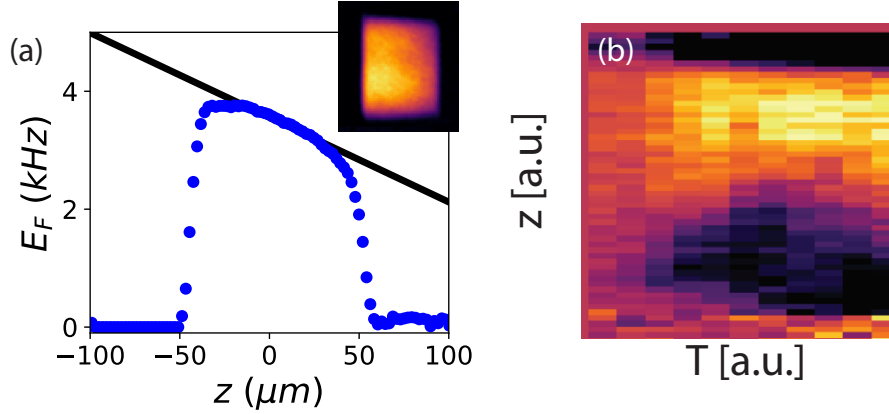
Figure 5-17: Tilting a homogenous unitary Fermi gas. (a): applying a magnetic field gradient shifts the minimum of the magnetic trap away from the center of the cloud This results in a force that causes a density gradient, which responds according to the compressibility of the system. (b) A sequence of 1D profiles shows a clear maximum in the gradient at a particular temperature. This is likely the superfluid transition.

It turns out the following quantity:

$$\alpha_T = \left(\frac{\partial E}{\partial P}\right)_T \tag{5.61}$$

is called the isothermal Joule-Thomson coefficient:

$$\alpha_T = \frac{3}{2}V(1 - \kappa P) \tag{5.62}$$

$$= \frac{3}{2}V\left(1 - \frac{3}{5}\tilde{\kappa}\tilde{p}\right) \tag{5.63}$$

$$= -\frac{9}{10}V\left(\tilde{\kappa}\tilde{p} - \frac{5}{3}\right) \tag{5.64}$$

We focus on the quantity in the parenthesis. In order to measure this quantity, a 12.4 Hz/μm magnetic field gradient is applied to the box. This results in a tilted axial density profile, as shown in Figure 5-17. The typical Fermi energy variation across the center 50μm of the trap is less than 20% of the average Fermi energy.

88
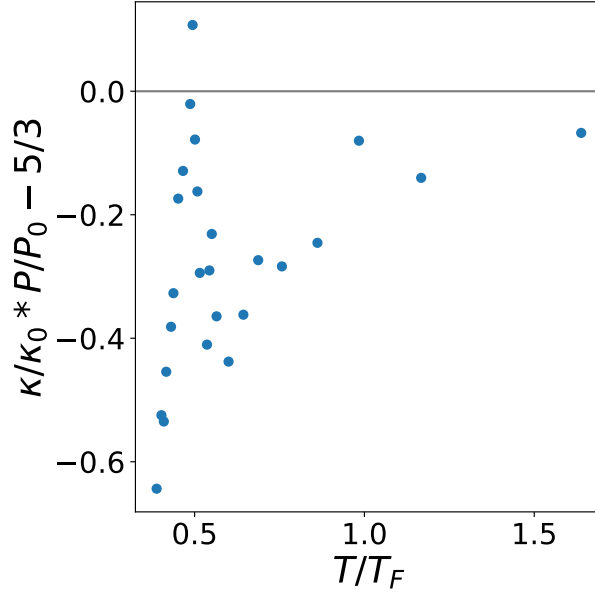
Figure 5-18: The Joule-Thomson coefficient of a unitary Fermi gas. These data show the temperature dependence of the Joule-Thomson coefficient. The trend is non-monotonic.

The initial temperature of the box is varied by a shaking method, and measured using the expansion thermometry outlined above. Before any quantitative analysis, it is evident that the homogeneous unitary Fermi gas is highly compressible near the superfluid transition. This can be seen by subtracting the coldest profile from each density profile. The resulting axial profile shows the compressibility of the gas relative to the coldest gas, where $\widetilde{\kappa} = 1/\xi$. The difference slope is zero for low temperatures, and peaks at the superfluid transition. This reflects the superfluid lambda point.

By fitting the Fermi energy profile at the center of the box with a linear slope, we can obtain the normalized compressibility Equation 5.27, and plot its variation with the normalized pressure $\widetilde{P} = P/P_0 = E/E_0$. From those two quantities, we can

obtain the Joule-Thomson coefficient normalized by the specific heat:

$$\alpha C_P \propto \kappa P - 1 \qquad (5.65)$$

$$\propto \widetilde{\kappa}\widetilde{P} - \frac{5}{3} \qquad (5.66)$$

This is plotted in Figure 5-18. Crucially, the sign of this quantity tells us what happens when the gas is expanded in a more traditional Joule-Thomson expansion. For a noninteracting gas, $\kappa p < 1$, so the JT coefficient is always negative. Thus, when a gas is expanded ($\delta P < 0$), it is expected to warm up ($\delta T > 0$). In contrast, the unitary Fermi gas shows a much more interesting sign variation. Above quantum degeneracy, attractive two-body interactions result in a positive JT coefficient (the gas would cool on expansion). Close to quantum degeneracy, Pauli pressure produces a quantum Joule-Thomson effect which has the opposite sign - the gas is expected to warm when expanded. The inversion temperature for this process is near $T \approx T_{\mathrm{F}}$. For context, the shape of the van der Waals interaction potential results in a classical inversion temperature for most gases - above room temperature for oxygen and nitrogen, and far below room temperature for helium and hydrogen [78]. This is why producing liquid helium and hydrogen is difficult: adiabatic expansion at room temperature no longer cools the gas. However, in our system, we measure a purely quantum JT inversion temperature due to the quantum statistical effect of Pauli pressure. The warming effect of Pauli blocking continues down to the lowest temperatures, except for a narrow window around the superfluid transition T_c. Here, pairing fluctuations cause the compressibility to briefly peak, making the JT coefficient positive near T_c. These multiple Joule-Thomson inversion temperatures illuminate the interplay between pairing, Pauli blocking and interactions in the unitary Fermi gas. As an outlook, it would be interesting to perform the classic Joule-Thomson expansion using two boxes connected with an aperture, much as Joule and Thomson did in 1852. Furthermore, Joule-Thomson cooling could provide a new method of cooling a Fermi

gas to even lower temperatures than evaporative cooling. However, as the pressure decreases, so does the Fermi energy, so a decrease in temperature may be offset by an increase in the Fermi temperature.

5.4 RF spectroscopy and the contact

The homogeneous Fermi box is an excellent tool for precision many-body physics. The uniform density allows us to integrate across the entire cloud, making global probes such as radio frequency (rf) spectroscopy easier to perform. In contrast, obtaining homogeneous spectroscopic measurements in previous experiments required tomographic methods that typically isolated shells of uniform density [134, 130, 54]. We begin this section by providing a quick overview of rf spectroscopy in our system: how it works, and why it is useful. Then, we provide details on rf spectroscopy in the hybrid, and specifically discuss diffusion of the transferred fraction in a nonuniform trap. We observe the effects of final state interactions on the rf spectra, and demonstrate the unique character of linear response in the unitary Fermi gas. We finally discuss measurements of the spectral response of the unitary Fermi gas, and our measurement of the temperature-dependent contact in the unitary Fermi gas.

5.4.1 RF spectroscopy

Radiofrequency (rf) radiation can be used to couple atomic states. Since rf wavelengths are very long ($\lambda \approx 3.7$m for 80MHz), the momentum transfer to the atoms is negligible. We can express the rf transfer operator as a spin-flip from state $|i\rangle$ to state $|j\rangle$:

$$V_{ij}(\omega) = \frac{\hbar\Omega_R}{2}\sum_k [c^\dagger_{\mathbf{k},i}c_{\mathbf{k},j} + c^\dagger_{\mathbf{k},j}c_{\mathbf{k},i}] \tag{5.67}$$

$$\rightarrow \frac{\hbar\Omega_R}{2}\sum_k c^\dagger_{\mathbf{k},j}c_{\mathbf{k},i} \tag{5.68}$$

where in the last line we have assumed that we are transferring atoms from the occupied state $|i\rangle$ to an empty final state $|j\rangle$. This is also known as *ejection* spectroscopy; the opposite is called *injection* spectroscopy.

When applied to an ensemble of atoms, the spin-flip operator described above prepares a coherent superposition of the initial and final states, whose relative phase depends on how long and how hard the two-level system is being driven. This is true regardless of the interparticle interactions. For spin-polarized fermions, Pauli blocking prevents atoms from interacting with each other. Applying an rf pulse to a spin-polarized Fermi gas would therefore result in Rabi oscillations in each atom at frequency $\Omega_R =$. For a fixed pulse time t, the resulting rf spectrum looks like a *sinc* function. This can be recognized as the Fourier transform of a rectangular window. If one were to properly deconvolve the window (or equivalently use an infinitely long pulse time, with infinitesimal power), the rf spectrum would approach a delta function. Typically for rf spectroscopy of ultracold gases, other broadening sources such as power broadening, thermal broadening, and the natural linewidth are negligible.

In the presence of interparticle interactions however, the coherent superposition prepared by the rf pulse decoheres into a mixed state. We use this process produce strongly-interacting spin-mixtures of fermions [123, 155]. Once created, the initial state is a many-body continuum of states encoding information ranging from the Pauli blocking at low momenta, the pairing near the Fermi surface, and the two-body short-range interactions at high momenta. In order to probe this spectrum of information, we can apply another rf pulse, this time applied between one of the spin-states in the interacting gas and a final state. In the limit of a long rf pulse with infinitely low power, the rf transfer rate is given by Fermi's golden rule:

$$\Gamma(\omega) = \frac{2\pi}{\hbar} \sum_f |\langle f| V |i\rangle|^2 \delta(E_f - E_i - \hbar\omega) \tag{5.69}$$

The resulting spectrum would then be $I(\omega) = t\Gamma(\omega)$. This is a sum of matrix elements representing the rf coupling between the initial state $|i\rangle$ with energy E_i (typically set to zero) and all possible final states $|f\rangle$ with energies E_f. In our case, the initial state is a many-body state, and the final states are (ideally) free particles that can be labeled in momentum space with $|k\rangle$. By transferring single atoms from the many-body state into free particles, rf spectroscopy probes the single-particle excitation spectrum. The rf response is in fact, a momentum-integrated measurement of the occupied part of the spectral function $A_-(k, \varepsilon)$ [65]:

$$I(\omega) = \hbar \int \frac{\mathrm{d}^3 k}{(2\pi)^3} A_-(\mathbf{k}, \varepsilon_k - \hbar\omega) \tag{5.70}$$

where $\varepsilon_k = \frac{\hbar^2 k^2}{2m}$. For a BCS many-body state, the spectral function is given by peaks at the particle and hole energies:

$$A(\mathbf{k}, \varepsilon) = u_{\mathbf{k}}^2 \delta(\varepsilon - E_{\mathbf{k}}^+) + v_{\mathbf{k}}^2 \delta(\varepsilon - E_{\mathbf{k}}^-) \tag{5.71}$$

where $u_{\mathbf{k}}$ and $v_{\mathbf{k}}$ are coefficients that satisfy $u_{\mathbf{k}}^2 + v_{\mathbf{k}}^2 = 1$. The excitation spectra are given by:

$$E_{\mathbf{k}}^\pm = \mu \pm \sqrt{(\varepsilon_{\mathbf{k}} - \mu)^2 - \Delta^2} \tag{5.72}$$

Here, μ is the chemical potential, ε is the energy, and Δ is the In contrast, the final state is characterized by a free spectral function

$$A_f(\mathbf{k}, \varepsilon) = \delta(\varepsilon - [E_f + \varepsilon_{\mathbf{k}}]) \tag{5.73}$$

These are shown in Figure 5-19(a). While the many-body state is no longer a BCS state at unitarity, it provides some intuition for the shape of the typical rf

93
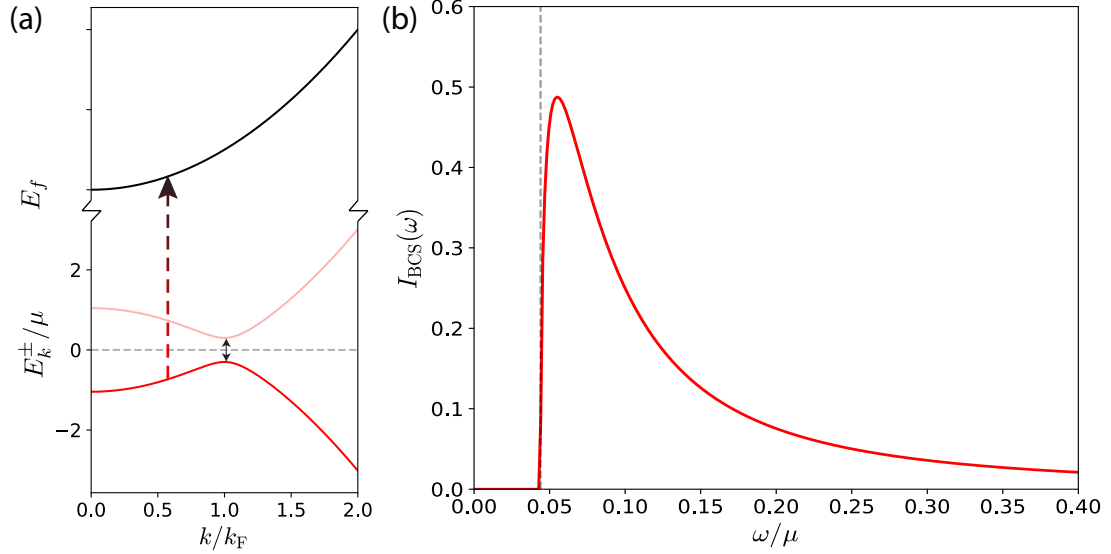
Figure 5-19: Spectral functions and rf spectroscopy. (a) The spectral function of a BCS state consists of delta functions that represent the particle and hole branches of excitations (red and light red lines). Near the avoided crossing at the Fermi momentum, the excitations involve pair-breaking, while away from the crossing, the excitations are dominantly particle-like or hole-like. The gap at k_F is Δ, the pairing gap. An rf photon (dotted vertical arrow) changes the internal state of an atom, and transfers population into a noninteracting final state. The final state has a quadratic spectral function due to the free particles. (b) The corresponding rf spectrum $I_{BCS}(\omega)$ is given by the transfer rate into the final state. The onset is marked with a dotted vertical line. In both plots $\Delta/\mu = 0.3$ is taken to be artificially large to mimic the case at unitarity.

spectra. A molecular rf spectrum is a delta function with a width set by the molecular size.. Similarly, to first order, the rf response of a paired BCS state is a broadened peak, with the form [65]:

$$I_{BCS}(\omega) = \frac{m^{3/2}}{2^{1/2}\pi^2\hbar^2}\left[\frac{\hbar\omega}{2} + \mu - \frac{\Delta^2}{2\hbar\omega}\right]^{1/2}\frac{\Delta^2}{2(\hbar\omega)^2} \tag{5.74}$$

Two features are immediately apparent in the previous equation. First, the spectrum has a well-defined onset at frequency $\omega = \sqrt{\Delta^2 + \mu^2} - \mu$. The second feature is the high frequency tails of the spectrum, which go as $\omega^{-3/2}$. Note that this is in

absence of final state interactions. In the presence of final state interactions, the spectrum can be shown to go as a different power law in the tails: $I(\omega) \sim \omega^{-5/2}$ [152, 116]. This effect will be discussed in subsection 5.4.5.

However, Equation 5.74 is limited in its scope. Even in the weakly-coupled BCS limit, the onset is less sharp, due to the rf excitation of atoms at momenta lower than k_F. Furthermore, the onset and peak shift of the rf spectrum are not only determined by the superfluid gap, but are dominated by so-called Hartree energies that are absorbed into the chemical potential. As a result, the true onset is not exponentially small, as might be assumed from a weakly-coupled BCS picture. In addition, the weight in the power-law tail is given by a thermodynamic quantity known as the contact, which is not exponentially small either. These limitations prevent simple BCS theory from applying to even the BCS side of the Feshbach resonance, and in general, make the computation of spectral functions at unitarity a challenge. In this section, we aim to provide observations of rf spectra at unitarity, as a function of temperature, in order to provide an experimental benchmark for theories that predict the spectral weight of strongly-interacting fermions.

5.4.2   RF spectra in the hybrid

For gases trapped in a typical harmonic potential, the line-of-sight integration during imaging prevents direct measurements of the response to global probes such as rf. Tomographic techniques cleverly avoid this difficulty, but suffer from added noise due to differentiation during the inverse Abel transform, or from the lower signal due to optically pumping away a majority of the atoms prior to measurement. This was a major drive for creating the hybrid trap, which combines the convenient scanning of a phase diagram through the local density approximation with the high signal to noise ratios afforded by a uniform trap. In addition, the known variation of the external potential along the z-axis allows a direct calibration of the equation of state, and provides a direct thermometer from the variation of the density in the wings of
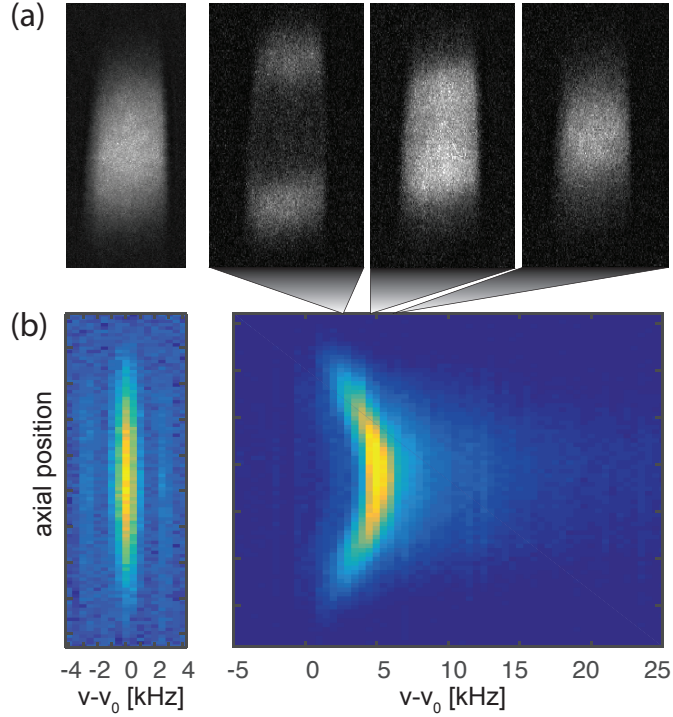
Figure 5-20: Noninteracting and interacting RF spectra in the hybrid.
(a) Here, rf transfers from $|1\rangle$ to $|3\rangle$ are shown for a spin-polarized cloud (left panel) and the balanced $|1\rangle - |2\rangle$ mixture at unitarity (right three panels). The transferred atomic profile reflects the insitu density profile, which is uniform along the horizontal axis in this figure, and harmonic (23Hz) in the vertical axis. In a spin-polarized gas, the rf transfers are not density dependent, while the spin-balanced cloud shows a clear density dependence. This is evident in (b), which shows integrated transfers as a function of rf detuning.

the cloud.

The results of the rf spectroscopy in the hybrid trap are shown in Figure 5-20. During the measurement, images of the initial cloud as well as the rf transferred fraction are taken for every rf detuning. The images are then integrated along the uniform axis to provide a map of the rf transfer as a function of z-position and detuning. Readily apparent is the density-dependence of the onset of the rf spectrum. Driven by mean-field interaction shifts of the energy, the peak moves towards higher detuning at the center of the trap, where the density is the greatest. Also apparent is the asymmetry of the spectrum - a sharp onset towards low detunings and a long

tail at high detunings.

At the $|1\rangle - |2\rangle$ Feshbach resonance of 832G, the scattering lengths to state $|3\rangle$ are $|a_{13}| = 3274a_0$ and $|a_{23}| = 16548a_0$. As a result, the three-body loss rate across $|1\rangle - |2\rangle - |3\rangle$ is relatively high, and we observe large losses even during short rf pulsetimes. To avoid these density-dependent (and hard to correct for) losses, we switched to the $|1\rangle - |3\rangle$ Feshbach resonance at 689G. Here, the other scattering lengths are significantly lower: $|a_{12}| = 1411a_0$ and $|a_{23}| = 1163a_0$. We achieve this by first performing a sweep from 1-5 and then 5-3. The mixture is stabilized as usual by a final evaporation in the box which shaves off any residual fluctuating imbalance.
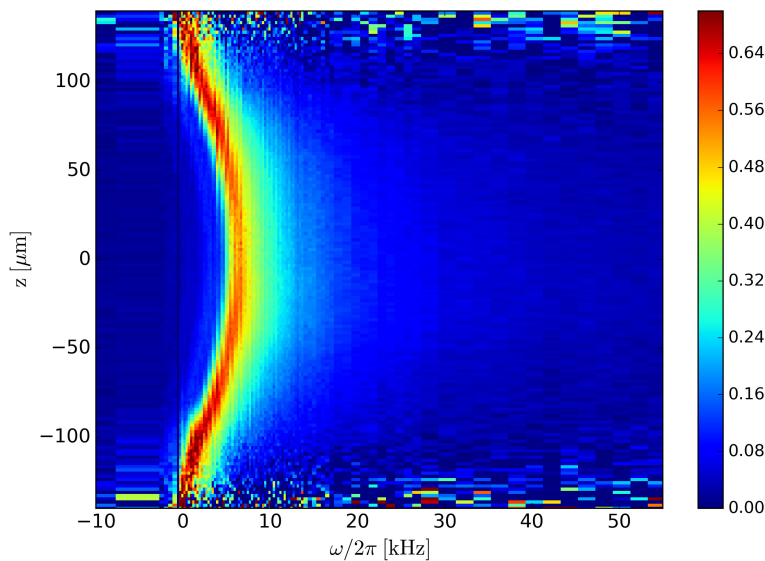
Figure 5-21: **Hybrid rf spectra**. The peak of the rf spectrum scales with the Fermi energy. Here the color axis shows normalized transfers in [a.u.].

5.4.3 Diffusion

rf spectroscopy offers a number of control knobs: the frequency, the power, and the pulse shape. In our experiments, we use a square pulse shape, which adds lobes in frequency space. For some applications, such as beyond linear response Bragg spectroscopy, these frequency lobes can be undesirable [8]. However, by setting the
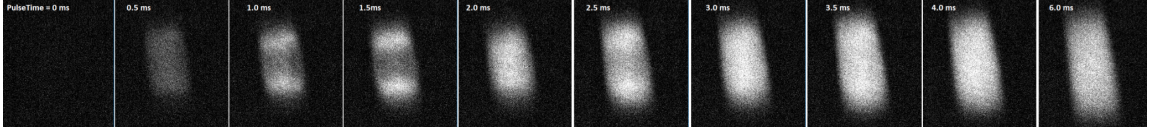
Figure 5-22: Varying rf pulse time. The rf transfers from the hybrid trap are qualitatively different depending on the pulse time used. Shorter pulsetimes (left) suffer from Fourier broadening, while longer pulsetimes (right) suffer from the ballistic expansion of transferred atoms.

overall rf power so that the sidebands carry a very small fraction of the total power, we find the distortion to the resulting rf spectra is minimal. This requirement fixes both the power and the pulse shape, leaving the pulse time as the only free parameter.

There are clearly two timescales that set bounds for the rf pulse time. The lower bound is set by the Fourier broadening imposed by a short time. For a pulse of width δt, the resulting Fourier broadening is on the order of $1/\delta t$. Since most spectral features are on the order of the Fermi energy, a Fourier-limited frequency resolution of $0.1E_\mathrm{F} \sim 1kHz$ seems reasonable. This sets the pulsetime to $1ms$. On the other hand, the LDA requires good spatial resolution of the transferred atoms. After the atoms are transferred, their mean free path l is set by the scattering length of the final states. Given a collision rate of $\Gamma \sim n\sigma v$, we can assume $l \sim v/\Gamma \sim 1/n\sigma \approx 15\mu$m. This means if we want a spatial resolution better than 15μm, the expansion of the transferred atoms is ballistic. For atoms that are transferred near the many-body peak, the initial velocity is set by the momentum distribution of the atoms that are addressed by the rf pulse. If we assume that the fastest subset of those atoms have a Fermi momentum k_F, their velocity is the Fermi velocity, which is roughly 30μm/ms. Thus, pulses longer than 1ms are likely to experience significant blurring due to expansion. This leaves a rather narrow window for the pulsetime.

In Figure 5-22 we show the effects of blurring in inhomogeneous traps as a function of pulse time. As seen before, since the energy scales are set by the Fermi energy, the rf transfers at a particular frequency depend on density. The extent of the blurring can be directly imaged in the hybrid trap, where an rf detuning less than the central

Fermi energy ideally results in bands of transferred atoms. For short pulse times, a wider shell of atoms are addressed under the broad Fourier envelope in frequency space. For long pulse times, although the atoms are being transferred from a narrow shell in the initial cloud, the transferred atoms move ballistically and are free to explore the harmonic trapping potential during the rf pulse.

Unfortunately, the window of pulse times for which the blurring is acceptable closes as we address atoms with greater and greater momentum. For transfers near the onset, a 0.5ms pulse allows for a roughly 15μm blurring. However, for transfers in the high-detuning wings, where we expect the two-body contact to contribute to the transfer rate, the final state kinetic energy can be estimated from the detuning provided: $E_k \sim h\delta$. For a detuning of 60kHz, the transferred atoms move at a speed of about 60μm/ms. A 0.5ms pulse time would result in a blurring of 30μm, which covers a third of the Thomas-Fermi radius of the gas in the 23Hz harmonic trap. We have confirmed this expansion rate using a pair of co-propagating Raman beams addressing a two-photon transition to the final state. With a two-photon detuning of 48 kHz and a pulsetime of 100μs, a $\sim 10\mu$m slice of the cloud was transferred from a $|1\rangle - |3\rangle$ mixture to $|2\rangle$. The transferred slice expands to $55\pm 5\mu$m, at which point the motion is likely diffusive and covers a large axial extent of the hybrid cloud. Thus, although the hybrid trap provides useful diagnostic insight into the evolution of the onset of the rf spectrum, it is unsuitable for measurements of the two-body contact, which require large detunings from the single-particle resonance. Nevertheless, we will see that measuring insitu variations of rf transfer can lead to a method for direct thermometry, and an observation of second sound in the unitary Fermi gas.

5.4.4 Linear Response

Beyond spatial blurring, longer pulse times can come with larger transfers, and a departure from the linear response regime. In Equation 5.68, we assumed the rf perturbation acts by transferring atoms into an empty final state. Once the final

state is populated with enough interacting atoms, this approximation no longer holds, and the response is no longer linear in the pulse time. For small transfers however, Fermi's golden rule asserts that the transfer is proportional to the pulse time and the Rabi frequency squared.

Fermi's golden rule is useful when considering transitions from a single state to a continuum, or as in our case, from a continuum many-body energy spectrum to a single final state. However, we know that the rf spectrum of a strongly-interacting paired superfluid is slightly 'molecular' - there is a clear peak that is defined by the shape of the Fermi surface. That means for sufficiently small pulse times, the Fourier broadening of the pulse is much larger than the width of the rf spectrum. Thus, to the broad rf probe, the peak looks sharp, and very short time transfers should look more like Rabi oscillations between well-defined single-particle states.

In short, we expect a transition from Rabi oscillations to golden rule linear response, to beyond linear response saturation, as we vary the pulse time. For fixed rf power and detuning, we measure transfers as a function of pulse time, shown in Figure 5-23. For short times ($t < 2\pi/\widetilde{\Omega_R}$) where $\widetilde{\Omega_R} = \sqrt{\Omega_R^2 + \delta^2}$ is the generalized Rabi frequency, we observe oscillations that suggest that the peak of the many-body spectrum is not resolved as a continuum. For longer times, we observe a gradually saturating transfer rate, whose initial slope can be used to find the true transfer rate.

5.4.5 Interacting final states

We now consider interactions between the state unaffected by the rf pulse and the final state. It has been shown that final state interactions result in a finite clock shift of the rf transition, while for a completely non-interacting final state, the clock shift should be infinite [7]. This can be seen by inspecting the sum rules for an rf transition
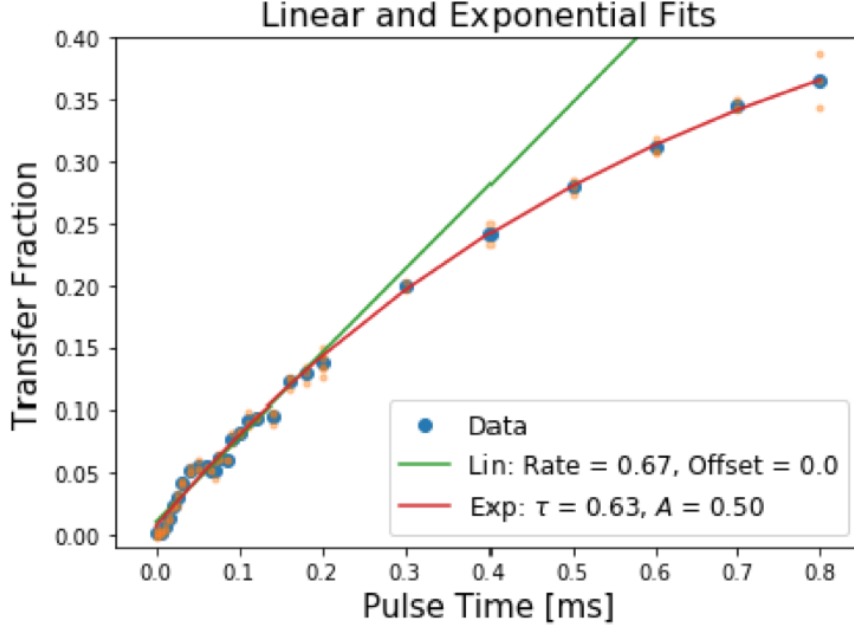
Figure 5-23: Linear response.. Plotted are rf transfers as a function of time, compared to a linear and an exponential fit. Here, the Rabi frequency is $\Omega_R = 2\pi \times 3.02\text{kHz}$, and the detuning from the single-particle resonance is $\delta = 2\pi \times 20\text{kHz}$, or $\delta/E_\text{F} = 0.36$.

$$\Omega_c = \frac{1}{2\pi\omega_R^2 N} \int_{-\infty}^{\infty} \omega I(\omega)d\omega \tag{5.75}$$

Assuming the effective range of the contact interaction is much smaller than the scattering lengths, the clockshift can be written in terms of the initial and final couplings g_{ij}, and g_{if}.

$$\Omega_c = \left(\frac{1}{g_{ij}} - \frac{1}{g_{if}}\right) \frac{1}{n_2} \frac{\partial(F/V)}{\partial g_{ij}^{-1}} \tag{5.76}$$

Here, the partial derivative of the free energy F with respect to the coupling, is related to the thermodynamic contact, with proportionality factors. When $g_{if} \to 0$, $\Omega_c \to \infty$. This is expected when the long tail of the rf spectrum $I(\omega) \to \omega^{-3/2}$, and the integral in Equation 5.75 is divergent. However for $g_{if} \neq 0$, clearly the long-tail

behavior of the spectrum must deviate from $\omega^{-3/2}$.

In 1968, Ken Wilson showed that a product of quantum operators can be expressed as an expansion of local operators [149]. This result can be used to express the product of quantum fields ψ_σ as [11]:

$$\psi_\sigma^\dagger(\mathbf{R} - \tfrac{1}{2}\mathbf{r})\psi_\sigma(\mathbf{R} + \tfrac{1}{2}\mathbf{r}) = \sum_n C_{\sigma,n}(\mathbf{r})O_n(\mathbf{R}) \tag{5.77}$$

where $C_{\sigma,n}(\mathbf{r})$ are known as Wilson coefficients, and $O_n(\mathbf{R})$ are operators that can be calculated using diagrammatic methods from the known contact interaction. As shown above, the full expression for the rf spectrum depends on the spectral function, which in turn depends on the momentum distribution

$$\rho_\sigma(\mathbf{k}) = \int \int d^3R \; d^3r \; e^{i\mathbf{k}\cdot\mathbf{r}} \langle \psi_\sigma^\dagger(\mathbf{R} - \tfrac{1}{2}\mathbf{r})\psi_\sigma(\mathbf{R} + \tfrac{1}{2}\mathbf{r})\rangle \tag{5.78}$$

Using the operator product expansion to replace the matrix element on the right, the momentum spectrum – and relevant to us – the tail of the rf spectrum can be calculated for arbitrary initial and final state interactions a_i and a_f [11]:

$$\Gamma(\omega) \to \frac{\Omega_R^2}{4\pi\sqrt{m}} \frac{(a_i^{-1} - a_f^{-1})^2}{(a_i^{-2} + m\omega)\omega^{-3/2}} C \tag{5.79}$$

Here, Ω_R is the Rabi frequency, and $\Gamma(\omega)$ is the rate at which atoms are produced in the final state. In our case, we start with effectively infinite initial state interactions $a_i \to \infty$. We can rewrite the spectrum as

$$I(\omega) = (N_f(\omega)/N_i)(E_F/\hbar\Omega_R^2 T_{Pulse}) \tag{5.80}$$
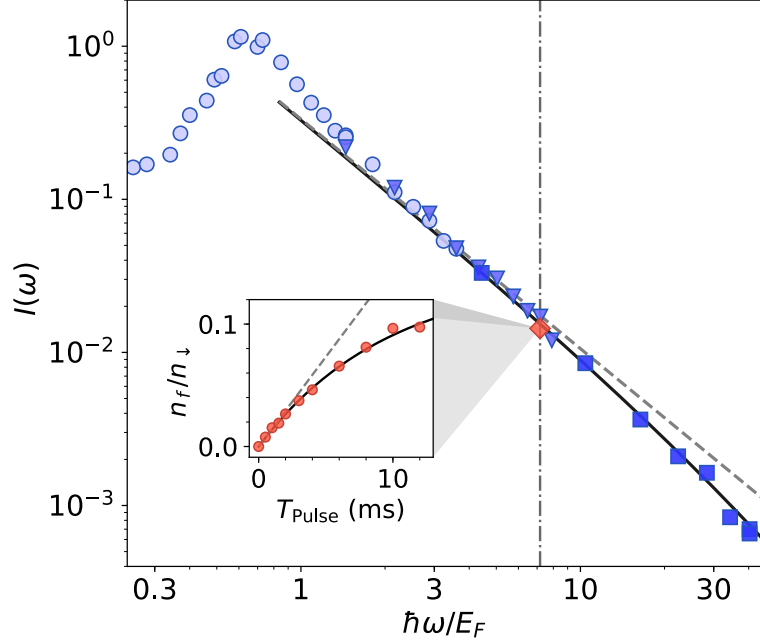
Figure 5-24: Final state interactions.. The rf spectrum of a spin-balanced fermionic superfluid at $T/T_F = 0.10(1)$ shows the effects of final state interactions. Without final state interactions the spectrum is expected to follow a power law given by $\omega^{-3/2}$ (dashed line). However, the data show an agreement with Equation 5.81 (solid black line). We ensure that all measurements are taken within the linear regime, even as we vary the Rabi frequency from $2\pi \times 0.54\text{kHz}$ (circles) to $2\pi \times 1.20\text{kHz}$ (triangles) to $2\pi \times 3.04\text{kHz}$ (squares).

in terms of the Fermi energy E_F and the binding energy of the final state $E_b = \hbar^2/ma_f^2 \approx h \times 433 \text{ kHz} \approx 40 E_F$ for our system:

$$\lim_{\omega \to \infty} I(\omega) = \left(\frac{C}{Nk_F}\right) \frac{1}{2\sqrt{2}\pi(1 + \hbar\omega/E_b)} \left(\frac{E_F}{\hbar\omega}\right)^{3/2} \tag{5.81}$$

For zero final state interactions, $a_f \to 0$ and $E_b \to \infty$, so we recover the expected $\omega^{-3/2}$ tails. However, for $\omega \sim E_b$ and $a_f \neq 0$, the spectrum follows a steeper power law: $I(\omega) \sim \omega^{-5/2}$. In Figure 5-24, we show a measured rf spectrum using a $|1\rangle - |3\rangle$ mixture at the lowest temperatures we can reach with our system: $T/T_F = 0.10(1)$. Using a range of Rabi frequencies, we are able to capture over three decades of

dynamic range in $I(\omega)$. By fitting data where $\hbar\omega > 3E_F$ to Equation 5.81, we observe a deviation from the typical $\omega^{-3/2}$ and a good agreement to the full expression given by the operator product expansion. Here, the dimensionless contact is the only free parameter, fitted to the low-temperature result $\tilde{C} = C/Nk_F = 3.07(6)$. This value is consistent with quantum Monte-Carlo ($\tilde{C} = 2.95(10)$)[36], the Luttinger-Ward calculation ($\tilde{C} = 2.95(10)$)[65] as well as previous measurements using losses ($\tilde{C} = 2.95(10)$)[85] and Bragg spectroscopy ($\tilde{C} = 2.95(10)$)[67].

5.4.6   The temperature dependence of the contact

In the previous sections, we have established that our rf spectroscopy technique obtains the dimensionless contact with precision. We have mitigated concerns regarding linear response, diffusion during the rf pulse, and final state interactions. The curve relating the dimensionless contact (C/Nk_F) to dimensionless temperature (T/T_F) is a universal curve – true for all unitary fermions. A precise measurement of that curve is a true many-body precision measurement, and should stand the test of time, until another experiment improves on errors, and reaches even lower temperatures.

For efficiency, we choose to measure the contact at a fixed detuning $\delta = 60\text{kHz}$ ($\hbar\omega/E_F \approx 6$). Since ω and k_F are known, we only need the transfer in the limit of linear response to measure the contact. We vary the initial temperature by oscillating the trapping potential near a mechanical resonance. The details of this heat injection method can be found in a separate publication that is beyond the scope of this thesis [114]. By varying the heating time, we can prepare the system in temperatures ranging from $T/T_F = 0.10$ to $T/T_F \sim 3$. For each temperature, we measure the number of atoms in the initial and final states by releasing the gas from the box trap. As the atoms expand in the magnetic curvature trap, the optical density drops to a level that allows for accurate atom counting. Using a double imaging camera, we image N_2, the atom number in the final state after the $|1\rangle - |2\rangle$ rf transfer, and N_3, the unperturbed state population. After measuring the transfer rate in the

limit of linear response, we solve Equation 5.81 for C/Nk_F, and plot the results in Figure 5-25.

Firstly, in the limit of high temperatures, the data show a good agreement to the third order virial expansion, indicating that we have a good control over systematic errors. Below $T \sim T_F$, the virial expansion is no longer reliable, and we compare our results to a wide range of theories that make vastly different predictions: Bold-diagrammatic Monte Carlo (BDMC) [124], QMC [59], Luttinger-Ward (LW) [40], large-N [39], and Gaussian pair fluctuations (GPF) [68]. Also shown is the homogeneous contact obtained from the equation of state (ENS-EOS) [105], from loss rate measurements (ENS-L) [85], and from rf spectroscopy by the JILA group [125] across a range of temperatures. We also observe a good agreement with data taken in Swinburne [15] simultaneously with our measurements. For temperatures above T_c, the BDMC data appear to accurately describe the changes in the contact.

At the superfluid transition, we measure the change in the contact. In order to verify our temperature calibration, we use the rapid ramp momentum focus technique described earlier to measure the condensate fraction. We observe a prominent rise in the contact at T_c. This follows prediction from the Luttinger-Ward calculation, in which the contact is sensitive to the pairing gap. Predictions that involve a pseudogap theory predict an even steeper rise exactly at the phase transition, which we do not observe here [116, 111, 97]. Instead, the rise we observe indicates an increase in short-range pair correlations that follow the onset of pairing. Since our measurements, a finite-temperature auxiliary-field quantum Monte Carlo (AFMC) method has calculated the temperature dependence of the contact below the superfluid transition [72]. By taking the continuum limit from a number of lattice calculations, they are able to directly compare their predictions to our measurements. Their results agree well with ours and the data from Swinburne - including in the region where $T > T_c$ where our data appear below most other theoretical predictions.
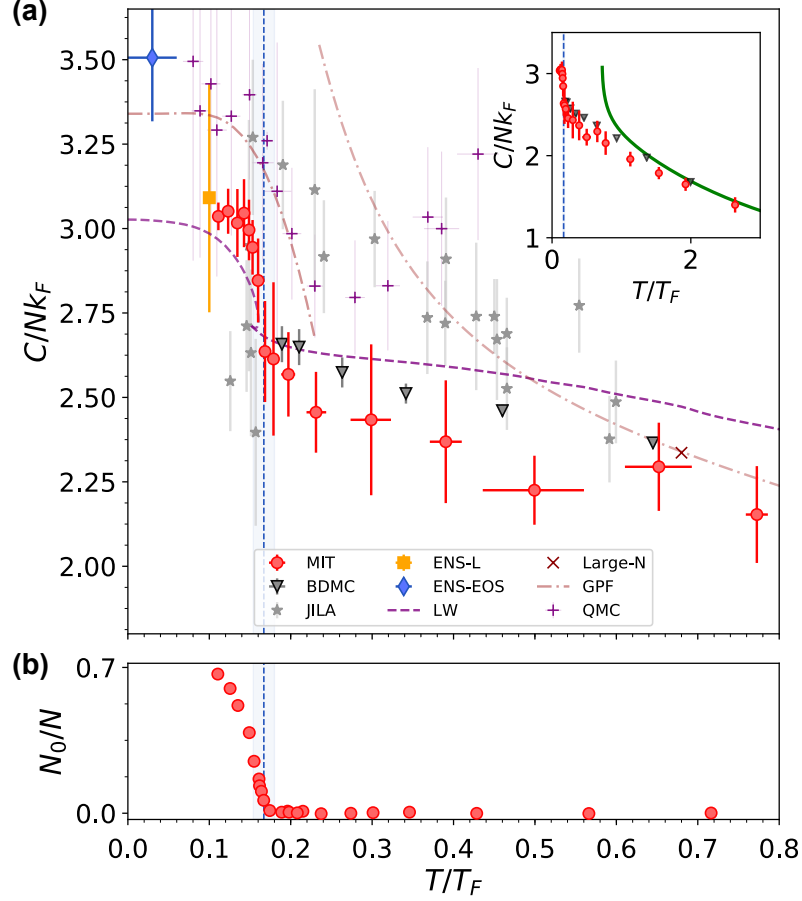
Figure 5-25: Contact vs T. (a) We measure the temperature dependence of the contact and compare the results to a range of theories (discussed in the main text). The contact rises prominently in the superfluid regime. (b) In order to precisely calibrate the superfluid transition, we also measure the condensate fraction using a rapid ramp method combined with a momentum focusing during free expansion. This method is discussed in section 5.2. The vertical blue dotted lines and light blue shaded vertical regions mark $T_c/T_F = 0.167(13)$ [81]. The green solid line shows the third-order virial expansion for the contact.

5.4.7 The many-body peak
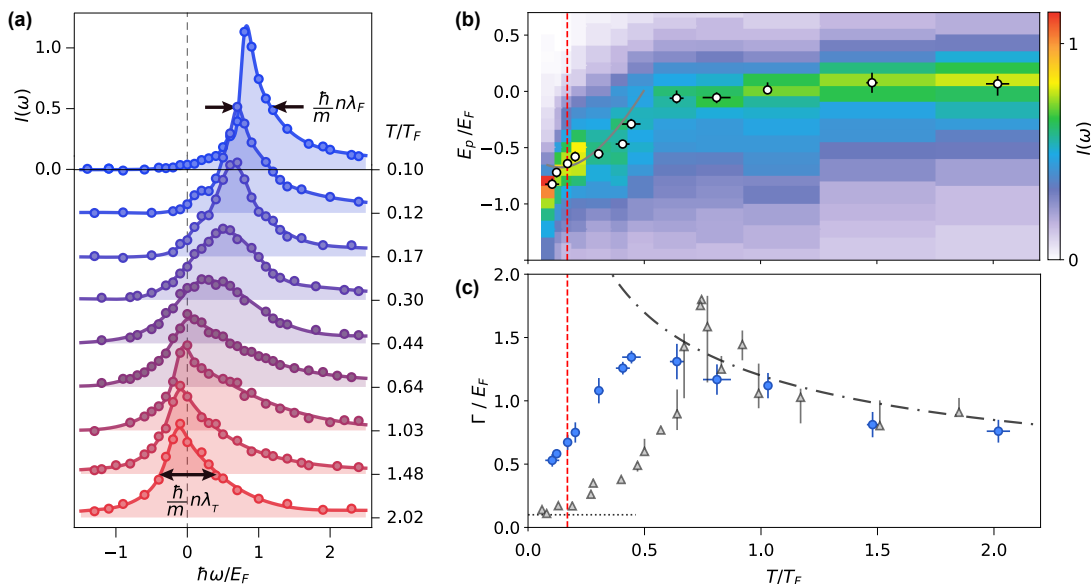
Figure 5-26: Spectral response. (a) Temperature dependence of the peak of the rf spectrum. As the temperature increases, the peak shifts towards zero detuning (b) and displays a non-monotonic change in width (c). Qualitative changes at the superfluid transition (vertical dashed red line in (b) and (c)) appear minimal. We compare the peak shift E_p, with white points marking the peaks, to the change in the energy of the finite temperature Cooper problem (gray line). In addition, the changes in widths (blue data in (c)) are compared to the corresponding widths for a gas of Fermi polarons at unitarity (gray triangles) [150]. The black dot-dashed line represents the temperature dependence of the width due to scattering in the high-temperature gas $\Gamma/E_F = 1.2\sqrt{T_F/T}$ [40, 138]

We now approach the first topic covered in [100]: the spectral response near the peak in the rf spectrum. The bulk of the spectral weight is contained in the many-body rf transfer peak. The rf transfer at these detunings consist of a wide range of momentum components, from $k = 0$ to near k_F. The position and width of this peak therefore contains information about the many-body system as a whole, from Hartree energies to the pairing gap [130]. While the pairing gap has been measured at low temperatures across the BEC-BCS crossover, its temperature dependence remains a mystery. Closely connected to this mystery is the possible existence of

a 'pseudogap' regime, where a pairing gap exists without superfluidity [97]. Hints of such a pseudogap regime in ultracold systems of fermions at unitarity have been observed [54].

However, in order to disentangle mean-field interaction energy shifts from shifts due to a spectral gap, it is necessary to populate both branches of the single-particle excitation spectrum. This can be achieved by preparing a slightly spin-polarized gas. Due to Pauli blocking, the unpaired excess fermions are required to live at the Fermi surface as quasiparticle excitations [130]. Like many of the rf measurements outlined earlier, inhomogeneous quasiparticle spectroscopy has so far depended on the inverse Abel transform. With a fully homogeneous cloud, quasiparticles could be resolved not only in rf detuning, but also in momentum space. A future homogeneous measurement of the full spectral function as a function of the temperature T and polarization σ can be directly compared with results from previous experiments as well as numerical methods [54, 65, 33].

In Figure 5-26, we show our results for the changes in the many-body peak as a function of temperature. Here, the spectrum $I(\omega)$ is defined in Equation 5.80, and the detuning is relative to the bare rf resonance. At high temperatures $T \gg T_{\mathrm{F}}$, the peak is unshifted, despite the presence of interactions. This is because at unitarity, the attractive and a repulsive branch are centered around zero and are separated by $\sim E_{\mathrm{F}}$. For large temperatures, both branches contribute equally to the shift, and cancel each other out [66]. For lower temperatures, the peak shifts towards the attractive branch, and reaches a maximum of $E_p \approx 0.8 E_{\mathrm{F}}$ for a paired superfluid.

To quantify the full widths at half maximum (FWHM) of the peaks, we fit quadratic functions to the peak and its flanks. The fit to the peak provides the center position and the height. The flank fits then provide the widths at half the fitted height. This procedure is robust to both noise as well as peak asymmetry. At high temperatures, the system is a Boltzmann gas with a scattering rate $\Gamma \sim n\sigma v$. Here, the scattering cross section $\sigma \sim \lambda_T^2$ is set by the thermal de-Broglie wavelength

and $v \sim \hbar/m\lambda_T$ is the thermally-averaged relative velocity. Thus, the scattering rate is proportional to λ_T, or inversely proportional to $\sqrt{T}$. This is reflected in the rf spectra for both the spin-polarized gas as well as the balanced gas. Both show identical peak widths for $T > T_\mathrm{F}$.

For degenerate gases however, the peak widths differ considerably. The spin-polarized gas shows a quadratic dependence on temperature. This observation agrees with a Fermi liquid picture, where minority gas is treated as a system of fermionic polarons, dressed by its interactions with the majority spin state [12, 150]. For very low temperatures, Pauli blocking prevents scattering, and the quasiparticles are long lived. This is reflected in our Fourier-limited observation of a sharp rf spectral peak. As the temperature of the system increases, the once sharp Fermi surface of the majority becomes blurred, and the phase space available for scattering increases; from dimensional analysis, the scattering rate of the Fermi polaron is $\Gamma \sim kT^2/T_\mathrm{F}$. Near $T \sim T_\mathrm{F}$, both rf spectra have widths $\gamma > E_\mathrm{F}$, reflecting the breakdown of the quasiparticle picture [109, 39, 53].

The spin-balanced Fermi gas displays a non-Fermi liquid rf spectral width for all temperatures. Instead of a quadratic dependence on temperature, the width varies linearly with T below T_F. This is significant as previous studies have suggested that the normal phase above T_c could be a Fermi liquid [105]. In fact across a broad quantum critical regime (near $\mu = 0$, $T/T_\mathrm{F} \approx 0.68$), the observed T-linear spectral widths mirror the enigmatic T-linear resistivities observed in a wide range of solid state systems [90, 24, 86]. This universality suggests a common underlying physical character across these quantum critical systems, despite the breakdown of the quasiparticle picture.

Unlike the gas of polarons, the spin-balanced Fermi gas displays a spectral function with a finite width at the lowest temperatures. This is because when the two Fermi surfaces overlap at sufficiently low temperatures, Pauli blocking plays a vastly different role. Unlike the momentum diffusion shielding in polarons, here Pauli block-
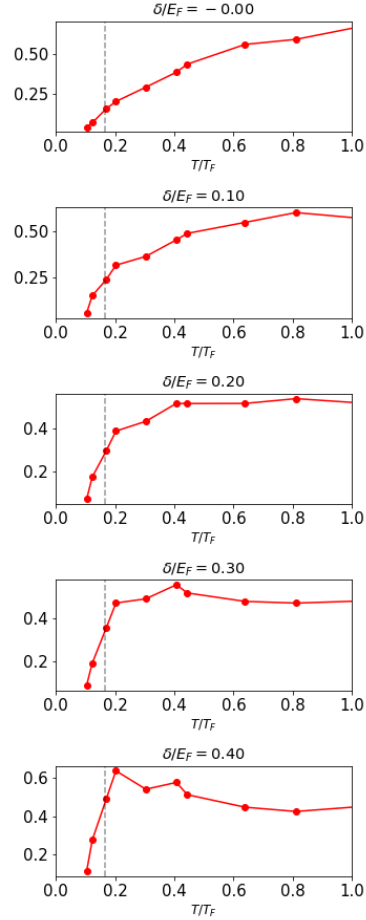
Figure 5-27: Temperature dependent spectral response. From top to bottom, these panels show the variation of the rf spectral response vs T/T_{F}, for five specific fixed rf frequency detunings. The vertical dotted line represents the superfluid transition. The slope relates the rf spectral response to changes in temperature.

ing results in correlations between opposite spin states and momenta, realizing pairing. At unitarity, the rf spectra are broadened by the spread of momenta in a pair. This is given by the Fermi momentum $k_{\mathrm{F}} = 1/\xi$, where $\xi \sim \lambda_F$ is the characteristic size of the pair. The expected spectral width is $\Gamma \sim \hbar n \lambda_F / m$. Thus, the finite pair size results in a finite spectral width.

5.4.8   A local thermometer

As part of an outlook, we present data that establish rf spectroscopy as an effective local thermometer. A quick inspection of Figure 5-26(a) shows a clear temperature dependence of the rf spectral response. A similar phenomenon drives thermal imaging. Due to Planck's law, the blackbody spectrum of an object varies with temperature. For temperatures between 300-1000K, the peak of the blackbody spectrum shifts from approximately 8 to 3 μm. This change in the energy spectrum allows thermal cameras to take spatially-resolved images of temperature. Crucial to this imaging is a careful calibration of spectroscopic imaging to temperature. In our system, this calibration is readily obtained from the data in Figure 5-26(a).

In Figure 5-27, we rearrange the same data for small detunings, now plotted against temperature. We observe that for cold gases (near and below the superfluid transition), the rf spectral response grows with temperature. This can be intuitively understood as measuring the density of thermal excitations such as broken pairs that populate the upper branch of the spectral function at higher temperatures. The closing gap near the superfluid transition is also expected to change the shape of the spectral function, contributing to an increased rf transfer in the flank of the main peak. In Landau's two-fluid model, the rf response for small detunings effectively couples to the normal fluid fraction, which changes with temperature. The slope of the curve $\frac{\partial n}{\partial T}\|_n$ provides the calibration and allows us to convert images of rf transfer into temperature.

As a demonstration of insitu thermometry, in Figure 5-28, we present an image of thermal gradients generated in a Fermi superfluid. We produce a density gradient by oscillating a gradient potential across the z-direction of the box. Due to a weak coupling between the density and temperature of a superfluid [142], this generates a temperature gradient across the box. We measure this by applying a 0.5ms rf pulse at a small detuning ($\delta/E_\mathrm{F} \approx 0.3$) from the bare atomic resonance. We then apply a rapid double imaging: first the transferred atoms in $|2\rangle$, followed by a reference
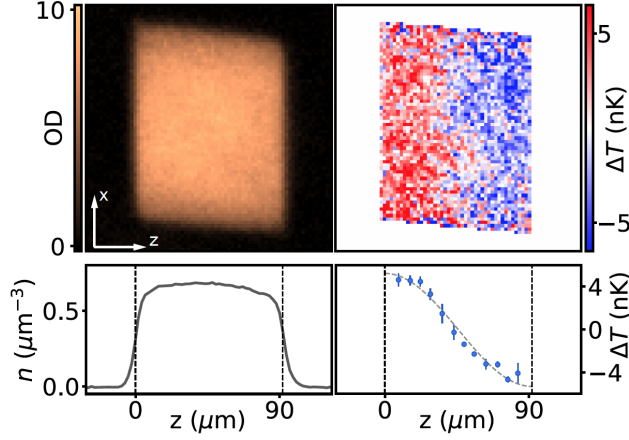
Figure 5-28: Insitu thermometry of a Fermi superfluid. Here we show the insitu density and thermal profiles of a gas in which a temperature gradient has been created. Although the density profile (left column) shows no obvious indication of thermal variations, the thermal profile (right column) obtained from insitu rf thermometry clearly shows a gradient in temperature.

density image. Using the thermometer calibration from the slope in Figure 5-27, the transferred fraction readily provides the temperature. A signal-to-noise ratio of 1 is achieved for sub-nanoKelvin temperature variations at $T = 63$nK or $0.75T_c$.

It is worth noting the spatial resolution of the insitu rf thermometer. Although our optical imaging is limited by our objective to $\sim 5\mu$m, the true insitu resolution of rf imaging is limited by the motion of the atoms during the pulse. Although the transferred energy from the rf pulse is small due to the small detuning, the rf addresses atoms across the Fermi sphere, including those at the Fermi momentum. This is after all what allows us to measure broken pairs and perform thermal imaging. Assuming a worst-case scenario where all transferred atoms are broken pairs that move with a Fermi momentum, the atoms would travel 13μm assuming ballistic expansion and a 10kHz Fermi energy. Although the final state interactions with $|2\rangle$ are weak, the motion is diffusive for sufficiently long timescales. As mentioned earlier, the mean free path for our system is $\ell = 1/(n\sigma) \approx 15\mu$m. So the motion is partially diffusive, and we can expect a blurring of 10-13μm. This is more than sufficient for measuring the lowest modes of the box, since our box length is fortunately $L \approx$

100μm. It turns out that higher second sound modes are significantly damped in our system, and we only observe the first two. In the main outlook section, we will provide a quick outline on how we have used this technique to measure the propagation of these second sound waves in a fermionic superfluid.

Chapter 6

Landau gauge wavefunctions

We now turn to our experiments on uniform rotating quantum gases. As discussed in chapter 3, rotating systems of neutral ultracold atoms are an ideal platform for studying the quantum Hall effect. In general, ultracold quantum gas experiments benefit from the measurement and control of a large number of degrees of freedom, such as the interaction strength, the local density, scalar potentials and gauge fields. As we shall show in this chapter, these characteristics have enabled us to study a fundamental building block of the quantum Hall effect: the Landau gauge wavefunction.

Since the demonstration of Bose-Einstein condensation, there has been significant interest and progress towards rotating ultracold atomic gases close to the lowest Landau level [132, 25]. However, in order to prepare perfectly degenerate Landau levels, the gas must be rotated at the trapping frequency, resulting in atoms that are untrapped in the rotating frame. This has remained a significant challenge, since ultracold atoms are usually studied inside trapping potentials. As a result, neutral atom quantum Hall experiments have been so far restricted to the study of non-uniform vortex lattices that are close, but not at, the limit of perfectly degenerate Landau levels.

Furthermore, past experiments have relied on the effective magnification from

a time-of-flight expansion [91, 1]. This prevents a quantitative study of unstable, untrapped quantum Hall systems using ultracold atoms. In recent years, high resolution insitu imaging has proved remarkably useful, especially for measurements of local quantities in many-body quantum systems [20, 113]. In order to understand the quantum Hall effect on a microscopic level, we probe the in situ evolution of individual Landau gauge wavefunctions in the lowest Landau level using a microscope objective.

We begin the chapter by describing our construction of the new experimental apparatus, with details on the design of the vacuum chamber and imaging system. We will give a wide overview of the apparatus and the steps we took to achieve BEC. For more details regarding the magnetic transport system, the slower, and the fermionic ^{6}Li laser system, we refer the reader to the other theses from this lab. We then describe the preparation of the first longitudinally-uniform Landau gauge wavefunctions in the lowest Landau level using a sodium BEC. We outline the experimental sequence, and summarize our measurements of the distribution of cyclotron guiding centers. We discuss deviations from the expected Hall response due to trap anharmonicity, and provide details on simulating BECs that are untrapped in the rotating frame. Lastly, we describe our observations of the effects of interactions on a Landau gauge wavefunction. We observe a spontaneous crystallization of a longitudinally homogeneous condensate. We characterize the interaction-driven crystallization, specifically outlining a smooth connection from a hydrodynamic instability to a quantum magneto-roton.

The research presented in this chapter has resulted in the following publications, the second of which is to appear in Nature:

*R. J. Fletcher, A. Shaffer, C. C Wilson, P. B Patel, Z. Yan, V. Crépel, B. Mukherjee, M. W. Zwierlein, "Geometric squeezing into the lowest Landau level," Science **372**, 6548, pp. 1318-1322 (2020) [51]*

B. Mukherjee, A. Shaffer, P. B Patel, Z. Yan, C. C Wilson, V. Crépel, R.

J. Fletcher, M. W. Zwierlein, "Crystallization of Bosonic Quantum Hall States,"
arXiv:2106.11300 (2021) [101]

6.1   A quantum Hall microscope

The design and construction of our newest cold atom machine was driven by a desire to revisit the study of rotating quantum gases. Nevertheless, we took a broader approach, and built a general-purpose dual species experimental apparatus instead of a specialized machine. To that end, it would be remiss to omit mention of our oldest cold atom machine, BEC1, the focus of the first part of this thesis, and the design inspiration for the new experiment. The success of BEC1 has spanned over two decades, covering aspects of the field hardly imaginable when the vacuum chamber was first designed. Indeed, this success is due to a combination of the hard work of the generations of students before us, and a flexible experimental design that has formed the blueprint of many experiments in the hallway. As BEC1 approached the end of its life, we endeavored to build a replacement, Fermi3: one that could continue the same experiments, was similarly flexible, but lacked the limitations of the old machine.

The heart of the experiment is almost identical to BEC1, sharing the same atomic species, oven design, slower length, and overall size (see Fig. 6-1). The reader is therefore encouraged to explore the theses from the old machine for a deeper understanding of the new one. Our first design choice concerned the atomic species. Fermionic ^{6}Li was a straightforward choice, given the presence of broad Feshbach resonances near 832G. At lower fields and lower interaction strengths, Pauli blocking prevents efficient evaporative cooling, necessitating the pre-cooling of fermions. A few experiments have achieved a single-species approach to this problem, generating fermionic clouds at sufficiently high phase-space density through direct laser cooling [69, 133, 112]. While the simplicity and potentially rapid development of
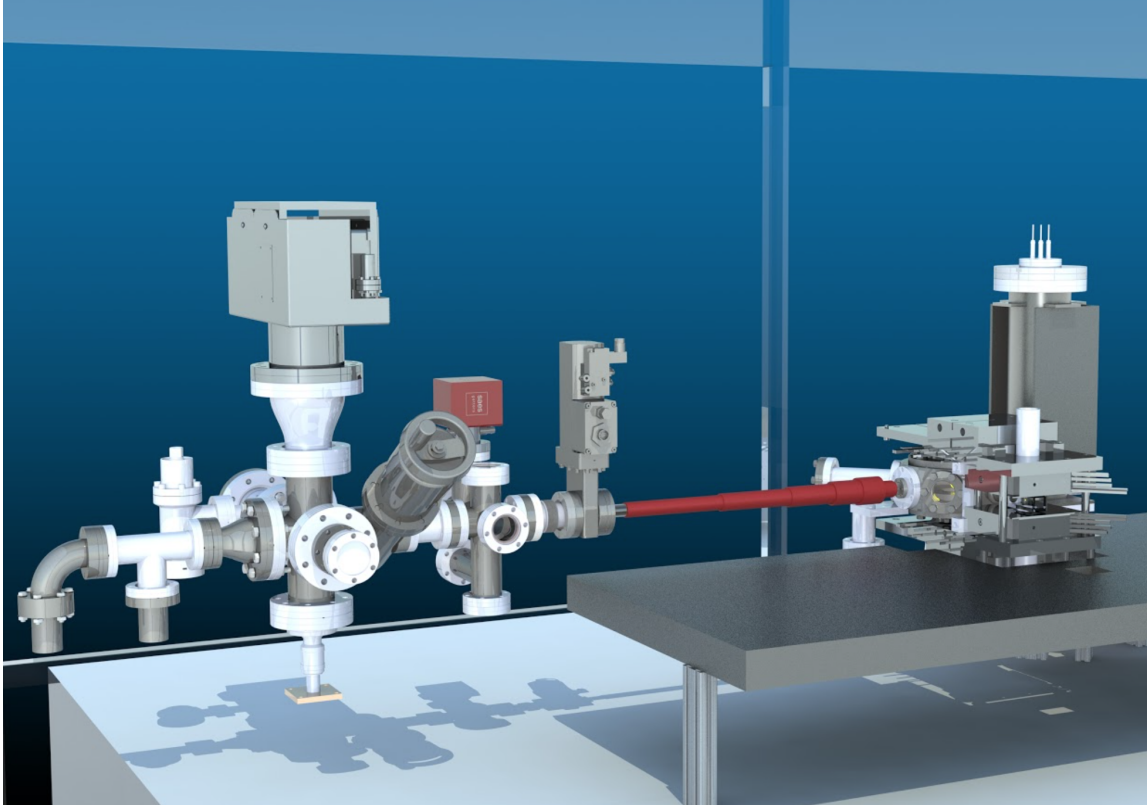
Figure 6-1: 3D CAD render of Fermi3.. The vacuum chamber consists of three gated subchambers. To the left is the source of the atoms: the oven chamber, containing the cups of alkali and the atomic beam nozzle. In the middle is an intermediate chamber, with ports for observation and potential transverse cooling. An electronic gate valve separates the main chamber, which consists of a slower tube, a Kimball physics octagon, a glass cell, and a pump tower. Also shown in this render are the magnetic coil holders around the main chamber, and the custom optical breadboards for mounting MOT and imaging optics.

a single-species machine seemed appealing at first, we decided to exploit the proven reliability of using a massive bosonic condensate of ^{23}Na as a coolant. In retrospect, this approach has produced not only large fermionic clouds, but also original scientific measurements using just the ^{23}Na BEC. Thus, the dual species machine will allow us to study a range of physics in bulk: from weakly-interacting BECs, to strongly-interacting fermionic superfluids.

While designing the optical system for homogeneous atomic Fermi gases in BEC1, we faced an important limitation of the old vacuum chamber: a lack of optical ac-

cess. While the bucket windows allowed us to place lenses relatively close to the atoms, the optical resolution was limited to a few microns. As a result, imprinting and imaging structures on the order of the superfluid healing length $\xi \sim 1\mu m$ remained out of reach. Furthermore, the deep buckets prevented a stable well-centered mounting system for the lens tubes placed inside. The cantilevered optics were sensitive to vibrations, and caused a slow but unavoidable heating of atoms placed inside all-optical potentials in BEC1. Thus, we prioritized optical resolution in the new experiment, and decided on using a glass cell as our 'science chamber'.

The MOT optics in the old experiment had presented another challenge. Large and bulky, they often stood in the way of science optics, and we placed a number of two inch motorized flipper mirrors to switch between the MOT loading and imaging stage of the sequence. The deep horizontal bucket windows in BEC1 admitted two counter-propagating MOT beams of 589 and 671nm each, two pumping beams, a 1064nm dipole trap, both low- and high-field imaging, and finally, the 532nm high-resolution axicon beam. Since passing the large well-collimated MOT beams through a dedicated objective was infeasible, the old machine required additional optics for 1:1 telescopes on either end. Additional optics resulted in additional mechanical instability, and additional alignment.

Separating the MOT loading optics from the science imaging optics would allow us to place objectives close to the glass cell and spread the optics over a larger volume. A simple solution is to transport the atoms from a MOT region to a science region. This can be achieved within the same chamber, limited to distances of a few inches. We have decided to transport the atoms from a dedicated MOT chamber into the glass cell (see Fig. 6-2). Following the philosophy of plug-and-play reliability, we opted for magnetic transport with no moving parts: overlapping coils that provide a moving zero to transport weak-field seeking atoms. Although the apparatus is designed to image atoms placed in the center of the glass cell, it can be in principle modified to transport and image atoms closer to a surface, without breaking vacuum. However,
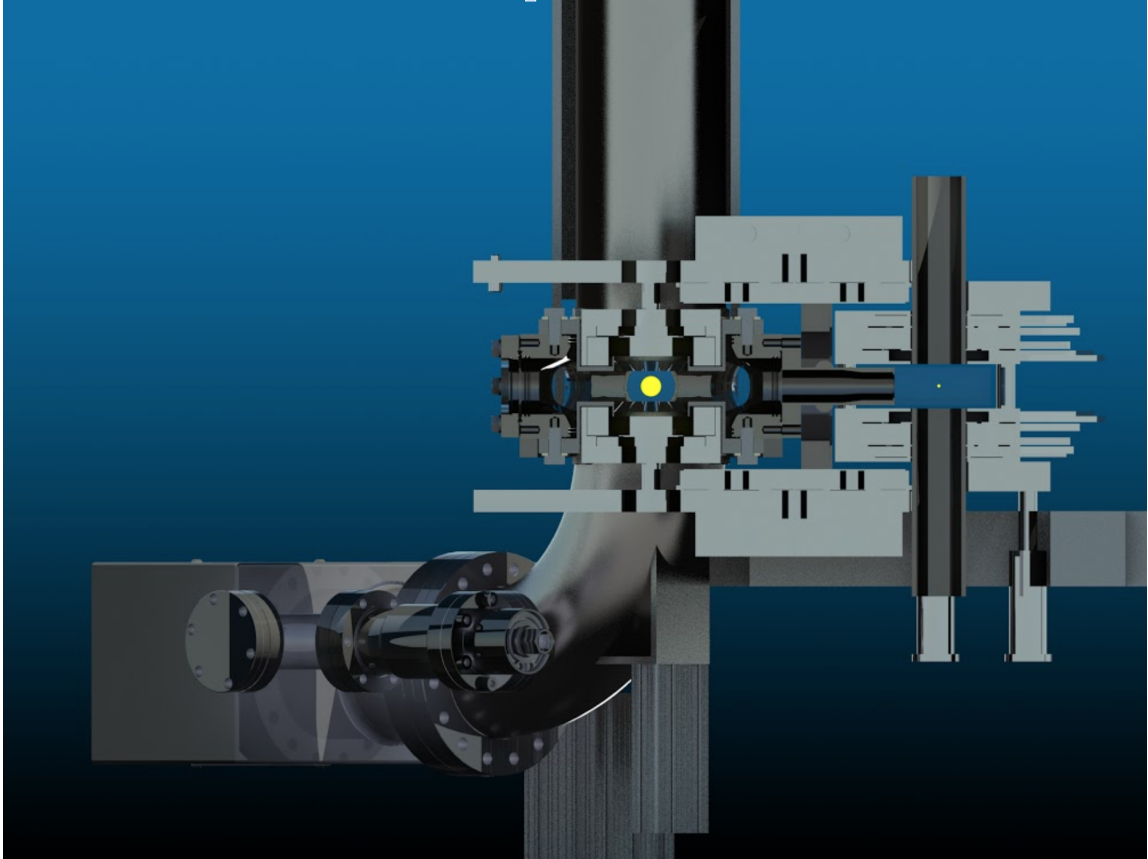
Figure 6-2: Main chamber section view render.. The MOT chamber octagon is directly pumped by the pump tower visible in the background. The atomic cloud (artistically depicted as a yellow sphere, not to scale) is captured in the quadrupole trap, and transported by overlapping anti-Helmholtz-like coils to the glass cell (on the right). The objectives (vertical tubes above and below the glass cell) are then used for measurement and optical control.

this would involve a significantly modified objective system, possibly involving a solid immersion hemispherical lens.

6.1.1 Vacuum apparatus

We start our description of the vacuum apparatus with the oven chamber. The oven chamber design is largely identical to BEC1, with the exception of the oven shutter, which uses a flag mounted on a bellows driven by a linear actuator instead of a rotary feedthrough. This has proved to be significantly more reliable. The nozzle is a 4mm

circular hole in an adjustable sheet of copper.

Due to the heat from the oven heating elements, the oven chamber is full of alkali vapor and other more undesirable gases that are usually adsorbed into cold metal chambers. Thus, the pressure is on the order of 10^{-7} Torr. Differential pumping enables us to maintain a far superior pressure in the main chamber than in the oven chamber. Specifically, there are two differential pumping tubes on either side of the intermediate chamber. A drawing of the intermediate chamber is shown in Fig. 6-3.
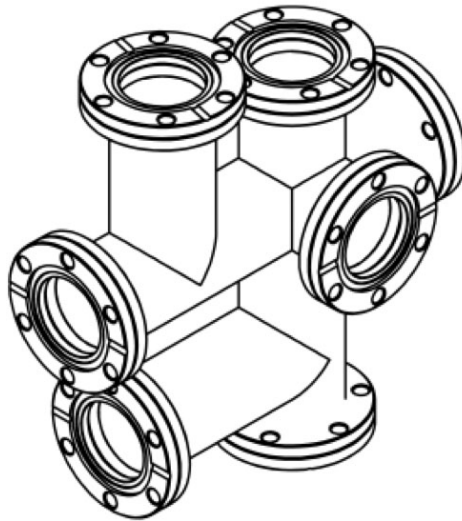
Figure 6-3: Intermediate chamber.. The intermediate chamber consists of a central 6-way with a set of 4 viewports that look directly into the atomic beam. Two of the atoms of the viewport cross are extended to allow for pipes that hold the Nextorr 50D vacuum pump, and a vacuum gauge. The ports are useful for monitoring, but could also be used for transverse cooling of the molecular beam.

The typical mean free path of a molecule in the chamber is given by the following formula from kinetic theory:

$$\ell = \frac{k_B T}{\sqrt{2}\pi d^2 p} \tag{6.1}$$

where T is the temperature, p is the pressure, and d is the typical diameter of the molecule. Since d is poorly-defined, it is often substituted for the Lennard-Jones

Pumping tube	OD	ID	L	C [L/s]	P_i/P_f
Oven-Intermediate	0.25"	0.194"	5"	0.11	900
Intermediate-Main	0.375"	0.305"	2.5"	0.781	128

Table 6.1: Differential pumping tubes.

parameter $\sigma \approx 0.24$nm for the intermolecular potential of H_2 [50]. For T=300K and pressures below 10^{-3} Torr, the typical mean free path for hydrogen is tens of centimeters, larger than most chamber parts. In this regime, the fluid dynamics of the gas is known as molecular flow. Here, the conductance of cm-size pipes is determined solely by its geometrical characteristics, and not by the pressure of the gas. The conductance of a pipe, for instance, is given by the following formula:

$$C = 12.1 \frac{D^3}{L} \tag{6.2}$$

in units of L/s. Here, D and L are the diameter and length of the pipe respectively, in centimeters. The parameters of the two differential pumping tubes are given in Table6.1. The diameter of the differential pumping tubes are chosen so that the slower beam is not clipped. The length is chosen to ensure a sufficiently large differential pumping P_i/P_f between the chambers connected. Since conductances in series add in vacuum just like like conductances in electronics, the total differential pumping between the intermediate and the main chamber is given by

$$\frac{1}{C_{tot}} = \frac{1}{C_{dp}} + \frac{1}{C_{slower}} \tag{6.3}$$

The conductance of the slower is $C_{slower} \approx 1.92\,L/s$, so $C_{tot} \approx 0.56$. Assuming that all chambers are pumped at $S = 100$L/s, this gives an estimate of the differential pumping $P_i/P_f = S/C_{tot} \approx 181$. In reality, the main chamber is pumped by not only an ion pump, but also a large getter surface that will be detailed further on. This surface should provide a significantly large pumping speed.

There are two gate valves in the experiment. The first is a manual VAT valve for isolating the intermediate and the main chamber from the oven during an oven change or a cleaning operation. This valve is intended to remain open overnight to avoid damage from repeated use. The diaphragm is capable of sustaining a 2atm pressure differential, so it should keep a good vacuum while it is closed and exposed to atmospheric pressure. The main nightly safety valve is the second valve: a pneumatic valve from MDC that isolates the intermediate from the main chamber. This valve is closed when the experiment is not actively running to prevent a leak in the oven or intermediate chambers from necessitating a full bakeout of the main chamber. Once fully constructed, the main chamber is surrounded closely by precisely-aligned optics. Removing or covering these for a bakeout could lose many valuable alignment days.

The slower design is an increasing field slower optimized for loading sodium, of length 50cm, divided into four sections. The first three starting from the nozzle side are low current, drawing about 35A. The last section near the MOT chamber draws 130A. In contrast to a decreasing field slower, the slower light is far off-resonant (≈ 1 GHz) with respect to the MOT. This results in a less heating and deflection of the MOT cloud from the slower beam. However, the magnetic field from the slower is higher in the MOT chamber, and has to be tapered down a few cm before to ensure that the MOT gradient isn't significantly perturbed along the slower axis. Like many other increasing field slower experiments, we counter the B-field offset at the MOT position using a 'slower x-bias' coil, wrapped on the other side of the MOT chamber from the slower.

The main chamber is comprised of an octagon manufactured by Kimball physics, with bucket windows from UKAEA, a glass cell, and a pump tower. Four of the smaller octagon ports and the bucket windows admit the cross arms of the MOT beams. The other four small ports connect to the slower, the pump tower, the glass cell, and a window for imaging. We will outline the imaging axes and other

experimental details in the next subsection.

In order to ensure maximum optical access into the MOT chamber, we designed the pump tower to hold the rather bulky ion pump out of the plane of the optical beams surrounding the MOT chamber. The ion pump is also oriented away from the glass cell to make further space for science optics. The pump tower is a J-shaped tube, holding titanium filaments on the vertical port, and the on pump on the bent horizontal port. The height of the tower is just high enough to ensure that the Ti filaments have no line-of-sight to either the slower port on the pump tower or any of the glass ports in the main chamber, as this would cause them to be coated during firing. The minimum horizontal beam height of the slower and the glass cell is set by the bottom of the ion pump being flush with the main optical table; in practice, this is mounted a few inches above to ensure a comfortable working space underneath the plane of the glass cell. Lugs welded onto the surface of the pump tower enable vertical mounting of breadboards for MOT and slower optics. This has proved to be particularly useful for saving space on the main optical table.

We perform our science in a glass cell, manufactured by ColdQuanta. The tube connecting the main chamber to the center of the cell has a conductance of 50L/s. This corresponds to a pressure differential of less than a factor of two between the main chamber and the science region. The cell windows are 5mm thick borofloat, resulting in aberrations to any imaging system using spherical optics; this is corrected for using custom-designed microscope objectives, detailed later.

We will detail two details in the assembly of the experiment here. The first concerns the alignment of the chamber nozzle. The second concerns the baking process. In order to facilitate the nozzle alignment, the machine has been designed with a bellows between the intermediate chamber and the slower. Before starting the bakes, we passed an aligning beam that simulates the solid angle occupied by the slower beam. We sent the beam towards the oven, centered on the slower window, traveling level with respect to the optical table (see Fig. 6-4 for a view from the open
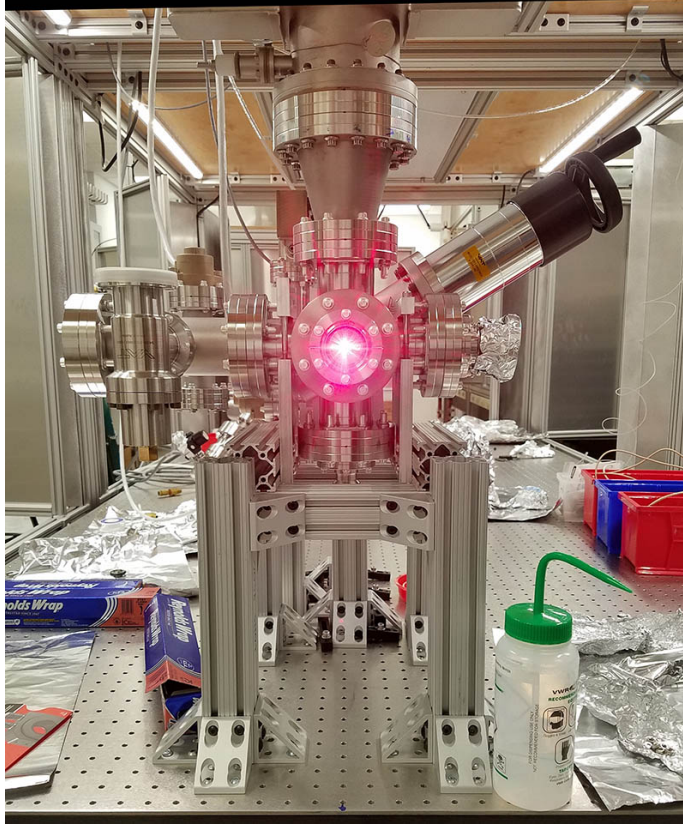
Figure 6-4: Nozzle alignment.. This photograph shows the nozzle alignment beam passing through the nozzle into the oven chamber (removed for alignment). The beam is centered with the main slower axis of the experiment.

oven). Without the cold plate installed, we placed a plumb line to mark the position of the beam. We ensured that the beam is circular by aligning the differential tubes using the bellows. Then, we aligned the hole in the cold plate to pass the beam, and lastly the oven nozzle. Finally, we closed the chamber by installing the oven part (without alkali), and prepared for the baking of the experiment.

Baking the machine under vacuum removes various chemicals that are adsorbed into the inner surfaces of the metal chambers. While this is a fairly well-covered topic in many theses, here we provide a few details into the idiosyncracies of baking Fermi3, and some errors in retrospect that could be avoided in future new experiments. As in other experiments, we wrapped the chamber with heating tape, and installed blanks instead of windows to bake the chamber at a higher temperature (The glass-
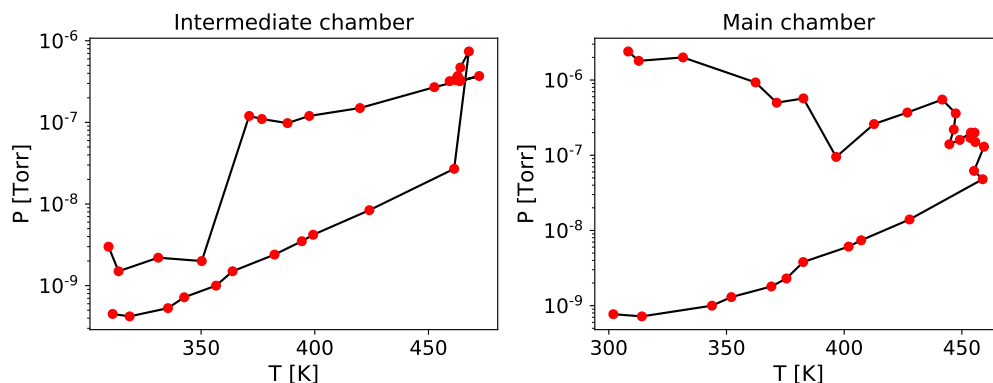
Figure 6-5: A sample bake.. Temperatures and pressures during an early bake we performed after switching the blanks with the windows.

to-metal seal of the chamber windows limits the temperatures of baking to 200C). The first windowless bake ended up reaching temperatures as high as 350C, and as a result, many gaskets had partly fused to the knife edges. The blanks installed on the octagon were particularly challenging to remove. So much so, the toughest to remove blank had to be knocked out with considerable force using a steel pipe through the opposite port (which had luckily come off using a pair of heavy-duty pliers). Ideally, the process of replacing a blank with a window after the first bake should be a roughly fast replacement, to prevent the reintroduction of water and other compounds into the inner surface of the chamber. In this case, the chamber had been opened for a few hours as we struggled to completely remove all blanks. A future experiment could do well to take care to keep temperatures below 350C. This can be achieved by placing thermocouples placed in close thermal contact to the knife edges near the blanks.

The first bake of the intermediate and the main chambers was done with with the manual valve closed, retaining a single window on the slower port. The cell port was replaced by a feedthrough holding three filaments consisting of 1mm diameter titanium, zirconium, and vanadium wire. After the bake, these filaments were fired in succession to coat the interior of the main chamber with a getter material. Although

126

the coating was undoubtably exposed to water vapor while replacing blanks, we hope that the subsequent cooler bake was sufficient to reactivate the getter material. During baking, individual heaters are gradually ramped up in temperature while the chamber is held under vacuum with the combination of the ion, turbo, and roughing pumps. As typical pressures in hot chambers can be drastically higher than those in colder chambers, it can be useful to visualize the baking progress combining both temperature and pressure. To that end, we plot $\log P$ vs T, as shown in Fig. 6-5. The high final temperatures are due to a faulty angle valve that was subsequently replaced, and the chamber was re-baked down to pressures near the detection limit of the ion gauges.

6.1.2 Condensate preparation

Atoms are transported from the MOT chamber into the glass cell using overlapping coils that slowly shift the position of the quadrupole zero into the glass cell. The coils for the magnetic transport are housed inside cooling plates that surround the chamber, but do not touch it. This is done so that sudden changes in the current of the coil are not transferred to the main chamber, and conversely, any movement of the main chamber are not transferred to the position of the atoms in the magnetic trap, set by the location of the coils. We use a plugged quadrupole trap to hold the atoms during the magnetic transport [28], and perform evaporation in the quadrupole trap within the glass cell. The first condensates imaged in our experiment are shown in Figure 6-6.

6.2 Rotating a superfluid

One of the outstanding challenges in rotating quantum gases is reaching the lowest Landau level. By this we mean the chemical potential is less than the cyclotron frequency $\omega_c = 2\omega$, i.e., the spacing between Landau levels. Of course, in order to even
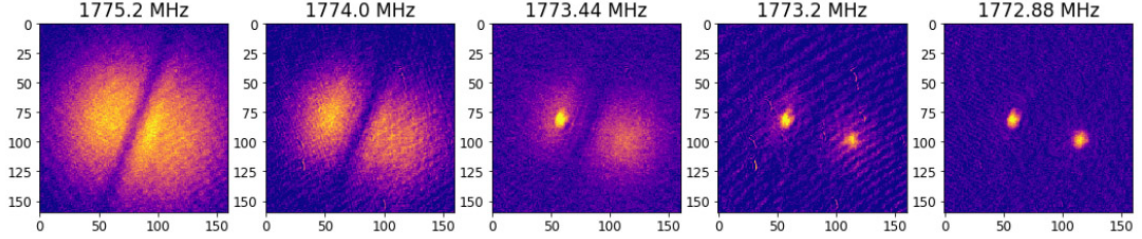
Figure 6-6: The first condensates in the new machine.. This is a view looking up into the MOT chamber from below. To the left is the high phase space density thermal cloud bisected by the 532nm plug beam. From left to right, the rf knife is lowered gradually. The left hand cloud started at a slightly higher number of atoms, and happened to condense first. The result is a set of two condensates separated by the plug beam. In subsequent experimental sequences, we transport the cloud away from the MOT chamber before reaching BEC.

have well-defined Landau levels, the rotation frequency Ω must be very close to the trapping frequency ω. This ensures a high degeneracy of each Landau level. Practically, these objectives place many limitations on experimental approaches. Firstly, as the rotation frequency approaches the trapping frequency, the effective trapping frequency of the gas in the rotating frame decreases until $\Omega = \omega$, when the gas is completely untrapped. Thus, a study that focuses on the ground state in the rotating frame, i.e. vortex lattices, will encounter the issue that the ground state is increasingly extended in real space. Secondly, reaching low chemical potentials requires low densities, and therefore measurements are often low in signal-to-noise ratio. Thirdly, the signature of reaching the lowest Landau level is often not obvious, especially with bosonic condensates. In solid state systems, the classic signature of Landau levels is the discrete jumps in the Hall conductivity under a varying magnetic field. A sharp Fermi surface and low disorder are important ingredients in the observation of the quantum Hall effect. In our experiments, bosons take the place of electrons. Due to the lack of Pauli blocking, there is no Fermi surface, and transport does not show plateaux when the chemical potential is between Landau levels. An alternative method to detect the bosonic occupation of the lowest Landau level has been to observe shear modes in vortex lattices [132]

Superfluids can be difficult to rotate. By the Landau criterion, superfluids are fluids that flow around obstacles without dissipation [118]. The first vortices were generated in superfluids through phase imprinting angular momentum [93], however this was typically limited to small numbers of vortices. As mentioned earlier, a major goal for rotating condensates has been to reach high angular momentum states. To achieve this, condensates are first prepared in a harmonic trap. Then, a trap deformation creates an angular asymmetry in the cloud, and is rotated to deliver angular momentum to the condensate. This deformation is either achieved using a laser beam, controlled with an acousto-optical deflector (AOD) [91, 1], or by turning on an elliptical deformation in a time-orbiting potential (TOP) trap [63]. The first method led to a clear demonstration of fermionic superfluidity [154]. The second method was further improved by applying an evaporative spin-up technique that selectively removed atoms with low angular momenta, near the center of the harmonic trap [38]. Doing so led to the observation of Tkachenko modes in large rapidly rotating vortex lattices near the lowest Landau level [132].

Here we briefly describe our implementation of a time-orbiting potential trap and a rotating elliptical deformation. We start with a normal Bose gas in the quadrupole trap, and turn on a time-orbiting bias field. This is generated using two sets of perpendicular bias coils, placed in the x-y plane around the glass cell. The electronics driving the TOP trap are show as a simplified schematic in Figure 6-7.

The TOP trap works by rapidly rotating the zero of the quadrupole trap in a circle. The TOP frequency must be significantly larger than typical energy scales in the system. In order to be compatible with large Fermi seas, we set our TOP frequency to $\nu_T = 15.475$kHz. The resulting bias field is given by

$$\mathbf{B_{bias}} = B_0 \cos(\nu_T t)\mathbf{x} + B_0 \cos(\nu_T t)\mathbf{y}. \tag{6.4}$$

In combination with the quadrupole magnetic field, this bias field results in a harmonic trap with frequencies ω_ρ, ω_z in cylindrical coordinates, with $\omega_\rho = \sqrt{k/m}$
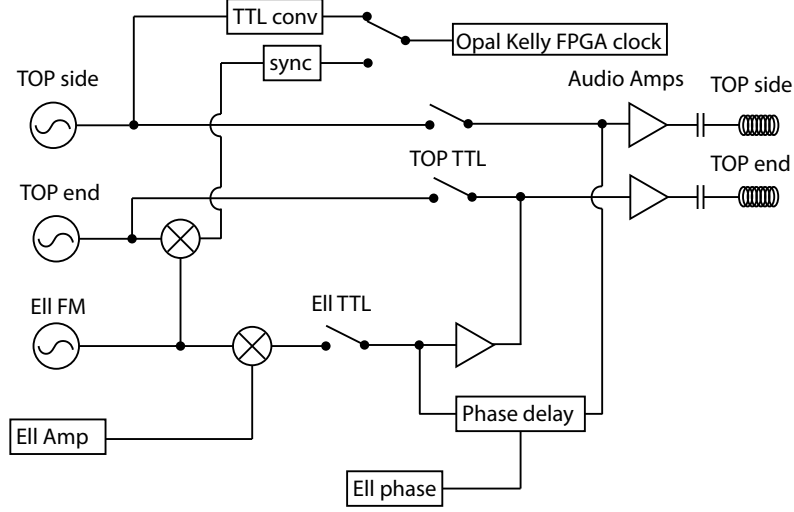
Figure 6-7: TOP trap driving schematic. We use three channels of function generators to produce a TOP trap with an elliptical deformation. The circularly-symmetric TOP is generated by two channels, whose relative phases and amplitudes are optimized to ensure the trap is as circular as possible. Here, "Ell" refers to components related to the ellipsifier. The two coil components on the right represent the perpendicular TOP coils. Note: all analog isolators are hidden in this schematic.

and $\omega_z = \sqrt{8}\omega_\rho$ [115, 96] . The spring constant is $k = |\mu|a^2/8B_0$, where $|\mu|$ is the magnetic moment of the atom and a is the quadrupole gradient at the origin. Anharmonicities appear as quartic terms in the potential. In our experiment, we can adjust the trapping frequency by changing the gradient of the magnetic quadrupole. The vast majority of the data presented in this paper was taken at a trap frequency of $\omega = 2\pi \times 88.\text{Hz}$.

On top of the TOP oscillation, we apply a phase-shifted bias field oscillating at the same frequency [23]. The amplitude of the additional oscillation is $\epsilon(t)$ and the phase shift is $\phi(t)$. Now, the bias field is given by:

$$\mathbf{B_{bias}} = B_0 \left(\cos(\nu_T t) + \epsilon\cos(\nu_T t + \phi t)\right)\mathbf{y} + B_0 \left(\sin(\nu_T t) + \epsilon\sin(\nu_T t + \phi t)\right)\mathbf{y} \quad (6.5)$$

Applying the trigonometric identity $\cos(x + y) = \cos x \cos y - \sin x \sin y$ will show that Equation 6.5 results in an elliptic path for the zero, with the major axis rotating

at a frequency $\Omega(t) = \frac{d\phi}{dt}$. In practice, we implement the ellipsifier with a single channel split in two. One of the paths is phase shifted using a voltage-controlled phase delay, and the two paths are combined with the usual TOP oscillators. We use a mixer to rapidly control the amplitude of the ellipse deformation. A synchronizing circuit allows us to trigger our imaging with a well-defined orientation of the ellipse.

Interestingly, suddenly turning on a rotating potential fails to generate an extended condensate. Intuition for this effect can be found in the solutions to the superfluid hydrodynamic equations. The Gross-Pitaevskii (GP) equation

$$i\hbar \frac{\partial \psi}{\partial t} = \left[-\frac{\hbar^2}{2m} \nabla^2 + U + g|\psi|^2 - \boldsymbol{\Omega}(t) \cdot \mathbf{L} \right] \psi \tag{6.6}$$

can be rewritten in terms of a phase ϕ and density ρ by expressing the wavefunction as a field $\psi = \sqrt{\rho} e^{i\phi/\hbar}$. The resulting equations are known as the superfluid hydrodynamic equations, which are so far identical to the GP equation:

$$\frac{\partial \rho}{\partial t} = -\boldsymbol{\nabla} \cdot \left[\rho \left(\frac{\nabla \phi}{m} - \boldsymbol{\Omega} \times \mathbf{r} \right) \right] \tag{6.7}$$

$$-\frac{\partial \phi}{\partial t} = U + g\rho - (\boldsymbol{\Omega} \times \mathbf{r}) \cdot \nabla \phi + \frac{1}{2m\sqrt{\rho}} \left[(\nabla \phi)^2 \sqrt{\rho} + \nabla^2 \sqrt{\rho} \right] \tag{6.8}$$

The last term in the equation for the phase is known as the quantum pressure: $\nabla^2 \sqrt{\rho} / 2m\sqrt{\rho}$. If the gas is in the Thomas-Fermi regime, we can neglect this term, since ρ is large compared to its curvature. These hydrodynamic equations can be solved using a polynomial ansatz, resulting in the following equation for the anisotropy $\alpha = R_{TFx}/R_{TFy}$ of the cloud profile [137]:

$$\alpha^3 + \left(1 - 2\frac{\Omega^2}{\omega^2} \right) \alpha - \frac{\Omega}{\omega} \epsilon = 0 \tag{6.9}$$

Here, $\omega = \frac{\omega_x}{\sqrt{1-\epsilon}} = \frac{\omega_y}{\sqrt{1+\epsilon}}$ is the radial trapping frequency. The solutions to the above equation are plotted in Figure 6-8. The two branches show two paths to large cloud ellipticity. One is an adiabatic approach from low frequencies, the other

131
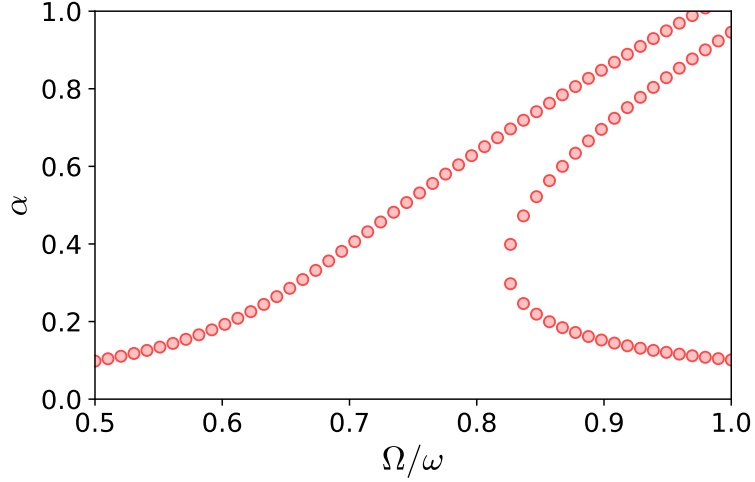
Figure 6-8: Cloud ellipticity from hydrodynamics. The ellipticity of the cloud α is plotted as a function of the rotation frequency Ω. Here, the ellipticity is set to $\epsilon = 0.1$. Points are solutions to Equation 6.9 [137].

from high frequencies. The exact shape of the adiabatic path is dependent on the ellipticity ϵ of the driving potential, but is independent of the interaction strength g. Intuitively, the shape of the curve is given by the rotation drive at $\Omega \approx 0.7\omega$ coupling to the quadrupole mode of the BEC at $\omega\sqrt{2}$ [137].

In our experiment, we apply a rotation frequency ramp given by the equation

$$\Omega(t) = A\omega \tanh\left(B\frac{t}{T_{max}}\right) \tag{6.10}$$

Here, $B = \tanh^{-1}(1/A)$, so that $\Omega(t = T_{max}) = \omega$. The tanh function ensures an adiabatic condition $\frac{d\Omega}{dt} \propto (\omega^2 - \Omega^2)$, or in words, the rate of change of the rotation frequency is proportional to the trapping potential energy in the rotating frame.

6.3   Pattern formation in rotating condensates

It is also possible to ramp the frequency too slowly. By linearizing the hydrodynamic equations, one can evaluate the stability of the solutions mentioned above [137]. It
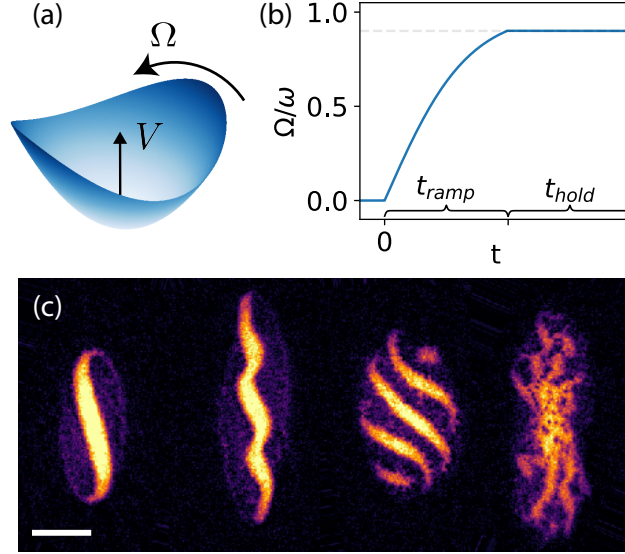
Figure 6-9: Pattern formation in 2D rotating condensates. The condensate is set into rotation at frequency Ω within an anisotropic harmonic trap characterized by an ellipticity ϵ (a). The rotation frequency is ramped from zero, and then held at a fixed value, e.g. $\Omega_f = 0.91\omega$ in this case (b). Absorption images taken after a variable hold time show the evolution of the resulting elliptical condensate (c). From left to right, $t_{hold} = 0, 40, 70$ and 100ms. Here, $\omega = 2\pi \times 88.6$Hz.

turns out that solutions in both branches are unstable to dynamical instabilities. These instabilities cover a wide range of the Ω, ϵ parameter space, and are explored in brief in this section. This dynamical instability is also closely connected to a spontaneous crystallization that we observe in Landau gauge wavefunctions, which we will cover at the end end of this chapter.

The hydrodynamic equations are linearized by assuming that $\rho = \rho_0 + \delta\rho$ and $\phi = \phi_0 + \delta\phi$ with small $\delta\rho$ and $\delta\phi$. Now the polynomial ansatz of degree n evolves with an operator $U_n(t)$. When at least one eigenvalue of $U_n(t)$ grows exponentially fast with t, the system is dynamically unstable to small perturbations. To probe this effect experimentally, we pause the rotation ramp at a particular value of Ω and hold for a variable time interval. The results are shown in ãutoreffig:2drotiniprep.

As the rotation is ramped up, the initially circular condensate extends into the weak axis of the rotating anisotropic potential. The condensate is intact through the
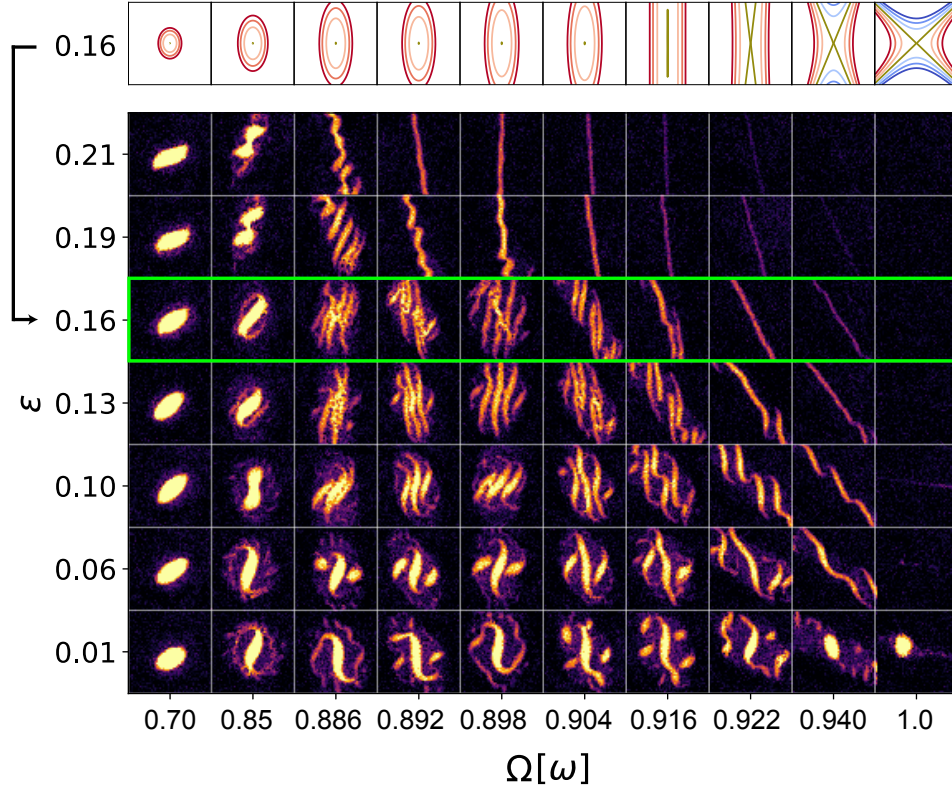
Figure 6-10: The instability phase diagram of a BEC in an anisotropic harmonic trap.. Here, images of the cloud at $t_{hold}/T = 7$ are shown for varying ellipticity ϵ and rotation frequency Ω. The corresponding potential contours are shown for $\epsilon = 0.16$ (top row).

initial ramp, but when the rotation frequency is held, it develops a density modulation. This modulation increases in amplitude until the condensate is fragmented into a number of pieces, which rotate at their own frequency. Over 10 rotation periods, the pieces interact with each other and produce vortices, which can be seen in the last insitu frame in Figure 6-9.

We further explore the (Ω, ϵ) parameter space by scanning both quantities and imaging when the density modulation has fragmented the condensate. The results are shown in tabular form in Figure 6-11, along with a set of potential contours in the rotating frame. As the rotation frequency increases, the scalar potential landscape turns from an elliptic parabola to a trough with no confinement along one axis, to a

saddle potential for $\Omega > \omega\sqrt{1-\epsilon}$ with one axis confined and the other anti-confined.

The phase diagram shows a rich variety of condensate shapes. To first order, we can classify these shapes by the number of components that they possess. This provides us with an estimate of the regions of dynamical instability, which we compare in Figure 6-11 with results from a stability analysis of the linearized superfluid hydrodynamic equations. We label the unstable regions by n, the degree of the polynomial ansatz, or in the case of the experiment, the number of pieces or nodes in the condensate wavefunction. We observe a qualitative agreement between the observations and the predictions from hydrodynamics. Specifically, as the wavefunction approaches the deconfinement limit, it develops a larger number of nodes. Beyond the deconfinement, there is no instability, at least while the system is continually driven (i.e. $\epsilon > 0$).

Many of the shapes are transient, evolving into a disordered system of vortices. In Figure 6-12, we show the evolution of a simply-connected condensate into a well-defined regular pattern, and into a turbulent state riddled with vortices. Vortices initially enter the cloud through the shear interfaces between the pieces of the pattern. Then, over many trapping periods, the vortices interact and rearrange chaotically. The corresponding images in reciprocal space show the development of peaks that correspond to the regular pattern. As the pattern self-destructs, the lobes split repeatedly until the dc peak is surrounded by noise that corresponds to the presence of randomly positioned vortices.

The turbulent state is an excellent starting point for generating large vortex lattices. We remove the excess energy by holding the rf evaporation on for ~ 500ms. This solidifies the vortex liquid into an Abrikosov lattice; a typical set of results are shown in Figure 6-13. These vortex lattices were generated by ramping to a final rotation frequency Ω and holding for 1s with $\epsilon = 0.12$. Then, the ellipse was turned off, returning the condensate to a circularly symmetric trap. An rf 'knife' that barely shaves the condensate was held on for 4s, followed by an absorption image. Across a
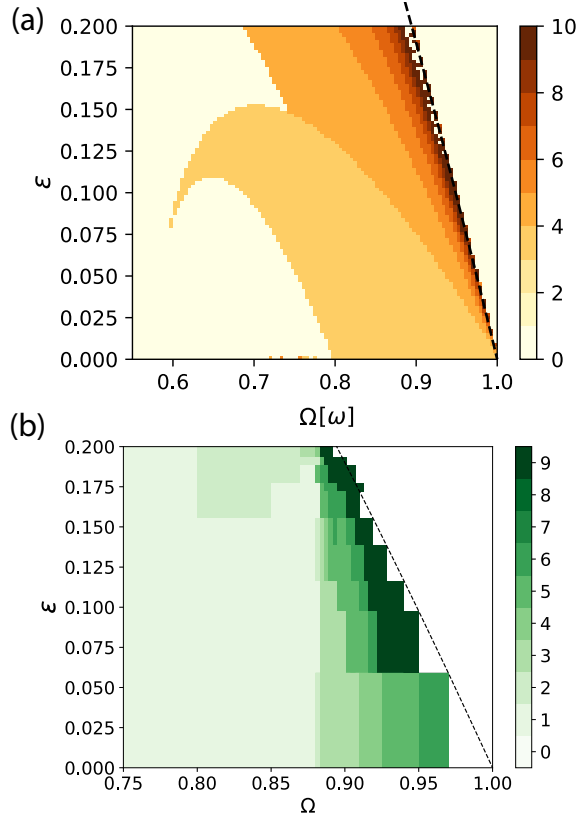
Figure 6-11: Regions of dynamical instability . (a) An instability plot of the superfluid hydrodynamic equations using a polynomial ansatz with varying degree, corresponding to the color [137]. (b) The number of components in the condensate can be counted after the pattern has formed, and before turbulent flow sets in. The region in which the superfluid is deconfined is shown here in white, since there is no dynamical instability that leads to pattern formation.

wide range of rotation frequencies, we see large vortex lattices form. As the rotation frequency increases, so does the spatial wavevector for the Abrikosov lattice. This is due to the increase in angular momentum, succinctly summarized in Feynman's rule for the vortex density $N_v \frac{h}{m} = 2\Omega A$ relating the number of vortices N_v in a given area A to the angular frequency Ω of a rotating superfluid [48]. In Figure 6-13, we compare the position of the main peaks in reciprocal space to the prediction for the lattice wavevector from Feynman's rule. The filling factor $\nu = N/N_v$, a quantity relating the number of atoms to the number of vortices, decreases as $\Omega \to \omega$. In this
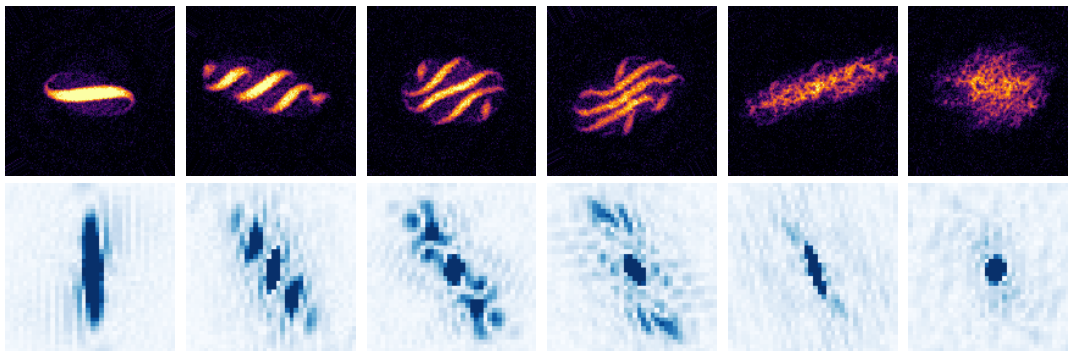
Figure 6-12: A route to turbulence.. These are frames from a time evolution of a 2D pattern. Here $\Omega = 0.9\omega$, and the frames are taken at t=0, 60, 80, 90, 120, and 160 ms after the initial ramp. The upper row shows images in real space, while the lower row shows them in reciprocal space.

limit, meanfield theory is expected to break down, and strongly-correlated bosonic quantum Hall states are expected to form [25, 47].

In the above results, we did not systematically vary the interaction parameter g. As we saw from the solutions of the hydrodynamic equations, without quantum pressure, the instability regions are independent of the interaction parameter. However, since quantum pressure is not negligible near the lowest Landau level, this interaction-driven instability will change in character. We investigate this regime for a one-dimensional version of the pattern formation, at the end of this chapter.

6.4   Geometric squeezing to the Lowest Landau Level

For $\Omega > \omega\sqrt{1-\epsilon}$, the condensate is unconfined, and a long-time evolution fails to generate large vortex lattices. Historically, rotating condensates have been imaged after a free expansion to magnify vortices [91, 1]. Interest has been mostly centered around trapped vortex lattices, and experiments that reached the rapid rotation limit stayed short of complete deconfinement [132]. However, insitu imaging reveals that this regime provides a direct pathway to the lowest Landau Level (LLL). In this section, we provide a brief outline on the preparation of Landau gauge wavefunctions
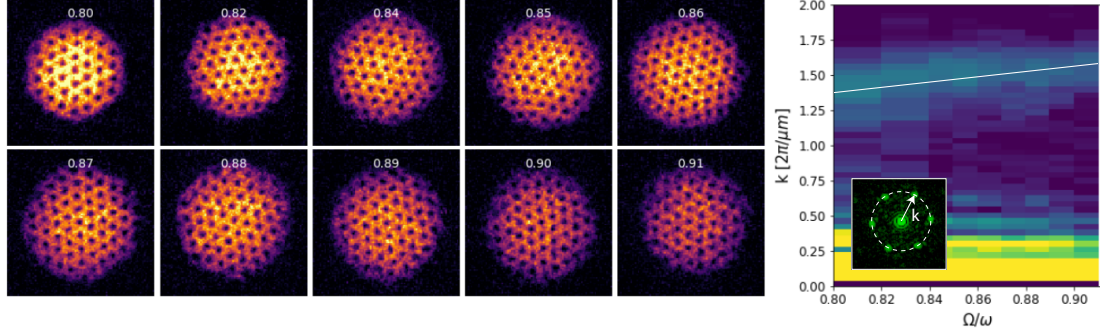
Figure 6-13: Well-ordered vortex lattice preparation. Insitu density images show vortex lattices prepared from rotating condensates at varying initial rotation frequencies (Ω labeled on each image). Faster spinning clouds show a higher density of vortices, and a lower atomic density. This can be seen in reciprocal space (right plot), where an azimuthal average shows the position of the six peaks that define the Abrikosov lattice (see inset, a 2D FFT of a single vortex lattice image). The white line shows the prediction from Feynman's rule for the density of vortices.

in the LLL. For further details, see [51].

We begin with a discussion of the shapes visible in Figure 6-11, for $\Omega > \omega\sqrt{1-\epsilon}$. The condensate extends out along an equipotential line, and atoms are constantly driven outwards while the scalar potential is left on. Classically, this can be understood through the Hall effect. Much like the conventional magnetic Hall effect, the rotational Hall effect requires only two ingredients: a gauge field and a scalar potential. From the rotational counterpart to the Lorentz force $\mathbf{F} = 2m\mathbf{v} \times \mathbf{\Omega}$, the Hall drift at $\Omega = \omega$ is given by

$$v_d = \frac{F}{2m\Omega} \tag{6.11}$$

$$= \frac{m\epsilon\omega^2 r}{2m\omega} \tag{6.12}$$

$$= \zeta r \tag{6.13}$$

where $\zeta = \epsilon\omega/2$.

where in the second line we identify the force with the gradient of the scalar potential due to the harmonic saddle $V = m\epsilon\omega^2(x^2 - y^2)/2$. We take the gradient on
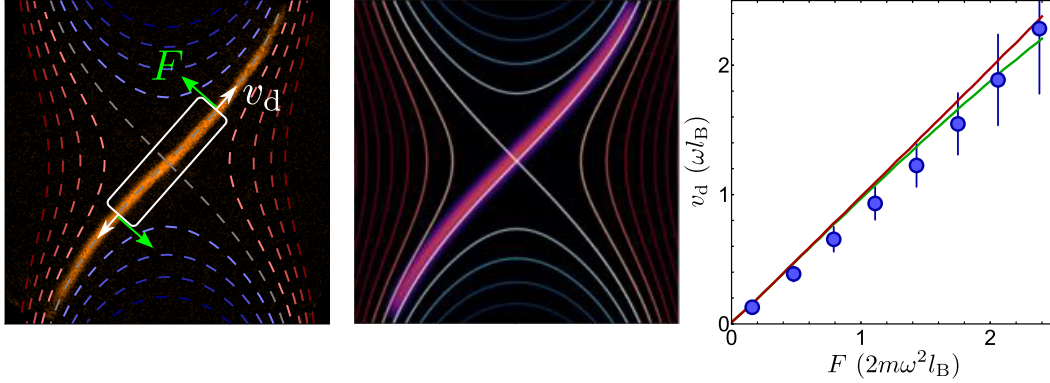
Figure 6-14: The Hall effect in a saddle potential.. Left: the condensate extends along equipotential lines, with a drift velocity v_d driven by the Hall force F. Image shows a single frame from the experiment. The rotation vector points out of the page. Center: A Gross-Pitaevskii (GP) simulation, incorporating the anharmonicity of the trapping potential, shows a very similar result. Right: The drift velocity along the diagonal is proportional to the force applied, assuming a perfectly harmonic saddle (red line). The data however, appear to slightly deviate from the line, which is captured in a GP numerical simulation that includes the quartic terms in the trapping potential.

the diagonal equipotential since that is the only allowed path for the guiding centers of cyclotron orbits. This is because the gauge field can do no work on the atoms. For a vector diagram, see Figure 6-14. Thus, for a perfectly harmonic saddle, both the drift velocity as well as the Hall force should scale linearly with distance.

From a continuity equation for a box of length L, the number of atoms leaving the box should be given by the drift velocity and density at the edges of the box. Integrating this equation $dN/dt = -2v_d n$ gives the equation

$$1 - \frac{N(t)}{N(0)} = 2v_d \int_0^t dt' \frac{n(t')}{N(0)} \tag{6.14}$$

The integration can be done for a range of lengths, and for each length, the drift velocity can be extracted from the slope of the line defined by the two sides of the last equation.

We now turn to a quantum picture of the process, using the language of creation
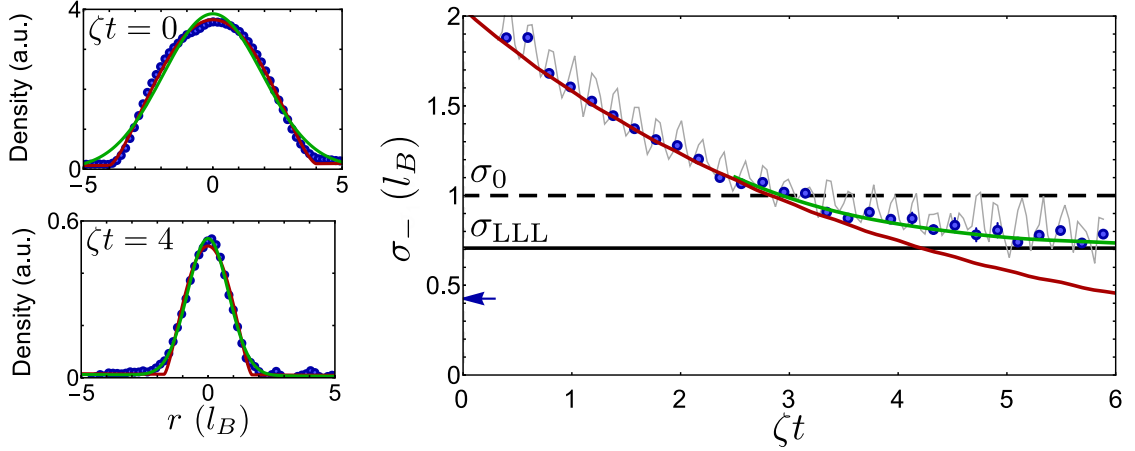
Figure 6-15: Geometric squeezing to the lowest Landau level.. The 1D transverse profiles (left) show a transition from a Thomas-Fermi profile for $gn \gg 2\hbar\omega$ (top) to a gaussian (bottom) for $gn \leq 2\hbar\omega$. The transverse width from a gaussian fit reflects this transition from a hydrodynamic prediction (red line) to the LLL limit of $\sigma_{LLL} = \ell_B/\sqrt{2}$. A numerical GP simulation shown in green captures the behavior in the intermediate regime.

and annihilation operators introduced in chapter 3. To the rotating 2D Hamiltonian in Equation 3.27 we add a scalar field defined by the saddle. We write the saddle Hamiltonian for $\Omega = \omega$ in terms of the ladder operators $\hat{a}$ and $\hat{b}$ for the cyclotron and guiding center respectively [51]:

$$H \approx 2\hbar\omega(a^\dagger a + 1/2) + \frac{\hbar\zeta}{2}(b^\dagger b^\dagger + bb) \qquad (6.15)$$

The second term is analogous to a squeezing operator in quantum optics. In this case, the configuration space is the space of guiding centers (X, Y), and he squeezing is geometric in nature. The full expression includes a term that also talks to the cyclotron modes, but due to a small ϵ, we find this term negligible [51].

In Figure 6-15, we show how the transverse profile of the condensate evolves during squeezing. We observe the quantum nature of the system in the long-time limit of squeezing. The crucial observation here is that the commutator of the guiding center and cyclotron coordinates $[X, Y] = -[\xi, \eta] = -i\ell_B^2$ leads to a minimal width

140

$\ell_B/\sqrt{2}$, where $\ell_B = \sqrt{\hbar/2m\omega}$ is the magnetic length. The saddle squeezing operator completely squeezes the guiding center orbits, resulting in a strip whose width is given by the minimum cyclotron orbit in the LLL. Thus, the width reveals the finite energy of the quantum mechanical ground state of the cyclotron harmonic oscillator.

At $t = 0$, the ramp from $\Omega = 0$ to $\Omega = \omega$ ends. The transverse profile is a Thomas-Fermi function, indicating a large occupation of Landau levels ($N_{LL} = \mu/(2\hbar\omega) \approx 10$). The time evolution of the width shows a small oscillation at the cyclotron frequency 2ω. As the saddle squeezes the guiding centers, the average width drops exponentially at first with a rate $\zeta/4$. After $t = 3/\zeta$, the widths saturate to $\ell_B/\sqrt{2}$, indicating the near complete squeezing of the guiding centers. The exact evolution of the transverse width agrees well with a GP numerical simulation that incorporates absorbing boundary conditions that handle the constant outflow of atoms. The final wavefunction is the groundstate in the Landau gauge Equation 3.49, with a gaussian transverse density profile.

6.5 Crystallization of Landau Gauge wavefunctions

In the previous section, we demonstrated that in the rotating frame, a saddle potential realizes a squeezing operator in the space of the geometric centers of cyclotron orbits. We use this squeezing to prepare states that are in the lowest Landau level, and realize a macroscopic wavefunction that is the ground state of the Hamiltonian in the Landau gauge.

A natural question at this point is: what happens when the saddle is turned off? In the lab, this corresponds to returning the BEC to an isotropic circularly symmetric trap with no ellipticity. Note that in the rotating frame, this corresponds to atoms living in flat land (see Fig. 6-16). There is no scalar potential, all that remains are the artificial gauge field from rotation, and the interparticle interactions. Would the cloud keep spinning as a Landau gauge strip? Would it fly apart (as we might expect
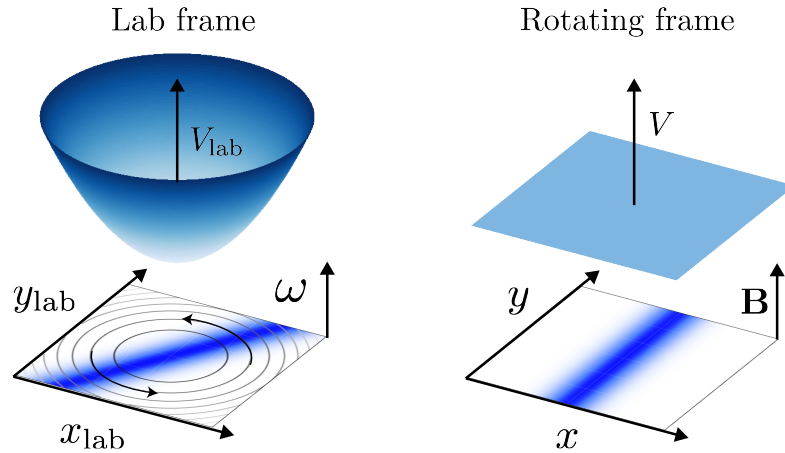
Figure 6-16: In flat land..   A cartoon depiction of the confining potential in the lab frame and in the rotating frame. The harmonic confinement in the lab frame exactly cancels the deconfinement from the centrifugal force of rotation. In the rotating frame, the cloud is static, and is only under the effects of the artificial gauge field, and the interparticle interactions.

from a BEC released from a confining potential)? What are the effects (if any) of interactions?

As a preview to the rest of this section, in Fig. 6-17 we show a sequence of frames with the time evolution of a typical Landau gauge wavefunction. For initial times, the strip rotates at the trapping frequency, and is static in the rotating frame. However, within 2T, where $T = \omega/2\pi$, the strip develops a density modulation at a well-defined lengthscale. This modulation grows until the cloud is fragmented into droplets. The droplets are separated by tendrils of condensate, which develop vortices as the system evolves. Two aspects of this evolution are apparent: the lengthscale of the density modulation, and the timescale over which it grows. In the following sections, we will focus on a few details on the methodology used. We direct the reader to Appendix F for further discussion on topics not covered here.

6.5.1   Lengthscales

We begin with a discussion of the characteristic lengthscales of spontaneous crystallization. Each OD image is summed along the transverse direction to obtain a
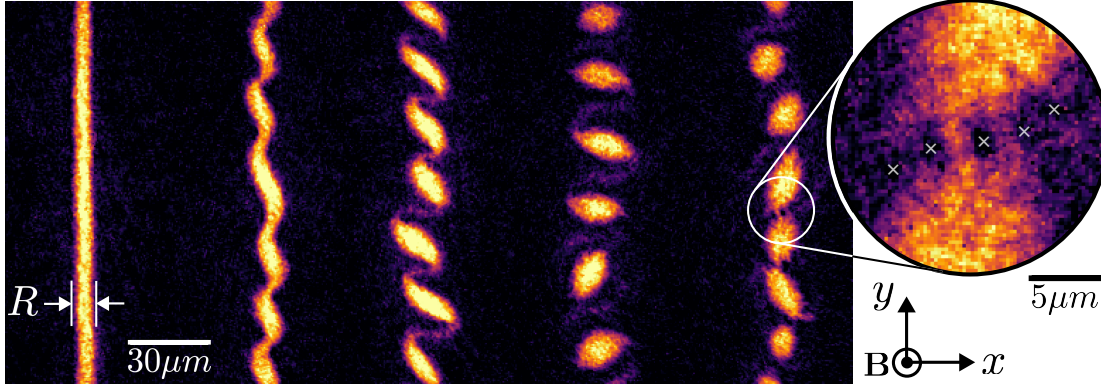
Figure 6-17: Spontaneous crystallization of a quantum Hall wavefunction.. A time sequence of images taken at intervals of 2.5 cyclotron periods show an instability of the Landau gauge wavefunction towards a well-ordered crystal phase. The density modulation grows until it fragments the strip into individual droplets which are still connected by thin tendrils of condensate. As the droplets rotate, they interfere, and the shear velocity results in the formation of vortices at the interface, shown in the inset to the right.

1D density $n_{1D}(y)$. The power spectrum of this profile is the static structure factor: $S_k = \frac{1}{N} \left| \int \mathrm{d}y\, n_{1D}(y)\, e^{-iky} \right|^2$ For each image, we calculate S_k, and fit a gaussian function to the prominent peak that corresponds to the coherent 1D crystal in reciprocal space. The width of the gaussian fit provides information about the coherence: the narrower the peak, the more well-defined the crystal is, at least within the window of our imaging. We filter the structure factors by placing a threshold on the fitted widths - this selects for the crystals that exhibit a high degree of coherence (e.g. unlikely to have blobs missing). Note that this process does not bias the position of the peak. We now average the ~ 40 remaining structure factors for each interaction strength and plot them in Figure 6-18.

We control the interaction strength (or equivalently the number of landau levels occupied) by squeezing for more, or less, time before switching off the saddle potential. We parameterize the interactions by comparing the width $R = FWHM/2\sqrt{\log 2}$ to the magnetic length ℓ_B. Note that when $gn \to 0$, $R \to \ell_B$. This procedure allows us to access R/ℓ_B ranging from 3, for minimal squeezing, to 1.2, for the longest
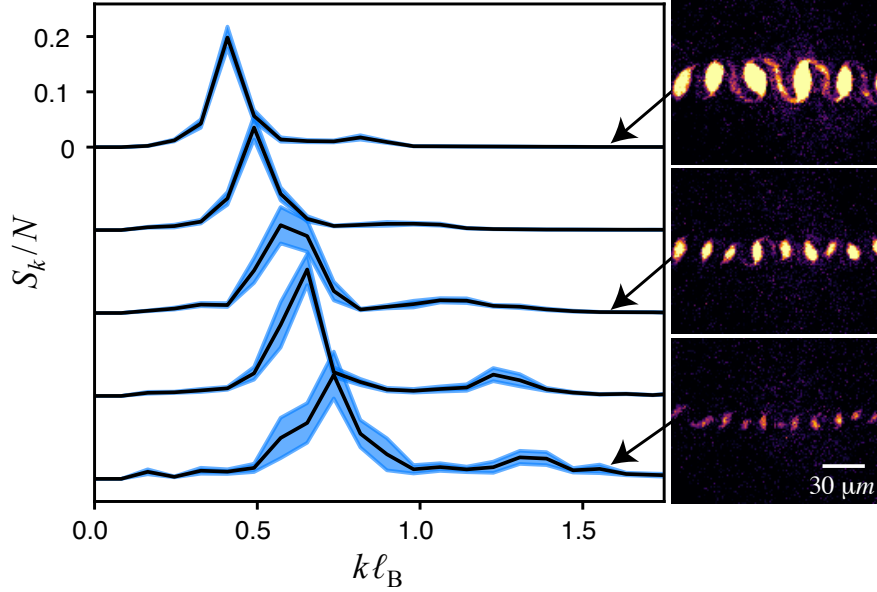
Figure 6-18: Structure factors of the spontaneous crystal.. We plot the structure factors S_k for a range of interaction strengths. We parameterize the interactions through the initial widths of the clouds, here $R/\ell_B = 2.58$, 1.75, 1.59, 1.28, 1.22 from top to bottom. On the right we show sample insitu images that correspond to the structure factors shown.

squeezing times. We are limited by signal-to-noise for the thinnest strips.

An interesting feature in the structure factors is the appearance of a second peak, at roughly twice the wavevector of the first. This smaller peak corresponds to the thin tendrils of atoms connecting the individual droplets, visible in the insitu images shown to the right. These features show the contiguous nature of the crystals, and hints at the preservation of phase coherence across the system.

More indication of the phase coherence can be seen in Figure 6-19. A GP simulations shows a coherent phase pattern defined by the positions of vortices. We use this knowledge to reconstruct the phase profile of the experimental density images. Although the presence of vortices does not necessarily imply global phase coherence, it is an indication that there is a well-defined relative phase between the droplets. Due to the continuous density profile, it is not unreasonable to conclude that the system is phase coherent. This satisfies a particular definition of a supersolid: a
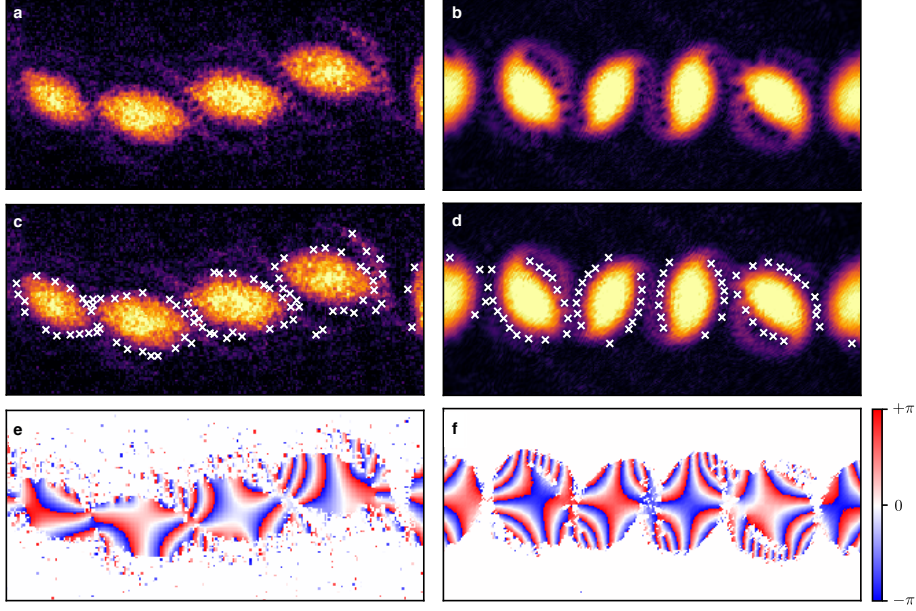
Figure 6-19: Vortex patterns and phase profiles. We compare the density (top row), vortex patterns (middle row) and phase profiles (bottom row) between the experimental data (left column) and GP simulations (right column). The experimental phase profile is reconstructed from the vortex positions.

combination of supersolidity and broken translational invariance. Note that another definition requires independently existing Goldstone modes, and precludes a vortex lattice from being a supersolid [147]. The modes of the crystal we observe are a topic of future investigation.

We find the peak positions of the averaged S_k with another final gaussian fit. As the system approaches the lowest Landau level, the most critical wavevector approaches $1/\ell_B$. This can be understood from a lowest Landau level picture, where interactions cause scattering from the $k = 0$ state to higher k states. Due to the presence of the gauge field, components of the wavefunction with finite momentum are displaced from the center. The resulting interference pattern exhibits a density modulation with $R/\ell_B \approx 1$.

On the other hand, for a hydrodynamic system in the Thomas-Fermi limit, the shear flow $\mathbf{v} = -2\omega x \hat{\mathbf{y}}$ results in a Kelvin-Helmholtz-like instability. This is a classical instability where a shear interface is unstable to rolling up into arrays of large
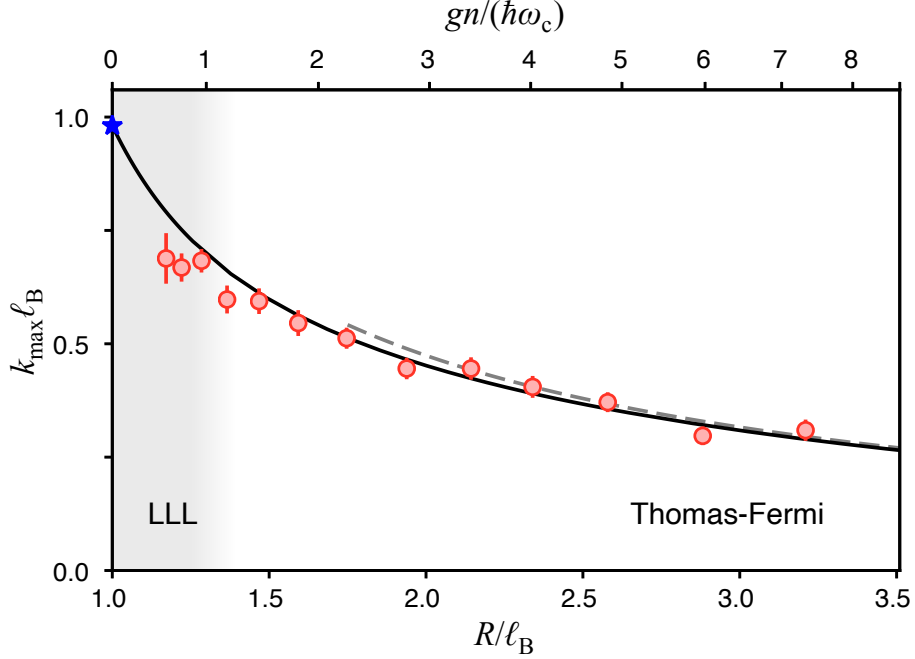
Figure 6-20: Lengthscale of the spontaneous crystal.. We compare the peaks of the structure factors k_{max} (red data) to predictions from linearized hydrodynamics (dashed line) and Bogliubov analysis (solid line). We see lengthscales approach $2\pi\ell_B$ for systems close to the lowest Landau level.

vortices [19, 82]. It has been observed in a wide range of systems [27, 17], and predicted to appear in Bose-Einstein condensates [5]. A solution to the hydrodynamic equations outlined in Equation 6.8 results in a critical wavevector $kmax = 1.12/R_{TF} = 0/95/R$. Here the Thomas-Fermi radius is $R_{TF} = \sqrt{\frac{gn}{\hbar\omega}}\ell_B$. We show the peak positions as a function of interactions in Figure 6-20. The data show good agreement to both the hydrodynamic prediction as well as a Bogoliubov analysis outlined in Appendix F.

6.5.2 Timescales

We now turn to the characteristic timescales over which the crystal develops. Within an LLL picture, the growth rate is set by the interaction strength gn, since that is the dominant energy scale. On the other hand, for high densities, the cyclotron

frequency $\omega_c = 2\omega$ provides the energy scale. In other words, as the interactions decrease and the system approaches a lowest Landau level wavefunction, there should be a transition from a fixed trap-determined growth rate to one set by the varying interaction strength.

The growth rates are well-described by the function $S_k(t) = A \cosh(2\Gamma t)$ [43]. In the long-time limit, this appears as an exponential growth. This is a two-parameter fit, which is highly sensitive to offsets due to noise. If there is a large spurious offset in S_k, the fit can compensate by increasing A, and decreasing Γ. To understand any potential offsets, we characterize the effects of shot noise on S_k. Assume $n_{1D}(y)$ is a noise vector with mean $\mu = 0$, and variance σ^2. Since the Fourier transform is a linear operator, and the 1D profile is a vector of independent random variables, the FFT shares the same variance and mean. So, the mean of the power spectrum is just the variance of the noise:

$$E[S(k)] = E[\frac{1}{N} \left| \int \mathrm{d}y\, n_{1\mathrm{D}}(y)\, e^{-iky} \right|^2] \tag{6.16}$$

$$= Var[\frac{1}{\sqrt{N}} \int \mathrm{d}y\, n_{1\mathrm{D}}(y)\, e^{-iky}] \tag{6.17}$$

$$= Var[n_{1D}] \tag{6.18}$$

$$= \sigma^2 \tag{6.19}$$

This makes sense: variances add, and so should independent sources of noise in power spectra. So, ideally we should be able to subtract a noise power spectrum from a signal power spectrum. However, the variance inside the condensate, where the optical density is nonzero is not equal to the variance outside the condensate. The variance in a region with finite OD is [127]:

$$Var[OD] = 0.5V_0(1 + \exp(OD)) \tag{6.20}$$

147
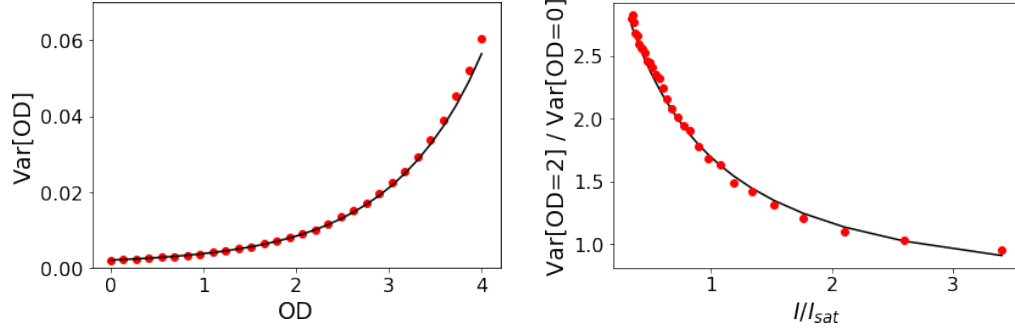
Figure 6-21: Noise variance. Left: The variance of the optical density (OD) depends exponentially on the mean OD. Here, the prediction from Equation 6.20 (black line) agrees well with data from a simulation (red points). Right: The OD dependence on the photon shot noise decreases with I/I_{sat}.

Now, given the variance V_0 of the OD outside the cloud, and the mean OD, we know what the offset to S_k should be. This equation assumes that we are in the low-intensity regime for imaging. If we include the linear term in the absorption equation, the equation for the variance becomes

$$Var[OD] = 0.5V_0 \left[1 + \left(\frac{1 + \gamma e^{-OD}}{1 + \gamma}\right)^2 e^{OD}\right] \tag{6.21}$$

where $\gamma = I/I_{sat}$. In Figure 6-21, we show how both the mean OD as well as the saturation factor γ affect the variance of the imaging. We show that we can predict the noise floor at any OD, given the noise floor in a background region (where $OD = 0$).

Armed with this understanding of offsets in S_k, we apply the following procedure to obtain the growth rates of S_k:

1. Find a region of interest in the images without atoms, and one with atoms

2. Evaluate S_k for each, and use Equation 6.20 to appropriately subtract the contribution to S_k from background shot noise.

3. Bin $S_k(t)$ in k-space. To find peak growth rates, first find the peak position
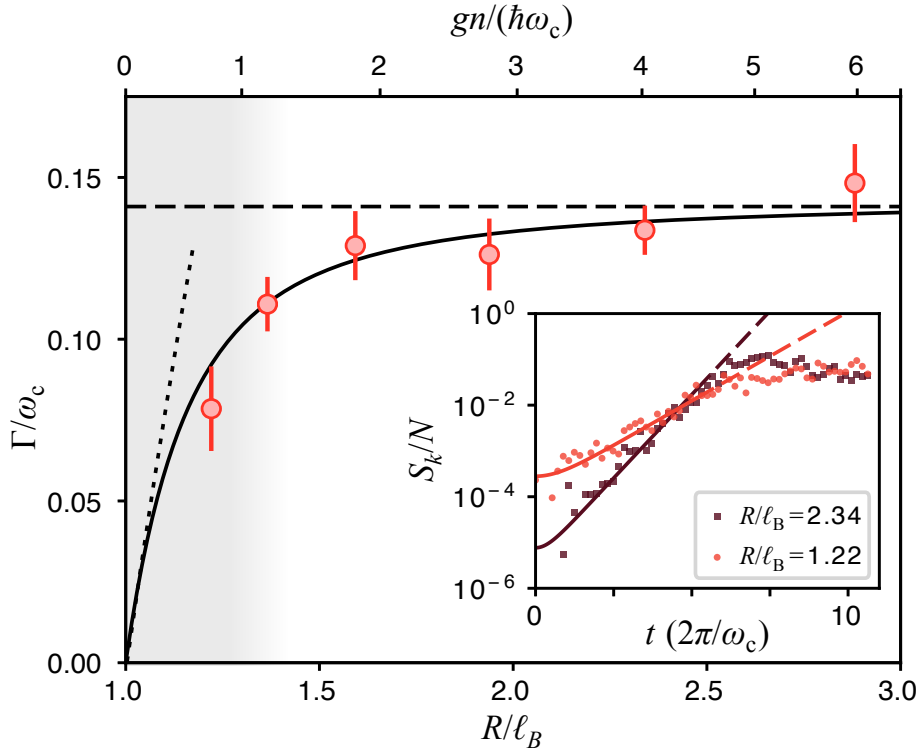
Figure 6-22: Growth rates of spectra. The growth rate of the structure factor depends on interactions: in the LLL, it is defined by the interaction strength $\Gamma = 0.21gn/\hbar$. The dashed horizontal line shows a prediction from hydrodynamics, where $\Gamma = 0.14\omega_c$. Inset: two sample S_k datasets and fits show significantly slower dynamics in the LLL. The black line shows the result of a Bogoliubov analysis (see Appendix F)

k_{max} from the saturated S_k, then bin in an interval $(0.9, 1.1)$ around k_{max}.

4. Fit $A\cosh(2\Gamma t)$ in linear space. Note that log space fitting does not work due to negative values from the offset subtraction.

5. Apply robust nonlinear fitting: label points that are more than 5σ away from the fit line as outliers, and mask them before applying a second round of fitting. This typically removes $< 10\%$ of the points, but greatly increases the stability of the fit.

Sample fits are shown in the inset of Figure 6-22, and the resulting peak growth rates are shown in the main figure. The growth of the structure factors is hyperbolic

at first, rising until it saturates. In terms of the insitu density profile, this corresponds to when the condensate fragments into a droplet array. For wavefunctions in the LLL, we observe a dramatic slowing of dynamics. The crystal grows half as fast for the narrowest clouds we observe, compared to the Thomas-Fermi limit.

Chapter 7

Outlook

In this chapter, we provide a brief outlook on future directions of research that might be of interest.

7.1 Homogeneous Fermi gases

A uniform system of interacting fermions is ideal for observing critical phenomena. Earlier in this thesis, we discussed the application of an insitu rf thermometer for measuring temperatures in a superfluid. We have used this method to measure the propagation of second sound, a phenomenon where heat propagates as a wave instead of diffusing. We note here as an outlook that the diffusivity of second sound is expected to show critical behavior near the superfluid transition: $D_2 \propto |T_c - T|^{-1/3}$ [64, 45, 57]. We do observe a rise in the diffusivity near T_c, which is reminiscent of ^{4}He, but we do not have the data to measure the exponent. The exponent could be confirmed with a more stable experimental system, possibly Fermi3.

Our spatial resolution for insitu thermometry is currently limited by the motion of ^{6}Li during the rf pulse. Performing a similar measurement in a heavier alkali system such as potassium might provide sharper details, and possibly allow us to measure heat fluctuations. Fluctuations are another indicator of criticality, and

would be fascinating to observe, in both the density as well as the heat channel. Insitu rf thermometry could provide us with a unique time-resolved insight into thermalization in bulk systems. We might be able to see how heat propagates in the lowest Landau Level, around vortices, and through narrow channels. In the Landau gauge wavefunctions that we prepare, the condensate approaches an effectively 1D system, likely with unique thermalization properties.

Lastly, spin imbalance remains an open frontier for many observations related to sound and criticality. Patches of superfluid at the Clogston limit might show up in a stable, high resolution experiment. The propagation of both first and sound through a homogeneous spin-imbalanced system would be a fascinating avenue of research.

7.2 Rotating Fermi gases

Fermi3, our latest experiment, is a dual species machine capable of rotating strongly-interacting systems of fermions. In the limit of high rotation, strongly-interacting systems of fermions are likely to exhibit exotic forms of excitations [25]. The integer quantum Hall effect requires a Fermi surface. Using fermions, we might be able to resolve discrete jumps in something akin to transverse resistivity. It is likely we will need to add some disorder in the rotating frame to localize states, in analogy to the quantum Hall effect in solid state systems.

Fermi 3 is an ideal apparatus for investigating quantum turbulence, discussed in chapter 3 and briefly demonstrated in chapter 6. The characteristic critical exponents of 2D quantum turbulence lends itself to a study using a uniform rotating gas. Furthermore, we observe that vortex lattices show a Kelvin-Helmholtz-like phenomenon when geometric squeezing is applied [51]. The well-ordered vortex lattice separates into individual rows, which form clusters, in analogy to a classical hydrodynamic roll-up of a shear interface. The long-time evolution of the system is reminiscent of the crystallization discussed in the context of Landau gauge wave-

functions, only in this case, the system is actively driven by a saddle potential in the rotating frame.

Lastly, the phase diagram of strongly-interacting fermions under spin-imbalance contains the exotic Ferrell-Fulde-Larkin-Ovchinnikov state [84, 83]. Appearing near the Chandrasekhar-Clogston limit, the state is characterized by a spatial modulation in the order parameter, here given by the gap Δ. The wavevector of the spatial modulation is given by the difference in the two Fermi wavevectors $k_{F\downarrow}$ and $k_{F\uparrow}$ of the two Fermi surfaces. Eluding direct observations for over half a century, this state could be observed in Fermi3. The two required ingredients are low temperatures (likely $T/T_F < 0.1$), and a stable experimental apparatus. We suspect that in BEC1, a large limitation to the stability is a long tube that holds a 1:1 imaging system for the box potential. This is held in a horizontal cantilever off of a gimbal mount, and is susceptible to mechanical vibrations. In Fermi3, due to the robust construction of the microscope objective mounts, and the floating tables, we expect the box potentials to be far more stable.

Appendix A

Interactive realtime GPU-accelerated GP simulations

Under weak interactions and at low temperatures, a Bose gas can be described using a mean-field theory, replacing the entire system with a macroscopic wavefunction representing the condensate order parameter. The Hamiltonian for the wavefunction Ψ is given in Equation 6.6. Low-energy excitations in Bose gases such as phonons and vortices can be quantitatively captured with this description. This section of the thesis describes a fast numerical solver for the GP equation built to compare our measurements with mean-field predictions. The code is available at [98].

A.1   Approach

We ran into a few challenges with available GP solver packages. Some, written in python and MATLAB were unfortunately too slow. These often relied on the central processing unit (CPU). Despite a fast clock rate and a slowly increasing number of cores, the CPU is a suboptimal engine for parallel processing. Developed for image processing and display, the graphics processing unit (GPU) is an ideal choice for general purpose parallel processing of arrays. BLAS algorithms recast and

Method	Time	Comments
Vanilla numpy	394	Slowest, but most convenient in python. No GPU acceleration
Scikit-cuda with copies	107	Copying from host to device on every iteration
cupy	64	Generates an FFT plan for every call. Good for one-off computations, with a numpy-like syntax
cufft+swig with copies	50	Copying is slow, but much faster than when using scikit-cuda
cufft+swig without copies	0.01	Major gains by avoiding copying and plan generation on each iteration.

Table A.1: An FFT benchmark, on random 4096 square arrays. Averaged over 100 iterations..

optimized for the GPU show strikingly impressive speedups over similar operations on the CPU. A benchmark test between a few common python FFT CPU routines and a direct FFT on the GPU shows the speedup clearly. We use a time-split spectral method [6] to numerically evolve the wavefunction. Since the TSSP scheme uses the FFT liberally, it's natural to implement it on the GPU.

Our approach is to combine the versatility of python programming with the speed of the GPU. While there are GPU libraries for python, we have found that they often perform hidden operations that slow their speed. In Table A.1, we outline the results of a few FFT benchmarks we ran from python. Instead, we opted to use python as an interface language. The python package calls C++ library routines and runs the required operations on the GPU. Realtime rendering is handled by OpenGL, which is significantly faster than copying the array to the memory and using the CPU to visualize each frame. We use a leap motion controller to interact in real-time with the condensate. This allows us to capture vortices and generate turbulent states with the swish of a finger.

A flowchart of the implementation is shown in Figure A-1. In both the python and the C++ code, we separate quantities directly related to the wavefunction (e.g.

the complex wavefunction $\Psi(x, y)$ itself, the methods needed for time evolution) from the environmental variables (such as the dimension of the grid, the field of view, and the potentials). Once the wavefunction is initialized in python, and time evolution is called as a method on the python object, the double precision complex-valued numpy array is sent using SWIG to a C++ array, and copied into the GPU memory. In C++, the main time evolution loop runs over the number of steps specified, and each step calls the appropriate CUDA kernels for split-step time evolution.

A.2 Results

In this section, we compare our experiment on Landau gauge wavefunctions to a GP simulation. We show a qualitative comparison in Figure A-2. Both GP and experimental data show vortices entering the bulk of the condensate through the shear interfaces between the droplets. Noise in the wavefunction is an essential ingredient in the simulation of spontaneous crystallization in the numerical simulation [101]. Due to the presence of seeding noise, the positions and shapes of the simulated droplets are random. As a result, quantitative measurements using the GP simulation require multiple repetitions with varying noise seeds, much like in a Monte Carlo experiment.

We note that the default boundary conditions are periodic - this makes it straightforward to simulate large uniform systems in the lab frame. To simulate systems with open boundaries, we apply absorbing boundary conditions enforced by an imaginary ring of death potential at a fixed radius. Time evolution under a locally imaginary potential results in an exponential decay of the wavefunction amplitude in that region. The rotational symmetry of the ring of death makes it especially well-suited for rotating condensates since there is a small probability of reflection or a phase shift due to the added potential.

A large grid size allows for a larger contrast between the field of view (the largest

possible wavefunction) and the spatial period of features in the wavefunction. For example, we observe a deviation in the growth rates of the spontaneous crystallization when the crystal period is on the order of the condensate length. This is likely due to edge effects, since despite the absorbing boundary conditions, there is a small chance that the edges will seed the instability. This is illustrated in Figure A-3, where for thick condenates, a 512x512 simulation fails to capture the growth rates we observe in the experiment, and deviate from the rates predicted by a Bogoliubov analysis. Doubling the grid dimension to 1024x1024 rectifies the issue.

Lastly in Figure A-4 we show how the addition of imaging noise results in an apparent decrease in fitted growth rates. We first generated simulated data on the crystallization of a wide range of initial condensate widths. Then, we extract the structure factor $S_k(t)$ for each $n_{1D}(z,t)$, and average over the peak of the structure factor. We follow an identical analysis procedure to the one described in chapter 6. We fit the resulting $S_{peak}(t)$ with the function $y = A \cosh(2\Gamma t)$ in linear space with a saturation point t_0, also a free parameter. The resulting growth rates agree well with a Bogoliubov analysis (left column). However, if we artificially include imaging noise (additive in $S_k(t)$), we observe deviations from the expected growth rates. Even minuscule amounts of noise, barely detectable in the structure factor plots, can change the apparent growth rates by up to a factor of two. Even a χ^2 analysis does not reveal the issues in the fits, and the fit errors remain small. This turned out to solve a mystery in our experimental data, since we had not been subtracting the contribution of the photon shot noise on S_k. The numerical simulation allows us to consider a situation with zero imaging noise, and independently verify analysis procedures used on experimental data.
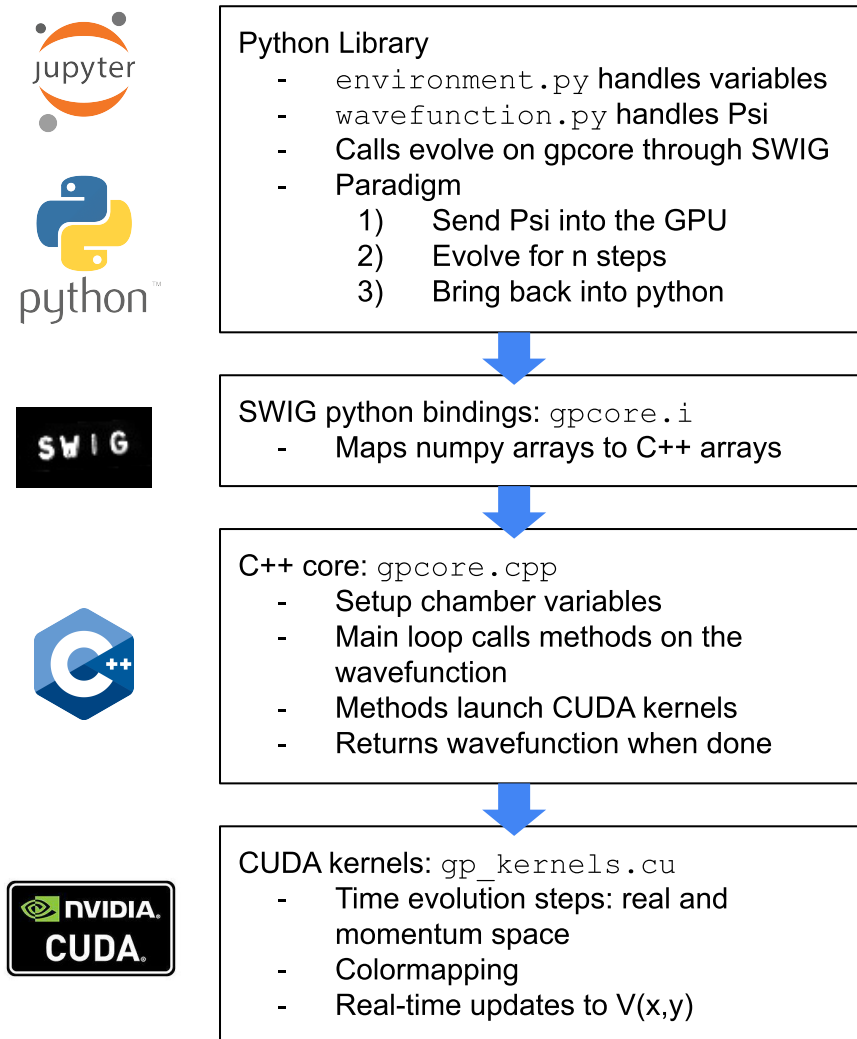
Figure A-1: Python and C++ based numerical simulation of the GP equation.. Here we outline the technical implementation of a GP solver. Information about the wavefunction and its environmental variables flow from a high-level interface API in python to the low-level implementation of CUDA kernels. Python bindings allow for a flexible experimental environment, written often in jupyter notebooks. The main evolution loop is called from C++ for performance.
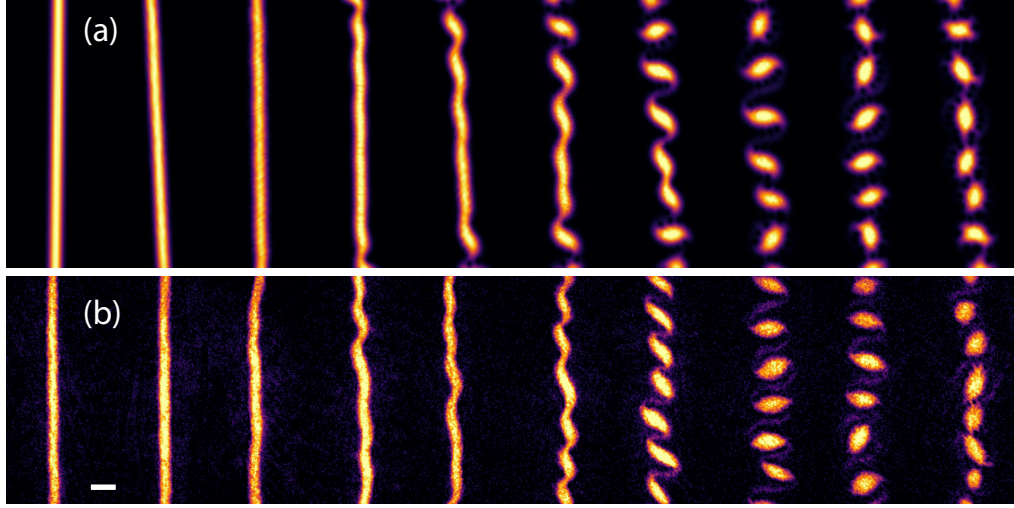
Figure A-2: Bosonic crystallization in GP and experiment.. The results of a GP simulation (a) and experimental data (b) show a good agreement. Here, $R/\ell_B = 2.3$. The white bar is $10\ell_B$ in length.
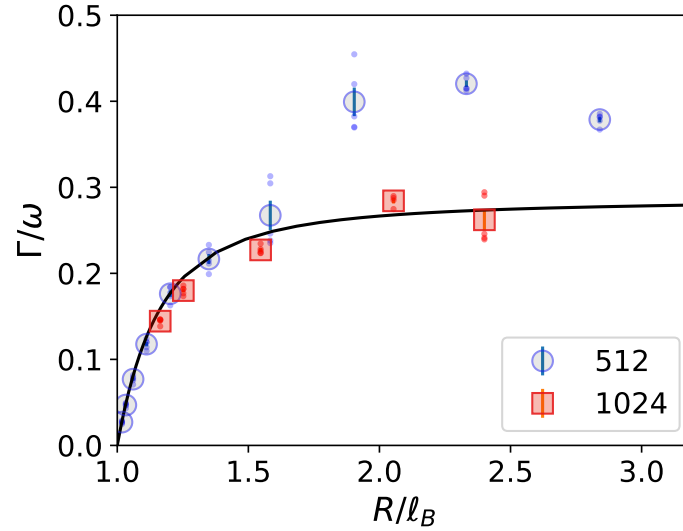
Figure A-3: Grid size in a GP simulation of crystallization growth rates . Here we show the results of a GP simulation of Landau gauge wavefunction crystal growth, in the same parameter regime as in Figure 6-22. We see that although a 512x512 simulation fails to capture the growth rates of condensates in the hydrodynamic regime, a 1024x1024 simulation does well. This is because the LLL is easier to simulate. The presence of interactions increases the cloud width, and makes it more likely that the edges contribute to the growth rates of the crystallization.
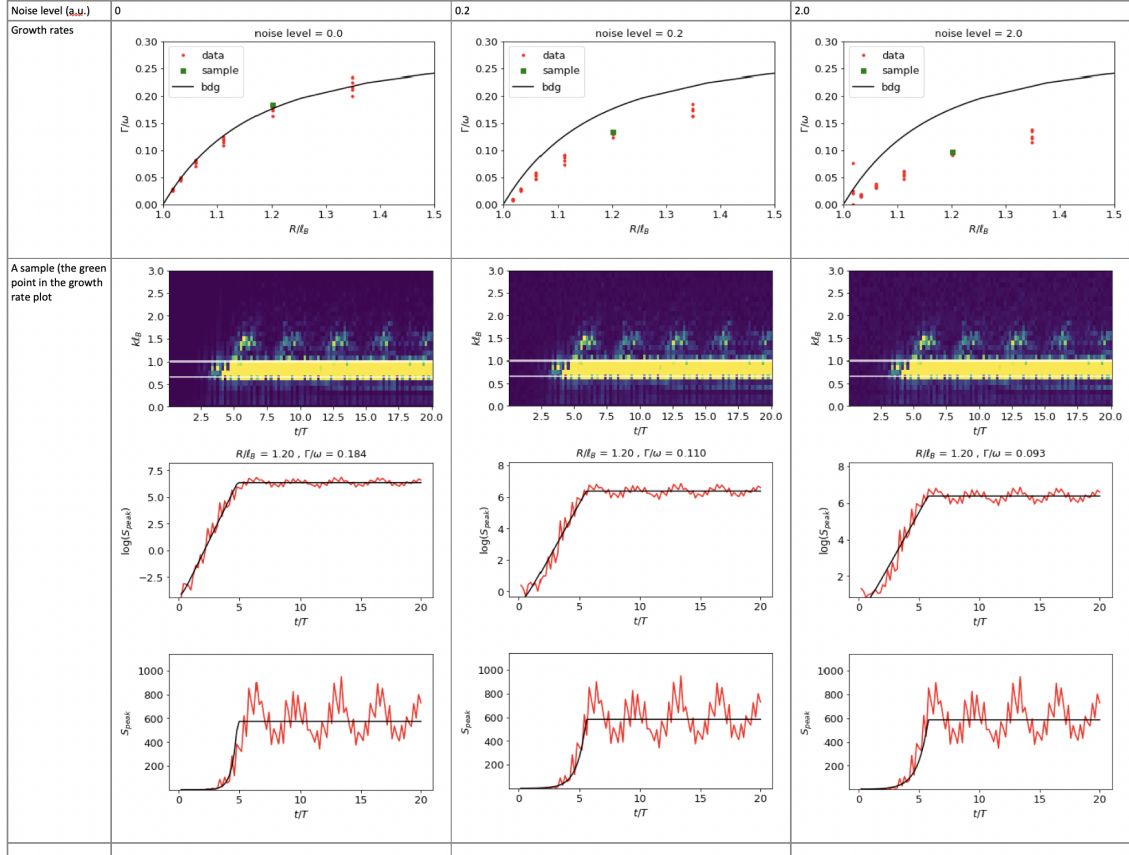
Figure A-4: The effect of imaging noise on measured growth rates. From left to right, increasing imaging noise results in an apparently slower growth rate. The imaging noise is added as an artificial noise source on top of GP simulations. The first row from top shows growth rates as a function of R/ℓ_B. The second row shows $S_k(t)$, with white lines demarcating the $k-$region over which S_k is averaged and fit to find the most critical growth rate. The third and fourth rows show the fit to S_{peak} in logarithmic and linear y-axes.

Appendix B

Microfabrication of silver photomasks

Imprinting high resolution potentials requires high intensities. We focus 1W of power on features as small as 10μm. As a result, chrome masks are insufficient for our needs. We chose silver due to its high reflectivity at 532nm. However, silver oxidizes, so we were required to apply a 20nm protective oxide layer on top of the 150nm Ag to ensure that the silver remains untarnished. We purchased AR-coated windows from thorlabs, and used the NSL facility at MIT to print custom patterns in silver. Here, we provide the fabrication process so that others may choose to replicate it:

B.1   Step 1: Write a negative mask

This step produces a master mask from which copies will be made.

1. Draw patterns as closed contours (no hatching) in Autocad

2. Load the .DxF file into the Heidelberg writer. Use Units:1000000

3. Load a 2.5" chrome mask - use the 2" suction

4. Verify the pattern, control panel-> focus

5. Write time should be $\sim$ 1.5h

6. Develop 60s in MF321 developer. Rinse, blow-dry, and check in the microscope

7. Place in the plasma etch / Asher: O_2 gas for 5-7 seconds at 200W

8. Chrome edge in CR-7 for 70s, rinse, dry, check

9. Strip resist with acetone for 5 min. Rinse with acetone methanol, and IPA

B.2   Step 2: Daughter (positive) mask

This step produces a copy of the master mask. Since writing on the Heidelberg is often a slow step, we want to make as few master masks as possible. These copies are easier to make, and are more disposable.

1. Take a normal 2.5 in mask, strip resist in acetone

2. Place in spinner: the O-ring should be smaller

3. Drop a puddle ($\sim$ 7 drops) of HMDS using a clean pipette

4. Dispose pipette, use a new one for $\sim$ 12 drops of NR9-1000Py(-) photo resist

5. Spin at 3k RPM to make a 1μm resist layer

6. Bake at 150 degrees C for 2.5 min on hot plate. Cool for 3 minutes

7. Expose in Tamarack UV floodlamp at 2mW/cm^2 for 3.5 min under the master mask

8. Bake again at 100 degrees C for 3.5 minutes. Let cool for 3 minutes.

9. Develop for 30 seconds in RD6 developer. Rinse, dry, inspect in the microscopy, and clean in the asher.

10. Wet etch in $CR - 7$ for 2 minutes. The background should clear out.

11. Inspect in the microscope. If the edges look clean, strip the resist, rinse in the usual sequence. Dry.

B.3   Step 3: Silver final mask

This step finally copies the mask patterns onto the coated windows.

1. Get a window with the proper AR coating from Thorlabs.

2. Spin clean with acetone, IPA

3. Spin HMDS, then NR9-1000PY at 3k RPM

4. Bake at 150 degrees C for 4 min

5. Expose for 3.5 min under the positive daughter mask. Clean before use. Carefully align the window to the daughter mask. If doing under a UV flood lamp, make sure there is no gap between the two surfaces by adapting a rubber gasket and using suction. This is often the most difficult step.

6. Bake for 4 min at 100C. Let fully cool, and then apply 5-7s of the asher.

7. Develop in RD6 for 30 seconds. Inspect in the microscope. The coating on the window should be exposed where the silver will be.

8. Give to the molecular beam deposition chamber owner for 150nm Ag + 20nm SiO_2 deposition.

9. When finished, prepare a beaker of acetone at 80 degrees C on hot plate

10. Hold window with plastic tweezers in beaker for ~ 4 min

11. Rinse with acetone -the background should peel off. Rinse in the usual sequence. Dry.

Appendix C

Fermi 3 Vacuum chamber schematics

The vacuum chamber in the Fermi 3 experiment consists of three chambers: the oven, the intermediate, and the main. In this appendix, we provide the drawings for the full vacuum setup, the oven 6-way, the custom intermediate chamber, and the custom pump tower.

Top view

B

Main science
chamber

Intermediate chamber

Oven Six-way

Side view

Pump tower

Pump tower supports

A

		UNLESS OTHERWISE SPECIFIED:		NAME	DATE			
		DIMENSIONS ARE IN INCHES TOLERANCES: FRACTIONAL ± ANGULAR: MACH± BEND ± TWO PLACE DECIMAL ± THREE PLACE DECIMAL ±	DRAWN			TITLE:		
			CHECKED					
			ENG APPR.					
			MFG APPR.					
		INTERPRET GEOMETRIC TOLERANCING PER:	Q.A.					
PROPRIETARY AND CONFIDENTIAL			COMMENTS:					
THE INFORMATION CONTAINED IN THIS DRAWING IS THE SOLE PROPERTY OF		MATERIAL				SIZE	DWG. NO.	REV
REPRODUCTION IN PART OR AS A WHOLE WITHOUT THE WRITTEN PERMISSION	NEXT ASSY	USED ON	FINISH				A	
PROHIBITED.		APPLICATION		DO NOT SCALE DRAWING		SCALE: 1:32	WEIGHT:	SHEET 1 OF 1

Full vacuum setup

2

1

4.5" CF flange

2.50   2.50

B

90.00°

4.15

ϕ 1.50

ϕ 2.50

B

B

4.15

2.75"
rotatable

SECTION B-B

B
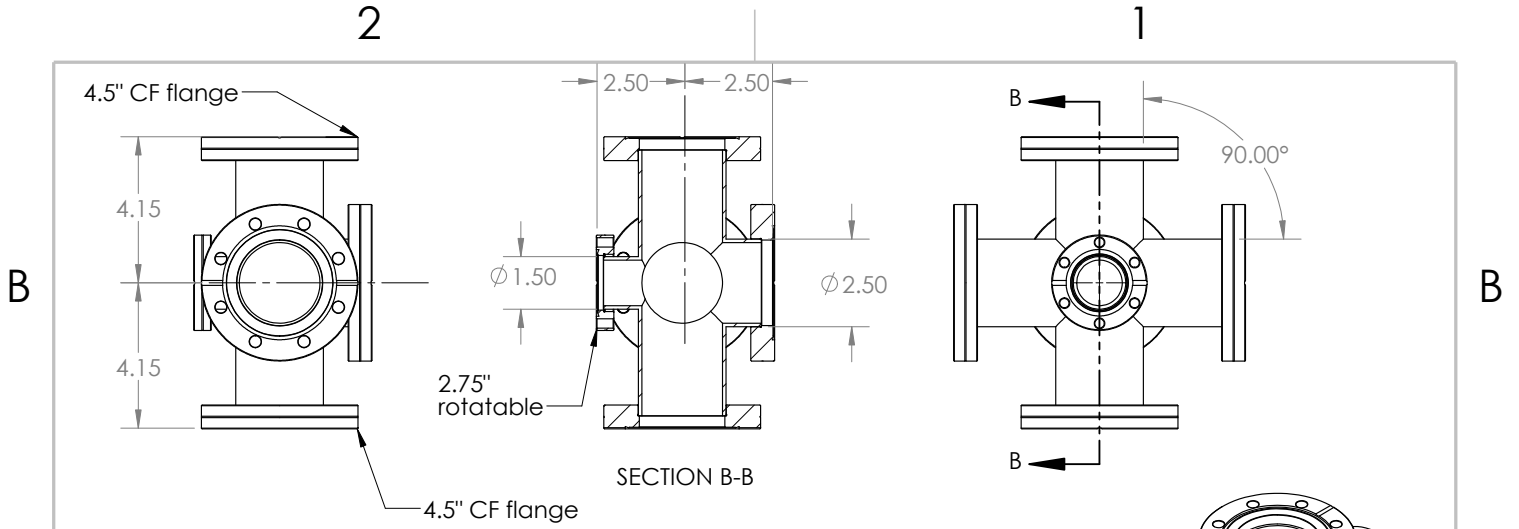
4.5" CF flange

5 Ways 2.5"OD pipe, 4.5" CF Flange

1 way 1.5" pipe, rotatable 2.75" CF flange

		UNLESS OTHERWISE SPECIFIED:	NAME	DATE			
		DIMENSIONS ARE IN INCHES TOLERANCES: FRACTIONAL ± ANGULAR: MACH ± BEND ± TWO PLACE DECIMAL ± THREE PLACE DECIMAL ±	DRAWN				
			CHECKED		TITLE:		
			ENG APPR.		Oven Chamber 6 way		
			MFG APPR.				
		INTERPRET GEOMETRIC TOLERANCING PER:	Q.A.				
			COMMENTS:				
		MATERIAL			SIZE A	DWG. NO.	REV
NEXT ASSY	USED ON	FINISH					
APPLICATION		DO NOT SCALE DRAWING			SCALE: 1:4	WEIGHT:	SHEET 1 OF 1

2

1

169

A

Nextorr pump

B

B

A

Blank; will
hold Agilent
UHV 24-P
ion gauge

2.75
viewport

A

SECTION A-A
SCALE 1 : 4

		UNLESS OTHERWISE SPECIFIED:		NAME	DATE				
		DIMENSIONS ARE IN INCHES TOLERANCES: FRACTIONAL ± ANGULAR: MACH ± BEND ± TWO PLACE DECIMAL ± THREE PLACE DECIMAL ±	DRAWN						
			CHECKED			TITLE:			
			ENG APPR.						
			MFG APPR.						
		INTERPRET GEOMETRIC TOLERANCING PER:	Q.A.						
PROPRIETARY AND CONFIDENTIAL		MATERIAL	COMMENTS:						
THE INFORMATION CONTAINED IN THIS DRAWING IS THE SOLE PROPERTY OF						SIZE	DWG. NO.		REV
REPRODUCTION IN PART OR AS A WHOLE WITHOUT THE WRITTEN PERMISSION	NEXT ASSY	USED ON	FINISH			A			
PROHIBITED.						SCALE: 1:8	WEIGHT:		SHEET 1 OF 1

Intermediate chamber_fu

APPLICATION   DO NOT SCALE DRAWING

Rotatable

All tubes 1.75" OD
All flanges 2.75" CF
non-rotatable unless otherwise
specified (3 rotatable flanges)

7.84

Rotatable

2.21

3.00

2.67

3.71

2.71

3.00

4.69

4.21

7.42

4.00

UNLESS OTHERWISE SPECIFIED:		NAME	DATE		
DIMENSIONS ARE IN INCHES TOLERANCES: FRACTIONAL ± ANGULAR: MACH ± BEND ± TWO PLACE DECIMAL ± THREE PLACE DECIMAL ±	DRAWN				
	CHECKED			TITLE:	
	ENG APPR.				
	MFG APPR.				
INTERPRET GEOMETRIC TOLERANCING PER:	Q.A.				
	COMMENTS:				
MATERIAL				SIZE	DWG. NO.	REV
FINISH				A7way flange	

NEXT ASSY   USED ON

APPLICATION

DO NOT SCALE DRAWING

SCALE: 1:4   WEIGHT: SHEET 1 OF 1

2

1

2

1

1.92
2.00
⌀ .25 thru
1.00
2.00
1.00

45.00°
3.84
7.64

7.00
7.00

⌀ .25 thru

Conical section
with 2.75" CF
rotatable. Connects
to threaded CF flange
on Kimball physics
octagon

1.00

.50

SECTION B-B

B   B

non-rotatable

.20

6" CF flange

⌀ 4.00
1.21

8.42   1.00
14.00°

7.00

1.39

4.00   6.00

.20

2.75 CF flange
rotatable

Flush with
center of 6" CF

6" rotatable CF

B   B

12.70   14.44

.20

3.18

1.64

Welded
L-bracket
for support

A   A

	UNLESS OTHERWISE SPECIFIED:		NAME	DATE		
	DIMENSIONS ARE IN INCHES	DRAWN			TITLE:	
	TOLERANCES: FRACTIONAL ± ANGULAR: MACH± BEND ± TWO PLACE DECIMAL ± THREE PLACE DECIMAL ±	CHECKED				
		ENG APPR.				
		MFG APPR.				
	INTERPRET GEOMETRIC TOLERANCING PER:	Q.A.				
PROPRIETARY AND CONFIDENTIAL		COMMENTS:				
THE INFORMATION CONTAINED IN THIS DRAWING IS THE SOLE PROPERTY OF	MATERIAL			SIZE	DWG. NO.	REV
REPRODUCTION IN PART OR AS A WHOLE WITHOUT THE WRITTEN PERMISSION	FINISH			APump Tower		
PROHIBITED.				SCALE: 1:8	WEIGHT:	SHEET 1 OF 1

NEXT ASSY   USED ON
APPLICATION   DO NOT SCALE DRAWING

2   1

172

Appendix D

Homogeneous Atomic Fermi Gases

This appendix contains a reprint of the following paper :

*B. Mukherjee, Z. Yan, P. B. Patel, T. Yefsah, J. Struck, M. W. Zwierlein, "Homogeneous Atomic Fermi Gases," Phys. Rev. Lett. **118**, 123401 (2017)[102]*

P H Y S I C A L   R E V I E W   L E T T E R S

Homogeneous Atomic Fermi Gases

Biswaroop Mukherjee,[1] Zhenjie Yan,[1] Parth B. Patel,[1] Zoran Hadzibabic,[1,2] Tarik Yefsah,[1,3]
Julian Struck,[1] and Martin W. Zwierlein[1]

[1]*MIT-Harvard Center for Ultracold Atoms, Research Laboratory of Electronics,
and Department of Physics, Massachusetts Institute of Technology, Cambridge, Massachusetts 02139, USA*
[2]*Cavendish Laboratory, University of Cambridge, J. J. Thomson Avenue, Cambridge CB3 0HE, United Kingdom*
[3]*Laboratoire Kastler Brossel, CNRS, ENS-PSL Research University, UPMC-Sorbonne Universités
and Collège de France, Paris 75005, France*

We report on the creation of homogeneous Fermi gases of ultracold atoms in a uniform potential. In the momentum distribution of a spin-polarized gas, we observe the emergence of the Fermi surface and the saturated occupation of one particle per momentum state: the striking consequence of Pauli blocking in momentum space for a degenerate gas. Cooling a spin-balanced Fermi gas at unitarity, we create homogeneous superfluids and observe spatially uniform pair condensates. For thermodynamic measurements, we introduce a hybrid potential that is harmonic in one dimension and uniform in the other two. The spatially resolved compressibility reveals the superfluid transition in a spin-balanced Fermi gas, saturation in a fully polarized Fermi gas, and strong attraction in the polaronic regime of a partially polarized Fermi gas.

Ninety years ago, Fermi derived the thermodynamics of a gas of particles obeying the Pauli exclusion principle [1]. The Fermi gas quickly became a ubiquitous paradigm in many-body physics; yet even today, Fermi gases in the presence of strong interactions pose severe challenges to our understanding. Ultracold atomic Fermi gases have emerged as a flexible platform for studying such strongly correlated fermionic systems [2–6]. In contrast to traditional solid state systems, quantum gases feature tunable spin polarization, dimensionality, and interaction strength. This enables the separation of quantum statistical effects from interaction-driven effects, and invites the exploration of rich phase diagrams, for example bulk Fermi gases in the BEC-BCS crossover [3–10] and Fermi-Hubbard models in optical lattices [11–20].

So far, Fermi gas experiments have been performed in inhomogeneous traps, where the nonuniform density leads to spatially varying energy and length scales. This poses a fundamental problem for studies of critical phenomena for which the correlation length diverges. Furthermore, in a gas with spatially varying density, a large region of the phase diagram is traversed, potentially obscuring exotic phases that are predicted to occur in a narrow range of parameters. This is most severe for supersolid states, such as the elusive FFLO state [21–23], where the emergent spatial period is well defined only in a homogeneous setting. A natural solution to these problems is the use of uniform potentials, which have recently proved to be advantageous for thermodynamic and coherence measurements with Bose gases [24–27].

Here, we realize homogeneous Fermi gases in a versatile uniform potential. For spin-polarized gases, we observe both the formation of the Fermi surface and the saturation at

one fermion per momentum state, due to Pauli blocking. Spatially uniform pair condensates are observed for spin-balanced gases, offering strong prospects for the exploration of long-range coherence, critical fluctuations, and supersolidity.

In cases where the local density approximation (LDA) is valid, the spatially varying local chemical potential in an inhomogeneous trap can be utilized for thermodynamic [28–31] and spectroscopic [7,32,33] measurements. However, reconstructing the local density from line-of-sight integrated density profiles typically increases noise, while spatially selecting a central region of the gas reduces signal. A potential that is uniform along the line-of-sight is the natural solution. Combining the desirable features of homogeneous and spatially varying potentials, we introduce a hybrid potential that is uniform in two dimensions and harmonic in the third. The line-of-sight integration is now turned into an advantage: instead of averaging over a wide region of the phase diagram, the integration yields a higher signal-to-noise measurement of the local density. Using this geometry, we observe the characteristic saturation of isothermal compressibility in a spin-polarized gas, while a strongly interacting spin-balanced gas features a peak in the compressibility near the superfluid transition [31].

In our experiment, we prepare atoms in the two lowest hyperfine states of ^{6}Li near a Feshbach resonance, and load them into the uniform potential of the optical box trap depicted in Fig. 1(a), after evaporative precooling in a crossed dipole trap. We typically achieve densities and Fermi energies of up to $n \approx 10^{12}$ cm^{-3} and $E_F \approx h \times 13$ kHz, corresponding to $\sim 10^6$ atoms per spin state in the box. The lifetime of the
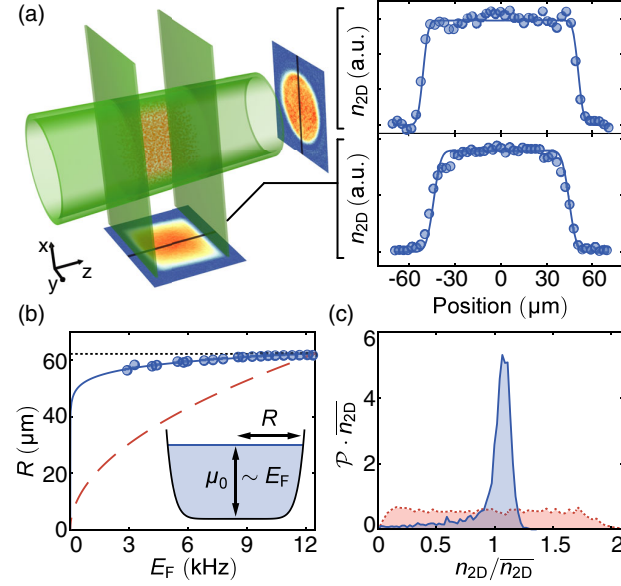
174

FIG. 1.   Homogeneous Fermi gas. (a) Schematic of the box trap and cuts through the column-integrated density profiles along the axial and radial directions. (b) Radius of the cloud as a function of the Fermi energy. The dotted black and dashed red lines correspond to a perfect box potential and a harmonic potential, respectively, and are scaled to converge at the highest E_F. The blue solid line corresponds to a power law potential $V(r) \sim r^{16}$. (c) Measured radial probability density $\mathcal{P}(n_{2D})$ for the column-integrated density n_{2D}, averaging about 20 in-trap images. The blue solid and red dashed lines correspond to the uniform and Gaussian traps, respectively.

Fermi gas in the box trap is several tens of seconds. The uniform potential is tailored using blue-detuned laser light for the confining walls. The sharp radial trap barrier is provided by a ring beam generated by an axicon [34,35], while two light sheets act as end caps for the axial trapping [36]. Furthermore, the atoms are levitated against gravity by a magnetic saddle potential [3]. The residual radial anticonfining curvature of the magnetic potential is compensated optically, while an axial curvature results in a weak harmonic potential described by a trapping frequency of $\omega_z = 2\pi \times$ 23.9 Hz. This typically results in a variation of the potential along the axial direction that is less than 5% of the Fermi energy. Note that the magnetic moments of the two spin states of ^{6}Li differ by less than 0.1% at unitarity, resulting in a negligible difference in trapping potentials. We characterize the steepness of the trap walls by measuring the radial extent R of the cloud as a function of Fermi energy [see Fig. 1(b)]. Modeling the trap walls with a power law potential, we obtain $V(r) \sim r^{16.2 \pm 1.6}$ [36].

A stringent measure of the homogeneity of the gas is the probability distribution $\mathcal{P}(n)$ for the atomic density n. Imaging along the z and x directions yields the radial and axial probability distribution $\mathcal{P}(n_{2D})$ for the column density n_{2D} (see Fig. 1(c) and Ref. [36]). The distribution for the

homogeneous gas is sharply peaked near the trap average density $\overline{n_{2D}}$. For comparison, we also show $\mathcal{P}(n_{2D})$ for an optical Gaussian trap, which is spread over a large range of densities.

Fermions at low temperatures are characterized by Pauli blocking [1]. Consequences of Pauli blocking have been observed in ultracold gases, for example, in nondegenerate samples, the reduction of collisions in spin-polarized gases below the p-wave threshold [2,37] and, upon entering degeneracy, Pauli pressure [38,39], reduced collisions [40,41], antibunching in noise correlations [42], and the reduction of density fluctuations [43,44]. In optical lattices under microscopes, Pauli blocking has been observed in real space through observations of band insulating states [16,17,45] and of the Pauli hole in pair correlations [20]. Typically obscured in the time of flight expansion of an inhomogeneous atomic gas, the Fermi surface has been observed by probing only the central region of a harmonically trapped gas [46]. Now, the uniform box potential enables us to directly observe the consequence of Pauli blocking in momentum space for degenerate gases: the Fermi-Dirac momentum distribution, featuring the emergence of a Fermi surface near the Fermi wave vector k_F and the saturated occupation of momentum states below k_F to one particle per momentum cell.

To measure the momentum distribution $f(\mathbf{k})$, we release a highly spin-imbalanced gas ($n_{\downarrow}/n_{\uparrow} < 0.05$, where $n_{\uparrow}$ and $n_{\downarrow}$ are the densities of the majority and minority spin components, respectively) from the uniform potential into the small residual axial harmonic potential (along the z axis). To ensure the ballistic expansion of the gas, the minority component is optically pumped into a weakly interacting state within 5 μs [36]. After a quarter period of expansion in the harmonic trap, the axial momenta k_z are mapped into real space via $z = \hbar k_z / m\omega_z$ [47–50]. In contrast to conventional time of flight measurements, this method is unaffected by the in-trap size of the gas. The measured integrated density profile $n_{1D}(z) = \iint dx dy n(x,y,z)$ reflects the integrated momentum distribution $f_{1D}(k_z) = (2\pi)^{-2} \iint dk_x dk_y f(k_x, k_y, k_z)$ via

$$f_{1D}(k_z) = \frac{2\pi\hbar}{V m \omega_z} n_{1D}(z). \qquad (1)$$

Here, V is the volume of the uniform trap. Figure 2(a) shows the integrated momentum distribution for different temperatures. Assuming a spherically symmetric momentum distribution, $f_k \equiv f(\mathbf{k}) = f(k)$. Noting that $\int dk_x dk_y f\left(\sqrt{k_x^2 + k_y^2 + k_z^2}\right) = \pi \int_{k_z^2}^{\infty} d(k^2) f(k)$, the three-dimensional momentum distribution can be obtained from the integrated momentum distribution by differentiation:

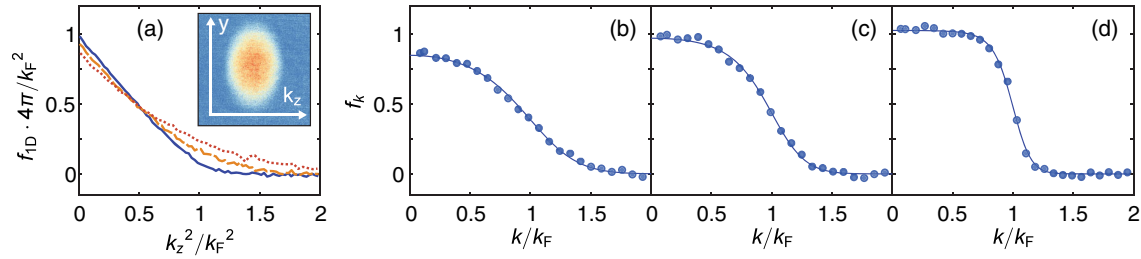$$f_k = -4\pi \frac{df_{1D}(k_z)}{dk_z^2}. \qquad (2)$$

FIG. 2.   Momentum distribution of the homogeneous spin-polarized Fermi gas. (a) Doubly integrated momentum distribution f_{1D} for different temperatures in the uniform trap. In order of decreasing temperature: red dotted line, orange dashed line, and blue solid line. Each line corresponds to averages over seven images. The optical density after momentum space mapping along z is shown in the inset. (b),(c),(d) Momentum distribution $f_k = -4\pi df_{1D}/dk^2$, showing Pauli blocking and Fermi surface formation. Fermi-Dirac fits (solid line) give (b) $T/T_F = 0.49(2)$, (c) $T/T_F = 0.32(1)$, and (d) $T/T_F = 0.16(1)$, with k_F ranging between 2.8 μm^{-1} and 3.7 μm^{-1}. The estimated systematic error in the measurement of f_k is 15%.

As the temperature is lowered, the momentum distribution develops a Fermi surface, and we observe a momentum state occupation of 1.04(15) at low momenta [see Figs. 2(b)–2(d)], where the error in f_k is dominated by the systematic uncertainties in the box volume and the imaging magnification [36]. This is the direct consequence of Pauli blocking and confirms saturation at one fermion per momentum state.

An important motivation for the realization of a homogeneous Fermi gas is the prospect of observing exotic strongly correlated states predicted to exist in narrow parts of the phase diagram, such as the FFLO state [21,22]. In a harmonic trap, such states would be confined to thin isopotential shells of the cloud, making them challenging to observe. We observe pair condensation in a uniformly trapped strongly interacting spin-balanced Fermi gas through a rapid ramp of the magnetic field during time of flight [3,51,52], as shown in Figs. 3(a)–3(c). The pair condensate at the end of the ramp barely expands in time of
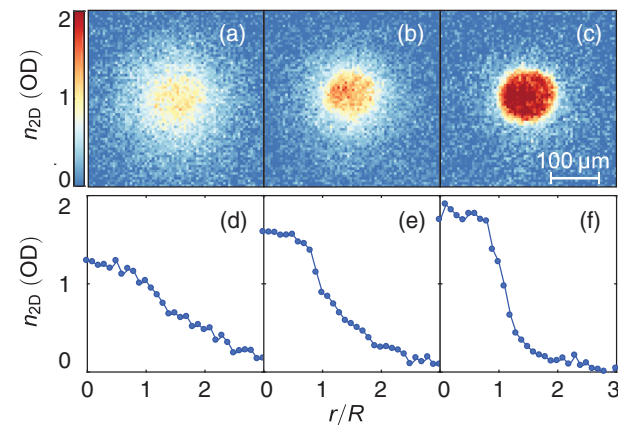

FIG. 3.   Pair condensation in the uniform trap. (a), (b), and (c) Absorption images after a rapid ramp of the magnetic field and 10 ms of time of flight. The temperature of the gas is lowered (left to right) by evaporation in the uniform trap. The onset of a bimodal distribution signals the formation of a pair condensate. (d), (e), and (f) show cuts through the images in the top row.

flight. As a result, the in-trap homogeneity is reflected in a flat top profile of the condensate [see Fig. 3(f)].

Although a fully uniform potential is ideal for measurements that require translational symmetry, a spatially varying potential can access a large region of the phase diagram in a single experimental run. To harness the advantages of both potentials, we introduce a hybrid geometry that combines the radially uniform cylinder trap with an axially harmonic magnetic trap along the z direction [see Fig. 4(a)]. As a benchmark for the hybrid trap, we perform a thermodynamic study of both a strongly spin-imbalanced and a spin-balanced unitary gas. Figures 4(c)–4(e) display for both cases the y-axis averaged local density, temperature, and compressibility. The data shown in Fig. 4 are extracted from an average of just six images per spin component. For comparison, precision measurements of the equation of state at unitarity, performed in conventional harmonic traps, required averaging of over 100 absorption images [31]. The temperature is obtained from fits to the known equations of state of the noninteracting and spin-balanced unitary Fermi gas, respectively. From the local density in the hybrid trap, we determine the normalized isothermal compressibility $\tilde{\kappa} = \kappa/\kappa_0 = -\partial E_F/\partial U|_T$ for the spin-imbalanced and the spin-balanced gas. Here, U is the external potential, and $\kappa_0 = \frac{3}{2}(1/nE_F)$ is the compressibility of the noninteracting Fermi gas at zero temperature [31].

The strongly spin-imbalanced cloud features two distinct regions in the trap. The center of the cloud is a partially polarized region in which $(n_\uparrow - n_\downarrow)/(n_\uparrow + n_\downarrow) > 0.64$, well above the Clogston-Chandrasekhar limit of superfluidity [53–55]. Surrounding the center is a fully polarized region, where the compressibility is seen to saturate: the real space consequence of the Pauli blocking in momentum space demonstrated in Fig. 2.

The majority spin component in the partially polarized region is affected by the presence of the minority spin component. We measure the compressibility $\tilde{\kappa}_\uparrow = -\partial E_{F\uparrow}/\partial U$ in the partially polarized region, and observe an increase compared to the fully polarized gas. This is expected as
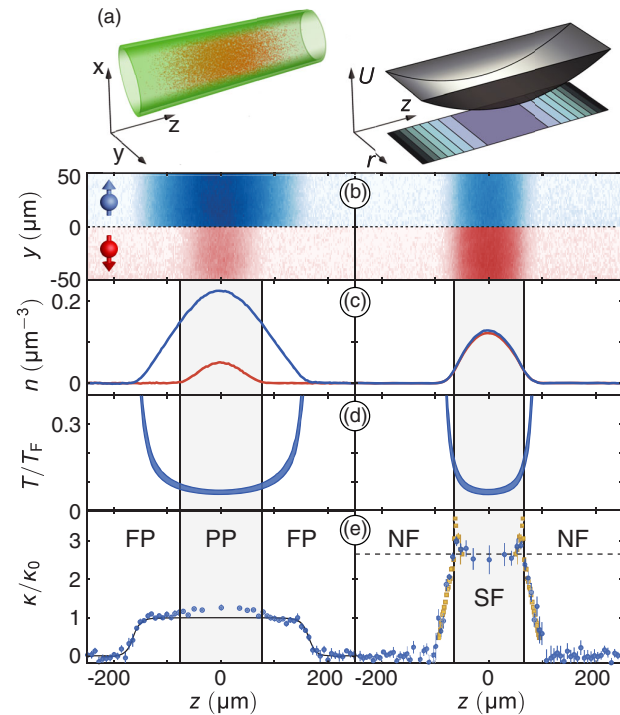
FIG. 4. Unitary Fermi gases in the hybrid trap. (a) Schematic and potential of the trap. The cloud is imaged along an equipotential direction (x axis). Left panels of (b)–(e) show a spin-imbalanced gas above the Clogston-Chandrasekhar limit, whereas the right side corresponds to a spin-balanced gas. The data are averaged over six images. (b) Local density for both spin components, obtained by dividing the column density by the column length. (c) Average density for each x-y equipotential slice. The blue (red) line shows the spin-up (-down) component. (d) Spatially resolved temperature of the gas. The blue shaded region represents the error in the temperature determination. (e) Compressibility of the gas. The solid line in the left panel is the compressibility for an ideal Fermi gas. The crossover from the fully polarized (FP) region to the partially polarized (PP) region is accompanied by an increase in $\tilde{\kappa}$. The yellow squares in the right panel correspond to a precision measurement of the balanced unitary equation of state in the harmonic trap [31]. The peaks in the compressibility signal the phase transition from normal (N) to superfluid (SF). The horizontal dashed line shows the zero-temperature equation of state $\kappa/\kappa_0 = 1/\xi$.

the minority atoms in the center of the trap attract majority atoms and form polarons [7,8]. The effect is indeed predicted by the polaron equation of state [29,30,56]. The observation of this subtle effect highlights the sensitivity of the hybrid potential for thermodynamic measurements.

In the spin-balanced case, κ/κ_0 is significantly larger than for the ideal Fermi gas due to strong interactions. The two prominent peaks in the reduced compressibility signal the superfluid transition at the two boundary surfaces between the superfluid core and the surrounding normal fluid. Near the center of the trap, the reduced compressibility agrees with the $T = 0$ equation of state $\kappa/\kappa_0 = 1/\xi = 2.65(4)$,

where ξ is the Bertsch parameter. The shaded region in the right column of Fig. 4 shows the superfluid part of the gas, where the temperature is below the critical temperature for superfluidity $T_c = 0.17T_F$ [31].

The realization of uniform Fermi gases promises further insight into phases and states of matter that have eluded observation or quantitive understanding. This includes the observation of the quasiparticle jump [57] in the momentum distribution of a Fermi liquid, critical fluctuations in the BEC-BCS crossover, and long-lived solitons [58]. Of particular interest are spin imbalanced mixtures that have been studied extensively in harmonic traps [29,30,55,59–62], where the trap drives the separation of normal and superfluid phases into a shell structure. This phase separation should occur spontaneously in a uniform spin-imbalanced gas, possibly forming domains of superfluid and eventually ordering into an FFLO state. In addition, the hybrid potential is a valuable tool for precision measurements that rely on an in-trap density variation. For example, spatially resolved rf spectroscopy [32] in the hybrid potential would measure the homogenous response of the system over a large range of normalized temperatures T/T_F in a single experimental run.

[1] E. Fermi, Rend. Fis. Acc. Lincei **3**, 145 (1926).
[2] B. DeMarco and D. S. Jin, Science **285**, 1703 (1999).
[3] *Ultra-cold Fermi Gases, Proceedings of the International School of Physics Enrico Fermi, Course CLXIV, Varenna 2006*, edited by M. Inguscio, W. Ketterle, and C. Salomon (IOS Press, Amsterdam, 2008).
[4] S. Giorgini, L. P. Pitaevskii, and S. Stringari, Rev. Mod. Phys. **80**, 1215 (2008).
[5] *The BCS-BEC Crossover and the Unitary Fermi Gas*, edited by W. Zwerger, Lecture Notes in Physics Vol. 836 (Springer-Verlag Berlin Heidelberg, Berlin, Heidelberg, 2012).
[6] M. W. Zwierlein, in *Novel Superfluids* (Oxford University Press, New York, 2014), pp. 269–422.
[7] A. Schirotzek, C.-H. Wu, A. Sommer, and M. W. Zwierlein, Phys. Rev. Lett. **102**, 230402 (2009).
[8] S. Nascimbène, N. Navon, K. J. Jiang, L. Tarruell, M. Teichmann, J. McKeever, F. Chevy, and C. Salomon, Phys. Rev. Lett. **103**, 170402 (2009).
[9] M. Koschorreck, D. Pertot, E. Vogt, B. Fröhlich, M. Feld, and M. Köhl, Nature (London) **485**, 619 (2012).
[10] C. Kohstall, M. Zaccanti, M. Jag, A. Trenkwalder, P. Massignan, G. M. Bruun, F. Schreck, and R. Grimm, Nature (London) **485**, 615 (2012).
[11] R. Jördens, N. Strohmaier, K. Günter, H. Moritz, and T. Esslinger, Nature (London) **455**, 204 (2008).

[12] U. Schneider, L. Hackermüller, S. Will, T. Best, I. Bloch, T. A. Costi, R. W. Helmes, D. Rasch, and A. Rosch, Science **322**, 1520 (2008).

[13] T. Esslinger, Annu. Rev. Condens. Matter Phys. **1**, 129 (2010).

[14] I. Bloch, J. Dalibard, and S. Nascimbène, Nat. Phys. **8**, 267 (2012).

[15] R. A. Hart, P. M. Duarte, T.-L. Yang, X. Liu, T. Paiva, E. Khatami, R. T. Scalettar, N. Trivedi, D. A. Huse, and R. G. Hulet, Nature (London) **519**, 211 (2015).

[16] D. Greif, M. F. Parsons, A. Mazurenko, C. S. Chiu, S. Blatt, F. Huber, G. Ji, and M. Greiner, Science **351**, 953 (2016).

[17] L. W. Cheuk, M. A. Nichols, K. R. Lawrence, M. Okan, H. Zhang, and M. W. Zwierlein, Phys. Rev. Lett. **116**, 235301 (2016).

[18] M. F. Parsons, A. Mazurenko, C. S. Chiu, G. Ji, D. Greif, and M. Greiner, Science **353**, 1253 (2016).

[19] M. Boll, T. A. Hilker, G. Salomon, A. Omran, J. Nespolo, L. Pollet, I. Bloch, and C. Gross, Science **353**, 1257 (2016).

[20] L. W. Cheuk, M. A. Nichols, K. R. Lawrence, M. Okan, H. Zhang, E. Khatami, N. Trivedi, T. Paiva, M. Rigol, and M. W. Zwierlein, Science **353**, 1260 (2016).

[21] A. J. Larkin and Y. N. Ovchinnikov, Zh. Eksp. Teor. Fiz. **47**, 1136 (1964).

[22] P. Fulde and R. A. Ferrell, Phys. Rev. **135**, A550 (1964).

[23] L. Radzihovsky and D. E. Sheehy, Rep. Prog. Phys. **73**, 076501 (2010).

[24] A. L. Gaunt, T. F. Schmidutz, I. Gotlibovych, R. P. Smith, and Z. Hadzibabic, Phys. Rev. Lett. **110**, 200406 (2013).

[25] T. F. Schmidutz, I. Gotlibovych, A. L. Gaunt, R. P. Smith, N. Navon, and Z. Hadzibabic, Phys. Rev. Lett. **112**, 040403 (2014).

[26] N. Navon, A. L. Gaunt, R. P. Smith, and Z. Hadzibabic, Science **347**, 167 (2015).

[27] L. Chomaz, L. Corman, T. Bienaimé, R. Desbuquois, C. Weitenberg, S. Nascimbène, J. Beugnon, and J. Dalibard, Nat. Commun. **6**, 6162 (2015).

[28] T.-L. Ho and Q. Zhou, Nat. Phys. **6**, 131 (2009).

[29] S. Nascimbène, N. Navon, K. J. Jiang, F. Chevy, and C. Salomon, Nature (London) **463**, 1057 (2010).

[30] N. Navon, S. Nascimbene, F. Chevy, and C. Salomon, Science **328**, 729 (2010).

[31] M. J. H. Ku, A. T. Sommer, L. W. Cheuk, and M. W. Zwierlein, Science **335**, 563 (2012).

[32] Y.-I. Shin, C. H. Schunck, A. Schirotzek, and W. Ketterle, Phys. Rev. Lett. **99**, 090403 (2007).

[33] A. Schirotzek, Y.-I. Shin, C. H. Schunck, and W. Ketterle, Phys. Rev. Lett. **101**, 140403 (2008).

[34] J. H. McLeod, J. Opt. Soc. Am. **44**, 592 (1954).

[35] I. Manek, Y. Ovchinnikov, and R. Grimm, Opt. Commun. **147**, 67 (1998).

[36] See Supplemental Material at http://link.aps.org/supplemental/10.1103/PhysRevLett.118.123401 for further information on making and characterizing the uniform trap, optical pumping for the momentum-space mapping, and calibrating the absorption imaging.

[37] R. Thomas, K. O. Roberts, E. Tiesinga, A. C. J. Wade, P. B. Blakie, A. B. Deb, and N. Kjærgaard, Nat. Commun. **7**, 12069 (2016).

[38] A. G. Truscott, K. E. Strecker, W. I. McAlexander, G. B. Partridge, and R. G. Hulet, Science **291**, 2570 (2001).

[39] F. Schreck, L. Khaykovich, K. L. Corwin, G. Ferrari, T. Bourdel, J. Cubizolles, and C. Salomon, Phys. Rev. Lett. **87**, 080403 (2001).

[40] B. DeMarco, S. B. Papp, and D. S. Jin, Phys. Rev. Lett. **86**, 5409 (2001).

[41] A. Sommer, M. Ku, and M. W. Zwierlein, New J. Phys. **13**, 055009 (2011).

[42] T. Rom, T. Best, D. van Oosten, U. Schneider, S. Fölling, B. Paredes, and I. Bloch, Nature (London) **444**, 733 (2006).

[43] T. Müller, B. Zimmermann, J. Meineke, J.-P. Brantut, T. Esslinger, and H. Moritz, Phys. Rev. Lett. **105**, 040401 (2010).

[44] C. Sanner, E. J. Su, A. Keshet, R. Gommers, Y.-I. Shin, W. Huang, and W. Ketterle, Phys. Rev. Lett. **105**, 040402 (2010).

[45] A. Omran, M. Boll, T. A. Hilker, K. Kleinlein, G. Salomon, I. Bloch, and C. Gross, Phys. Rev. Lett. **115**, 263001 (2015).

[46] T. E. Drake, Y. Sagi, R. Paudel, J. T. Stewart, J. P. Gaebler, and D. S. Jin, Phys. Rev. A **86**, 031601 (2012).

[47] I. Shvarchuck, C. Buggle, D. S. Petrov, K. Dieckmann, M. Zielonkovski, M. Kemmann, T. G. Tiecke, W. von Klitzing, G. V. Shlyapnikov, and J. T. M. Walraven, Phys. Rev. Lett. **89**, 270404 (2002).

[48] A. H. van Amerongen, J. J. P. van Es, P. Wicke, K. V. Kheruntsyan, and N. J. van Druten, Phys. Rev. Lett. **100**, 090402 (2008).

[49] S. Tung, G. Lamporesi, D. Lobser, L. Xia, and E. A. Cornell, Phys. Rev. Lett. **105**, 230408 (2010).

[50] P. A. Murthy, D. Kedar, T. Lompe, M. Neidig, M. G. Ries, A. N. Wenz, G. Zürn, and S. Jochim, Phys. Rev. A **90**, 043611 (2014).

[51] C. A. Regal, M. Greiner, and D. S. Jin, Phys. Rev. Lett. **92**, 040403 (2004).

[52] M. W. Zwierlein, C. A. Stan, C. H. Schunck, S. M. F. Raupach, A. J. Kerman, and W. Ketterle, Phys. Rev. Lett. **92**, 120403 (2004).

[53] B. S. Chandrasekhar, Appl. Phys. Lett. **1**, 7 (1962).

[54] A. M. Clogston, Phys. Rev. Lett. **9**, 266 (1962).

[55] M. W. Zwierlein, A. Schirotzek, C. H. Schunck, and W. Ketterle, Science **311**, 492 (2006).

[56] Y.-I. Shin, Phys. Rev. A **77**, 041603 (2008).

[57] G. D. Mahan, *Many-Particle Physics* (Springer, Boston, MA, 2000).

[58] M. J. H. Ku, B. Mukherjee, T. Yefsah, and M. W. Zwierlein, Phys. Rev. Lett. **116**, 045304 (2016).

[59] G. B. Partridge, W. Li, R. I. Kamar, Y.-A. Liao, and R. G. Hulet, Science **311**, 503 (2006).

[60] Y.-I. Shin, M. W. Zwierlein, C. H. Schunck, A. Schirotzek, and W. Ketterle, Phys. Rev. Lett. **97**, 030401 (2006).

[61] Y.-I. Shin, C. H. Schunck, A. Schirotzek, and W. Ketterle, Nature (London) **451**, 689 (2008).

[62] Y.-A. Liao, A. S. C. Rittner, T. Paprotta, W. Li, G. B. Partridge, R. G. Hulet, S. K. Baur, and E. J. Mueller, Nature (London) **467**, 567 (2010).

Supplemental Material:
Homogeneous Atomic Fermi Gases

Biswaroop Mukherjee,[1] Zhenjie Yan,[1] Parth B. Patel,[1]
Zoran Hadzibabic,[1,2] Tarik Yefsah,[1,3] Julian Struck,[1] and Martin W. Zwierlein[1]

[1] *MIT-Harvard Center for Ultracold Atoms, Research Laboratory of Electronics, and Department*
of Physics, Massachusetts Institute of Technology, Cambridge, Massachusetts 02139, USA
[2] *Cavendish Laboratory, University of Cambridge, J. J. Thomson Avenue, Cambridge CB3 0HE, United Kingdom*
[3] *Laboratoire Kastler Brossel, CNRS, ENS-PSL Research University,*
UPMC-Sorbonne Universités and Collège de France, Paris, France

CYLINDER-SHAPED TRAP

For the repulsive optical potential, we use laser light that is blue detuned with respect to the D-lines of ^{6}Li at 671 nm. The laser source is a multi-mode 10W laser at 532 nm. Figure S1 shows the optical setup that is used to shape the beam into a hollow core cylinder. A collimated gaussian beam propagates through an axicon and a microscope objective, generating a hollow cylindrical beam in the Fourier plane [S2, S3]. An opaque circular silver mask is placed in the focal plane to block the residual light inside the ring and provide a sharper inner edge. The resulting intensity distribution at the focal plane is imaged onto the atoms along the z-axis. This confines the atoms into a cylinder oriented along the axial direction (z-axis).

In addition to the radial cylinder-shaped trap, the uniform trap requires sharp end cap walls that confine the atoms along the axial direction. For the endcaps, we use second 532 nm beam from the same laser source and detuned it by 160 MHz to avoid interference between the beams. The end cap beam is split into two elliptically shaped beams with opposite polarizations, which are fo-

FIG. S2. Determination of the power law exponent of the radial wall potential. Log-log plot of the data shown in Fig. 1(b). The blue dotted line is a linear fit, with a slope of $m = 16.2 \pm 1.6$ for the power law exponent.

cused onto the edges of a rectangular opaque mask. The intensity distribution at the mask is projected onto the atoms and provides two sharp confining walls.

TRAP CHARACTERIZATION

Radial Trap Wall: Power Law Potential

To describe the radial extent of the gas as a function of the Fermi energy, we model our radial potential with a power law $U(r) = \alpha r^m$. Within the local density approximation, the local chemical potential is then determined by $\mu(r) = \mu_0 - \alpha r^m$, where $\mu_0 = \mu(r = 0)$. The radius measurements have been performed with a spin-balanced superfluid. Assuming $T = 0$, the cloud has a well defined Thomas-Fermi radius R, where the density drops to zero:

$$\mu_0 = \xi E_{\mathrm{F}} = \alpha R^m, \tag{S1}$$

with the Bertsch parameter ξ. Fitting the data shown in Fig. S2 with a power-law gives $m = 16.2 \pm 1.6$.

FIG. S1. Optical setup for cylinder-shaped trap. From left to right: A gaussian beam propagates through an axicon resulting in a Bessel beam in the near field. Subsequently the Bessel beam is focused through a microscope objective. In the focal plane, the resulting intensity pattern is a ring with gaussian rim. A matched circular opaque mask is used to block out residual light in the center of the ring. Finally the mask is projected through an imaging system onto the atoms, creating the cylinder-shaped trap for the atoms. A small variation of cylinder radius is unavoidable when using a single axicon [S1].

179

FIG. S3. Axial probability distribution. The blue solid line (red dashed line) shows $\mathcal{P}(n_{avg})$ for the uniform (hybrid) trap. Absorption images are taken along x-axis. The line of sight averaged local density n_{avg} is calculated assuming a uniform cylindrical trap.

Axial Probability Distribution

To extract information about the axial homogeneity of the gas, we image the atoms along the x-axis. We obtain the line-of-sight averaged local density n_{avg} from the column density by dividing by the local column length. Figure S3 shows the probability distribution $\mathcal{P}(n_{avg})$ for the line-of-sight averaged density of the uniform and hybrid trap. The axial probability distribution shows a narrow peak similar to the one observed for the radial distribution. The probability distribution for the hybrid trap is broadened due to the harmonic trapping along the z direction.

OPTICAL PUMPING OF THE MINORITY ATOMS FOR MOMENTUM-SPACE MAPPING
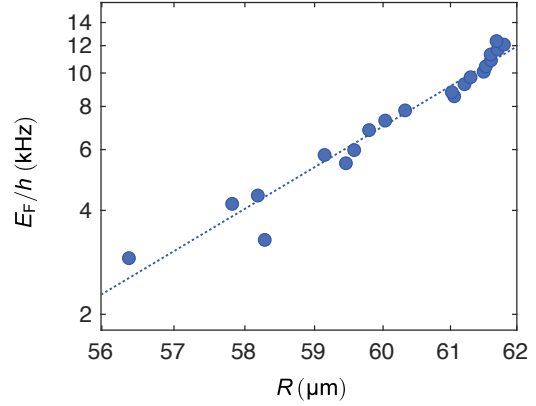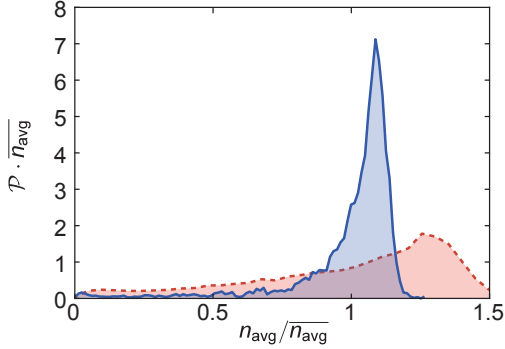
The measurement of the momentum distribution relies on ballistic expansion of the gas immediately after release from the trap. However, the expansion of the atoms is strongly influenced by a small minority fraction ($< 5\%$) of strongly interacting atoms admixed to ensure the thermalization of the gas. To eliminate the interactions between the two spin states during the expansion, the minority atoms are optically pumped into the hyperfine state $|m_J = +1/2, m_I = 0\rangle$ that is weakly interacting with the majority cloud. The $5\,\mu s$ pumping pulse is applied right before the release of the atoms into the harmonic trap. On average, 1.5 photons are required to pump an atom into the weakly interacting hyperfine state. The transitions involved in this pumping scheme are shown in the inset of Fig. S4. Figure S4 shows the integrated momentum distribution of the gas obtained using momentum-space mapping with and without pumping of minority atoms. Note that without the optical pumping of the minority atoms, $f_{1D}(k_z^2)$ is distorted
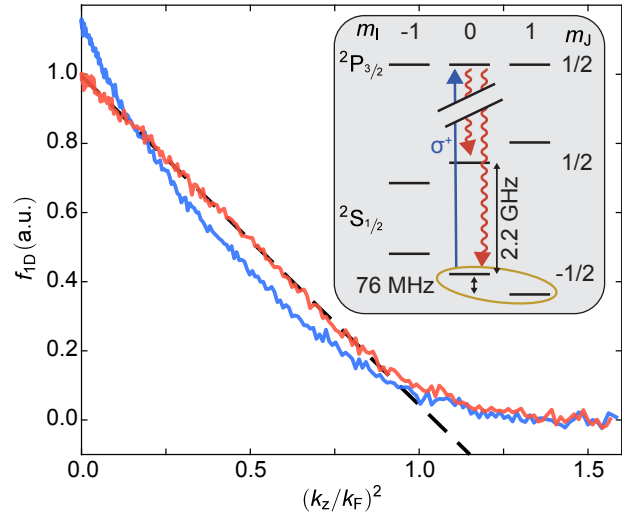
FIG. S4. Influence of the minority atoms on the expansion of the majority cloud. The blue (red) line corresponds to the observed integrated momentum distribution without (with) optical pumping of the minority atoms. The dashed line is a guide to the eye. The inset displays the level scheme for the optical pumping at a magnetic field of $B = 832\,$G. The yellow ellipse marks the two strongly interacting spin states, where the minority is in $|m_J = -1/2, m_I = 0\rangle$. The pumping transition is shown as the blue line and the spontaneous decay channels with red curvy lines.

from the triangular shape expected for a low temperature Fermi gas.

DENSITY MEASUREMENT WITH ABSORPTION IMAGING

For heavy atoms, such as Rb and Cs, and imaging intensities that are small compared to the saturation intensity (I_{sat}), the column density $n_{col} = -(1/\sigma_0) \log{(I_f/I_i)}$ is determined by the Beer-Lambert law. Here, I_i and I_f are the intensities of the imaging beam before and after the atoms, respectively, and σ_0 is the absorption cross-section. However, for light atoms such as Li, the Doppler effect plays a dominant role in realistic experimental scenarios, where a low imaging intensity and short exposure time is in conflict with a high signal to noise ratio. For our experiment, depending on the column density of the sample, preferred values for the imaging intensities are $0.1 - 0.5\,I_{sat}$ at an exposure time of $4 - 10\,\mu s$. Under these conditions, each ^{6}Li atom scatters up to 35 photons. The corresponding photon recoil results in a Doppler shift of up to 6 MHz, which is comparable to the natural linewidth of ^{6}Li.

In order to account for the Doppler and saturation effects, we numerically solve two coupled differential equations for the local, time-dependent saturation parameter
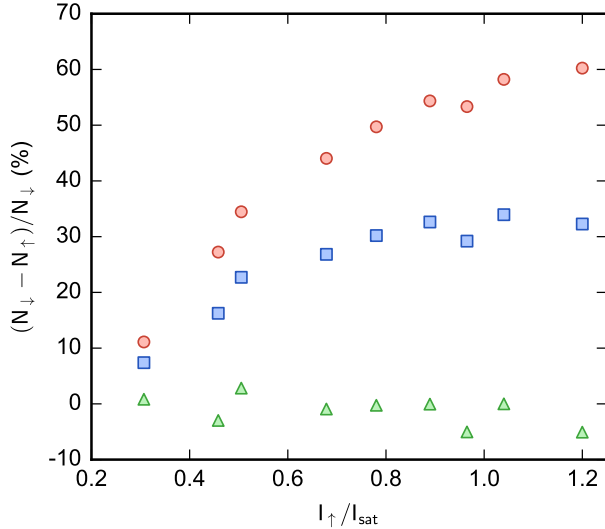
FIG. S5. Apparent atom count for the spin up component ($N_\uparrow$) measured at different imaging intensities ($I_\uparrow$). A reference atom count ($N_\downarrow$) is obtained by subsequently imaging a second spin component at a fixed imaging intensity ($I_\downarrow = 0.23 I_{sat}$). Red circles, blue squares, and green triangles are obtained using Beer-Lambert, saturated Beer-Lambert, and Doppler Beer-Lambert, respectively. Spin balanced clouds are used for these measurements.

$s(z, t) = I(z, t)/I_{sat}$ and velocity $v(z, t)$;

$$\frac{\partial s}{\partial z} = -n\sigma_0 \frac{s}{1 + s + (2kv/\Gamma)^2}. \qquad \text{(S2a)}$$

$$\frac{\partial v}{\partial t} = \frac{\hbar k \Gamma}{2m} \frac{s}{1 + s + (2kv/\Gamma)^2}. \qquad \text{(S2b)}$$

Here, σ_0, k, m and Γ are the bare scattering cross-section, photon wave vector, atomic mass and natural linewidth.

In the limit where the Doppler effect is negligible ($v = 0$), the analytical solution of Eq. S2 is $n_{col}\sigma_0 = -\log(s_f/s_i) - (s_f - s_i)$. Here, s_i and s_f are reduced imaging intensities before and after the atoms, respectively. This is the modified version of the Beer-Lambert law that includes saturation of the atomic transition. For the general case, we numerically solve Eq. S2 to find the Doppler-corrected relation between I_i and I_f (which we call the "Doppler Beer-Lambert" law).

We compare these aforementioned methods by subsequently imaging the two spin states of a spin-balanced gas with a fast SCMOS camera. The first image is taken with fixed saturation intensity of $s_\downarrow = 0.23$ and serves as the density reference. The second absorption image for the other spin component, with a variable $s_\uparrow$, is obtained $15\,\mu$s after the first image. Figure S5 shows the differences in the measured total atom numbers between two spin components for various $s_\uparrow$ calculated using the Beer-Lambert law (red circles), the saturated Beer-Lambert law (blue squares) and Doppler Beer-Lambert (green triangles). For the atom number differences calculated using the Doppler Beer-Lambert law, the mean deviation from the reference density is only 3% compared to 27% and 46% for the saturated Beer-Lambert and the basic Beer-Lambert law, respectively.

[S1] A. L. Gaunt, *Degenerate Bose Gases : Tuning Interactions & Geometry*, PhD, University of Cambridge (2014).
[S2] J. H. McLeod, Journal of the Optical Society of America **44**, 592 (1954).
[S3] I. Manek, Y. Ovchinnikov, and R. Grimm, Optics Communications **147**, 67 (1998).

Appendix E

Spectral Response and Contact of the Unitary Fermi Gas

This appendix contains a reprint of the following paper :

B. Mukherjee, P. B. Patel, Z. Yan, R. J. Fletcher, J. Struck, M. W. Zwierlein, "Spectral Response and Contact of the Unitary Fermi Gas," Phys. Rev. Lett. **122**, *203402 (2019)[100]*

Editors' Suggestion   Featured in Physics

Spectral Response and Contact of the Unitary Fermi Gas

Biswaroop Mukherjee,[1] Parth B. Patel,[1] Zhenjie Yan,[1] Richard J. Fletcher,[1]
Julian Struck,[1,2] and Martin W. Zwierlein[1]

[1]*MIT-Harvard Center for Ultracold Atoms, Research Laboratory of Electronics, and Department of Physics,*
Massachusetts Institute of Technology, Cambridge, Massachusetts 02139, USA
[2]*Département de Physique, Ecole Normale Supérieure / PSL Research University, CNRS, 24 rue Lhomond, 75005 Paris, France*

We measure radio frequency (rf) spectra of the homogeneous unitary Fermi gas at temperatures ranging from the Boltzmann regime through quantum degeneracy and across the superfluid transition. For all temperatures, a single spectral peak is observed. Its position smoothly evolves from the bare atomic resonance in the Boltzmann regime to a frequency corresponding to nearly one Fermi energy at the lowest temperatures. At high temperatures, the peak width reflects the scattering rate of the atoms, while at low temperatures, the width is set by the size of fermion pairs. Above the superfluid transition, and approaching the quantum critical regime, the width increases linearly with temperature, indicating non-Fermi-liquid behavior. From the wings of the rf spectra, we obtain the contact, quantifying the strength of short-range pair correlations. We find that the contact rapidly increases as the gas is cooled below the superfluid transition.

Understanding fermion pairing and pair correlations is of central relevance to strongly interacting Fermi systems such as nuclei [1,2], ultracold gases [3–6], liquid ³He [7], high temperature superconductors [8], and neutron stars [9]. Strong interactions on the order of the Fermi energy challenge theoretical approaches, especially methods that predict dynamic properties such as transport or the spectral response at finite temperature [10]. Atomic Fermi gases at Feshbach resonances realize a paradigmatic system where the gas becomes as strongly interacting as allowed by unitarity [3–6,11]. Here, the system becomes universal, requiring only two energy scales: the Fermi energy E_F and thermal energy $k_B T$, where k_B is the Boltzmann constant and T is the temperature. The corresponding length scales are the interparticle spacing $\lambda_F = n^{-1/3}$ and the thermal de Broglie wavelength $\lambda_T = h/\sqrt{2\pi m k_B T}$, where m and n are the mass and number density of the atoms, respectively. When the two energy scales are comparable, the system enters a quantum critical regime separating the high temperature Boltzmann gas from the fermionic superfluid [12]. Quantum criticality is often associated with the absence of quasiparticles [10,12,13], spurring a debate on the applicability of Fermi liquid theory to the degenerate normal fluid below the Fermi temperature $T_F = E_F/k_B$ but above the superfluid transition temperature $T_c \approx 0.167 T_F$ [14–16]. It has been conjectured that preformed pairs exist above T_c, up to a pairing temperature T^* [3,5,11,17–21].

Radio frequency (rf) spectroscopy measures the momentum integrated, occupied spectral function, providing a powerful tool for studying interactions and correlations in Fermi gases [22–27]. Here, a particle is ejected from the interacting many-body state and transferred into a weakly interacting final state. Shifts in rf spectra indicate attractive or repulsive interactions in the gas. At high temperatures, the width of the rf spectrum reflects the scattering rate in the gas, while at low temperatures, the width has been used to infer the pair size of superfluid fermion pairs [26].

The high frequency tails of the rf spectra are sensitive to the spectral function at high momenta and, therefore, are governed by short range correlations quantified by the contact, which also determines the change of the energy with respect to the interaction strength [28–30]. From the momentum distribution within nuclei [1,2] to the frequency dependence of the shear viscosity in ultracold fermionic superfluids [31,32], the contact is central to Fermi gases dominated by short-range interactions. Since the contact is proposed to be sensitive to the superfluid pairing gap, it could signal a pseudogap regime above T_c [32–35]. Although the temperature dependence of the contact near T_c has been the subject of many theoretical predictions, a consensus has not been reached [32,36–38].

Initial studies of unitary Fermi gases using rf spectroscopy were affected by inhomogeneous densities in harmonic traps, yielding doubly peaked spectra that were interpreted as observations of the pairing gap [25,39], and from the influence of interactions in the final state, which caused significantly narrower spectra and smaller shifts than expected [22,39–41]. Measurements of the contact, made using both rf [42,43] and Bragg [44–46] spectroscopy, were also broadened by inhomogeneous potentials. To avoid trap broadening, tomographic techniques have been used to measure local rf spectra, yielding measurements of the superfluid gap [47], the spectral function [17,18], and the

184

contact [48]. A recent advance has been the creation of uniform box potentials [49–51]. These are ideal for rf spectroscopy and precision measurements of the contact: since the entire cloud is at a constant density, global probes such as rf address all atoms, and benefit from a stronger signal.

In this Letter, we report on rf spectroscopy of the homogeneous unitary Fermi gas in a box potential. A single peak is observed for all temperatures from the superfluid regime into the high temperature Boltzmann gas. The tails of the rf spectra reveal the contact, which shows a rapid rise as the temperature is reduced below T_c.

We prepare ^{6}Li atoms in two of the three lowest hyperfine states $|\downarrow\rangle = |1\rangle$ and $|\uparrow\rangle = |3\rangle$ at a magnetic field of 690 G, where interspin interactions are resonant. A uniform optical box potential with cylindrical symmetry is loaded with $N \sim 10^6$ atoms per spin state (with Fermi energies $E_F \sim h \times 10$ kHz), creating spin-balanced homogeneous gases at temperatures ranging from $T/T_F = 0.10$ to 3.0 [50]. A square rf pulse transfers atoms from state $|\downarrow\rangle$ into state $|f\rangle = |2\rangle$. Final state interactions between atoms in state $|f\rangle$ and atoms in states $|\uparrow\rangle$ and $|\downarrow\rangle$ are small ($k_F a_f \lesssim 0.2$, where a_f is the scattering length characterizing collisions between atoms in the final and initial states, and $\hbar k_F = \sqrt{2mE_F}$ is the Fermi momentum)

[26]. After the rf pulse, we measure the atom numbers $N_\downarrow$ and N_f in the initial and final states. Within linear response, according to Fermi's golden rule, N_f is proportional to the pulse time T_{Pulse}, the square of the single-particle Rabi frequency Ω_R, and an energy density of states. Thus, we define a normalized, dimensionless rf spectrum as $I(\omega) = [N_f(\omega)/N_\downarrow](E_F/\hbar\Omega_R^2 T_{\text{Pulse}})$ [52,57]. Because of the scale invariance of the balanced unitary Fermi gas, this dimensionless function can only depend on T/T_F and $\hbar\omega/E_F$.

For thermometry, we release the cloud from the uniform potential into a harmonic trap along one direction [57]. Since the cloud expands isoenergetically, the resulting spatial profile after thermalization provides the energy per particle, which can be related to the reduced temperature, T/T_F, using a virial relation and the measured equation of state [14]. To clearly identify the superfluid transition, we measure the pair momentum distribution by a rapid ramp of the magnetic field to the molecular side of the Feshbach resonance before releasing the gas into a harmonic trap for a quarter period [50,52].

Initially, we focus on changes in the line shape for rf frequencies within $\sim E_F/\hbar$ of the bare (single-particle) resonance [see Fig. 1(a)], and follow the changes in
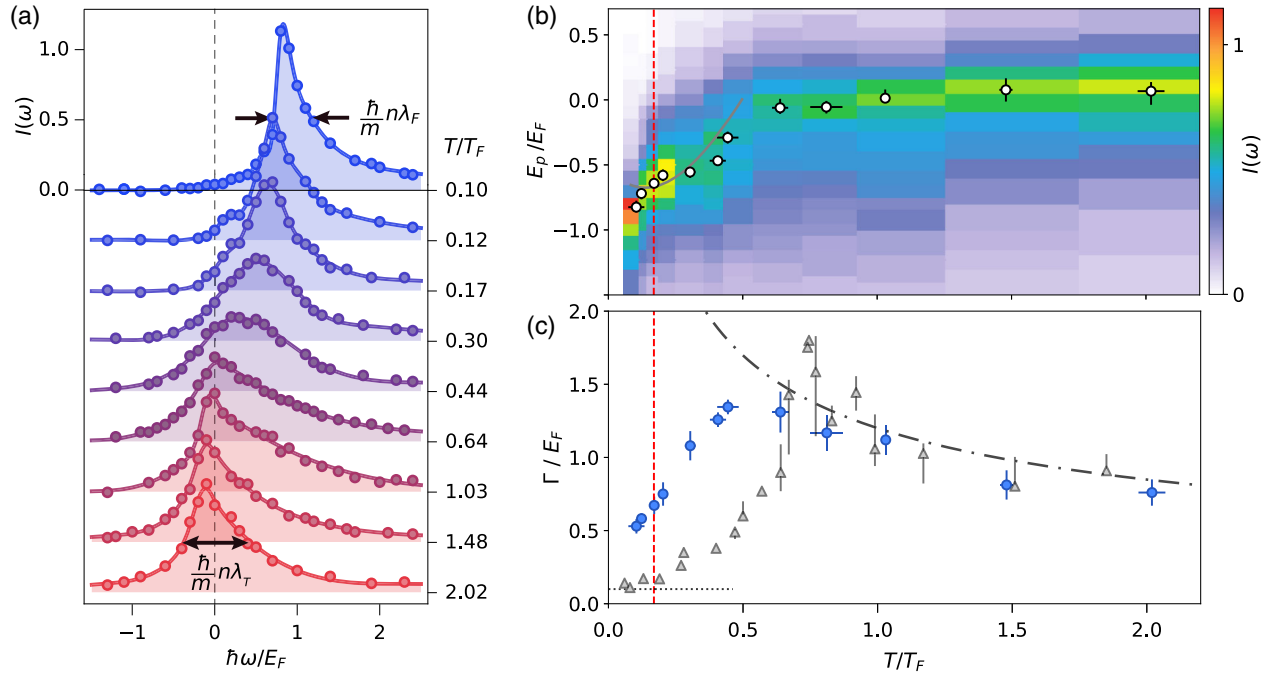
FIG. 1.   (a) Thermal evolution of rf spectra. The Rabi frequency is $\Omega_R = 2\pi \times 0.5$ kHz and the pulse duration is $T_{\text{Pulse}} = 1$ ms. The solid lines are guides to the eye. (b) Frequency of the peak ($E_p = -\hbar\omega$) of the rf spectra as a function of temperature shown as white dots on an intensity plot of the rf response. The grey solid line is a solution to the Cooper problem at nonzero temperature [52]. (c) The full width at half maximum Γ of the rf peak as a function of T/T_F. The black dotted-dashed line $\Gamma/E_F = 1.2\sqrt{T_F/T}$ shows the temperature dependence of the width due to scattering in the high-temperature gas [32,60]. The grey triangles are the corresponding width measurements of a highly spin-imbalanced gas [57]. The horizontal black dotted line represents the Fourier broadening of $0.1E_F$ [52]. The vertical dashed red line in both (b) and (c) marks the superfluid transition [14].

the peak position E_p [shown in Fig. 1(b)]. As the hot spin-balanced Fermi gas is cooled below the Fermi temperature, the peak shift decreases from roughly zero for temperatures $T \gtrsim T_F$, to $E_p \approx -0.8 E_F$ for temperatures below the superfluid transition temperature [see Fig. 1(b)]. At high temperatures, one might naïvely expect a shift on the order of $E_p \sim \hbar n \lambda_T / m$ due to unitarity-limited interactions in the gas. However, there exists both an attractive and a repulsive energy branch, which are symmetric about zero at unitarity [58], and when $T \gg T_F$, their contributions to the shift cancel [32,59,60]. As to the interpretation of the peak shift at degenerate temperatures, a solution to the Cooper problem in the presence of a $T > 0$ Fermi sea shows that it is energetically favorable to form pairs when $T \lesssim 0.5 T_F$ [52], and the resulting pair energy agrees qualitatively with the observed shifts [grey line in Fig. 1(b)]. However, it is known that fluctuations suppress the onset of pair condensation and superfluidity to $0.167(13)T_F$ [5,11,14,61]. In a zero-temperature superfluid, BCS theory would predict a peak shift given by the pair binding energy $E_B = \Delta^2 / 2E_F$, where Δ is the pairing gap [3]. Including Hartree terms is found to result in an additional shift of the peak [27,47].

Now, we turn to the widths, Γ, defined as the full width at half maximum of the rf spectra [see Fig. 1(c)]. As the gas is cooled from the Boltzmann regime, the width gradually increases, and attains a maximum of $\Gamma = 1.35(5)E_F$ near $T = 0.44(4)T_F$. For temperatures much higher than T_F, the system is a Boltzmann gas of atoms scattering with a unitarity limited cross section $\sigma \sim \lambda_T^2$. Transport properties and short-range pair correlations are governed by the scattering rate $\Gamma = n_\downarrow \sigma \langle v_{\rm rel} \rangle \sim \hbar n_\downarrow \lambda_T / m$ and a mean-free path $l = (n_\downarrow \sigma)^{-1} \sim (n_\downarrow \lambda_T^2)^{-1}$, where $n_\downarrow$ is the density of atoms in $|\downarrow\rangle$, and $\langle v_{\rm rel} \rangle \sim \hbar / m \lambda_T$ is the thermally averaged relative velocity. This leads to a width that scales as $\Gamma \propto 1/\sqrt{T}$, shown as the dotted-dashed line in Fig. 1(c) [32].

As the cloud is cooled below $T \approx 0.5 T_F$, the width decreases linearly with temperature to $\Gamma \sim 0.52 E_F / \hbar$ in the coldest gases measured [$T = 0.10(1)T_F$]. For temperatures below T_c, we expect the gas to consist of pairs of size ξ. The rf spectrum will be broadened by the distribution of momenta $\sim \hbar / \xi$ inside each pair, leading to a spread of possible final kinetic energies $\hbar^2 k^2 / m \sim \hbar^2 / m \xi^2$ and a corresponding spectral width $\hbar / m \xi^2$. At unitarity and at $T = 0$, the pair size is set by the interparticle spacing λ_F [3,5,26]. Thus, the rf width at low temperatures is $\Gamma \sim \hbar n \lambda_F / m$.

For temperatures above T_c, it has been suggested that the normal fluid can be described as a Fermi liquid [15,62]. This would imply a quadratic relation between the peak width and the temperature [63], as observed in the widths of the rf spectra of Fermi polarons at unitarity [57]. However, the measured width of the spin-balanced Fermi gas changes linearly in temperature, implying non-Fermi
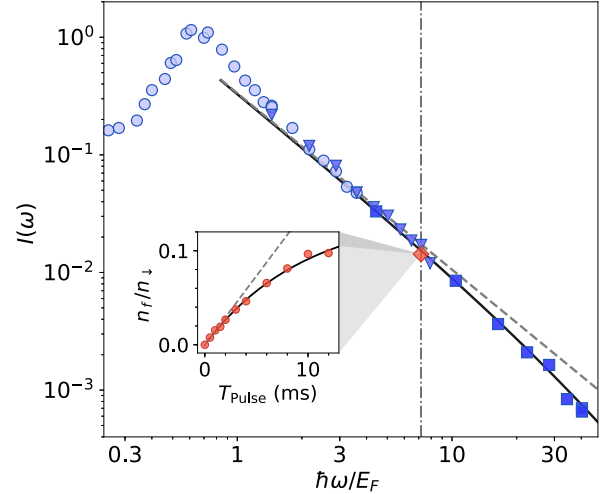
FIG. 2. Rf spectrum at high frequencies. Here, the temperature of the gas is $T/T_F = 0.10(1)$, the pulse duration is $T_{\rm Pulse} = 1$ ms, and the Rabi frequencies are $2\pi \times 536$ Hz (light blue circles), $2\pi \times 1.20$ kHz (medium blue triangles), and $2\pi \times 3.04$ kHz (dark blue squares). The black solid line shows a fit of Eq. (1) to the data, while the grey dashed line shows the fit neglecting final state interactions. The contact can be directly obtained from the transfer rate at a fixed detuning of 60 kHz ($\hbar\omega/E_F \sim 7.1$) (dotted-dashed vertical line). Inset: we vary the pulse time at this fixed detuning, and extract the initial slope (dashed line) of the exponential saturating fit (solid line). The rf transfer rate obtained from the initial linear slope is shown as the red diamond in the main plot. Here, $\Omega_R = 2\pi \times 1.18$ kHz.

liquid behavior in the normal fluid. In addition, $\Gamma > E_F / \hbar$ for $0.3 \lesssim T/T_F \lesssim 1.2$, indicating a breakdown of well-defined quasiparticles over a large range of temperatures near the quantum critical regime [10,12,13].

We now consider the rf spectrum at frequencies much larger than $E_F / \hbar$, where the rf-coupled high-momentum tails reveal information about the short-range pair correlations between atoms. In a gas with contact interactions, the pair correlation function at short distances is $\lim_{r\to 0} \langle n_\uparrow (\mathbf{r_0} + \mathbf{r}/2) n_\downarrow (\mathbf{r_0} - \mathbf{r}/2) \rangle = C/(4\pi r)^2$. The contact C connects a number of fundamental relations, independent of the details of the short-range interaction potential [28]. In particular, the contact governs the momentum distribution at large momenta: $\lim_{k\to\infty} n(k) = C/k^4$. For rf spectroscopy, the density of final states scales as $\sqrt{\omega}$, and the energy cost to flip a spin at high momenta is $\lim_{k\to\infty} \hbar\omega = \hbar^2 k^2 / m$. Thus, the number of atoms transferred by the rf pulse at high frequencies in linear response is $\propto C/\omega^{3/2}$ [5,27]. Including final state interactions, the general expression for the rf transfer rate in a gas with unitarity-limited initial state interactions is [64]

$$\lim_{\omega\to\infty} I(\omega) = \left(\frac{C}{N k_F}\right) \frac{1}{2\sqrt{2}\pi(1 + \hbar\omega/E_b)} \left(\frac{E_F}{\hbar\omega}\right)^{3/2}, \quad (1)$$

where $N = N_\uparrow + N_\downarrow$ is the total number of atoms, and the final state molecular binding energy is $E_b = \hbar^2/ma_f^2 \approx h \times 433$ kHz $\approx 40 E_F$. Figure 2 shows a typical rf spectrum at $T/T_F = 0.10$, with a fit of Eq. (1) to data with detunings $\hbar\omega > 3E_F$, using the dimensionless contact $\tilde{C} = C/Nk_F$ as the only free parameter. At detunings larger than about $10\ E_F$, the data deviate from a typical $\omega^{-3/2}$ tail, and are better described by the full expression Eq. (1) including final state interactions. Here, the Rabi frequency was varied across the plot to ensure small transfers near the peak and a high signal-to-noise ratio at detunings up to $\hbar\omega/E_F = 31$. The fit of Eq. (1) to the data gives a low-temperature contact of $\tilde{C} = 3.07(6)$, consistent with a quantum Monte Carlo result $\tilde{C} = 2.95(10)$ [65], the Luttinger-Ward (LW) calculation $\tilde{C} = 3.02$ [27], as well as previous measurements using losses $\tilde{C} = 3.1(3)$ [66] and Bragg spectroscopy $\tilde{C} = 3.06(8)$ [46].

For a more efficient measurement of the contact across a range of temperatures, we vary the pulse time at a fixed detuning of 60 kHz ($\hbar\omega/E_F \gtrsim 6$) that is large compared to the Fermi energy and temperature. [52]. Deviations from linear response are observed for transfers as small as 5% (see inset of Fig. 2). We fit the transfers to an exponentially saturating function $A[1 - \exp(-T_{\text{Pulse}}/\tau)]$, and find the initial linear slope A/τ in order to extract the contact for each temperature using Eq. (1). This ensures that every measurement is taken in the linear response regime.

In Fig. 3(a), we show the temperature dependence of the contact. As the gas is cooled, the contact shows a gradual increase down to the superfluid transition T_c. Entering the superfluid transition, the contact rapidly rises by approximately 15%. The changes in the contact reveal the temperature dependence of short-range pair correlations in the spin-balanced Fermi gas. At temperatures far above T_F, the contact reflects the inverse mean free path in the gas $1/l \sim 1/T$. At lower temperatures, the behavior of the contact is better described by a third-order virial expansion [see inset of 3(a)] [36]. Near T_c, predictions of the contact vary considerably. In the quantum critical regime, a leading-order $1/N$ calculation (equivalent to a Gaussian pair fluctuation or Nozières–Schmitt-Rink method) results in a prediction $\tilde{C}(\mu = 0, T \approx 0.68 T_F) = 2.34$ [10], which is consistent with our measurement of $\tilde{C}[T = 0.65(4)T_F] = 2.29(13)$. For temperatures above the superfluid transition, our data agree well with both a bold diagrammatic Monte Carlo calculation [38], and, especially near T_c, the LW calculation [32]. The contact rises as the temperature is decreased below T_c, a feature captured by the LW formalism, in which the contact is directly sensitive to pairing: $\tilde{C} \sim (\Delta/E_F)^2$ [27,33]. While short-range pair correlations do not necessarily signify pairing [35], the rapid rise of the contact below T_c is strongly indicative of an additional contribution from fermion pairs, as predicted
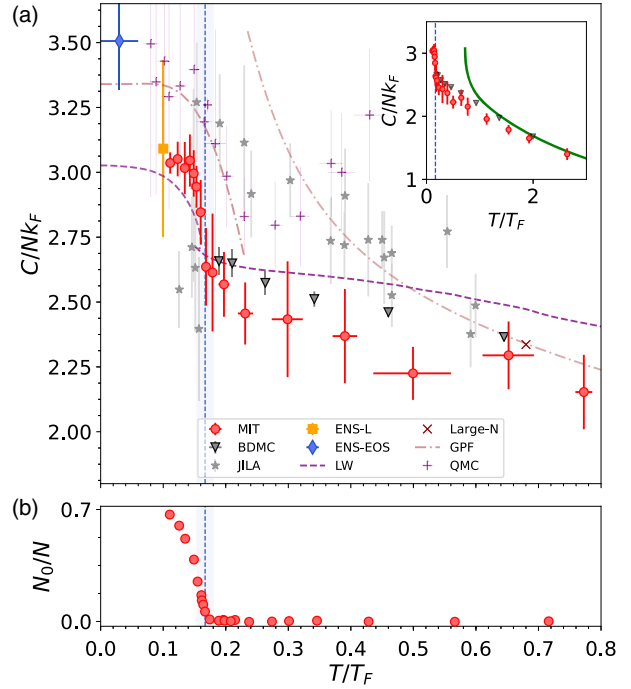
FIG. 3. The dimensionless contact C/Nk_F (a) and condensate fraction N_0/N (b) of the unitary Fermi gas as a function of the reduced temperature T/T_F. Our measurements of the contact (red points) are compared with a number of theoretical estimates: bold-diagrammatic Monte Carlo (BDMC) [38], quantum Monte Carlo (QMC) [37], Luttinger-Ward (LW) [32], large N [10], and Gaussian pair fluctuations (GPF) [36]. Also shown is the homogeneous contact obtained from the equation of state at the École normale supérieure (ENS-EOS) [62], from loss rate measurements (ENS-L) [66], and from rf spectroscopy by the JILA group [18] across a range of temperatures. The vertical blue dotted lines and light blue shaded vertical regions mark $T_c/T_F = 0.167(13)$ [14]. The inset of (a) shows the contact over a wider range of temperatures and marks the high-temperature agreement with the third order virial expansion. The error bars account for the statistical uncertainties in the data.

by LW. At temperatures $T \ll T_c$, below the reach of our experiment, phonons are likely the only remaining excitations in the unitary Fermi gas, and are expected to contribute to the contact by an amount that scales as T^4 [67].

In conclusion, rf spectroscopy of the homogeneous unitary Fermi gas reveals strong attractive interactions, the non-Fermi-liquid nature of excitations in the gas across the quantum critical regime, and a rapid increase in short-range pair correlations upon entering the superfluid regime. The strong variation with temperature of the position of the spectral peak may serve as a local thermometer in future studies of heat transport in ultracold Fermi gases. Furthermore, these measurements of the contact provide a benchmark for many-body theories of the unitary Fermi gas. The uniform trap enables direct access to homogeneous measurements of thermodynamic quantities,

and increases sensitivity to abrupt changes of those quantities near phase transitions. This could be particularly useful in the limit of high spin imbalance, where the nature of impurities suddenly transitions from Fermi polarons to molecules. [68,69].

We note that measurements of the temperature dependence of the contact were simultaneously performed at Swinburne using Bragg spectroscopy [70]. Their data are in excellent agreement with the present results.

[1] O. Hen *et al.*, Science **346**, 614 (2014).
[2] R. Weiss, B. Bazak, and N. Barnea, Phys. Rev. Lett. **114**, 012501 (2015).
[3] W. Ketterle and M. W. Zwierlein, in "Ultra-Cold Fermi Gases," *Proceedings of the International School of Physics "Enrico Fermi," Course CLXIV*, edited by M. Inguscio, W. Ketterle, and C. Salomon (IOS Press, Amsterdam, 2008), pp. 247–422.
[4] S. Giorgini, L. P. Pitaevskii, and S. Stringari, Rev. Mod. Phys. **80**, 1215 (2008).
[5] W. Zwerger, in "Quantum Matter at Ultralow Temperatures," *Proceedings of the International School of Physics "Enrico Fermi" Course CLXCI*, edited by M. Inguscio, W. Ketterle, S. Stringari, and G. Roati (IOS Press, Amsterdam, 2016), pp. 63–142.
[6] M. W. Zwierlein, in *Novel Superfluids* (Oxford University Press, Oxford, 2014), pp. 269–422.
[7] A. J. Leggett, Phys. Rev. Lett. **29**, 1227 (1972).
[8] P. A. Lee, N. Nagaosa, and X.-G. Wen, Rev. Mod. Phys. **78**, 17 (2006).
[9] G. Baym, C. Pethick, and D. Pines, Nature (London) **224**, 673 (1969).
[10] T. Enss, Phys. Rev. A **86**, 013616 (2012).
[11] M. Randeria and E. Taylor, Annu. Rev. Condens. Matter Phys. **5**, 209 (2014).
[12] P. Nikolic and S. Sachdev, Phys. Rev. A **75**, 033608 (2007).
[13] B. Frank, J. Lang, and W. Zwerger, J. Exp. Theor. Phys. **127**, 812 (2018).
[14] M. J. H. Ku, A. T. Sommer, L. W. Cheuk, and M. W. Zwierlein, Science **335**, 563 (2012).
[15] S. Nascimbène, N. Navon, S. Pilati, F. Chevy, S. Giorgini, A. Georges, and C. Salomon, Phys. Rev. Lett. **106**, 215303 (2011).
[16] I. Z. Rothstein and P. Shrivastava, Phys. Rev. B **99**, 035101 (2019).

[17] J. P. Gaebler, J. T. Stewart, T. E. Drake, D. S. Jin, A. Perali, P. Pieri, and G. C. Strinati, Nat. Phys. **6**, 569 (2010).
[18] Y. Sagi, T. E. Drake, R. Paudel, R. Chapurin, and D. S. Jin, Phys. Rev. Lett. **114**, 075301 (2015).
[19] A. Perali, P. Pieri, G. C. Strinati, and C. Castellani, Phys. Rev. B **66**, 024510 (2002).
[20] H. Hu, X. J. Liu, P. D. Drummond, and H. Dong, Phys. Rev. Lett. **104**, 240407 (2010).
[21] P. Magierski, G. Wlazłowski, and A. Bulgac, Phys. Rev. Lett. **107**, 145304 (2011).
[22] S. Gupta, Z. Hadzibabic, M. W. Zwierlein, C. A. Stan, K. Dieckmann, C. H. Schunck, E. G. Van Kempen, B. J. Verhaar, and W. Ketterle, Science **300**, 1723 (2003).
[23] C. A. Regal and D. S. Jin, Phys. Rev. Lett. **90**, 230404 (2003).
[24] C. A. Regal, C. Ticknor, J. L. Bohn, and D. S. Jin, Nature (London) **424**, 47 (2003).
[25] C. Chin, M. Bartenstein, A. Altmeyer, S. Riedl, S. Jochim, J. Denschlag, and R. Grimm, Science **305**, 1128 (2004).
[26] C. H. Schunck, Y.-I. Shin, A. Schirotzek, and W. Ketterle, Nature (London) **454**, 739 (2008).
[27] R. Haussmann, M. Punk, and W. Zwerger, Phys. Rev. A **80**, 063612 (2009).
[28] S. Tan, Ann. Phys. (Amsterdam) **323**, 2971 (2008).
[29] S. Tan, Ann. Phys. (Amsterdam) **323**, 2952 (2008).
[30] S. Tan, Ann. Phys. (Amsterdam) **323**, 2987 (2008).
[31] E. Taylor and M. Randeria, Phys. Rev. A **81**, 053610 (2010).
[32] T. Enss, R. Haussmann, and W. Zwerger, Ann. Phys. (Amsterdam) **326**, 770 (2011).
[33] P. Pieri, A. Perali, and G. C. Strinati, Nat. Phys. **5**, 736 (2009).
[34] F. Palestini, A. Perali, P. Pieri, and G. C. Strinati, Phys. Rev. A **82**, 021605(R) (2010).
[35] E. J. Mueller, Rep. Prog. Phys. **80**, 104401 (2017).
[36] H. Hu, X. J. Liu, and P. D. Drummond, New J. Phys. **13**, 035007 (2011).
[37] O. Goulko and M. Wingate, Phys. Rev. A **93**, 053604 (2016).
[38] R. Rossi, T. Ohgoe, E. Kozik, N. Prokof'ev, B. Svistunov, K. Van Houcke, and F. Werner, Phys. Rev. Lett. **121**, 130406 (2018).
[39] C. H. Schunck, Y. Shin, A. Schirotzek, M. W. Zwierlein, and W. Ketterle, Science **316**, 867 (2007).
[40] G. Baym, C. J. Pethick, Z. Yu, and M. W. Zwierlein, Phys. Rev. Lett. **99**, 190407 (2007).
[41] M. Punk and W. Zwerger, Phys. Rev. Lett. **99**, 170404 (2007).
[42] J. T. Stewart, J. P. Gaebler, T. E. Drake, and D. S. Jin, Phys. Rev. Lett. **104**, 235301 (2010).
[43] C. Shkedrov, Y. Florshaim, G. Ness, A. Gandman, and Y. Sagi, Phys. Rev. Lett. **121**, 093402 (2018).
[44] E. D. Kuhnle, H. Hu, X. J. Liu, P. Dyke, M. Mark, P. D. Drummond, P. Hannaford, and C. J. Vale, Phys. Rev. Lett. **105**, 070402 (2010).
[45] E. D. Kuhnle, S. Hoinka, P. Dyke, H. Hu, P. Hannaford, and C. J. Vale, Phys. Rev. Lett. **106**, 170402 (2011).
[46] S. Hoinka, M. Lingham, K. Fenech, H. Hu, C. J. Vale, J. E. Drut, and S. Gandolfi, Phys. Rev. Lett. **110**, 055305 (2013).
[47] A. Schirotzek, Y.-I. Shin, C. H. Schunck, and W. Ketterle, Phys. Rev. Lett. **101**, 140403 (2008).

[48] Y. Sagi, T. E. Drake, R. Paudel, and D. S. Jin, Phys. Rev. Lett. **109,** 220402 (2012).

[49] A. L. Gaunt, T. F. Schmidutz, I. Gotlibovych, R. P. Smith, and Z. Hadzibabic, Phys. Rev. Lett. **110,** 200406 (2013).

[50] B. Mukherjee, Z. Yan, P. B. Patel, Z. Hadzibabic, T. Yefsah, J. Struck, and M. W. Zwierlein, Phys. Rev. Lett. **118,** 123401 (2017).

[51] K. Hueck, N. Luick, L. Sobirey, J. Siegl, T. Lompe, and H. Moritz, Phys. Rev. Lett. **120,** 060402 (2018).

[52] See Supplemental Material at http://link.aps.org/supplemental/10.1103/PhysRevLett.122.203402 for further information, which includes Refs. [53–56].

[53] L. N. Cooper, Phys. Rev. **104,** 1189 (1956).

[54] M. Y. Veillette, D. E. Sheehy, and L. Radzihovsky, Phys. Rev. A **75,** 043614 (2007).

[55] L. Pisani, P. Pieri, and G. C. Strinati, Phys. Rev. B **98,** 104507 (2018).

[56] M. Naraschewski and D. M. Stamper-Kurn, Phys. Rev. A **58,** 2423 (1998).

[57] Z. Yan, P. B. Patel, B. Mukherjee, R. J. Fletcher, J. Struck, and M. W. Zwierlein, Phys. Rev. Lett. **122,** 093401 (2019).

[58] T.-L. Ho and E. J. Mueller, Phys. Rev. Lett. **92,** 160404 (2004).

[59] R. J. Fletcher, R. Lopes, J. Man, N. Navon, R. P. Smith, M. W. Zwierlein, and Z. Hadzibabic, Science **355,** 377 (2017).

[60] M. Sun and X. Leyronas, Phys. Rev. A **92,** 053611 (2015).

[61] P. Nozières and S. Schmitt-Rink, J. Low Temp. Phys. **59,** 195 (1985).

[62] S. Nascimbène, N. Navon, K. J. Jiang, F. Chevy, and C. Salomon, Nature (London) **463,** 1057 (2010).

[63] P. Nozieres and D. Pines, *The Theory of Quantum Liquids, Vol I: Normal Fermi Liquids*, 1st ed. (W.A. Benjamin, New York, 1966).

[64] E. Braaten, D. Kang, and L. Platter, Phys. Rev. Lett. **104,** 223004 (2010).

[65] J. E. Drut, T. A. Lähde, and T. Ten, Phys. Rev. Lett. **106,** 205302 (2011).

[66] S. Laurent, M. Pierce, M. Delehaye, T. Yefsah, F. Chevy, and C. Salomon, Phys. Rev. Lett. **118,** 103403 (2017).

[67] Z. Yu, G. M. Bruun, and G. Baym, Phys. Rev. A **80,** 023615 (2009).

[68] M. Punk, P. T. Dumitrescu, and W. Zwerger, Phys. Rev. A **80,** 053605 (2009).

[69] A. Schirotzek, C.-H. Wu, A. Sommer, and M. W. Zwierlein, Phys. Rev. Lett. **102,** 230402 (2009).

[70] C. Carcy, S. Hoinka, M. G. Lingham, P. Dyke, C. C. N. Kuhn, H. Hu, and C. J. Vale, preceding Letter, Phys. Rev. Lett. **122,** 203401 (2019).

Supplemental Material:
Spectral response and contact of the unitary Fermi gas

Biswaroop Mukherjee,[1] Parth B. Patel,[1] Zhenjie Yan,[1]
Richard J. Fletcher,[1] Julian Struck,[1,2] and Martin W. Zwierlein[1]

[1] *MIT-Harvard Center for Ultracold Atoms, Research Laboratory of Electronics, and Department*
of Physics, Massachusetts Institute of Technology, Cambridge, Massachusetts 02139, USA
[2] *Département de Physique, Ecole Normale Supérieure / PSL Research University, CNRS, 24 rue Lhomond, 75005 Paris, France*

DENSITY CALIBRATION IN THE HOMOGENEOUS TRAP

The density of atoms in the homogeneous trap is measured using *in situ* absorption imaging [S1]. The absolute atom numbers are calibrated by loading a spin-imbalanced gas into a hybrid trap that is axially harmonic and radially homogeneous [S2]. In Fig. S1, we plot the 1D density profile given by the integrated profile along the two homogeneous directions and the isothermal compressibility $\kappa/\kappa_0 = -\partial E_{\mathrm{F}\uparrow}/\partial U$ of the majority component, where $\kappa_0 = \frac{3}{2n_\uparrow E_F}$ is the compressibility of an ideal Fermi gas at density $n_\uparrow$. The compressibility in the spin-polarized region provides the calibration of our measurement of density.
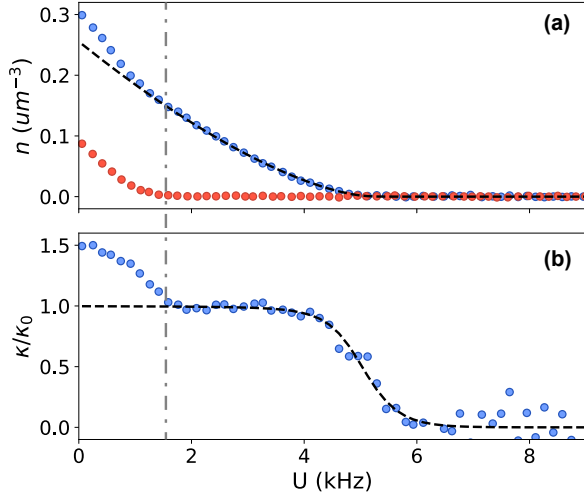
FIG. S1. Density calibration using the spin-imbalanced Fermi gas in the axially harmonic, radially homogeneous trap. Here, the majority Fermi energy is $E_{\mathrm{F}\uparrow}/h = 5.7(1)\,$kHz, $T/T_{\mathrm{F}\uparrow} = 0.05(1)$ and the imbalance is $N_\downarrow/N_\uparrow = 0.18$. (a) Majority (minority) density profiles in blue (red) data points. The dashed line is a fit to the ideal equation of state for the spin-polarized Fermi gas, restricted to the polarized wings of the cloud (outside the minority component edge, marked with the dot-dashed line). (b) The isothermal compressibility of the majority component as a function of position.

RF SPECTROSCOPY MEASUREMENTS

For rf spectroscopy measurements, two images are taken within several μs of each other. The first image records the transferred cloud in state $|f\rangle = |2\rangle$, while the second image allows for counting the number of atoms in the initial state $|\downarrow\rangle = |1\rangle$. For measurements of the full spectrum, the pulse time is set to $T_{\mathrm{Pulse}} = 1\,$ms, giving a Fourier-limited spectral resolution of 1 kHz. For measurements of the contact, we select a detuning that is large compared to both the Fermi energy and the temperature of the cloud. This ensures that atoms are transferred from the high-momentum tails, and the transfer rate accurately measures the contact. For detunings between $\hbar\omega \approx 5E_F$ and $\hbar\omega \approx 13E_F$, we verified that the measured value of $\tilde{C}$ is constant within statistical errors. The Rabi frequencies are adjusted between $\Omega_R = 2\pi \times 500$ Hz and $\Omega_R = 2\pi \times 1\,$kHz to maintain a high signal to noise ratio.

COOPER PROBLEM AT FINITE TEMPERATURE

In the Cooper problem [S3] one searches for the binding energy of two opposite-spin fermions on top of the filled Fermi sea. The Fermi sea is treated as "inert", its only role being to block momentum states that would otherwise be available to the scattering pair. This constraint alone already leads to pairing in three dimensions. Cooper's solution can be extended to non-zero temperature, in the search of a bound state on top of a finite temperature Fermi gas. A standard approach [S4] yields an equation for the bound state energy E_c for Cooper pairs:

$$-\frac{m}{4\pi\hbar^2 a} = \int \frac{\mathrm{d}^3 p}{(2\pi)^3} \left(\frac{(1 - n_F(\xi_p))^2}{2\xi_p - E_c} - \frac{1}{2\epsilon_p} \right), \quad \text{(S1)}$$

where $n_F(\epsilon) = (1 + \exp(\epsilon/T))^{-1}$ is the Fermi function, $\xi_p = \frac{p^2}{2m} - \mu$, and μ the chemical potential of the non-interacting Fermi gas at temperature T. The factor $(1 - n_F(\xi_p))^2$ represents Pauli blocking of momentum states already occupied in the spin up and the spin down Fermi sea. Without it, there would be no pairing of two

190

particles, as is well known in three dimensions. This simplest approach to pairing in a Fermi gas predicts a Cooper pair energy at resonance ($1/a = 0$) of $E_c = -0.61 E_F$ at zero temperature, and an onset of pairing ($E_c < 0$) at $T^*/T_F = 0.41 E_F$. To look for binding in the full many-body framework, one searches for poles of the pair propagator. In the lowest-order T-matrix calculation or equivalently to lowest order in a $1/N$ expansion [S5, S6] (where $2N$ is the number of spin components of the Fermi gas), one finds an equation for this pole that is nearly identical to the above:

$$-\frac{m}{4\pi\hbar^2 a} = \int \frac{\mathrm{d}^3 p}{(2\pi)^3} \left(\frac{(1-n_F(\xi_p))^2 - n_F(\xi_p)^2}{2\xi_p - E_c} - \frac{1}{2\epsilon_p} \right).$$
(S2)

Compared to the simple Cooper problem, the many-body approach yields an additional contribution to the integral from occupied momentum states $\propto -n_F(\xi_p)^2$ as fermions within the Fermi sea now also profit from pairing. This does not change the prediction for the $T = 0$ binding energy $E_c = -0.61 E_F$, but it yields stronger binding at finite temperature, and predicts an onset of pairing at $T^*/T_F = 0.5$. In the main text, we show E_c from this lowest-order many-body approach. As is well-known, fluctuations reduce the onset of superfluidity to lower T_c. The next order in the $1/N$ expansion yields [S5] $T_c/T_F = 0.14$, and the self-consistent T-matrix approach [S7] yields $T_c/T_F = 0.16$, in agreement with the experimental value $T_c/T_F = 0.167(13)$ [S8]. However, T^* is often interpreted as the crossover temperature scale for pair formation [S9], and the region between T_c and T^* is the putative "pseudogap" regime. For a recent analysis of pair correlations see [S10].

CONDENSATE FRACTION

The condensate fraction is measured by performing a momentum space mapping of the pair wavefunction. The atoms are released from the optical box potential into a magnetic harmonic trap with a confining trapping frequency $\omega_z = 2\pi \times 23$ Hz along the z-direction. Simultaneously, the bias field is rapidly ramped from the Feshbach resonance to a value near a zero crossing of the scattering length, which associates existing fermion pairs into bosonic molecules, and preserves the center of mass momentum. Assuming the resulting molecules are non-interacting, the density profile of the cloud after a quarter-period oscillation in the harmonic trap provides the pair center of mass momentum distribution [S2]. The measured integrated profiles $n_{1D}(z)$ are functions of the momentum $k_z = m\omega_z z/\hbar$ along the z direction (see Fig. S2). We fit the wings with the momentum distribution for a thermal gas of non-interacting bosons [S11]:

$$n_{1D}(k_z) = \frac{1}{(2\pi k_B T)^{3/2}} g_{3/2}\left(e^{-|\hbar^2 k_z^2/2m - \mu|/k_B T} \right) \quad \text{(S3)}$$
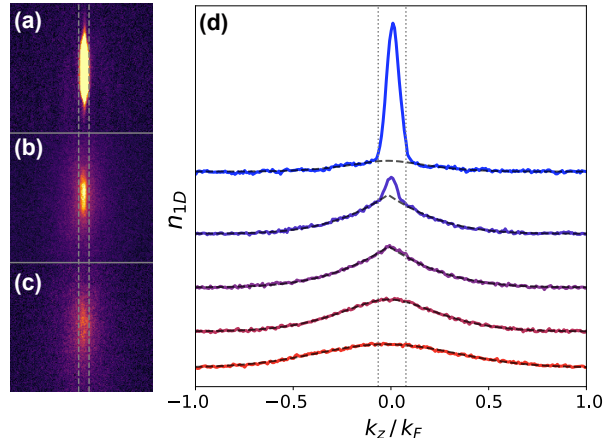
FIG. S2. Momentum space mapping of the box pair wavefunction. (a)-(c) Images of the cloud at $T/T_F = 0.13$ in (a), 0.16 in (b), and 0.18 in (c), after a quarter-period release along the horizontal direction. (d) From top to bottom, $T/T_F = 0.13$, 0.16, 0.18, 0.21, 0.43. Here, n_{1D} is the two-axis integrated pair center of mass momentum distribution, and the dashed black lines are polylogarithm fits to the thermal wings. The dashed vertical lines in (a)-(c) and the dotted vertical lines in (d) mark the condensate region excluded from the fit ($\approx \pm 0.07 k_F$). Here, k_F is the Fermi wavevector in the uniform trap.

As the gas is cooled, the profiles display an increased occupation near zero momentum, and at T_c, a clear condensate peak emerges. We define the condensate fraction N_0/N as the difference in area between the observed profile and the fit to the thermal wings.

[S1] Z. Yan, P. B. Patel, B. Mukherjee, R. J. Fletcher, J. Struck, and M. W. Zwierlein, (2018).

[S2] B. Mukherjee, Z. Yan, P. B. Patel, Z. Hadzibabic, T. Yefsah, J. Struck, and M. W. Zwierlein, Phys. Rev. Lett. **118**, 123401 (2017).

[S3] L. N. Cooper, Phys. Rev. **104**, 1189 (1956).

[S4] W. Ketterle and M. W. Zwierlein, *Ultra-cold Fermi Gases*, Proceedings of the International School of Physics Enrico Fermi, Course CLXIV, Varenna 2006, edited by M. Inguscio, W. Ketterle, and C. Salomon (IOS Press, Amsterdam, 2008) pp. 247–422.

[S5] P. Nikolic and S. Sachdev, Phys. Rev. A **75**, 033608 (2007).

[S6] M. Y. Veillette, D. E. Sheehy, and L. Radzihovsky, Phys. Rev. A **75**, 043614 (2007).

[S7] W. Zwerger, *Proceedings of the International School of Physics "Enrico Fermi" - Course 191 "Quantum Matter at Ultralow Temperatures"*, edited by M. Inguscio, W. Ketterle, S. Stringari, and G. Roati (IOS Press, Amsterdam; SIF Bologna, 2016) pp. 63–142.

[S8] M. J. H. Ku, A. T. Sommer, L. W. Cheuk, and M. W. Zwierlein, Science **335**, 563 (2012).

[S9] M. Randeria and E. Taylor, Annual Review of Condensed Matter Physics **5**, 209 (2014).

[S10] L. Pisani, P. Pieri, and G. C. Strinati, Phys. Rev. B **98**, 104507 (2018).

[S11] M. Naraschewski and D. M. Stamper-Kurn, Phys. Rev. A **58**, 2423 (1998).

Appendix F

Crystallization of Bosonic Quantum Hall States in a Rotating Quantum Gas

This appendix contains a reprint of the following paper, in press at Nature, to be published in 2022 :

B. Mukherjee, A. Shaffer, P. B Patel, Z. Yan, C. C Wilson, V. Crépel, R. J. Fletcher, M. W. Zwierlein, "Crystallization of Bosonic Quantum Hall States," arXiv:2106.11300 (2021) [101]

Crystallization of Bosonic Quantum Hall States in a Rotating Quantum Gas

Biswaroop Mukherjee, Airlia Shaffer, Parth B. Patel, Zhenjie Yan,

Cedric C. Wilson, Valentin Crépel, Richard J. Fletcher, Martin Zwierlein

MIT-Harvard Center for Ultracold Atoms, Research Laboratory of Electronics, and Department
of Physics, Massachusetts Institute of Technology, Cambridge, Massachusetts 02139, USA
(Dated: October 22, 2021)

The dominance of interactions over kinetic energy lies at the heart of strongly correlated quantum matter, from fractional quantum Hall liquids [1], to atoms in optical lattices [2] and twisted bilayer graphene [3]. Crystalline phases often compete with correlated quantum liquids, and transitions between them occur when the energy cost of forming a density wave approaches zero. A prime example occurs for electrons in high magnetic fields, where the instability of quantum Hall liquids towards a Wigner crystal [4–9] is heralded by a roton-like softening of density modulations at the magnetic length [7, 10–12]. Remarkably, interacting bosons in a gauge field are also expected to form analogous liquid and crystalline states [13–21]. However, combining interactions with strong synthetic magnetic fields has been a challenge for experiments on bosonic quantum gases [18, 21]. Here, we study the purely interaction-driven dynamics of a Landau gauge Bose-Einstein condensate [22] in and near the lowest Landau level (LLL). We observe a spontaneous crystallization driven by condensation of magneto-rotons [7, 10], excitations visible as density modulations at the magnetic length. Increasing the cloud density smoothly connects this behaviour to a quantum version of the Kelvin-Helmholtz hydrodynamic instability, driven by the sheared internal flow profile of the rapidly rotating condensate. At long times the condensate self-organizes into a persistent array of droplets, separated by vortex streets, which are stabilized by a balance of interactions and effective magnetic forces.

When electrons are placed in a magnetic field, their kinetic energy is quenched. The single particle states form discrete, highly degenerate Landau levels, and correspond to wavepackets localized to the magnetic length ℓ_B. In the presence of interactions between electrons, owing to the absence of kinetic energy, one naturally expects the formation of a Wigner crystal of periodicity $\sim \ell_B$ [4–6, 8, 9, 23]. Famously however, the interplay of the macroscopic degeneracy and interactions instead typically favours the strongly correlated fractional quantum Hall liquids, which host fractional charges, anyonic exchange statistics, and topologically protected transport properties [1]. The tendency to crystallize is still apparent in a pronounced minimum in the collective excitation spectrum at wavevectors $k \sim 1/\ell_B$ [7, 10–12]. In analogy with the roton minimum in ^{4}He, also considered a precursor of solidification [24], these excitations are called magneto-rotons [7, 11, 12].

The fate of interacting bosons in the presence of a gauge field is of fundamental importance in the classification of topological states of matter [19]. Quantum Hall states [13, 16, 20], exotic vortex lattices [14] and vortex-free states under extreme fields [17] were predicted. Quantum phase transitions between such states were found to be signaled by the softening of a roton-like collective mode [15, 25].

Bosonic quantum gases in artificial magnetic fields [18, 21] have been generated via spin-orbit coupling [21, 26, 27], phase imprinting in lattices [28–32], and by rotation of the trapped gas [16, 22, 33, 34]. The latter approach uses the analogy between the Lorentz force on a charged particle in a magnetic field, and the Coriolis force on a massive particle in a frame rotating at frequency Ω, giving $\omega_c = 2\Omega$ and $\ell_B = \sqrt{\hbar/(m\omega_c)}$ as the rotational analog of the cyclotron frequency and the magnetic length, respectively.

Signatures of physics near the lowest Landau level have been observed in rotating Bose gases [33, 34]. In recent work at MIT, condensates have been prepared directly in the lowest Landau gauge wavefunction using geometric squeezing [22]. In this mean-field quantum Hall regime [13], all bosons occupy a single wavefunction, whose subsequent dynamics subject to a gauge field can be studied, offering a microscopic insight into the individual building blocks of quantum Hall systems. An advantage of rotation is that the interactions between atoms are decoupled from the induced gauge potential, in contrast to other methods for which the effective magnetic field appears within a dressed-atom picture, leading to additional unwanted interaction terms [35].

Here, we directly observe the evolution of an interacting Bose-Einstein condensate occupying a single Landau gauge wavefunction in the LLL. We find that the Landau gauge condensate is unstable under the influence of interactions, exhibiting spontaneous growth of a snaking mode leading to a persistent density wave order at the magnetic length ℓ_B as illustrated in Fig. 1. At the heart of this crystallization is the coupling between the relative momentum and spatial overlap of two particles in a gauge field. This lowers the interaction energy cost of populating higher-momentum states, and leads to the dynamical instability of the lowest (Goldstone) collective excitation branch [15, 36]. The ensuing proliferation of excitations at momenta near $\hbar/l_B$ can be viewed as condensation of magneto-rotons, in analogy to the Wigner crystal instability of quantum Hall systems [4–9].

Condensation at non-zero momentum has been predicted in superfluid helium above a critical velocity [37–39]. Roton-like excitations and instabilities in Bose-Einstein condensates were induced via cavity mediated interactions [40, 41], spin-

orbit coupling [42, 43], shaken optical lattices [44, 45], driven interactions [46] and dipolar interactions [47–49]. These instabilities were tightly connected to evidence for supersolidity, the simultaneous existence of spatial and superfluid order [39, 41, 43, 50–52]. In our case, the instability to density-wave order arises purely from the interplay of contact interactions and a gauge field. No external drive is present, nor is there any residual scalar potential in the rotating frame. The absence of kinetic energy in the LLL directly implies that the crystallization rate is set solely by the interaction energy of the gas.

By increasing the condensate density such that many Landau levels become populated, we observe a crossover from LLL behaviour to a hydrodynamic instability driven by the sheared internal velocity profile. Analogous phenomena are ubiquitous throughout hydrodynamics, from the diocotron instability in charged plasmas [53] and fragmentation of electron beams [54], to the Kelvin-Helmholtz instability in atmospheric and astrophysical systems [55, 56]. In the context of superfluids, for which the circulation is quantized, the Kelvin-Helmholtz instability has been detected in liquid helium [57], and theoretically predicted at the boundary between counter-flowing condensates [58]. In our superfluid hydrodynamic setting, we directly observe streets of quantized vortices separating emergent droplets, revealing the quantum nature of the instability at the most microscopic level.

To analyze the instability, consider the condensate in the frame rotating at the frequency ω of the isotropic harmonic trap, where it experiences a synthetic magnetic field but no scalar potential (see Fig. 1a,b), and thus evolves under the Hamiltonian

$$\hat{H} = \int \mathrm{d}^2 r\, \hat{\Psi}^\dagger \left[\frac{(\hat{\mathbf{p}} - q\mathbf{A})^2}{2m} + \frac{g}{2} \hat{\Psi}^\dagger \hat{\Psi} \right] \hat{\Psi}. \quad (1)$$

Here $\hat{\Psi}^\dagger(\mathbf{r})$ is the bosonic field operator, $\hat{\mathbf{p}}$ is the canonical momentum, q and $\mathbf{A}$ are the charge and vector potential in the equivalent magnetic problem, and g is the two-dimensional mean-field coupling constant. Geometric squeezing prepares a translationally-invariant condensate most conveniently described within the Landau gauge $q\mathbf{A} = (0, m\omega_c x)$ [22] for which the Hamiltonian becomes

$$\hat{H} = \int \mathrm{d}^2 r\, \hat{\Psi}^\dagger \left[\frac{\hat{p}_x^2}{2m} + \frac{1}{2} m\omega_c^2 \left(\hat{x} - \frac{\hat{p}_y \ell_B^2}{\hbar} \right)^2 + \frac{g}{2} \hat{\Psi}^\dagger \hat{\Psi} \right] \hat{\Psi}. \quad (2)$$

Cyclotron motion of the atoms is reflected in an effective harmonic oscillator along the x-direction of frequency $\omega_c = 2\omega$, whose non-interacting energy states correspond to different Landau levels (see Fig. 1b). Each level is macroscopically degenerate since it costs no energy to translate the centers of cyclotron orbits. Initially, the y-momentum of all atoms is zero, and their cyclotron motion centred at $x = 0$ with a two-dimensional number density $n_{2\mathrm{D}}(x)$. The condensate has uniform phase and thus features a sheared velocity profile

$\mathbf{v} = -q\mathbf{A}/m = (0, -\omega_c x)$ proportional to the vector potential (see Fig. 1c). We parameterize the crossover from LLL to hydrodynamic behaviour by the ratio $\frac{gn}{\hbar\omega_c}$ of the condensate's mean-field energy $\sim gn$ to the Landau level spacing $\hbar\omega_c$, giving a measure for the number of occupied Landau levels [22, 33]. Here $n = n_{2\mathrm{D}}(0)$ is the peak density. In our experiment $\frac{gn}{\hbar\omega_c}$ varies from 0.6 to 7.3, corresponding to a central filling fraction $n\ell_B^2$ of 50 and higher, meaning the condensate lies within the mean-field quantum Hall regime [13, 16].

The dynamical instability illustrated in Fig. 1 can be understood in the low- and high-density limits as follows. When $gn \lesssim \hbar\omega_c$, the condensate is restricted to the LLL and shows a Gaussian transverse density profile with a $1/e$ radius of ℓ_B [22, 36]. A Bogoliubov analysis around this state generically results in a Hamiltonian of the form [15]

$$\hat{H}_{\mathrm{LLL}} = \sum_{k>0} A_k \left(\hat{a}_k^\dagger \hat{a}_k + \hat{a}_{-k}^\dagger \hat{a}_{-k} \right) + B_k \left(\hat{a}_k^\dagger \hat{a}_{-k}^\dagger + \hat{a}_k \hat{a}_{-k} \right), \quad (3)$$

where $\hat{a}_k$ is the annihilation operator for a particle with momentum $\hbar k$ along the y-direction. This Hamiltonian describes pairs of modes $\pm k$, with natural frequency $A_k/\hbar$ and coupled by a pair-creation operator of strength B_k which corresponds to a two-mode squeezing interaction in the language of quantum optics. In a non-rotating uniform condensate, $A_k = \frac{\hbar^2 k^2}{2m} + gn$ and $B_k = gn$ [59] and hence pair-creation is always weaker than the mode energy, leading to stable excitations However, the effective magnetic field profoundly changes this picture. First, in the LLL there is no kinetic energy contribution to A_k. Second, as illustrated in Fig. 1c, the coupling between momentum and position means that states with $k \neq 0$ have a reduced overlap with the condensate and a correspondingly lower interaction energy. One finds [15] $A_k = gn \left[2\exp(-k^2\ell_B^2/2) - 1 \right]/\sqrt{2}$ and $B_k = gn \exp(-k^2\ell_B^2)/\sqrt{2}$, and the resulting dispersion $\varepsilon_k = \sqrt{|A_k|^2 - |B_k|^2}$ is shown in Fig. 1d. The spectrum is imaginary for an entire range of wavevectors $k > 0$ beyond the zero-energy Goldstone mode at $k = 0$, indicating dynamical instability of the Goldstone branch and correlated exponential growth of $\pm k$ pairs of these modes. Their interference with the $k = 0$ condensate results in a density modulation (see Fig. 1c). The fastest growth occurs at a wavevector $\sim 1/\ell_B$ giving a spatial modulation wavelength $\sim 2\pi$ times the magnetic length. This mode eventually becomes macroscopically occupied, corresponding to condensation of magneto-rotons and yielding a density modulation contrast of order unity. Crucially, since interactions provide the only energy scale in the LLL, the instability growth rate is determined purely by the interaction energy gn.

In the high-density limit where $gn \gg \hbar\omega_c$, a hydrodynamic description neglecting quantum pressure is valid. In this regime, the condensate initially exhibits a Thomas-Fermi density profile $n_{2\mathrm{D}} \propto 1 - x^2/R_{\mathrm{TF}}^2$ where $R_{\mathrm{TF}} = \sqrt{\frac{2gn}{m\omega_c^2}} = \sqrt{\frac{2gn}{\hbar\omega_c}} \ell_B$ [36, 60]. The Coriolis force $2m\mathbf{v} \times \boldsymbol{\Omega}$ on each fluid element resulting from the shear flow

$\mathbf{v} = (0, -\omega_c x)$ perfectly balances the local gradient of mean-field energy, resulting in an inhomogeneous equilibrium density despite the absence of any scalar potential. Our hydrodynamic stability analysis about this equilibrium state reveals a dynamical snaking instability of the cloud [36], in analogy to the Kelvin-Helmholtz instability of counterflow in fluid layers [55, 56], and the diocotron instability of charged plasmas and electron beams [53, 54]. The absence of quantum pressure means that the Thomas-Fermi radius and cyclotron frequency provide the only lengthscale and rate. Within the hydrodynamic analysis the instability develops at a wavevector set by the condensate width, as in the LLL, but at a density-independent rate $\propto \omega_c$ in striking qualitative contrast to the growth rate in the LLL.

From these arguments, for all condensate densities we anticipate an emergent density modulation with a lengthscale set by the width of the initial cloud. For a quantitative analysis, from our experimental images (see Fig. 1e) we obtain the static structure factor $S_k \equiv |n_k|^2/N$, where $n_k = \int \mathrm{d}y\, n_{1D}(y)\, e^{-iky}$ is the Fourier transform of the one-dimensional number density $n_{1D}(y)$ and $N = \int \mathrm{d}y\, n_{1D}(y)$ [48]. In Fig. 2a we show examples of S_k obtained once the density modulation has fully developed, which show a well-defined peak at a wavevector k_{max}. We attribute the much smaller secondary peak at $2k_{max}$ to the contiguous traces of condensate linking adjacent droplets. In Fig. 2c we show k_{max} as a function of the condensate density, which is parameterized by the ratio R/ℓ_B where R is the full-width-at-half-maximum of the initial cloud divided by $2\sqrt{\log 2}$. This normalization is chosen such that $R/\ell_B \to 1$ for vanishing gn, while in the high-density limit $R/\ell_B = \sqrt{gn/(\hbar\omega_c \log 2)}$. At all densities, we indeed find an instability lengthscale of order the cloud width, $k_{max} \sim 1/R$. The star indicates the LLL prediction $k_{max} = 0.98/\ell_B$ and the dashed line shows the hydrodynamic result $k_{max} = 0.95/R$ [36] neglecting quantum pressure. The solid line presents k_{max} that we obtain from a numerical solution of the Bogoliubov equations [36], showing excellent agreement with the data without any free parameters.

While the cloud width sets the instability lengthscale in both the LLL and hydrodynamic regimes, the growth rate shows qualitatively different behaviour. In Fig. 3a, we show S_k as a function of time for several different condensate densities. In addition to the decrease in the instability lengthscale at lower densities, we observe a concurrent reduction of the growth rate. At each wavevector we fit the time-evolution of the structure factor with the theoretically expected function $S_k(t) = A\cosh(2\Gamma t)$ [36], and extract the instability growth rate $\Gamma(k)$. This is reported in Fig. 3b, along with the imaginary component of the corresponding Bogoliubov spectrum which shows good agreement without any free parameters. We note that the experimental data also reveal some growth in S_k at higher wavevectors than the unstable region predicted by the linear Bogoliubov analysis. We attribute this to non-linear effects, and have performed numerical simulations of the Gross-Pitaevskii (GP) equation, finding that these exhibit

the same behaviour [36].

We capture the typical crystallization rate corresponding to a particular condensate density by the growth rate of the dominant instability, $\Gamma(k_{max})$, and in Fig. 3c plot this as a function of R/ℓ_B. When $R/\ell_B \gg 1$ the rate is density-independent and consistent with our hydrodynamic result $\Gamma = 0.14\,\omega_c$, shown by the dashed line. However, for lower interaction energies the gas enters the LLL where gn provides the only energy scale. We observe a concurrent slowing down of the instability, and the data approach the LLL prediction $\Gamma = 0.21 gn/\hbar$ indicated by a dotted line. At all densities, the data show good agreement with the rate obtained from our Bogoliubov analysis, reported as the solid line.

After its initial hyperbolic growth, S_k reaches a steady-state as shown in the inset of Fig. 3c. The emergent crystal is long-lived, with each droplet stabilized by a balance of the outward mean-field pressure and an inwards Coriolis force. This arises from the circulating flow within each droplet which is imposed by the gauge field, and is evident from vortices intersecting adjacent droplets (see Fig. 1e). The counterflow speed at the interface of two droplets of radius R is $\sim \omega_c R$, giving a gradient of $m\omega_c R/\hbar$ in the relative phase and a vortex spacing of $2\pi\ell_B^2/R$. Adjacent droplets are therefore separated by $\sim (R/\ell_B)^2$ vortices. In the limit of classical hydrodynamics this number is large and the quantization of circulation is irrelevant, while in the LLL adjacent droplets are separated by a single vortex [15].

While the dynamical instability drives the growth of a density modulation, the initial seeding of the unstable mode must arise from thermal or quantum fluctuations in the gas density at $t = 0$ [36]. Since the phase of these fluctuations is random, this results in spontaneous breaking of the initial translational symmetry of the condensate. In Fig. 4 we show the phase and visibility of the density modulation observed in different iterations of our experiment. To account for small fluctuations in the overall cloud position, we fit the one-dimensional density profile with a sinusoidal function modulated by a Gaussian envelope, and obtain the modulation phase ϕ relative to the centre-of-mass of the cloud. At all densities we find that the phase is uncorrelated between different experimental realizations, indicating spontaneous breaking of the initial translational symmetry.

The emergent crystallization observed here offers a pristine example of collective physics arising purely from the interplay of interparticle interactions and a gauge field. The steady state breaks both the $U(1)$ symmetry associated with the wavefunction's phase as well as translational symmetry and thus displays supersolid properties [39]. A natural immediate direction concerns the Goldstone mode associated with the spontaneous breaking of translational symmetry, corresponding to magneto-phonons in the droplet array [9]. This would be a remarkable instance of a propagating mode arising intrinsically from interactions, in the absence of any single-particle dynamics. While the densities in our experiment correspond to tens of atoms per flux quantum, our protocol can be straightforwardly extended to prepare clouds of lower filling fractions,

which are expected to host beyond-mean-field, strongly correlated bosonic quantum Hall states [13–17, 19, 20, 60].

---

[1] H. L. Stormer, D. C. Tsui, and A. C. Gossard, "The fractional quantum Hall effect," Rev. Mod. Phys. **71**, S298 (1999).

[2] I. Bloch, J. Dalibard, and W. Zwerger, "Many-body physics with ultracold gases," Rev. Mod. Phys **80**, 885 (2008).

[3] Y. Cao, V. Fatemi, S. Fang, K. Watanabe, T. Taniguchi, E. Kaxiras, and P. Jarillo-Herrero, "Unconventional superconductivity in magic-angle graphene superlattices," Nature **556**, 43–50 (2018).

[4] E. Wigner, "On the interaction of electrons in metals," Phys. Rev. **46**, 1002–1011 (1934).

[5] D. Yoshioka and H. Fukuyama, "Charge density wave state of two-dimensional electrons in strong magnetic fields," Journal of the Physical Society of Japan **47**, 394–402 (1979).

[6] P. K. Lam and S. M. Girvin, "Liquid-solid transition and the fractional quantum-Hall effect," Phys. Rev. B **30**, 473–475 (1984).

[7] S. M. Girvin, A. H. MacDonald, and P. M. Platzman, "Magneto-roton theory of collective excitations in the fractional quantum Hall effect," Phys. Rev. B **33**, 2481–2494 (1986).

[8] H. W. Jiang, R. L. Willett, H. L. Stormer, D. C. Tsui, L. N. Pfeiffer, and K. W. West, "Quantum liquid versus electron solid around ν=1/5 Landau-level filling," Phys. Rev. Lett. **65**, 633–636 (1990).

[9] J. Jang, B. M. Hunt, L. N. Pfeiffer, K. W. West, and R. C. Ashoori, "Sharp tunnelling resonance from the vibrations of an electronic Wigner crystal," Nature Physics **13**, 340–344 (2017).

[10] F. D. M. Haldane and E. H. Rezayi, "Finite-size studies of the incompressible state of the fractionally quantized Hall effect and its excitations," Phys. Rev. Lett. **54**, 237–240 (1985).

[11] A. Pinczuk, B. S. Dennis, L. N. Pfeiffer, and K. West, "Observation of collective excitations in the fractional quantum Hall effect," Phys. Rev. Lett. **70**, 3983–3986 (1993).

[12] I. V. Kukushkin, J. H. Smet, V. W. Scarola, V. Umansky, and K. von Klitzing, "Dispersion of the Excitations of Fractional Quantum Hall States," Science **324**, 1044–1047 (2009).

[13] T. L. Ho, "Bose–Einstein condensates with large number of vortices," Phys. Rev. Lett. **87**, 060403 (2001).

[14] M. Ö Oktel, "Vortex lattice of a Bose-Einstein condensate in a rotating anisotropic trap," Phys. Rev. A **69**, 023618 (2004).

[15] S. Sinha and G. V. Shlyapnikov, "Two-dimensional Bose–Einstein condensate under extreme rotation," Phys. Rev. Lett. **94**, 150401 (2005).

[16] N. R. Cooper, "Rapidly rotating atomic gases," Advances in Physics **57**, 539–616 (2008).

[17] A. Aftalion, X. Blanc, and N. Lerner, "Fast rotating condensates in an asymmetric harmonic trap," Phys. Rev. A **79**, 011603 (2009).

[18] J. Dalibard, F. Gerbier, G. Juzeliūnas, and P. Öhberg, "Colloquium: Artificial gauge potentials for neutral atoms," Rev. Mod. Phys. **83**, 1523–1543 (2011).

[19] X. Chen, Z.-C. Gu, Z.-X. Liu, and X.-G. Wen, "Symmetry-protected topological orders in interacting bosonic systems," Science **338**, 1604–1606 (2012).

[20] T. Senthil and M. Levin, "Integer quantum Hall effect for bosons," Phys. Rev. Lett. **110**, 046801 (2013).

[21] N. Goldman, G. Juzeliūnas, P. Öhberg, and I. B. Spielman, "Light-induced gauge fields for ultracold atoms," Reports on Progress in Physics **77**, 126401 (2014).

[22] R. J. Fletcher, A. Shaffer, C. C. Wilson, P. B. Patel, Z. Yan, V. Crépel, B. Mukherjee, and Martin W. Z. Zwierlein, "Geometric squeezing into the lowest Landau level," Science **372**, 1318–1322 (2021).

[23] D. C. Tsui, H. L. Stormer, and A. C. Gossard, "Two-dimensional magnetotransport in the extreme quantum limit," Phys. Rev. Lett. **48**, 1559–1562 (1982).

[24] P. Nozières, "Is the roton in superfluid ^{4}He the ghost of a Bragg spot?" Journal of Low Temperature Physics **137**, 45–67 (2004).

[25] T. Graß, P. Bienias, M. J. Gullans, R. Lundgren, J. Maciejko, and A. V. Gorshkov, "Fractional quantum Hall phases of bosons with tunable interactions: From the Laughlin liquid to a fractional Wigner crystal," Phys. Rev. Lett. **121**, 253403 (2018).

[26] V. Galitski and I. B. Spielman, "Spin–orbit coupling in quantum gases," Nature **494**, 49–54 (2013).

[27] T. Chalopin, T. Satoor, A. Evrard, V. Makhalov, J. Dalibard, R. Lopes, and S. Nascimbene, "Probing chiral edge dynamics and bulk topology of a synthetic Hall system," Nature Physics **16**, 1017–1021 (2020).

[28] J. Struck, C. Ölschläger, M. Weinberg, P. Hauke, J. Simonet, A. Eckardt, M. Lewenstein, K. Sengstock, and P. Windpassinger, "Tunable gauge potential for neutral and spinless particles in driven optical lattices," Phys. Rev. Lett. **108**, 225304 (2012).

[29] G. Jotzu, M. Messer, R. Desbuquois, M. Lebrat, T. Uehlinger, D. Greif, and T. Esslinger, "Experimental realization of the topological Haldane model with ultracold fermions," Nature **515**, 237–240 (2014).

[30] M. Aidelsburger, M. Lohse, C. Schweizer, M. Atala, J. T. Barreiro, S. Nascimbène, N. R. Cooper, I. Bloch, and N. Goldman, "Measuring the Chern number of Hofstadter bands with ultracold bosonic atoms," Nature Physics **11**, 162–166 (2015).

[31] B. K. Stuhl, H.-I. Lu, L. M. Aycock, D. Genkina, and I. B. Spielman, "Visualizing edge states with an atomic Bose gas in the quantum Hall regime," Science **349**, 1514–1518 (2015).

[32] M. Mancini, G. Pagano, G. Cappellini, L. Livi, M. Rider, J. Catani, C. Sias, P. Zoller, M. Inguscio, M. Dalmonte, and L. Fallani, "Observation of chiral edge states with neutral fermions in synthetic Hall ribbons," Science **349**, 1510–1513 (2015).

[33] V. Schweikhard, I. Coddington, P. Engels, V. P. Mogendorff, and E. A. Cornell, "Rapidly rotating Bose–Einstein condensates in and near the Lowest Landau Level," Phys. Rev. Lett. **92**, 040404 (2004).

[34] V. Bretin, S. Stock, Y. Seurin, and J. Dalibard, "Fast rotation of a Bose–Einstein condensate," Phys. Rev. Lett. **92**, 050403 (2004).

[35] M. Bukov, L. D'Alessio, and A. Polkovnikov, "Universal high-frequency behavior of periodically driven systems: from dynamical stabilization to Floquet engineering," Advances in Physics **64**, 139–226 (2015).

[36] See supplementary information.

[37] S V Iordanskiĭ and Lev P Pitaevskiĭ, "Bose condensation of moving rotons," Soviet Physics Uspekhi **23**, 317–318 (1980).

[38] L P Pitaevskii, "Layered structure of superfluid ^{4}He with super-critical motion," JETP Letters **39**, 511–514 (1984).

[39] G. I. Martone, A. Recati, and N. Pavloff, "Supersolidity of cnoidal waves in an ultracold Bose gas," Phys. Rev. Research **3**, 013143 (2021).

[40] R. Mottl, F. Brennecke, K. Baumann, R. Landig, T. Donner, and T. Esslinger, "Roton-Type Mode Softening in a Quantum Gas with Cavity-Mediated Long-Range Interactions," Science **336**, 1570–1573 (2012).

[41] J. Léonard, A. Morales, P. Zupancic, T. Esslinger, and T. Donner, "Supersolid formation in a quantum gas breaking a continu-

ous translational symmetry," Nature **543**, 87 (2017).

[42] S.-C. Ji, L. Zhang, X.-T. Xu, Z. Wu, Y. Deng, S. Chen, and J.-W. Pan, "Softening of roton and phonon modes in a Bose-Einstein condensate with spin-orbit coupling," Phys. Rev. Lett. **114**, 105301 (2015).

[43] J.-R. Li, J. Lee, W. Huang, S. Burchesky, B. Shteynas, F. Top, A. O J., and W. Ketterle, "A stripe phase with supersolid properties in spin-orbit-coupled Bose-Einstein condensates," Nature **543**, 91 (2017).

[44] L.-C. Ha, L. W. Clark, C. V. Parker, B. M. Anderson, and C. Chin, "Roton-maxon excitation spectrum of Bose condensates in a shaken optical lattice," Phys. Rev. Lett. **114**, 055301 (2015).

[45] L. Feng, L. W Clark, A. Gaj, and C. Chin, "Coherent inflationary dynamics for Bose-Einstein condensates crossing a quantum critical point," Nature Physics **14**, 269–272 (2018).

[46] Z. Zhang, K.-X. Yao, L. Feng, J. Hu, and C. Chin, "Pattern formation in a driven Bose–Einstein condensate," Nature Physics **16**, 652–656 (2020).

[47] D. Petter, G. Natale, R. M. W. van Bijnen, A. Patscheider, M. J. Mark, L. Chomaz, and F. Ferlaino, "Probing the roton excitation spectrum of a stable dipolar Bose gas," Phys. Rev. Lett. **122**, 183401 (2019).

[48] J. Hertkorn, J.-N. Schmidt, F. Böttcher, M. Guo, M. Schmidt, K. S. H. Ng, S. D. Graham, H. P. Büchler, T. Langen, M. Zwierlein, and T. Pfau, "Density fluctuations across the superfluid-supersolid phase transition in a dipolar quantum gas," Phys. Rev. X **11**, 011037 (2021).

[49] J.-N. Schmidt, J. Hertkorn, M. Guo, F. Böttcher, M. Schmidt, K. S. H. Ng, S. D. Graham, T. Langen, M. Zwierlein, and T. Pfau, "Roton excitations in an oblate dipolar quantum gas," Phys. Rev. Lett. **126**, 193002 (2021).

[50] M. Guo, F. Böttcher, J. Hertkorn, J.-N. Schmidt, M. Wenzel, H. P. Büchler, T. Langen, and T. Pfau, "The low-energy Goldstone mode in a trapped dipolar supersolid," Nature **574**, 386–389 (2019).

[51] L. Tanzi, S. M. Roccuzzo, E. Lucioni, F. Famà, A. Fioretti, C. Gabbanini, G. Modugno, A. Recati, and S. Stringari, "Supersolid symmetry breaking from compressional oscillations in a dipolar quantum gas," Nature **574**, 382–385 (2019).

[52] L Chomaz, D Petter, P Ilzhöfer, G Natale, A Trautmann, C Politi, G Durastante, R M W van Bijnen, A Patscheider, M Sohmen, M J Mark, and F Ferlaino, "Long-Lived and Transient Supersolid Behaviors in Dipolar Quantum Gases," Phys. Rev. X **9**, 21012 (2019).

[53] R. C. Davidson, H.-W. Chan, C. Chen, and S. Lund, "Equilibrium and stability properties of intense non-neutral electron flow," Rev. Mod. Phys. **63**, 341–374 (1991).

[54] A. J. Cerfon, "Vortex dynamics and shear-layer instability in high-intensity cyclotrons," Phys. Rev. Lett. **116**, 174801 (2016).

[55] S. C. Chandrasekhar, *Hydrodynamic and hydromagnetic stability* (Clarendon Press, Oxford, 1961).

[56] L. D. Landau and E. M. Lifshitz, *Fluid Mechanics* (Pergamon Press, New York, 1987).

[57] A. P. Finne, V. B. Eltsov, R. Hänninen, N. B. Kopnin, J. Kopu, M. Krusius, M. Tsubota, and G. E. Volovik, "Dynamics of vortices and interfaces in superfluid ^{3}He," Reports on Progress in Physics **69**, 3157–3230 (2006).

[58] A. W. Baggaley and N. G. Parker, "Kelvin-Helmholtz instability in a single-component atomic superfluid," Phys. Rev. A **97**, 053608 (2018).

[59] A. L. Fetter and J. D. Walecka, *Quantum Theory of Many-Particle Systems* (McGraw-Hill, New York, 1971).

[60] A. Recati, F. Zambelli, and S. Stringari, "Overcritical rotation of a trapped Bose–Einstein condensate," Phys. Rev. Lett. **86**, 377 (2001).

Methods

Preparation of Landau gauge condensates We prepare condensates occupying a single Landau gauge wavefunction using the geometric squeezing protocol described in [22]. We begin with a condensate of $8.1(1) \times 10^5$ atoms of ^{23}Na in an elliptical time-orbiting-potential (TOP) trap [61], with a rms radial frequency $\omega = 2\pi \times 88.6(1)$ Hz, ellipticity $0.125(4)$, and axial frequency $2.8\,\omega$. We then rotate the ellipticity of the trap, ramping the rotation frequency from zero to ω. In the rotating frame, atoms experience both a synthetic magnetic field and a scalar saddle potential. Isopotential flow on this saddle, in analogy to the $\mathbf{E} \times \mathbf{B}$ Hall drift of electromagnetism, leads to elongation and contraction of the condensate along orthogonal directions and effecting unitary squeezing of the atomic density distribution [22]. We then turn off the saddle potential by setting the trap ellipticity to zero, which halts the outward flow of atoms. This results in an equilibrium, quasi-translationally-invariant condensate freely rotating at ω, which we allow to evolve for a variable time t. Finally, we obtain an absorption image of the in situ density distribution.

Imaging setup Our imaging resolution is sufficient to observe vortices in situ with a contrast of $\sim 60\%$ [22]. In the Thomas-Fermi regime, these have a characteristic size set by the healing length, which is ~ 300 nm in our system. This is significantly smaller than the quantum-mechanical ground state size of cyclotron orbits, set by the rotational analog of the magnetic length, $\ell_B = \sqrt{\hbar/(2m\omega)} = 1.6\ \mu$m.

Coupling constant Given interaction energies close to the LLL, the axial motion at frequency $2.8\,\omega$ is predominantly in its ground state. The coupling constant is then $g = \frac{4\pi\hbar^2 a}{m}\int dz\,|\phi(z)|^4$, where a is the three-dimensional s-wave scattering length, and $\phi(z)$ is the axial wavefunction with normalization $\int dz\,|\phi(z)|^2 = 1$.

Stability analysis To theoretically investigate the crystallization process, we perform a stability analysis of the initial Landau gauge condensate. In the Thomas-Fermi limit, we may neglect the quantum pressure term in the superfluid hydrodynamic equations. We linearize the equations about the original unperturbed condensate [62], and find an exact analytical solution for the density and the velocity perturbations in terms of the Heun function [63]. The initial counterflow leads to an instability of Kelvin-Helmholtz type, and the analysis displays a dynamical instability with a most critical wavevector at $k_{\max} = 1.12/R_{\mathrm{TF}} = 0.95/R$ and a rate $\Gamma = 0.14\,\omega_c$. To treat the entire region from the LLL to the Thomas-Fermi regime, we perform a numerical Bogoliubov analysis. In the LLL limit, the crystallization growth rate is given by $\Gamma = 0.21\,gn/\hbar$, and the most critical wavevector is $k_{\max} \to 0.981/\ell_B$. The Bogoliubov analysis shows that the growth rate of the dominant wavevector evolves smoothly from being interaction dominated ($\Gamma \sim 0.21\,gn/\hbar$) in the LLL regime, to being set by the cyclotron frequency ($\Gamma \sim \omega_c$) in

the Thomas-Fermi regime. Further details are provided in the supplementary information.

Gross-Pitaevskii simulation To provide insight into the crystallization dynamics beyond what can be captured in the linear stability analysis, we perform a numerical simulation of our experiment based upon the Gross-Pitaevskii (GP) equation. Within a single-mode approximation, the condensate wavefunction $\psi(\mathbf{r}, t)$ evolves in the rotating frame as,

$$i\hbar\frac{\partial}{\partial t}\psi = \left[\frac{-\hbar^2\nabla^2}{2m} + V + g|\psi|^2 - \mathbf{\Omega} \cdot \mathbf{L}\right]\psi. \quad (4)$$

Here, m denotes the atomic mass of ^{23}Na, $g = \sqrt{8\pi}\frac{\hbar^2 a_s}{m l_z}$ is the two-dimensional mean-field coupling constant, $a_s = 3.3$ nm is the scattering length, $l_z = \sqrt{\frac{\hbar}{m\omega_z}}$ is the harmonic oscillator length of the axial trap, $\omega_z = 2.8\,\omega$ is the trap frequency in the z-direction, $\omega = 2\pi \times 88.6$ Hz is the rms radial trap frequency, $\mathbf{\Omega} = \Omega(t)\hat{z}$ is the angular velocity, $\mathbf{L}$ is the angular momentum operator, and V is a complex scalar potential. The real part $\mathrm{Re}(V) = \frac{1}{2}m\omega^2[(1+\varepsilon)x^2 + (1-\varepsilon)y^2]$ is the radial trapping potential with ellipticity ε, while the imaginary part $\mathrm{Im}(V) \propto 1 + \mathrm{erf}[(r - R_\infty)/\sigma)]$ serves as an absorbing circular boundary. The absorbing radius R_∞ is chosen to be much larger than the transverse size of the condensate, and we use a wall thickness $\sigma = R_\infty/10$. We implement the evolution of Eq. (4) on a square grid using the time-splitting spectral method [64] and accelerate the simulation by performing the bulk of the computation on a graphics processing unit (GPU).

The simulated experimental sequence is identical to the experiment. We first perform geometric squeezing of an initially circular condensate [22], before setting the trap ellipticity $\varepsilon \to 0$ after which the condensate evolves freely for a time t in the rotating frame.

We find that without the explicit addition of noise, the condensate does not exhibit any instability except near the boundaries, due to residual edge effects not mitigated by the absorbing potential (see Extended Data Fig. 1a). On the other hand, seeding of the dynamical instability by the addition of gaussian phase noise at time $t = 0$ results in a very similar simulated evolution (Extended Data Fig. 1b) compared to the experiment (Extended Data Fig. 1c).

We perform an identical analysis procedure as in the experiment (see main text) on the simulated density profiles in order to obtain the structure factor $S_k(t)$, shown in Extended Data Figs. 1d-e, and the instability growth rate shown in Extended Data Fig. 1f. The red points show the experimental instability growth rate as a function of wavevector k, while the black line shows the prediction of our Bogoliubov analysis. For comparison, the blue line shows the rate extracted from the simulation, which captures the observed growth at higher wavevectors than the unstable range predicted by the Bogoliubov approach. This suggests that such growth can indeed be attributed to nonlinear effects, which are not captured by the perturbative Bogoliubov approach. In addition to oscillations in S_k at the cyclotron frequency ω_c, a slower modulation is

also observed. We attribute this oscillation to rotation of the individual droplets in the crystal.

In both experiment and simulation the emergent crystal is long-lived, persisting for $\omega_c t/(2\pi) > 20$. In the experiment the lifetime is only limited by the weak $\propto r^4$ anharmonicities in the trapping potential, leading to a slow S-shaped distortion of the linear crystal, similar to the Kerr effect on non-classical states in quantum optics.

Vortex detection and phase profile: In the rotating frame, each droplet exhibits an irrotational flow profile, with vortices surrounding the droplets. These vortices are directly visible in the experimental density image, and can be used to reconstruct the phase profile of the crystal in the rotating frame (see Extended Data Fig. 2(a, c, e)). The phase is determined by the locations of the vortices, which are assumed to each have a single unit of circulation $2\pi\hbar/m$. Most vortices are outside of the bulk of the condensate, making their detection challenging. Nevertheless, a numerical solution of the GP equation shows similarly located vortices (Extended Data Fig. 2d), as well as a similar irrotational flow profile in the rotating frame (Extended Data Fig. 2f).

[61] W. Petrich, M. H. Anderson, J. R. Ensher, and E. A. Cornell, "A stable, tightly confining magnetic trap for evaporative cooling of neutral atoms," Phys. Rev. Lett. **74**, 3352 (1995).

[62] S. Sinha and Y. Castin, "Dynamic instability of a rotating Bose-Einstein condensate," Phys. Rev. Lett. **87**, 190402 (2001).

[63] A. Ronveaux, ed., *Heun's Differential Equations* (Oxford University Press, New York, 1995).

[64] W. Bao and H. Wang, "An efficient and spectrally accurate numerical method for computing dynamics of rotating Bose-Einstein condensates," Journal of Computational Physics **217**, 612 – 626 (2006).
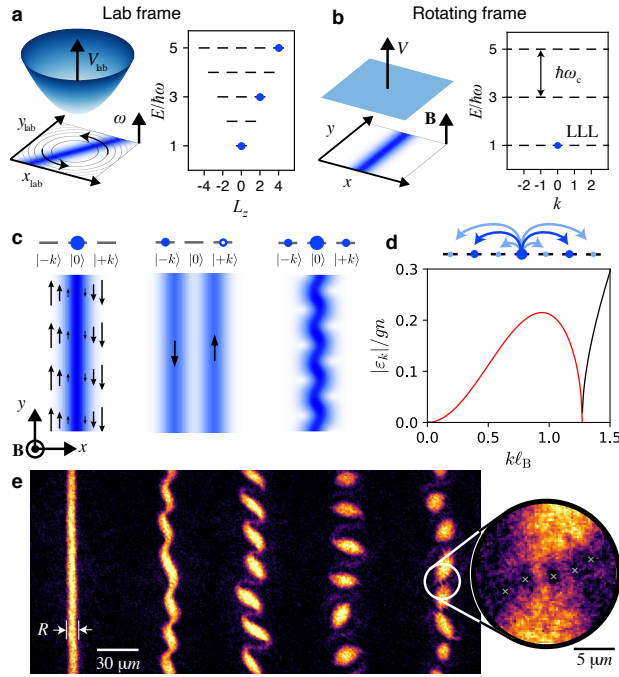
FIG. 1. **Spontaneous crystallization of an interacting Bose-Einstein condensate in an artificial magnetic field. (a)** In the laboratory frame, the condensate freely rotates in a circularly symmetric harmonic trap at the trapping frequency ω. Occupied states in the energy spectrum are sketched (L_z: angular momentum). **(b)** In the rotating frame, the condensate experiences an effective magnetic field B but no scalar potential. The energy spectrum is flattened into Landau levels (k: momentum along y). Only the $k = 0$ Landau gauge wavefunction is occupied. **(c)** The irrotationality of the condensate in the laboratory frame imposes a sheared velocity profile in the rotating frame which is dynamically unstable towards a periodic density modulation. Motion with momentum $\hbar k$ along the y-direction is tied to sideways displacement of the wavefunction along x. The reduced overlap of $|k| > 0$ states with the $k = 0$ condensate lowers the interaction energy cost of collective excitations, leading to spontaneous population of $\pm k$ pairs whose interference with the condensate results in a density modulation. **(d)** This dynamical instability is reflected in a (Goldstone) collective excitation branch which is imaginary across a range of wavevectors, shown by a red line. The spectrum shown is calculated for a condensate in the LLL, for which the interaction energy gn provides the only relevant energy scale and the magnetic length $\ell_B = 1.6\,\mu\text{m}$ sets the length scale. Here g is the mean-field coupling constant, and $n = n_{2\text{D}}(0)$ is the peak 2D density. **(e)** Absorption images of the evolution of the condensate density in the rotating frame, displaying a snake-like instability and the formation of droplet arrays. Here, the cloud width $R = 2.34\,\ell_B$, and the frames are taken at 0, 5, 6.2, 8.5, and 10 cyclotron periods ($2\pi/\omega_c = 5.6\,\text{ms}$). The zoom-in reveals vortex streets between adjacent droplets, indicating counterflow at their interface.
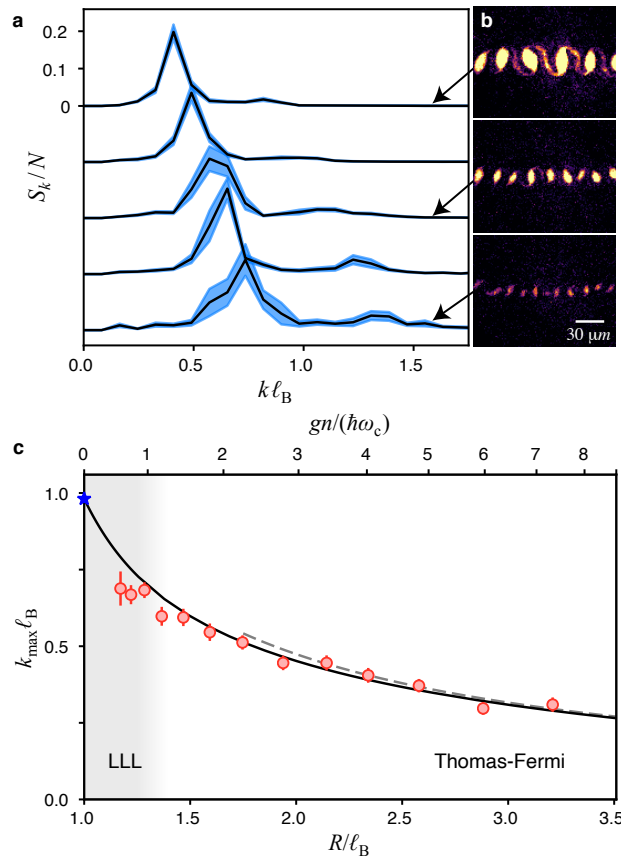
FIG. 2. **Structure factor and lengthscale of the emergent crystal. (a)** The static structure factor, S_k, measured once the density modulation has reached steady-state for condensates with initial widths $R/\ell_B = 2.58$, 1.75, 1.59, 1.28, and 1.22 (top to bottom). The prominent peak reflects the periodic modulation of the cloud density. **(b)** Corresponding images of the steady-state crystal, illustrating the decrease in the modulation lengthscale with falling condensate density. **(c)** Dependence of the dominant modulation wavevector, $k_{\max}$, on the cloud width, R/ℓ_B. The LLL and hydrodynamic results are indicated by the star and dashed line respectively (see text). The solid line shows the prediction of our Bogoliubov analysis [36], which shows excellent agreement with our data with no free parameters.
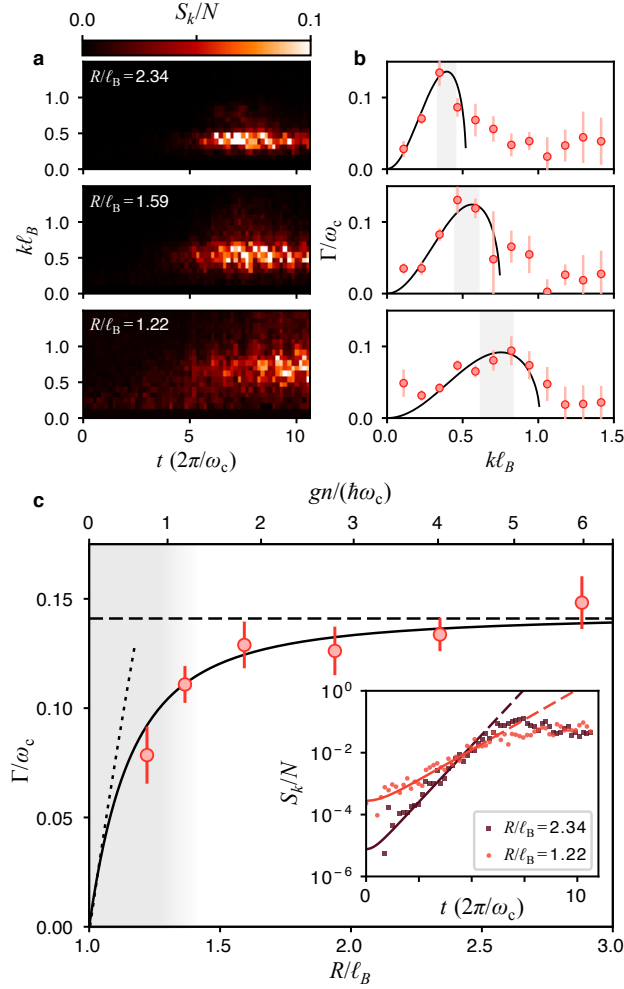
FIG. 3. **Instability growth dynamics.** (a) The temporal evolution of the static structure factor, $S_k(t)$, for condensates with different initial widths which reveals a density-dependence of both the modulation lengthscale and growth rate. (b) The measured instability growth rate, Γ, as a function of wavevector. The solid line shows the rate obtained from our Bogoliubov analysis [36] and captures the data well with no free parameters. (c) The instability growth rate at the dominant unstable wavevector shown as a function of the condensate width. The growth rate is obtained by averaging points from the shaded regions in (b). At high densities we find good agreement with the density-independent hydrodynamic rate $\Gamma = 0.14\,\omega_c$ (dashed line). As the density falls, we observe a crossover to the LLL scaling $\Gamma = 0.21gn/\hbar$ (dotted line). Solid line: Bogoliubov analysis [36]. The inset shows $S_k(t)$ at $k_{\max}$ for condensates in the hydrodynamic regime (dark red) and the LLL (light red), along with the corresponding fits used to extract the rate (see text).
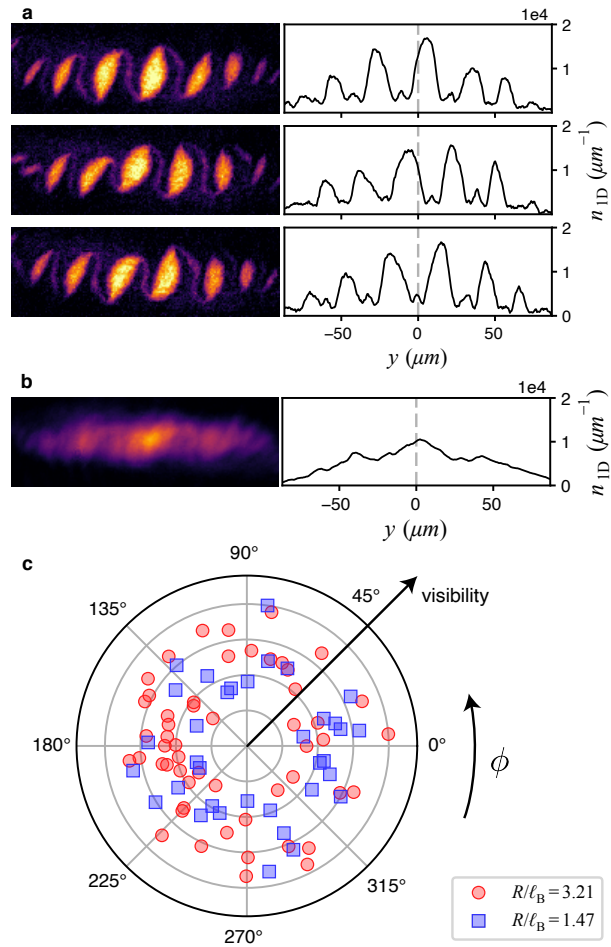
FIG. 4. **Spontaneous breaking of translational symmetry.** **(a)** Images of the emergent crystal in three experimental iterations, along with the integrated one-dimensional density profiles $n_{1D}(y)$. The vertical dashed line shows the position of the centre-of-mass of the cloud, relative to which the modulation phase is random. **(b)** An image of the cloud averaged over 60 iterations, in which the density modulation is no longer visible. **(c)** The phase, ϕ, and visibility of the density modulation measured for multiple iterations of the experiment, for two different initial condensate densities. The visibility appears largely independent of the phase chosen by the modulation. The phase is randomly distributed between 0 and 2π, indicating spontaneous breaking of the initial translational symmetry of the cloud.
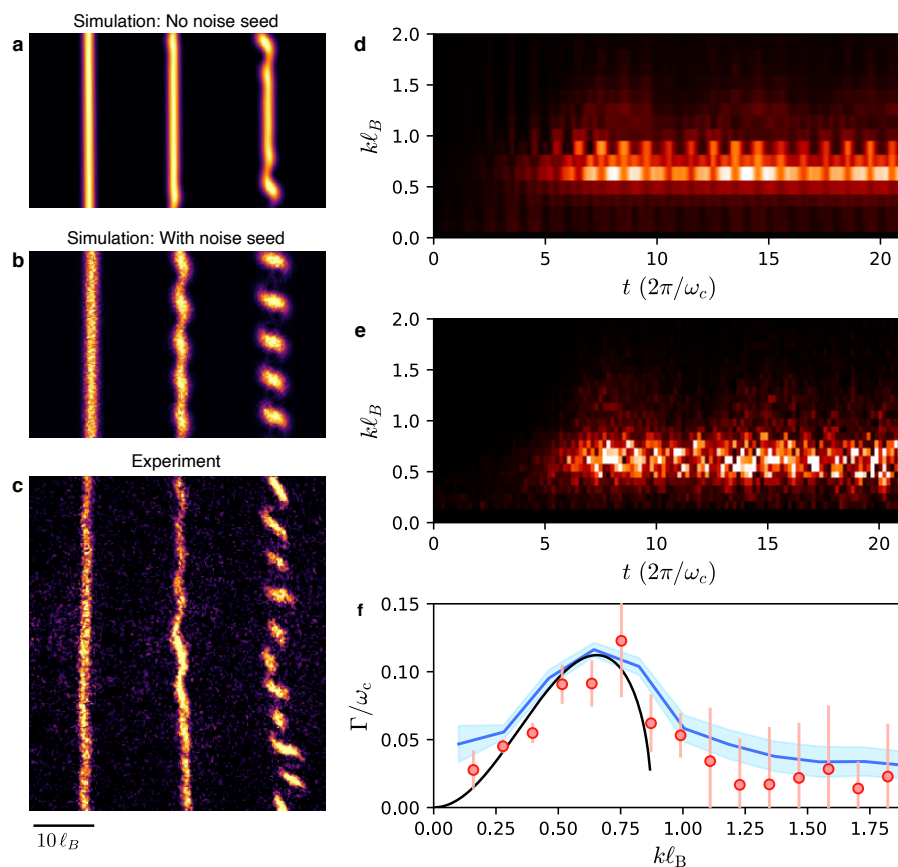
Extended Data Figure 1. **Numerical GP simulation of the condensate evolution in the rotating frame.** **(a-c)** Time evolution of the condensate density without the addition of noise (top), with added phase noise (middle), and in the experiment (bottom). The frames correspond to times $\omega_{\rm c} t/(2\pi) = 0$, 4, and 6. **(d-e)** Evolution of the structure factor $S_k(t)$ extracted from the simulation (d) and the experiment (e) which show good agreement. **(f)** The extracted instability growth rate as a function of wavevector k. The experimental measurements are shown by red points, and the Bogoliubov prediction by the black line. The blue line shows the result of the GP simulation. Here, the blue shading and the red error bars indicate 1σ standard error. This model captures the experimentally measured growth at wavevectors above the instability region provided by the linear Bogoliubov description.
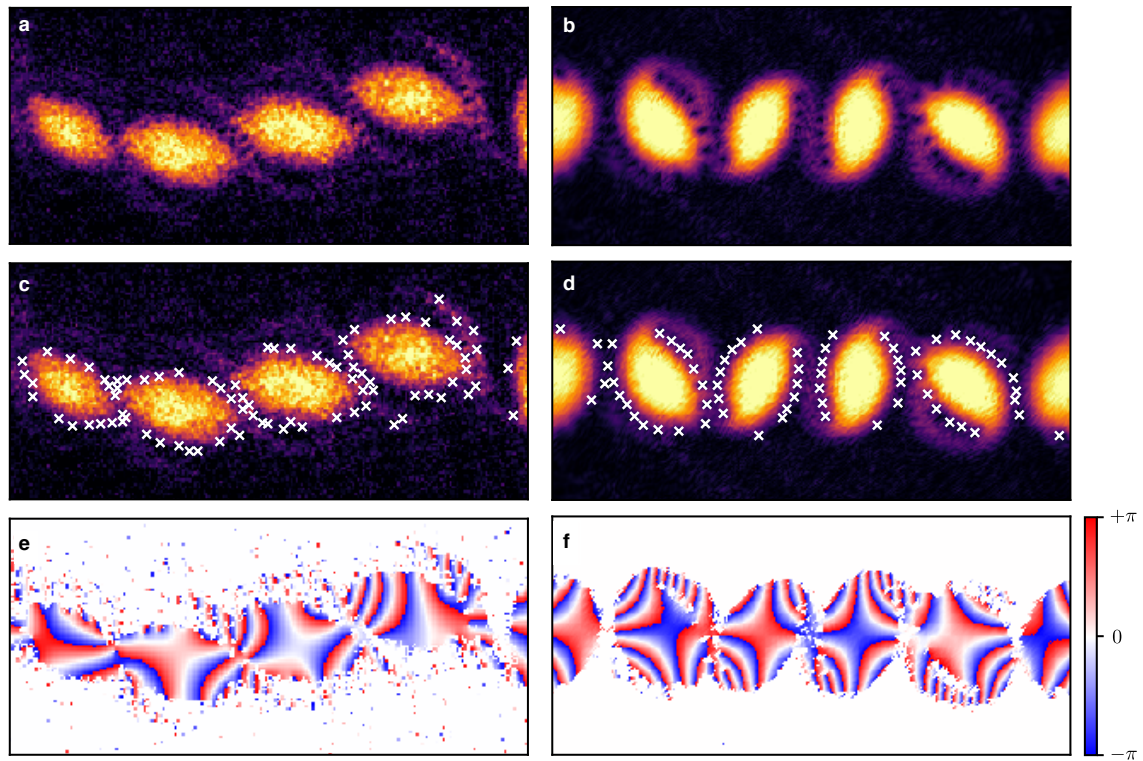
Extended Data Figure 2. **Phase profile of the crystal (a, b)** The density profiles of the crystals in the experiment (a) and GP simulation (b) appear to contain vortices which are marked in **(c, d)**. **(e)** The phase of the macroscopic wavefunction can be inferred from the locations of the vortices in the experimental image. Note that additional contributions from undetected vortices may exist. **(f)** The simulated phase profile from a GP simulation shows a similar structure of irrotational flow within each segment of the crystal. In both (e) and (f), the phase shown is in the rotating frame.

Crystallization of Bosonic Quantum Hall States in a Rotating Quantum Gas
Supplementary Information

Biswaroop Mukherjee, Airlia Shaffer, Parth B. Patel, Zhenjie Yan,
Cedric C. Wilson, Valentin Crépel, Richard J. Fletcher, Martin Zwierlein

*MIT-Harvard Center for Ultracold Atoms, Research Laboratory of Electronics, and Department
of Physics, Massachusetts Institute of Technology, Cambridge, Massachusetts 02139, USA*

BOGOLIUBOV STABILITY ANALYSIS OF LANDAU GAUGE CONDENSATES

A condensate prepared to have uniform phase in the Landau gauge - a "Landau gauge condensate" - is energetically unstable: an infinitely extended Bose gas has lower energy. However, in the absence of dissipation - as in the experiment - this does not itself lead to an instability. The question is whether the system is dynamically unstable, which would cause exponential growth of excitations and an isoenergetic transition into a new state. To search for dynamically unstable modes and to obtain their growth rate and spatial structure we perform a stability analysis of Landau gauge condensates via the Bogoliubov approach [1–3]. We expect the initial unmodulated condensate to be well-described within a single-mode framework, and expand the Hamiltonian in the Landau gauge, Eq. 2 of the main text, to second order in small fluctuations $\delta\hat{\psi}$ of the bosonic field $\hat{\Psi} = \psi_0 + \delta\hat{\psi}$ about the initial condensate wavefunction ψ_0 [1–3]. To ensure number conservation one employs the grand-canonical Hamiltonian $\hat{K} = \hat{H} - \mu\hat{N}$ with chemical potential μ:

$$\hat{K} = \hat{H} - \mu\hat{N} \approx \text{const.} + \int \mathrm{d}^2 r \, \delta\hat{\psi}^\dagger \left(\hat{h} - \mu_0 + 2g \left| \psi_0 \right|^2 \right) \delta\hat{\psi} + \frac{1}{2} g \int \mathrm{d}^2 r \left(\psi_0^{*2} \delta\hat{\psi} \, \delta\hat{\psi} + \delta\hat{\psi}^\dagger \delta\hat{\psi}^\dagger \psi_0^2 \right). \tag{1}$$

with the single-particle Hamiltonian in the Landau gauge $\hat{h} = \frac{\hat{p}_x^2}{2m} + \frac{1}{2} m\omega_c^2 \left(\hat{x} - \frac{\hat{p}_y l_B^2}{\hbar} \right)^2$ and the constant term a function of ψ_0. Terms first order in $\delta\hat{\psi}$ vanish if ψ_0 obeys the stationary Gross-Pitaevskii (GP) equation $\hat{h}\psi_0 + g \left| \psi_0 \right|^2 \psi_0 = \mu_0 \psi_0$. Since the initial wavefunction $\psi_0 = \psi_0(x)$ is translationally invariant along y, this reads

$$\left(-\frac{\hbar^2}{2m} \frac{\mathrm{d}^2}{\mathrm{d}x^2} + \frac{1}{2} m\omega_c^2 x^2 + g \left| \psi_0(x) \right|^2 \right) \psi_0(x) = \mu_0 \psi_0(x), \tag{2}$$

which is formally equivalent to the GP equation of a Bose-Einstein condensate in a one-dimensional harmonic oscillator (h.o.) potential of frequency ω_c. We solve Eq. 2 numerically via imaginary time evolution, choosing $\psi_0(x)$ to be real and normalized such that $\int \mathrm{d}x \left| \psi_0(x) \right|^2 = n_{1D}$, where n_{1D} is the initial one-dimensional number density. A dimensionless quantity measuring the interaction energy, relative to the cyclotron level spacing $\hbar\omega_c$, is $\tilde{g} \equiv \frac{g n_{1D}}{l_B \hbar\omega_c}$. Near the lowest Landau level, the interaction is a small perturbation, resulting in the gaussian density $\psi_0^2(x) = \frac{n_{1D}}{\sqrt{\pi} l_B} e^{-x^2/l_B^2}$ and $\mu_0 \approx \frac{\hbar\omega_c}{2} \left(1 + \sqrt{\frac{2}{\pi}} \tilde{g} \right)$, close to the ground-state cyclotron energy. In the Thomas-Fermi regime, where the term $\hat{p}_x^2/2m$ can be neglected, one obtains $g\psi_0^2(x) = \mu_0 - \frac{1}{2} m\omega_c^2 x^2$ with $\mu_0 = \frac{1}{2} \hbar\omega_c \left(\frac{3}{2} \tilde{g} \right)^{2/3}$.

Translation invariance of $\psi_0(x)$ and $\hat{h}$ along y allows expanding $\delta\hat{\psi} = \sum_k \frac{1}{\sqrt{L}} e^{iky} \hat{\phi}_k(x)$ into bosonic fields $\hat{\phi}_k(x)$ of well-defined y-momentum $\hbar k$, with L the spatial extent of the system in the y-direction. The quadratic part of Eq. 1 then becomes, using matrix notation,

$$\hat{K}_2 = \frac{1}{2} \sum_k \int \mathrm{d}x \left(\hat{\phi}_k^\dagger \ \hat{\phi}_{-k} \right) \begin{pmatrix} \hat{h}_k - \mu_0 + 2g\psi_0^2 & g\psi_0^2 \\ g\psi_0^2 & \hat{h}_{-k} - \mu_0 + 2g\psi_0^2 \end{pmatrix} \begin{pmatrix} \hat{\phi}_k \\ \hat{\phi}_{-k}^\dagger \end{pmatrix}$$

$$= \frac{1}{2} \sum_k \langle \hat{\boldsymbol{\Phi}}_k | \hat{\mathbf{H}}_k | \hat{\boldsymbol{\Phi}}_k \rangle \tag{3}$$

with $\hat{h}_k = \frac{\hat{p}_x^2}{2m} + \frac{1}{2} m\omega_c^2 \left(x - k l_B^2 \right)^2$, $\hat{\boldsymbol{\Phi}}_k = \left(\hat{\phi}_k \ \hat{\phi}_{-k}^\dagger \right)^{\mathrm{T}}$, $\hat{\mathbf{H}}_k(x)$ the 2×2 matrix operator of the first line in Eq. 3, and $\langle \mathbf{f} | \mathbf{g} \rangle = \int \mathrm{d}x \, \mathbf{f}^\dagger(x) \cdot \mathbf{g}(x)$ for vectors $\mathbf{f}, \mathbf{g}$. Momentum conservation along y ensures that allowed scattering processes result in either the simultaneous creation or simultaneous annihilation of a pair of states with momenta k and $-k$. Consequently the Hamiltonian only mixes a particle with y-momentum k with a hole of y-momentum $-k$, as is explicit in the 2×2 particle/hole matrix notation. The Bogoliubov Hamiltonian $\hat{\mathbf{H}}_k(x)$ in Eq. 3 is Hermitian, has only real eigenvalues (bounded from below

by $-\mu_0$) and thus $\hat{K}_2$ has only real expectation values in any state. However, the time evolution of the bosonic field operators $\hat{\phi}_k(x,t)$ evolving under the grand-canonical Hamiltonian $\hat{K}$ is given by $i\hbar\frac{\partial}{\partial t}\hat{\phi}_k = \left[\hat{\phi}_k, \hat{K}\right]$, and with the bosonic commutation relations $\left[\hat{\phi}_k(x), \hat{\phi}_{k'}^\dagger(x')\right] = \delta_{k,k'}\delta(x-x')$ we have

$$i\hbar\frac{\partial}{\partial t}\hat{\boldsymbol{\Phi}}_k = \begin{pmatrix} \hat{h}_k - \mu_0 + 2g\psi_0^2 & g\psi_0^2 \\ -g\psi_0^2 & -(\hat{h}_{-k} - \mu_0 + 2g\psi_0^2) \end{pmatrix} \hat{\boldsymbol{\Phi}}_k = \eta\hat{\mathbf{H}}_k\hat{\boldsymbol{\Phi}}_k \tag{4}$$

with $\eta = \begin{pmatrix} 1 & 0 \\ 0 & -1 \end{pmatrix}$ acting in particle-hole space [4, 5]. The evolution of the field operators is thus governed by an operator $\eta\hat{\mathbf{H}}_k$ that is in general *non*-Hermitian and can thus feature complex eigenvalues, leading to exponential growth of fluctuations - the system features dynamical instabilities [6].

Symmetries, eigenvectors and eigenvalues of $\eta\hat{\mathbf{H}}_k$

For each k, the Hamiltonian matrix $\hat{\mathbf{H}}_k$ is real, $\hat{\mathbf{H}}_k^* = \hat{\mathbf{H}}_k$, and symmetric under simultaneous reflection of space $\hat{R}$ (i.e. $\hat{R}x\hat{R} = -x$) and exchange of particles and holes, i.e. $\hat{\mathbf{H}}_k = \gamma\hat{R}\hat{\mathbf{H}}_k\hat{R}\gamma$ with $\gamma = \begin{pmatrix} 0 & 1 \\ 1 & 0 \end{pmatrix}$ exchanging particles and holes. It follows that given an eigenvector $\mathbf{V}_{k,n}$ of $\eta\hat{\mathbf{H}}_k$ with eigenvalue $\epsilon_{k,n}$, the vector $\mathbf{V}_{k,n}^*$ is also an eigenvector with eigenvalue $\epsilon_{k,n}^*$, and $\gamma\hat{R}\mathbf{V}_{k,n}$ and $\gamma\hat{R}\mathbf{V}_{k,n}^*$ are eigenvectors with eigenvalues $-\epsilon_{k,n}$ and $-\epsilon_{k,n}^*$, respectively. The latter follows from $\gamma\eta = -\eta\gamma$. We also note that $\hat{\mathbf{H}}_{-k} = \hat{R}\hat{\mathbf{H}}_k\hat{R}$ implying that $\hat{R}\mathbf{V}_{k,n} \equiv \mathbf{V}_{-k,n}$ is eigenvector of $\eta\hat{\mathbf{H}}_{-k}$ with eigenvalue $\epsilon_{-k,n} = \epsilon_{k,n}$. In general, the four values $\epsilon_{k,n}$, $\epsilon_{k,n}^*$, $-\epsilon_{k,n}$ and $-\epsilon_{k,n}^*$ are all different, implying an oscillatory evolution of exponentially increasing and decreasing amplitudes. The instability studied in the present work concerns the mode of lowest $|\epsilon_{k,n}|$ for given k, the Goldstone branch which we label by $n=0$. It is smoothly connected to the Goldstone mode at $k=0$ of zero frequency, $\epsilon_{0,0}=0$, that reflects the free choice of the overall phase of the condensate, i.e. its $U(1)$ symmetry. An associated second mode with zero eigenvalue of $(\eta\hat{\mathbf{H}}_0)^2$ describes the global phase fluctuations [7]. The next excited mode, $n=1$, is correlated near $k=0$ with the cyclotron oscillation. At $k=0$ the $n=1$ mode lies precisely at the cyclotron energy $\epsilon_{0,1} = \hbar\omega_c$, according to Kohn's theorem [8, 9]. The modes at $k>0$ of the Goldstone branch, connecting to the Goldstone density and phase modes at $k=0$, are thus well separated from any other excitations, so that this branch is described by only two, not four, distinct eigenvalues. This implies that either $\epsilon_{k,0} = \epsilon_{k,0}^*$, i.e. one has two real eigenvalues $\pm\epsilon_{k,0}$, or $\epsilon_{k,0} = -\epsilon_{k,0}^*$, i.e. one has two purely imaginary eigenvalues $\pm\epsilon_{k,0}$. For excitations of non-rotating condensates in their ground state, only the first case occurs and corresponds to the usual Bogoliubov phonon excitations. Here, instead, we find, in an entire range of momenta between $k=0$ and a maximum $k=k_c$, the case of purely imaginary frequencies $\epsilon_{k,0}$, corresponding to the exponential growth of correlated excitations at $\pm k$ that causes the "snake-like" dynamical instability. Results of the numerical solution of $\eta\hat{\mathbf{H}}_k\mathbf{V}_{k,n} = \epsilon_{k,n}\mathbf{V}_{k,n}$ are shown in Fig. 1, from deep in the lowest Landau level ($\tilde{g} \lesssim 1$) to the Thomas-Fermi regime ($\tilde{g} \gg 1$).

Relation between eigenvalues of $\hat{\mathbf{H}}_k$ and $\eta\hat{\mathbf{H}}_k$

The difference between stable and dynamically unstable excitations is analogous to the difference between the stable motion in a harmonic oscillator potential and the unstable motion of a particle in an inverted harmonic oscillator. The correspondence becomes explicit if we introduce the Hermitian operators $\hat{Q}_k(x) = \left(\hat{\phi}_k(x) + \hat{\phi}_k^\dagger(x)\right)/\sqrt{2}$ and $\hat{P}_k(x) = -i\left(\hat{\phi}_k(x) - \hat{\phi}_k^\dagger(x)\right)/\sqrt{2}$ obeying $\left[\hat{Q}_k(x), \hat{P}_{k'}(x')\right] = i\delta_{k,k'}\delta(x-x')$. They are related to the density and current fluctuations of the condensate, as the density operator is

$$\hat{n}(x,y) = \hat{\Psi}^\dagger\hat{\Psi} \approx |\psi_0|^2 + \psi_0(\delta\hat{\psi} + \delta\hat{\psi}^\dagger) = |\psi_0|^2 + \psi_0\sqrt{\frac{2}{L}}\sum_k \cos(ky)\hat{Q}_k(x) - \sin(ky)\hat{P}_k(x)$$

and $\hat{\mathbf{j}} \approx |\psi_0|^2\nabla\hat{\Theta}$ with the linear fluctuation part of the velocity potential operator [2]

$$\hat{\Theta} = \frac{\hbar}{2mi\psi_0}\left(\delta\hat{\psi} - \delta\hat{\psi}^\dagger\right) = \frac{\hbar}{2m\psi_0}\sqrt{\frac{2}{L}}\sum_k \cos(ky)\hat{P}_k(x) + \sin(ky)\hat{Q}_k(x)$$
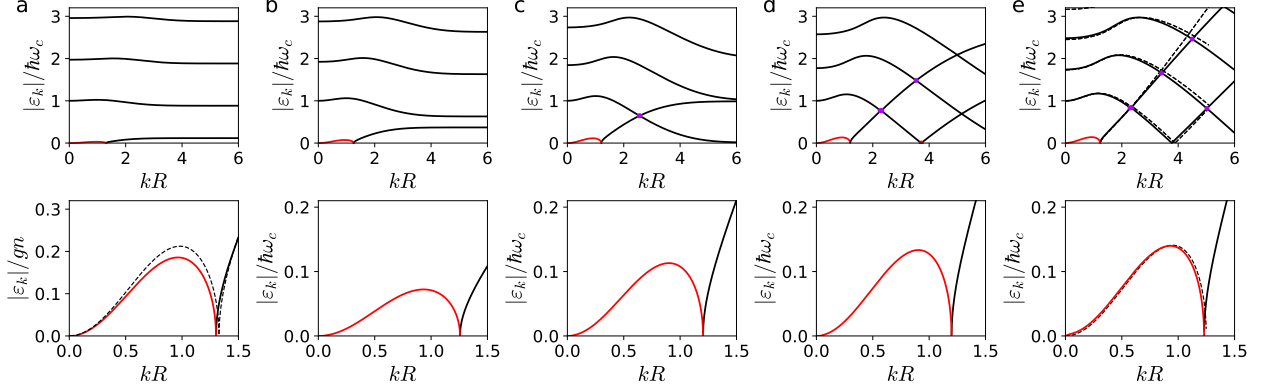
FIG. 1. Bogoliubov spectra from the Lowest Landau Level to the Thomas-Fermi regime. The interaction parameters $\tilde{g} \equiv \frac{g n_{1D}}{l_B \hbar \omega_c}$ for (a-e) are 0.3, 1, 3, 10, 40, corresponding to $R/l_B = 1.04, 1.14, 1.39, 2.01, 3.28.$, capturing the evolution from the flat spectra deep in the LLL to the more intricate crossings in the Thomas-Fermi regime. The bottom panel shows a zoomed-in region focusing on the unstable Goldstone branch (red). In the bottom panel of (a), the growth rate/excitation frequencies are normalized by gn, with $n = |\psi_0(0)|^2 = n_{1D}/(\sqrt{\pi} l_B)$ the central 2D density in the LLL. The dashed line in this panel shows the result in the deep LLL limit using [10]. In the Thomas-Fermi regime, the dashed line in e) shows the result of the hydrodynamic calculation (see text). Note the existence of complex eigenvalues with $\mathrm{Re}(\epsilon_k) \neq 0$ near the curve crossings, indicated by purple lines.

In terms of $\hat{Q}_k$ and $\hat{P}_k$, we have $\hat{K}_2 = \frac{1}{4} \sum_k \langle \hat{\mathbf{Q}}_k | \hat{\mathbf{H}}_k | \hat{\mathbf{Q}}_k \rangle + \langle \hat{\mathbf{P}}_k | \eta \hat{\mathbf{H}}_k \eta | \hat{\mathbf{P}}_k \rangle$ with $\hat{\mathbf{Q}}_k^T = (\hat{Q}_k \ \hat{Q}_{-k})$ and $\hat{\mathbf{P}}_k^T = (\hat{P}_k \ \hat{P}_{-k})$. So we can think of $\hat{\mathbf{H}}_k$ as representing the matrix of "spring constants" and $\eta \hat{\mathbf{H}}_k \eta$ the matrix of "inverse masses" in the oscillator analogy. Dynamical instabilities can arise in an oscillator when either a spring constant becomes negative, while the mass remains positive, or vice versa.

The time evolution $\frac{d}{dt} \hat{\mathbf{Q}}_k = [\hat{\mathbf{Q}}_k, \hat{K}_2] = \eta \hat{\mathbf{H}}_k \eta \hat{\mathbf{P}}_k$ and $\frac{d}{dt} \hat{\mathbf{P}}_k = -\hat{\mathbf{H}}_k \hat{\mathbf{Q}}$ yields $\frac{d^2}{dt^2} \hat{\mathbf{Q}}_k = -\eta \hat{\mathbf{H}}_k \eta \hat{\mathbf{H}}_k \hat{\mathbf{Q}}_k \overset{!}{=} -\epsilon_k^2 \hat{\mathbf{Q}}_k$ showing that eigenfrequencies of the motion correspond indeed to the eigenvalues of the operator $\eta \hat{\mathbf{H}}_k$. The Hermitian operators $\hat{\mathbf{H}}_k$ and $\eta \hat{\mathbf{H}}_k \eta$ share their (real) eigenvalues, and if $\mathbf{U}_{k,n}$ is an eigenvector of $\hat{\mathbf{H}}_k$ of eigenvalue $E_{k,n}$, then $\eta \mathbf{U}_{k,n}$ is the eigenvector of $\eta \hat{\mathbf{H}}_k \eta$ with that same eigenvalue. With $\mathcal{O}_{k,nm} = \langle \mathbf{U}_{k,n} | \eta | \mathbf{U}_{k,m} \rangle = \int dx \, \mathbf{U}_{k,n}(x) \eta \mathbf{U}_{k,m}(x)$ the matrix effecting the basis change, which is symmetric and orthonormal (so $\mathcal{O}_k^2 = \mathbb{1}$), we have $\langle \mathbf{U}_{k,n} | \eta \hat{\mathbf{H}}_k \eta | \mathbf{U}_{k,m} \rangle = \sum_l \mathcal{O}_{k,nl} E_{k,l} \mathcal{O}_{k,lm} = (\mathcal{O}_k \mathcal{E}_k \mathcal{O}_k)_{nm}$, with $\mathcal{E}_k$ the diagonal matrix of eigenvalues of $\hat{\mathbf{H}}_k$ (the "spring constants"). The squared eigenfrequencies ϵ_k^2 are thus eigenvalues of $\mathcal{O}_k \mathcal{E}_k \mathcal{O}_k \mathcal{E}_k$, and so the eigenfrequencies ϵ_k themselves are eigenvalues of $\mathcal{O}_k \mathcal{E}_k$, the matrix describing $\eta \hat{\mathbf{H}}_k$ in the basis of eigenvectors of $\hat{\mathbf{H}}_k$. Importantly, whenever a "spring constant" or "inverse mass" equals zero, i.e. one of the eigenvalues of $\hat{\mathbf{H}}_k$ equals zero, one eigenfrequency ϵ_k of $\eta \hat{\mathbf{H}}_k$ also equals zero. Regions in the variable k featuring dynamical instabilities with purely imaginary eigenfrequency are thus bounded by values of k where consecutive eigenvalues E_k of $\hat{\mathbf{H}}_k$ equal zero. This is analogous to a harmonic oscillator slowing down and becoming dynamically unstable as its spring constant changes from positive to negative, followed by its mass diverging and changing sign to yield again a dynamically stable, but thermodynamically unstable, oscillator. A famous example of the latter situation is the magnetron motion in Penning traps [11].

Since $\hat{\mathbf{H}}_k$ commutes with simultaneous reflection and particle-hole exchange, i.e. with $\gamma \hat{R}$, eigenvectors of $\hat{\mathbf{H}}_k$ can be found as eigenvectors of $\gamma \hat{R}$ with eigenvalue $\sigma = +1$ or -1, which are states of the form $\mathbf{U}_\pm = (u(x), \pm u(-x))^T$, leading to the two eigenequations

$$(\hat{h}_k - \mu_0 + 2g\psi_0^2)u_{k,n\pm}(x) \pm g\psi_0^2 u_{k,n\pm}(-x) = E_{k,n\pm} u_{k,n\pm}(x)$$

The lowest energy for $\sigma = -1$ and $k=0$ is $E_{0,0-}=0$, for $u(x) = \psi_0(x)$, and $\mathbf{U}_{0,0-}(x) = (\psi_0(x), -\psi_0(x))^T/\sqrt{2}$ is the Goldstone mode. Since $\psi_0(x)$ is the ground state for a condensate trapped in a 1D harmonic oscillator, the Hamiltonian $\hat{\mathbf{H}}_0(x)$, describing fluctuations that are translation invariant along y, is positive semi-definite, with eigenvalues $E_{0,n\pm}$ all positive or zero. For $k > 0$, the decreasing overlap of the eigenfunction $u_{k,0-}$ with the condensate centered at $x = 0$ causes the eigenvalue $E_{k,0-}$ to become negative, corresponding to the case of a negative spring constant. $\hat{K}_2$ then contains a term corresponding to an inverted oscillator potential, $\frac{1}{2}E_{k,0-}\hat{Q}_{k,0-}^2$ with $\hat{Q}_{k,n\sigma} \equiv \langle \mathbf{U}_{k,n\sigma}|\hat{\mathbf{Q}}_k \rangle$ the "position" operators, with the canonically conjugate "momentum" operators $\hat{P}_{k,n\sigma} \equiv \langle \mathbf{U}_{k,n\sigma}|\hat{\mathbf{P}}_k \rangle$ and commutation relations $[\hat{Q}_{k,n\sigma}, \hat{P}_{k,m\sigma'}] = i\delta_{nm}\delta_{\sigma\sigma'}$.
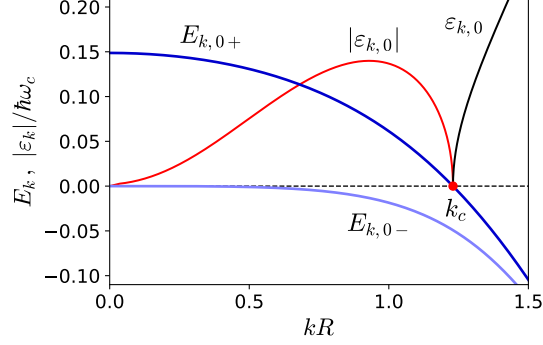
FIG. 2. Relation between Goldstone branch instability and eigenenergies of the Bogoliubov Hamiltonian $\hat{\mathbf{H}}_k$. The decrease of overlap with the condensate at non-zero k renders the lowest eigenvalue $E_{k,0-}$ of $\hat{\mathbf{H}}_k$ negative, corresponding to an inverted oscillator potential (negative spring constant). The Goldstone branch is unstable, $\epsilon_{k,0}$ being purely imaginary, until the second eigenvalue $E_{k,0+}$ of $\hat{\mathbf{H}}_k$ becomes negative, corresponding to a negative mass oscillator and resulting in stable motion, with $\epsilon_{k,0}$ real.

To obtain the matrix of inverse masses, we note that since η anti-commutes with particle-hole exchange, $\eta\gamma = -\gamma\eta$, it only connects states of opposite $\gamma\hat{R}$ symmetry, so $\langle U_{k,n+}|\eta|U_{k,m+}\rangle = \langle U_{k,n-}|\eta|U_{k,m-}\rangle = 0$. With $\mathcal{O}_{k,nm}^{+-} \equiv \langle \mathbf{U}_{k,n+}|\eta|\mathbf{U}_{k,m-}\rangle = \int \mathrm{d}x\, u_{k,n+}(x)u_{k,m-}(x) = \mathcal{O}_{k,mn}^{-+}$ we find for the "inverse mass" matrix $\langle \mathbf{U}_{k,n+}|\eta\hat{\mathbf{H}}_k\eta|\mathbf{U}_{k,m+}\rangle = \left(\mathcal{O}_k^{+-}\mathcal{E}_{k-}\mathcal{O}_k^{-+}\right)_{nm}$ and $\langle \mathbf{U}_{k,n-}|\eta\hat{\mathbf{H}}_k\eta|\mathbf{U}_{k,m-}\rangle = \left(\mathcal{O}_k^{-+}\mathcal{E}_{k+}\mathcal{O}_k^{+-}\right)_{nm}$ with $\mathcal{E}_{k\sigma}$ the diagonal matrix of eigenvalues $E_{k,\sigma}$. The squared Bogoliubov eigenfrequencies ϵ_k^2 are thus eigenvalues of the matrix $\mathcal{O}_k^{-+}\mathcal{E}_{k+}\mathcal{O}_k^{+-}\mathcal{E}_{k-}$.

Fig. 2 shows the generic case. The branch $E_{k,0-}$, the lowest eigenvalue of $\hat{\mathbf{H}}_k$, is negative for any non-zero k, and the Goldstone branch $\epsilon_{k,0}$ (eigenvalue of $\eta\hat{\mathbf{H}}_k$) is correspondingly purely imaginary and thus dynamical unstable, until at $k=k_c$ the second branch $E_{k,0+}$ crosses zero, and $\epsilon_{k,0}$ becomes real. This is the situation of having both a negative mass and a negative spring constant, corresponding to dynamically stable motion. The point at $k = k_c$ is called an exceptional point in the theory of non-Hermitian physics [6]. k_c is always on the order of the inverse cloud radius $k_c \sim 1/R$, and the maximum instability growth rate $|\epsilon_{k,0}|$ is also only slightly below k_c.

Normal form of $\hat{K}_2$

An inverted harmonic oscillator Hamiltonian $H = \frac{p^2}{2m} - \frac{1}{2}\kappa q^2$ with negative spring constant ($-\kappa < 0$), and mass $m > 0$ can be canonically transformed via $q' = \frac{1}{\sqrt{2m\Gamma}}p + \sqrt{\frac{\kappa}{2\Gamma}}q$ and $p' = \frac{1}{\sqrt{2m\Gamma}}p - \sqrt{\frac{\kappa}{2\Gamma}}q$ into $H = \frac{1}{2}\Gamma(q'\,p' + p'\,q')$, where $\Gamma = \sqrt{\kappa/m}$, with equations of motion $\frac{\mathrm{d}}{\mathrm{d}t}q' = \Gamma q'$ and $\frac{\mathrm{d}}{\mathrm{d}t}p' = -\Gamma p'$, generating squeezing of p' and exponential growth of q'. In terms of bosonic operators $a = (q' + ip')/\sqrt{2}$ and $a^\dagger = (q' - ip')/\sqrt{2}$ with $[a,a^\dagger] = 1$ the Hamiltonian is of the squeezing form $H = \Gamma\frac{1}{2i}(aa - a^\dagger a^\dagger)$. Analogously we will find that $\hat{K}_2$, in the dynamically unstable region $0 < k < k_c$, will contain a term of the squeezing form, $\sum_k \Gamma_k \left(\hat{a}_k\hat{a}_{-k} + \hat{a}_k^\dagger\hat{a}_{-k}^\dagger\right)$ associated with the spontaneous pairwise creation of excitations at $\pm k$. Here, $\epsilon_k = i\Gamma_k$ with $\Gamma_k > 0$ is purely imaginary (we omit the index 0 in $\epsilon_{k,0}$ for simplicity), and we have, since $\epsilon_k = -\epsilon_k^*$, two instead of four associated eigenvectors of $\eta\hat{\mathbf{H}}_k$, labelled $\mathbf{V}_k$ and $\mathbf{W}_k = \mathbf{V}_k^*$, associated with the different eigenvalues ϵ_k and $\epsilon_k^* = -\epsilon_k$. To have $\epsilon_k = -\epsilon_k^*$, $\mathbf{V}_k$ and $\gamma\hat{R}\mathbf{V}_k^* = \gamma\mathbf{V}_{-k}^*$ must be linearly dependent, related by a complex phase $e^{i\theta}$. Choosing this phase corresponds to a particular choice of the spatial phase of the emergent crystal. We here set $\mathbf{V}_k = -\gamma\hat{R}\mathbf{V}_k^*$, and we then also have $\mathbf{W}_k = -\gamma\hat{R}\mathbf{W}_k^*$. From this follows that $\mathbf{V}_k = (u_k(x), -u_k^*(-x))^{\mathrm{T}}$ and $\mathbf{W}_k = (u_k^*(x), -u_k(-x))^{\mathrm{T}}$. We see $\langle \mathbf{V}_k|\eta|\mathbf{V}_k\rangle = 0 = \langle \mathbf{W}_k|\eta|\mathbf{W}_k\rangle$ but we can choose the normalization of $u_k(x)$ such that $\langle \mathbf{W}_k|\eta|\mathbf{V}_k\rangle = \int \mathrm{d}x\,\left(u_k(x)^2 - u_k^*(x)^2\right) = i$. Then the action of $\hat{\mathbf{H}}_k$ on the subspace relevant to ϵ_k is

$$\hat{\mathbf{H}}_k = \Gamma_k\,\eta|\mathbf{V}_k\rangle\langle\mathbf{W}_k|\eta + \Gamma_k\,\eta|\mathbf{W}_k\rangle\langle\mathbf{V}_k|\eta + \dots$$

with ... the part of $\hat{\mathbf{H}}_k$ corresponding to modes with $n > 0$. Inserting this in Eq. 3, and noting that $\mathbf{V}_{-k} = \hat{R}\mathbf{V}_k$ and so $u_{-k}(x) = u_k(-x)$ gives

$$\hat{K}_2 = \frac{1}{2}\sum_k \Gamma_k \left(\langle \hat{\boldsymbol{\Phi}}_k|\eta|\mathbf{V}_k\rangle\langle\mathbf{W}_k|\eta|\hat{\boldsymbol{\Phi}}_k\rangle + \langle\hat{\boldsymbol{\Phi}}_k|\eta|\mathbf{W}_k\rangle\langle\mathbf{V}_k|\eta|\hat{\boldsymbol{\Phi}}_k\rangle \right) + \dots$$

$$= \frac{1}{2}\sum_k \Gamma_k \left(\hat{p}_k\hat{q}_{-k} + \hat{q}_k\hat{p}_{-k} \right) + \dots$$

$$= \sum_{k>0}\Gamma_k\frac{1}{i}\left(\hat{a}_k\hat{a}_{-k} - \hat{a}_k^\dagger\hat{a}_{-k}^\dagger \right) + \dots$$

where the dots denote contributions from stable modes of higher excitation energies $|\epsilon_{k,n}|$ and the $k{=}0$ Goldstone mode's "kinetic energy" term corresponding to free global phase diffusion [7], and we defined

$$\hat{p}_k \equiv \langle\hat{\boldsymbol{\Phi}}_k|\eta|\mathbf{V}_k\rangle = \int \mathrm{d}x \left(u_k(x)\phi_k^\dagger + u_k^*(-x)\phi_{-k} \right)$$

$$\hat{q}_k \equiv \langle\hat{\boldsymbol{\Phi}}_k|\eta|\mathbf{W}_k\rangle = \int \mathrm{d}x \left(u_k^*(x)\phi_k^\dagger + u_k(-x)\phi_{-k} \right)$$

$$\hat{p}_k^\dagger \equiv \langle\mathbf{V}_k|\eta|\hat{\boldsymbol{\Phi}}_k\rangle = \int \mathrm{d}x \left(u_k^*(x)\phi_k + u_k(-x)\phi_{-k}^\dagger \right) = \hat{p}_{-k}$$

$$\hat{q}_k^\dagger \equiv \langle\mathbf{W}_k|\eta|\hat{\boldsymbol{\Phi}}_k\rangle = \int \mathrm{d}x \left(u_k(x)\phi_k + u_k^*(-x)\phi_{-k}^\dagger \right) = \hat{q}_{-k}$$

with $[\hat{q}_k, \hat{p}_{-k}] = i$ and other commutators zero and $\hat{a}_k = (\hat{q}_k+i\hat{p}_k)/\sqrt{2}$, accordingly $\hat{a}_k^\dagger = \left(\hat{q}_k^\dagger - i\hat{p}_k^\dagger\right)/\sqrt{2} = (\hat{q}_{-k}-i\hat{p}_{-k})/\sqrt{2}$ and $\left[\hat{a}_k, \hat{a}_k^\dagger\right] = 1$ with other commutators zero. Other choices of the phase between $\mathbf{V}_k$ and $\gamma\mathbf{V}_{-k}^*$ yield equivalent forms of the squeezing Hamiltonian [12] such as $\Gamma_k\left(\hat{a}_k\hat{a}_{-k} + \hat{a}_k^\dagger\hat{a}_{-k}^\dagger\right)$. The time-dependence of the operators is then:

$$\hat{a}_k(t) = \cosh(\Gamma_k t)\hat{a}_k(0) - i\sinh(\Gamma_k t)\hat{a}_{-k}^\dagger(0),$$
$$\hat{a}_{-k}^\dagger(t) = \cosh(\Gamma_k t)\hat{a}_{-k}^\dagger(0) + i\sinh(\Gamma_k t)\hat{a}_k(0). \tag{5}$$

Structure factor

The structure factor S_k is obtained as follows. From the density operator $\hat{n}(x,y)$ we obtain the density fluctuation operator, only retaining the contribution from unstable modes

$$\delta\hat{n}(x,y) = \psi_0(x)\frac{1}{\sqrt{L}}\sum_k \left(\bar{u}_k(x)e^{iky}\hat{a}_k + \bar{v}_k^*(x)e^{iky}\hat{a}_{-k}^\dagger + \bar{u}_k^*(x)e^{-iky}\hat{a}_k^\dagger + \bar{v}_k(x)e^{-iky}\hat{a}_{-k} \right). \tag{6}$$

where $\bar{u}_k = (u_k^* - iu_k)/\sqrt{2}$ and $\bar{v}_k = -(u_k - iu_k^*)/\sqrt{2}$. Integrating along x and taking the Fourier transform along y yields the Fourier component of the one-dimensional density profile with a wavevector q in the y-direction,

$$\delta\hat{n}_q = \int \mathrm{d}x \int \mathrm{d}y\, \delta\hat{n}(x,y)e^{-iqy}$$

$$= \sqrt{n_{1D}}\int \mathrm{d}x\, \tilde{\psi}_0(x)\left[(\bar{u}_q(x) + \bar{v}_{-q}(x))\hat{a}_q + (\bar{u}_{-q}^*(x) + \bar{v}_q^*(x))\hat{a}_{-q}^\dagger \right] \tag{7}$$

Here we define $\psi_0 = \sqrt{n_{1D}}\tilde{\psi}_0$ such that $\int \mathrm{d}x\,|\tilde{\psi}_0(x)|^2 = 1$. We also have $\int \mathrm{d}x\,(|\bar{u}_k(x)|^2 - |\bar{v}_{-k}(x)|^2) = 1$. The structure factor is defined as [13]

$$S_q = \frac{1}{N}\langle\delta\hat{n}_q\delta\hat{n}_q^\dagger\rangle$$

$$= \langle\left(A_q\hat{a}_q + A_q^*\hat{a}_{-q}^\dagger\right)\left(A_q^*\hat{a}_q^\dagger + A_q\hat{a}_{-q}\right)\rangle$$

$$= |A_q|^2\left(\langle 1 + \hat{a}_q^\dagger\hat{a}_q + \hat{a}_{-q}^\dagger\hat{a}_{-q}\rangle + \frac{1}{i}\langle\hat{a}_q\hat{a}_{-q} - \hat{a}_q^\dagger\hat{a}_{-q}^\dagger\rangle \right)$$

$$= |A_q|^2\,(1+\nu)\cosh(2\Gamma_k t) \tag{8}$$

where $N = Ln_{1D}$ is the total atom number. Since $\langle \hat{a}_q \hat{a}_{-q} - \hat{a}_q^\dagger \hat{a}_{-q}^\dagger \rangle$ is an expectation value of an operator which commutes with the Hamiltonian, it is a constant of motion and here taken to be zero. The terms $\langle \hat{a}_q^\dagger \hat{a}_q \rangle$ and $\langle \hat{a}_{-q}^\dagger \hat{a}_{-q} \rangle$ correspond to the occupation numbers of modes $\pm q$. They are related to their values at $t = 0$ using the operator time-dependence given in Eq. (5), and we denote the initial mode populations by $\nu = \langle \hat{a}_q^\dagger(0)\hat{a}_q(0) \rangle + \langle \hat{a}_{-q}^\dagger(0)\hat{a}_{-q}(0) \rangle$. The contribution of a single quantum to S_k is determined by the overlap integral $A_q = A_{-q} = \int \mathrm{d}x\, \tilde{\psi}_0(x)(\bar{u}_q(x) + \bar{v}_{-q}(x))$.

Limit of the Lowest Landau Level

The Bogoliubov analysis in the lowest Landau level was performed in [10], focussing on the stable regime occurring in a rotating saddle potential $V(x,y) = \frac{1}{2}m\epsilon\omega^2(x^2 - y^2)$ (in the rotating frame coordinates). The rotation frequency was chosen such that the centrifugal force precisely cancelled the trapping force in the weaker (y-)direction, i.e. $\Omega = \omega\sqrt{1-\epsilon}$. The experiment performed here corresponds to no rotating saddle at all, i.e. $\epsilon = 0$. The Bogoliubov Hamiltonian is

$$\hat{K}_2 = \sum_k \left(\frac{\hbar^2 k^2}{2m^*} + 2g^* n_{1D} e^{-k^2 l_B^2/2} \right) \hat{a}_k^\dagger \hat{a}_k + \frac{g^* n_{1D}}{2} \sum_k e^{-k^2 l_B^2} \left(\hat{a}_k^\dagger \hat{a}_{-k}^\dagger + \hat{a}_k \hat{a}_{-k} \right)$$

with an effective 1D coupling constant $g^* = g/\sqrt{2\pi}l_B$ and where the effective mass m^* of excitations is given by $1/m^* = 1/m \left(1 - \frac{4\Omega^2}{\omega_c^2} \right)$ with the cyclotron frequency $\omega_c = \omega\sqrt{4 - 2\epsilon}$ modified by the anharmonic potential. One has $m^* \approx \frac{2}{\epsilon}m$ for small ϵ. We see that in the case relevant to the present experiment $\epsilon = 0$ we have $1/m^* = 0$, corresponding to "infinitely heavy" excitations, i.e. a flat band without a kinetic mass term. Importantly, although only contact interactions are present, evolution in the rotating frame yields a k-dependent effective interaction, and correspondingly a magneto-roton minimum which evolves into a dynamical instability as the anharmonicity ϵ decreases. The excitation spectrum follows as [10]

$$\epsilon_k^2 = \left[\frac{\hbar^2 k^2}{2m^*} + g^* n_{1D} \left(2e^{-k^2 l_B^2/2} - 1 \right) \right]^2 - g^{*2} n_{1D}^2 e^{-2k^2 l_B^2} \tag{9}$$

In the limit $\epsilon = 0$ one has an unstable Goldstone branch between $k = 0$ and $k = k_c = \sqrt{2\log\left(\frac{1}{\sqrt{2}-1}\right)}/l_B = 1.33/l_B$. The maximum growth rate of the instability occurs at $k_{\max} l_B = \sqrt{2\log\left(\frac{2}{\sqrt{5}-1}\right)} = 0.98$ and is $\Gamma_{k_{\max}} = \sqrt{\frac{5}{2}\sqrt{5} - \frac{11}{2}}\, g^* n_{1D} = 0.3\, g^* n_{1D} = 0.21gn$. This is shown in Fig. 1a).

Evolution from stable magneto-roton excitations to dynamical instability

The expression Eq. 9 allows us to follow the excitation spectrum in the 1D regime of motion in a rotating anharmonic saddle as $\epsilon \to 0$. This evolution is shown in Fig. 3, varying the parameter introduced in [10] $\beta = \frac{n_{1D}g^*}{\hbar^2/2m^* l_B^2}$, comparing the interaction energy to the kinetic energy of excitations at momentum $\sim 1/\ell_B$. The present experiment corresponds to $\beta = \infty$, i.e. zero kinetic energy, infinite effective mass of excitations and purely interaction-driven dynamics. The figure shows how an initially stable branch consisting of phonons at low momenta k develops a magneto-roton minimum at $k \approx 1/l_B$. This minimum lowers in energy as it becomes more and more favorable to create magneto-rotons, excitations which avoid the condensate mean-field repulsion due to their spatial shift by $kl_B^2 \approx l_B$. Beyond a critical $\beta = 4.9$, a dynamical instability near $k \sim 1/l_B$ develops, corresponding to the onset of magneto-roton condensation - in analogy to roton condensation considered in [14, 15]. Eventually, for $\beta \to \infty$, the case of the present experiment, the entire Goldstone branch up to $k = k_c$ is dynamically unstable, with maximum growth at $k = k_{\max} \sim 1/l_B$.

Thomas-Fermi limit - Hydrodynamics

The Gross-Pitaevskii equation for the wavefunction $\psi = \sqrt{\rho}\, e^{iS}$ can be equivalently rewritten as hydrodynamic equations for the density $\rho = |\psi|^2$ and the velocity $\mathbf{v} = \frac{\hbar}{m}\nabla S$. The equation for the velocity is:

$$\frac{\partial \mathbf{v}}{\partial t} = -\nabla \left(-\frac{\hbar^2}{2m^2\sqrt{\rho}}\nabla^2\sqrt{\rho} + \frac{1}{2}\mathbf{v}^2 - \mathbf{v} \cdot (\mathbf{\Omega} \times \mathbf{r}) + \frac{1}{m}U + \frac{g\rho}{m} \right). \tag{10}$$
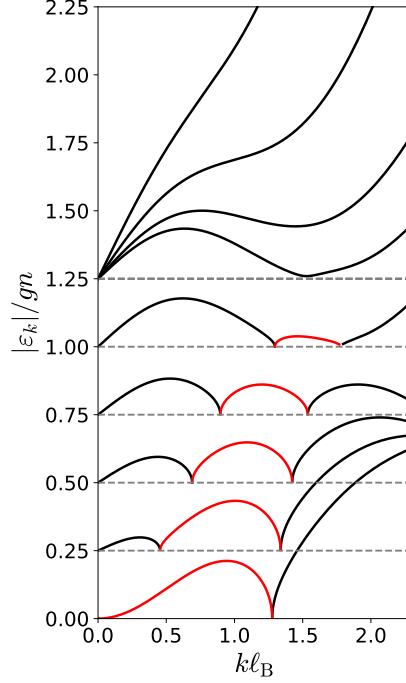
FIG. 3. Evolution from stable phonon and magneto-roton excitations to dynamically unstable excitations as the anharmonicity ϵ of a rotating saddle potential is reduced to zero. From top to bottom, the value of the parameter β, measuring the strength of interaction energy to kinetic energy, is varied from $\beta = 1, 2, 3.5, 4.9$ (the critical value where the magneto-roton minimum touches zero [10]), $5.1, 7, 10, 20, 100000$.

Here, $U(\vec{r}, t) = \frac{1}{2} m\omega^2 \left(x^2(1+\epsilon) + y^2(1-\epsilon) \right)$ is a rotating anisotropic potential - in the experiment $\epsilon = 0$. Introducing the "convective derivative" moving with a fluid element,

$$\frac{D}{Dt} = \frac{\partial}{\partial t} + (\mathbf{v}_{\mathrm{rot}} \cdot \nabla) \tag{11}$$

this can be written as

$$m\frac{D\mathbf{v}_{\mathrm{rot}}}{Dt} = 2m\mathbf{v}_{\mathrm{rot}} \times \boldsymbol{\Omega} + m\Omega^2 \mathbf{r} - \nabla \left(-\frac{\hbar^2}{2m\sqrt{\rho}}\nabla^2\sqrt{\rho} + U + g\rho \right). \tag{12}$$

with $\mathbf{v}_{\mathrm{rot}} = \mathbf{v} - \boldsymbol{\Omega} \times \mathbf{r}$ the velocity in the rotating frame. This is Newton's law in the rotating frame, featuring the Coriolis force $2m\mathbf{v}_{\mathrm{rot}} \times \Omega$, the centrifugal force $m\Omega^2\mathbf{r}$ and the force acting on a fluid particle derived from the quantum pressure $-\frac{\hbar^2}{2m\sqrt{\rho}}\nabla^2\sqrt{\rho}$, the mean-field potential $g\rho$, and the external potential U. The continuity equation in the rotating frame $\frac{\partial \rho}{\partial t} = -\nabla \cdot (\rho \mathbf{v}_{\mathrm{rot}})$ can also be written using the convective derivative:

$$\frac{D\rho}{Dt} = -\rho\nabla \cdot \mathbf{v}_{\mathrm{rot}}. \tag{13}$$

Linearizing the hydrodynamic equations - including the quantum pressure term - is equivalent to the Bogoliubov approach [2]. We now drop the quantum pressure term, considering the Thomas-Fermi limit.

We perturb the density and phase around stationary solutions ρ_c and S_c

$$\rho = \rho_c + \delta\rho$$
$$S = S_c + \delta S \tag{14}$$

and obtain the linearized hydrodynamic equations [16]

$$\frac{D\delta\rho}{Dt} = -\frac{\hbar}{m}\nabla \cdot (\rho_c \nabla\delta S)$$
$$\hbar\frac{D\delta S}{Dt} = -g\delta\rho \tag{15}$$

Hydrodynamics in the Landau gauge

The Landau gauge corresponds to setting $S_c = -\frac{m\Omega}{\hbar}xy$, and we specialize to $\Omega = \omega\sqrt{1-\epsilon}$, where the centrifugal potential exactly cancels the (y-)direction of weak confinement. The case in the experiment is $\epsilon = 0$. Neglecting the quantum pressure term (Thomas-Fermi limit), the stationary density profile is $g\rho_c(x) = \mu - \frac{1}{2}m\omega_c^2 x^2$, the velocity profile is $\mathbf{v}_c = \frac{\hbar}{m}\nabla S_c$ and we have $\mathbf{v}_{\text{rot}} = \mathbf{v}_c - \mathbf{\Omega} \times \mathbf{r} = -2\Omega x\,\hat{\mathbf{y}}$. The coupled linearized hydrodynamic equations become

$$\frac{\partial\delta\rho}{\partial t} - 2\Omega x\partial_y\delta\rho = -\frac{\hbar}{m}\partial_x\left(\rho_c(x)\partial_x\delta S\right) - \frac{\hbar}{m}\rho_c(x)\partial_y^2\delta S$$
$$\frac{\partial\delta S}{\partial t} - 2\Omega x\partial_y\delta S = -\frac{1}{\hbar}g\delta\rho \tag{16}$$

As there is no explicit dependence on y, one may choose $\delta\rho = \text{Re}(e^{iky}\delta\rho_k)$ and $\delta S = \text{Re}(e^{iky}\delta S_k)$. We omit the index k in the following and find

$$\frac{\partial\delta\rho}{\partial t} - 2i\Omega kx\,\delta\rho = -\frac{\hbar}{m}\partial_x\left(\rho_c(x)\partial_x\delta S\right) + \frac{\hbar k^2}{m}\rho_c(x)\delta S$$
$$\frac{\partial\delta S}{\partial t} - 2i\Omega kx\,\delta S = -\frac{1}{\hbar}g\delta\rho \tag{17}$$

Using $g\rho_c(x) = \mu - \frac{1}{2}m\omega_c^2 x^2$ and $\partial_x g\rho_c(x) = -m\omega_c^2 x$ we have

$$\frac{\partial g\delta\rho}{\partial t} - 2i\Omega kx\,g\delta\rho = \omega_c^2 x\partial_x\,\hbar\delta S - \frac{1}{m}\left(\mu - \frac{1}{2}m\omega_c^2 x^2\right)\left(\partial_x^2 - k^2\right)\hbar\delta S \tag{18}$$

Measuring rates and inverse times in units of ω_c (such as $\tilde{\Omega} = \Omega/\omega_c$), energies in units of $\hbar\omega_c$ (writing $\delta\tilde{\rho} = g\delta\rho/(\hbar\omega_c)$), and lengths in units of the Thomas-Fermi radius $R_{\text{TF}} = \sqrt{2\mu/(m\omega_c^2)}$, the equations become (tildes are dropped for brevity)

$$\frac{\partial\delta\rho}{\partial t} - 2i\Omega kx\,\delta\rho = \left(x\partial_x - \frac{1}{2}(1-x^2)(\partial_x^2 - k^2)\right)\delta S$$
$$\frac{\partial\delta S}{\partial t} - 2i\Omega kx\,\delta S = -\delta\rho \tag{19}$$

The operator $\mathcal{L} \equiv x\partial_x - \frac{1}{2}(1-x^2)\partial_x^2 = -\frac{1}{2}\partial_x\left((1-x^2)\partial_x\right)$ is Legendre's differential operator, whose eigenfunctions are the Legendre polynomials $P_n(x)$:

$$\mathcal{L}P_n(x) = \frac{1}{2}n(n+1)P_n(x) \tag{20}$$

In terms of $\mathcal{L}$, the coupled equations are

$$\frac{\partial\delta\rho}{\partial t} - 2i\Omega kx\,\delta\rho = \left(\mathcal{L} + \frac{k^2}{2}(1-x^2)\right)\delta S$$
$$\frac{\partial\delta S}{\partial t} - 2i\Omega kx\,\delta S = -\delta\rho \tag{21}$$

Looking for a time-dependence $\sim e^{-i\omega t}$, the equations become

$$-i(\omega + 2\Omega kx)\delta\rho = \left(\mathcal{L} + \frac{k^2}{2}(1-x^2)\right)\delta S$$
$$-i(\omega + 2\Omega kx)\delta S = -\delta\rho \tag{22}$$

and thus

$$(\omega + 2\Omega kx)^2\delta S = \left(\mathcal{L} + \frac{k^2}{2}(1-x^2)\right)\delta S \tag{23}$$

The equation is formally solved by the confluent Heun function [17], with eigenfrequencies obtained by demanding the solution to be regular everywhere inside the Thomas-Fermi radius ($|x| < 1$). In particular, for $\epsilon = 0$ and so $2\Omega = \omega_c$ we have $\delta S = e^{\sqrt{3}kx}\,\text{H}_C\left[2(k^2 + k(\sqrt{3} - 2\omega) + \omega^2), 4k(\sqrt{3} - 2\omega), 1, 1, 4\sqrt{3}k, \frac{1+x}{2}\right]$, where $\text{H}_C[q, \alpha, \gamma, \delta, \kappa, z]$ satisfies the confluent Heun differential equation $z(z-1)y'' + (\gamma(z-1) + \delta z + z(z-1)\kappa)y' + (\alpha z - q)y = 0$ [17]. Notably, exceptional points where $\omega = 0$ are obtained as special zeroes of the confluent Heun function: $\text{H}_C\left[2k^2 + 2\sqrt{3}k, 4\sqrt{3}k, 1, 1, 4\sqrt{3}k, \frac{1}{2}\right] = 0$. The critical $k = k_c$ separating the dynamically unstable modes for $0 < k < k_c$ and the stable excitations for $k > k_c$ is obtained as the first zero of this particular Heun function, at $k_c = 1.47/R_{\text{TF}} = 1.25/R$. Below we find limiting cases, a series expansion for the solution, and identify the minimal set of modes responsible for the instability: The Goldstone mode, dipole mode and breathing mode of the unperturbed condensate.

For $k = 0$ the problem is just that of finding the excitation spectrum of a Bose-Einstein condensate in a one-dimensional harmonic oscillator:

$$\omega^2 \delta S = \mathcal{L} \delta S \tag{24}$$

with eigenvalues $\omega_n = \sqrt{\frac{1}{2} n(n+1)}$, in units of ω_c, and eigenfunctions $\delta S = P_n(x)$. The case $n = 1$ is the sloshing mode, oscillating at the cyclotron frequency with $\omega_1 = \omega_c$, unshifted from the result for the non-interacting harmonic oscillator, in accordance with Kohn's theorem [8, 9]. Including the long-wavelength modulation $\propto \sin(ky)$, the mode is described by

$$\delta S(x, y, t) \propto x \cos(\omega_c t) \sin(ky)$$
$$\delta\rho(x, y, t) \propto x \sin(\omega_c t) \sin(ky)$$

which is a time-dependent "snaking" mode, sloshing back and forth along x at frequency ω_c.

The case $n = 2$ is the breathing mode, at $\omega_2 = \sqrt{3}\omega_c$, shifted from the non-interacting case $(2\omega_c)$ by the interactions, and describing a time-dependent compression / decompression mode that periodically alternates along y.

The case $n = 0$ and $k = 0$ is the Goldstone mode at $\omega_0 = 0$, with $\delta S(x) = $ const. a constant phase offset, and $\delta\rho = 0$, i.e. no density modulation, describing the zero cost of changing the phase of the wavefunction globally. For the case in the experiment $\epsilon = 0$, i.e. $\Omega = \omega$, and neglecting coupling to the breathing mode, one still has the zero-energy solution $\omega_0 = 0$, since there is zero energy cost to displace the wavefunction along x. The mode profile is $\delta\rho(x, y, t) \propto \Omega k x \cos(ky)$, corresponding to a stationary "snake"-like deformation. With coupling to the breathing mode, it will grow exponentially.

Solution by expansion in Legendre polynomials

To solve the equations for $\delta\rho$ and δS, we expand them in the basis of normalized Legendre polynomials $p_n(x) \equiv \sqrt{\frac{2n+1}{2}} P_n(x)$ (with $P_n(x)$ the traditional Legendre polynomials):

$$\delta\rho(x) = \sum_n \rho_n p_n(x)$$
$$\delta S(x) = \sum_n s_n p_n(x)$$

The $p_n(x)$ are orthonormal for integration over $x \epsilon [-1, 1]$ (while the $P_n(x)$ are not):

$$\langle n|m \rangle = \int_{-1}^{1} dx \, p_n(x) p_m(x) = \delta_{n,m}$$

where $\langle f|g \rangle = \int_{-1}^{1} dx \, f(x) g(x)$ defines a scalar product. The $p_n(x)$ are eigenfunctions of $\mathcal{L}$, but the terms in x and in x^2 in the equations 22 couple Legendre polynomials whose index differs by 1 or 2, respectively. A recurrence relation for Legendre polynomials gives

$$x P_n = \frac{n+1}{2n+1} P_{n+1} + \frac{n}{2n+1} P_{n-1}$$

which for the orthonormal p_n reads

$$x p_n = \frac{n+1}{\sqrt{(2n+1)(2n+3)}} p_{n+1} + \frac{n}{\sqrt{(2n+1)(2n-1)}} p_{n-1}$$

from which one finds

$$X_{nm} \equiv \langle n|x|m \rangle = \int_{-1}^{1} dx \, p_n(x) x p_m(x) = \frac{1}{\sqrt{(2n+1)(2m+1)}} (n \, \delta_{m,n-1} + m \, \delta_{n,m-1})$$

$$\left(X^2\right)_{nm} = \langle n|x^2|m\rangle = \sum_j \langle n|x|j\rangle\,\langle j|x|m\rangle = \sum_j X_{nj}X_{jm}$$

$$= \sum_j \frac{1}{\sqrt{(2n+1)(2m+1)}}\frac{1}{2j+1}\left(n\delta_{j,n-1}+j\delta_{n,j-1}\right)\left(j\delta_{m,j-1}+m\delta_{j,m-1}\right)$$

$$= \frac{(2n(n+1)-1)}{(2n-1)(2n+3)}\delta_{n,m}+\frac{1}{\sqrt{(2n+1)(2m+1)}}\left(\frac{m(m-1)}{(2m-1)}\delta_{m,n+2}+\frac{n(n-1)}{(2n-1)}\delta_{n,m+2}\right)$$

The equations 22 can then be written

$$\frac{\partial \rho_n}{\partial t} = i2\Omega k X_{nm}\rho_m + \mathcal{L}^{(k)}_{nm}s_m$$

$$\frac{\partial s_n}{\partial t} = i2\Omega k X_{nm}s_m - \rho_n \tag{25}$$

(using convention to sum over repeated indices) or in vector notation $\vec{\rho} = (\rho_0, \rho_1, \dots)^T$

$$\frac{\partial \vec{\rho}}{\partial t} = i2\Omega k X\vec{\rho} + \mathcal{L}^{(k)}\vec{s}$$

$$\frac{\partial \vec{s}}{\partial t} = i2\Omega k X\vec{s} - \vec{\rho} \tag{26}$$

where X is the matrix with entries X_{nm}, and where

$$\mathcal{L}^{(k)}_{nm} = \left(\frac{1}{2}n(n+1)+\frac{k^2}{2}\right)\delta_{nm} - \frac{k^2}{2}\left(X^2\right)_{nm}$$

This linear system is solved by choosing a cutoff in the degree n of polynomials used in the expansion. Alternatively, we can start with Eq. 23, which is particularly useful for the case relevant to the present experiment $\epsilon = 0$, so $2\Omega = \omega_c \equiv 1$ in dimensionless units. We have

$$(\omega + kx)^2 - \frac{k^2}{2}(1-x^2) = \omega^2 + 2\omega kx + k^2\left(\frac{3}{2}x^2 - \frac{1}{2}\right) = \omega^2 P_0 + 2\omega k P_1 + k^2 P_2$$

since $P_2(x) = \frac{3}{2}x^2 - \frac{1}{2}$. So the equation to solve is

$$\mathcal{L}\,\delta S = (k^2 P_2 + 2\omega k P_1 + \omega^2 P_0)\delta S$$

This way of writing the equation makes it explicit that the cause of the instability of the Goldstone mode ($\omega = 0$ for $k = 0$) is coupling to the breathing mode with $n = 2$, caused by P_2. The term multiplying P_1, which could in principle couple the Goldstone to the dipole mode, is zero for $\omega = 0$ and thus is not responsible for the instability. In the basis of orthonormal Legendre polynomials, we have

$$(P_2(x))_{nm} = \frac{3}{2}\left(X^2\right)_{nm} - \frac{1}{2}\delta_{nm}. \tag{27}$$

On the off-diagonals, it acts like $\frac{3}{2}(X^2)_{nm}$, but on the diagonal one finds the simpler

$$(P_2(x))_{nn} = \frac{n(n+1)}{(2n-1)(2n+3)} \tag{28}$$

This yields the equation for the s_n:

$$\left(\frac{1}{2}n(n+1)\left(1-\frac{2k^2}{(2n-1)(2n+3)}\right)-\omega^2\right)s_n = 2\omega k X_{nm}s_m + \frac{3}{2}k^2\sum_{m\neq n}\left(X^2\right)_{nm}s_m$$

$$= 2\omega k\left(\frac{n}{\sqrt{(2n-1)(2n+1)}}s_{n-1}+\frac{n+1}{\sqrt{(2n+1)(2n+3)}}s_{n+1}\right)$$

$$+\frac{3}{2}k^2\left(\frac{(n+1)(n+2)}{(2n+3)\sqrt{(2n+1)(2n+5)}}s_{n+2}+\frac{n(n-1)}{(2n-1)\sqrt{(2n-3)(2n+1)}}s_{n-2}\right)$$

With a finite cutoff in the polynomial degree n this represents a sparse matrix, and eigenfrequencies are found by setting its determinant to zero. In general, eigenfrequencies can be complex and one finds an unstable Goldstone branch. The result is shown as the dashed lines in Fig. 1e).

Insight is obtained by truncating the Hilbert space. Including the Goldstone, dipole and breathing mode, so p_0, p_1 and p_2 gives equations for the coefficients (s_0, s_1, s_2)

$$
\begin{pmatrix}
\omega^2 & \frac{2k\omega}{\sqrt{3}} & \frac{k^2}{\sqrt{5}} \\
\frac{2k\omega}{\sqrt{3}} & \frac{2k^2}{5} + \omega^2 - 1 & \frac{4k\omega}{\sqrt{15}} \\
\frac{k^2}{\sqrt{5}} & \frac{4k\omega}{\sqrt{15}} & \frac{2k^2}{7} + \omega^2 - 3
\end{pmatrix}
\begin{pmatrix}
s_0 \\
s_1 \\
s_2
\end{pmatrix} = 0
$$

This minimal model already yields a dynamically unstable Goldstone branch which will lead to exponential growth for small k. To find the critical $k=k_c$ where $\omega = 0$ one solves

$$
\begin{vmatrix}
0 & 0 & \frac{k^2}{\sqrt{5}} \\
0 & \frac{2k^2}{5} - 1 & 0 \\
\frac{k^2}{\sqrt{5}} & 0 & \frac{2k^2}{7} - 3
\end{vmatrix} = 0 \tag{29}
$$

from which one finds $k_c R_{\mathrm{TF}} = \sqrt{\frac{5}{2}} = 1.58$. This is already close to the exact result $k_c R_{\mathrm{TF}} = 1.47$. The maximum instability is found at $k_{\max} R_{\mathrm{TF}} \approx 1.18$ with $\mathrm{Im}\,\omega = 0.148\,\omega_c$, close to the exact maximum in the Thomas-Fermi limit at $k_{\max} R_{\mathrm{TF}} = 1.12\ldots$ with $\mathrm{Im}\,\omega = 0.141\,\omega_c$.

[1] N. N. Bogoliubov, "On the theory of superfluidity," J. Phys. (USSR) **11**, 23 (1947).
[2] A. L. Fetter, "Ground state and excited states of a confined condensed Bose gas," Phys. Rev. A. **53**, 4245 (1996).
[3] Yuki Kawaguchi and Masahito Ueda, "Spinor bose–einstein condensates," Physics Reports **520**, 253–381 (2012), spinor Bose–Einstein condensates.
[4] Jean-Paul Blaizot and Georges Ripka, *Quantum Theory of Finite Systems* (MIT Press, 1986).
[5] R. Barnett, "Edge-state instabilities of bosons in a topological band," Phys. Rev. A **88**, 063631 (2013).
[6] Y. Ashida, Z Gong, and M Ueda, "Non-hermitian physics," Advances in Physics **69**, 249–435 (2020).
[7] Y. Castin and R. Dum, "Low-temperature Bose–Einstein condensates in time-dependent traps: Beyond the u(1) symmetry-breaking approach," Phys. Rev. A **57**, 3008 (1998).
[8] W. Kohn, "Cyclotron resonance and de haas-van alphen oscillations of an interacting electron gas," Phys. Rev. **123**, 1242–1244 (1961).
[9] Alexander L. Fetter and Daniel Rokhsar, "Excited states of a dilute bose-einstein condensate in a harmonic trap," Phys. Rev. A **57**, 1191–1201 (1998).
[10] S. Sinha and G. V. Shlyapnikov, "Two-dimensional Bose–Einstein condensate under extreme rotation," Phys. Rev. Lett. **94**, 150401 (2005).
[11] H.G. Dehmelt, "Radiofrequency spectroscopy of stored ions i: Storage**part ii: Spectroscopy is now scheduled to appear in volume v of this series." (Academic Press, 1968) pp. 53–72.
[12] L. J. Garay, J. R. Anglin, J. I. Cirac, and P. Zoller, "Sonic Analog of Gravitational Black Holes in Bose-Einstein Condensates," Phys. Rev. Lett. **85**, 4643–4647 (2000).
[13] L. Pitaevskii and S. Stringari, *Bose–Einstein Condensation* (Oxford University Press, Oxford, 2003).
[14] S V Iordanskiĭ and Lev P Pitaevskiĭ, "Bose condensation of moving rotons," Soviet Physics Uspekhi **23**, 317–318 (1980).
[15] L P Pitaevskii, "Layered structure of superfluid ^{4}He with supercritical motion," JETP Letters **39**, 511–514 (1984).
[16] Subhasis Sinha and Yvan Castin, "Dynamic instability of a rotating Bose-Einstein condensate," Phys. Rev. Lett. **87**, 190402 (2001).
[17] A. Ronveaux, ed., *Heun's Differential Equations* (Oxford University Press, New York, 1995).

Bibliography

[1] J R Abo-Shaeer, C Raman, J M Vogels, and W Ketterle. Observation of Vortex Lattices in Bose-Einstein Condensates. *Science*, 292(5516):476–479, 2001.

[2] Amandine Aftalion, Xavier Blanc, and Jean Dalibard. Vortex patterns in a fast rotating Bose-Einstein condensate. *Phys. Rev. A*, 71(2):23611, feb 2005.

[3] Altechna. Plano-Convex Axicons, 2021.

[4] M H Anderson, J R Ensher, M R Matthews, C E Wieman, and E A Cornell. Observation of Bose-Einstein condensation in a dilute atomic vapor. *Science*, 269(5221):198–201, 1995.

[5] A W Baggaley and N G Parker. Kelvin-Helmholtz instability in a single-component atomic superfluid. *Phys. Rev. A*, 97(5):53608, may 2018.

[6] Weizhu Bao, Dieter Jaksch, and Peter A. Markowich. Numerical solution of the Gross-Pitaevskii equation for Bose-Einstein condensation. *Journal of Computational Physics*, 187(1):318–342, 2003.

[7] Gordon Baym, C. J. Pethick, Zhenhua Yu, and Martin W. Zwierlein. Coherence and clock shifts in ultracold fermi gases with resonant interactions. *Phys. Rev. Lett.*, 99(19):1–4, 2007.

[8] Ulf Bissbort, Sören Götze, Yongqiang Li, Jannes Heinze, Jasper S Krauser, Malte Weinberg, Christoph Becker, Klaus Sengstock, and Walter Hofstetter. Detecting the Amplitude Mode of Strongly Interacting Lattice Bosons by Bragg Scattering. *Phys. Rev. Lett.*, 106(20):205303, may 2011.

[9] S N Bose. Plancks Gesetz und Lichtquantenhypothese. *Z. Phys.*, 26:178, 1924.

[10] Fabian Böttcher, Jan-Niklas Schmidt, Matthias Wenzel, Jens Hertkorn, Mingyang Guo, Tim Langen, and Tilman Pfau. Transient Supersolid Properties in an Array of Dipolar Quantum Droplets. *Phys. Rev. X*, 9(1):11051, mar 2019.

[11] Eric Braaten, Daekyoung Kang, and Lucas Platter. Short-Time Operator Product Expansion for rf Spectroscopy of a Strongly Interacting Fermi Gas. *Phys. Rev. Lett.*, 104(22):223004, jun 2010.

[12] G. M. Bruun, A. Recati, C. J. Pethick, H. Smith, and S. Stringari. Collisional properties of a polarized fermi gas with resonant interactions. *Physical Review Letters*, 100(24):3–6, 2008.

[13] H. Büchler and G Blatter. Supersolid versus Phase Separation in Atomic Bose-Fermi Mixtures. *Phys. Rev. Lett.*, 91:130404, 2003.

[14] C Cao, E Elliott, J Joseph, H Wu, J Petricka, T Schäfer, and J E Thomas. Universal Quantum Viscosity in a Unitary Fermi Gas. *Science*, 331(6013):58 – 61, jan 2011.

[15] C. Carcy, S. Hoinka, M. G. Lingham, P. Dyke, C. C. N. Kuhn, H. Hu, and C. J. Vale. Contact and sum-rules in a near-uniform Fermi gas at unitarity. (1):1–5, 2019.

[16] Yvan Castin, Zoran Hadzibabic, Sabine Stock, Jean Dalibard, and Sandro Stringari. Quantized Vortices in the Ideal Bose Gas: A Physical Realization of Random Polynomials. *Phys. Rev. Lett.*, 96(4):40405, feb 2006.

[17] A J Cerfon. Vortex Dynamics and Shear-Layer Instability in High-Intensity Cyclotrons. *Phys. Rev. Lett.*, 116(17):174801, apr 2016.

[18] B. S. Chandrasekhar. A note on the maximum critical field of high-field superconductors. *Applied Physics Letters*, 1(1):7–8, 1962.

[19] S. Chandrasekhar. *Hydrodynamic and hydromagnetic stability.* Clarendon Press, Oxford, 1961.

[20] Lawrence W Cheuk, Matthew A Nichols, Katherine R Lawrence, Melih Okan, Hao Zhang, and Martin W Zwierlein. Observation of 2D Fermionic Mott Insulators of ^{40}K with Single-Site Resolution. *Phys. Rev. Lett.*, 116(23):235301, jun 2016.

[21] L. Chomaz, R. M.W. Van Bijnen, D. Petter, G. Faraoni, S. Baier, J. H. Becher, M. J. Mark, F. Wächtler, L. Santos, and F. Ferlaino. Observation of roton mode population in a dipolar quantum gas. *Nature Physics*, 14(5):442–446, 2018.

[22] A. M. Clogston. Upper limit for the critical field in hard superconductors. *Phys. Rev. Lett.*, 9(6):266–267, 1962.

[23] I Coddington. *Vortices in a Highly Rotating Bose Condensed Gas.* PhD thesis, 2004.

[24] Piers Coleman and Andrew J Schofield. Quantum criticality. *Nature*, 433(7023):226–229, 2005.

[25] N R Cooper. Rapidly rotating atomic gases. *Advances in Physics*, 57(6):539–616, 2008.

[26] Andrea Damascelli, Zahid Hussain, and Zhi Xun Shen. Angle-resolved photoemission studies of the cuprate superconductors. *Reviews of Modern Physics*, 75(2):473–541, 2003.

[27] R C Davidson, H.-W. Chan, C Chen, and S Lund. Equilibrium and stability properties of intense non-neutral electron flow. *Rev. Mod. Phys.*, 63(2):341–374, apr 1991.

[28] K. B. Davis. *Evaporative cooling of sodium atoms*. PhD thesis, Massachusetts Institute of Technology, 1995.

[29] K. B. Davis, M.-O. Mewes, M. R. Andrews, N. J. van Druten, D. S. Durfee, D. M. Kurn, and W Ketterle. Bose–Einstein Condensation in a Gas of Sodium Atoms. *Phys. Rev. Lett.*, 75:3969–3973, 1995.

[30] K B Davis, M.-O. Mewes, M A Joffe, M R Andrews, and W Ketterle. Evaporative Cooling of Sodium Atoms. *Phys. Rev. Lett.*, 74:5202–5205, 1995.

[31] B. DeMarco and D. S. Jin. Onset of Fermi Degeneracy in a Trapped Atomic Gas. *Science*, 285(5434):1703–1706, sep 1999.

[32] P.A.M. Dirac. On the Theory of Quantum Mechanics. *Proceedings of the Royal Society of London Series A*, 112(762):661–677, oct 1926.

[33] Elmer V.H. Doggen and Jami J. Kinnunen. Momentum-resolved spectroscopy of a Fermi liquid. *Scientific Reports*, 5, 2015.

[34] Russell J Donnelly and Charles E Swanson. Quantum turbulence. *Journal of Fluid Mechanics*, 173:387–429, 1986.

[35] T. E. Drake, Y. Sagi, R. Paudel, J. T. Stewart, J. P. Gaebler, and D. S. Jin. Direct observation of the Fermi surface in an ultracold atomic gas. *Physical Review A*, 86(3):031601, sep 2012.

[36] Joaquin E Drut, Timo A Lahde, and Timour Ten. Momentum Distribution and Contact of the Unitary Fermi Gas. *Phys. Rev. Lett.*, 106(20):205302, may 2011.

[37] A Einstein. Quantentheorie des einatomigen idealen Gases. *Sitzungsberichte/Physikalische Klasse, Preussische Akademie der Wissenschaften*, 22:261, 1924.

[38] P Engels, I Coddington, P C Haljan, V Schweikhard, and E A Cornell. Observation of Long-Lived Vortex Aggregates in Rapidly Rotating Bose-Einstein Condensates. *Phys. Rev. Lett.*, 90(17):170405, may 2003.

[39] Tilman Enss. Quantum critical transport in the unitary Fermi gas. *Phys. Rev. A*, 86(1):013616, jul 2012.

[40] Tilman Enss, Rudolf Haussmann, and Wilhelm Zwerger. Viscosity and scale invariance in the unitary Fermi gas. *Annals of Physics*, 326(3):770–796, 2011.

[41] O et al Hen. Momentum sharing in imbalanced Fermi systems. *Science*, 346(6209):614–617, 2014.

[42] C Fefferman. Existence and smoothness of the Navier-Stokes equation. *The Millennium Prize Problems*, 2006.

[43] L Feng, L W Clark, A Gaj, and C Chin. Coherent inflationary dynamics for Bose-Einstein condensates crossing a quantum critical point. *Nature Physics*, 14(3):269–272, 2018.

[44] Enrico Fermi. Sulla quantizzazione del gas perfetto monoatomico. *Rend. Lincei*, 3:145–149, 1926.

[45] R A Ferrell, N Menyhard, H Schmidt, F Schwabl, and P Szepfalusy. Dispersion in Second Sound and Anomalous Heat Conduction at the Lambda Point of Liquid Helium. *Phys. Rev. Lett.*, 18:891–894, 1967.

[46] H Feshbach. Unified theory of nuclear reactions. *Ann. Phys.*, 5:337, 1958.

[47] A L Fetter. Bose-Einstein condensate in a rapidly rotating non-symmetric trap. 2009.

[48] R. P. Feynman. Application of quantum mechanics to liquid helium. In C. J. Gorter, editor, *Progress in Low Temperature Physics*, volume 1, page 17. North-Holland, North Holland Publishing Co., Amsterdam, 1955.

[49] R P Feynman. Simulating physics with computers. *International Journal of Theoretical Physics*, 21:467–488, 1982.

[50] Susana Figueroa-Gerstenmaier, S Giudice, L Cavallo, and G Milano. A molecular model for H(2) interactions in aliphatic and aromatic hydrocarbons. *Physical chemistry chemical physics : PCCP*, 11 20:3935–3942, 2009.

[51] R. J. Fletcher, A Shaffer, C C Wilson, P B Patel, Z Yan, V Crépel, B Mukherjee, and Martin W Z Zwierlein. Geometric squeezing into the lowest Landau level. *Science*, 372(6548):1318–1322, 2021.

[52] Richard J Fletcher, Jay Man, Raphael Lopes, Panagiotis Christodoulou, Julian Schmitt, Maximilian Sohmen, Nir Navon, Robert P Smith, and Zoran Hadzibabic. Elliptic flow in a strongly interacting normal Bose gas. *Phys. Rev. A*, 98(1):11601, jul 2018.

[53] B Frank, J Lang, and W Zwerger. Universal Phase Diagram and Scaling Functions of Imbalanced Fermi Gases. *Journal of Experimental and Theoretical Physics*, 127(5):812–825, nov 2018.

[54] J. P. Gaebler, J. T. Stewart, T. E. Drake, D. S. Jin, A. Perali, P. Pieri, and G. C. Strinati. Observation of pseudogap behaviour in a strongly interacting Fermi gas. *Nature Physics*, 6(8):569–573, 2010.

[55] Alexander L Gaunt, Tobias F Schmidutz, Igor Gotlibovych, Robert P Smith, and Zoran Hadzibabic. Bose-Einstein Condensation of Atoms in a Uniform Potential. *Phys. Rev. Lett.*, 110(20):200406, may 2013.

[56] Stefano Giorgini, Lev P. Pitaevskii, and Sandro Stringari. Theory of ultracold atomic Fermi gases. *Reviews of Modern Physics*, 80(4):1215–1274, oct 2008.

[57] Lori S Goldner, Norbert Mulders, and Guenter Ahlers. Second sound very near $T\lambda$. *Journal of Low Temperature Physics*, 93(1):131–182, 1993.

[58] Igor Gotlibovych, Tobias F. Schmidutz, Alexander L. Gaunt, Nir Navon, Robert P. Smith, and Zoran Hadzibabic. Observing properties of an interacting homogeneous Bose-Einstein condensate: Heisenberg-limited momentum spread, interaction energy, and free-expansion dynamics. *Physical Review A - Atomic, Molecular, and Optical Physics*, 89(6), 2014.

[59] Olga Goulko and Matthew Wingate. Numerical study of the unitary Fermi gas across the superfluid transition. *Phys. Rev. A*, 93(5):053604, may 2016.

[60] M Greiner, C A Regal, and D S Jin. Emergence of a molecular Bose–Einstein condensate from a Fermi gas. *Nature*, 426:537, 2003.

[61] Z Hadzibabic, C A Stan, K Dieckmann, S Gupta, M W Zwierlein, A Görlitz, and W Ketterle. Two-Species Mixture of Quantum Degenerate Bose and Fermi Gases. *Phys. Rev. Lett.*, 88(16):160401, apr 2002.

[62] P C Haljan, I Coddington, P Engels, and E A Cornell. Driving Bose–Einstein-Condensate Vorticity with a Rotating Normal Cloud. *Phys. Rev. Lett.*, 87(21):210403, nov 2001.

[63] P C Haljan, I Coddington, P Engels, and E A Cornell. Driving Bose-Einstein-Condensate Vorticity with a Rotating Normal Cloud. *Phys. Rev. Lett.*, 87(21):210403, nov 2001.

223

[64] B I Halperin and P C Hohenberg. Generalization of Scaling Laws to Dynamical Properties of a System Near its Critical Point. *Phys. Rev. Lett.*, 19(12):700–703, sep 1967.

[65] R. Haussmann, M. Punk, and W. Zwerger. Spectral functions and rf response of ultracold fermionic atoms. *Phys. Rev. A*, 80(6):063612, 2009.

[66] Tin-Lun Ho. Universal Thermodynamics of Degenerate Quantum Gases in the Unitarity Limit. *Phys. Rev. Lett.*, 92(9):90402, mar 2004.

[67] Sascha Hoinka, Marcus Lingham, Kristian Fenech, Hui Hu, Chris J Vale, Joaquin E Drut, and Stefano Gandolfi. Precise Determination of the Structure Factor and Contact in a Unitary Fermi Gas. *Phys. Rev. Lett.*, 110(5):055305, jan 2013.

[68] Hui Hu, Xia Ji Liu, and Peter D. Drummond. Universal contact of strongly interacting fermions at finite temperatures. *New Journal of Physics*, 13, 2011.

[69] Klaus Hueck, Niclas Luick, Lennart Sobirey, Jonas Siegl, Thomas Lompe, and Henning Moritz. Two-Dimensional Homogeneous Fermi Gases. *Phys. Rev. Lett.*, 120(6):60402, feb 2018.

[70] M Inguscio, W Ketterle, and C Salomon, editors. *Ultra-cold Fermi Gases, Proceedings of the International School of Physics Enrico Fermi, Course CLXIV, Varenna 2006.* Amsterdam, 2008.

[71] S Inouye, M R Andrews, J Stenger, H.-J. Miesner, D M Stamper-Kurn, and W Ketterle. Observation of Feshbach resonances in a Bose–Einstein condensate. *Nature*, 392:151–154, 1998.

[72] S. Jensen, C. N. Gilbreth, and Y. Alhassid. Contact in the Unitary Fermi Gas across the Superfluid Phase Transition. *Physical Review Letters*, 125(4):43402, 2020.

[73] S Jochim, M Bartenstein, A Altmeyer, G Hendl, S Riedl, C Chin, J Hecker-Denschlag, and R Grimm. Bose–Einstein Condensation of Molecules. *Science*, 302:2101, 2003.

[74] Shaun P Johnstone, Andrew J Groszek, Philip T Starkey, Christopher J Billington, Tapio P Simula, and Kristian Helmerson. Evolution of large-scale flow from turbulence in a two-dimensional superfluid. *Science*, 364(6447):1267–1271, 2019.

[75] James Prescott Joule and William Thomson. LXXVI. On the thermal effects experienced by air in rushing through small apertures. *The London, Edinburgh, and Dublin Philosophical Magazine and Journal of Science*, 4(28):481–492, 1852.

[76] W Ketterle, D Durfee, and D Stamper-Kurn. Making, probing and understanding Bose-Einstein condensates. *Bose-Einstein condensation in atomic gases: Proceedings of the International School of Physics "Enrico Fermi", Course CXL*, pages 67–176, 1999.

[77] W Ketterle and M W. Zwierlein. Making, probing and understanding ultracold Fermi gases. *Rivista del Nuovo Cimento*, 31(5-6):247–422, 2008.

[78] C Kittel, H K Charles Kittel, K Charles, H Kroemer, and K Herbert. *Thermal Physics*. W. H. Freeman, 1980.

[79] A Kolmogorov. The Local Structure of Turbulence in Incompressible Viscous Fluid for Very Large Reynolds' Numbers. *Akademiia Nauk SSSR Doklady*, 30:301–305, jan 1941.

[80] D S Kothari and B N Srivasava. Joule-Thomson Effect and Quantum Statistics. *Nature*, 140(3553):970–971, 1937.

[81] Mark J H Ku, A. T. Sommer, L. W. Cheuk, and M. W. Zwierlein. Revealing the Superfluid Lambda Transition in the Universal Thermodynamics of a Unitary Fermi Gas. *Science*, 335(6068):563–567, 2012.

[82] L D Landau and E M Lifshitz. *Fluid Mechanics*. Pergamon Press, New York, 1987.

[83] A. I. Larkin and Y N. Ovchinnikov. No Title. *Sov. Phys. JETP*, 20:762, 1965.

[84] A. J. Larkin and Y. N. Ovchinnikov. Nonuniform state of superconductors. *Zh. Eksp. Teor. Fiz.*, 47(3):1136–1146, 1964.

[85] Sébastien Laurent, Matthieu Pierce, Marion Delehaye, Tarik Yefsah, Frédéric Chevy, and Christophe Salomon. Connecting Few-Body Inelastic Decay to Quantum Correlations in a Many-Body System: A Weakly Coupled Impurity in a Resonant Fermi Gas. *Phys. Rev. Lett.*, 118(10):103403, mar 2017.

[86] A. Legros, S. Benhabib, W. Tabis, F. Laliberté, M. Dion, M. Lizaire, B. Vignolle, D. Vignolles, H. Raffy, Z. Z. Li, P. Auban-Senzier, N. Doiron-Leyraud, P. Fournier, D. Colson, L. Taillefer, and C. Proust. Universal T-linear resistivity and Planckian dissipation in overdoped cuprates. *Nature Physics*, 15(2):142–147, 2019.

[87] J E Lennard-Jones. Cohesion. 43(5):461–482, sep 1931.

[88] Julian Léonard, Andrea Morales, Philip Zupancic, Tilman Esslinger, and Tobias Donner. Supersolid formation in a quantum gas breaking a continuous translational symmetry. *Nature*, 543:87, mar 2017.

[89] Jun-Ru Li, Jeongwon Lee, Wujie Huang, Sean Burchesky, Boris Shteynas, Furkan Çağrı Top, Alan O Jamison, and Wolfgang Ketterle. A stripe phase with supersolid properties in spin–orbit-coupled Bose–Einstein condensates. *Nature*, 543:91, mar 2017.

[90] H v. Löhneysen, T Pietrus, G Portisch, H G Schlager, A Schröder, M Sieck, and T Trappmann. Non-Fermi-liquid behavior in a heavy-fermion alloy at a magnetic instability. *Phys. Rev. Lett.*, 72(20):3262–3265, may 1994.

[91] K W Madison, F Chevy, W Wohlleben, and J Dalibard. Vortex Formation in a Stirred Bose-Einstein Condensate. *Phys. Rev. Lett.*, 84(5):806–809, jan 2000.

[92] G I Martone, A Recati, and N Pavloff. Supersolidity of cnoidal waves in an ultracold Bose gas. *Phys. Rev. Research*, 3(1):13143, feb 2021.

[93] M R Matthews, B P Anderson, P C Haljan, D S Hall, C E Wieman, and E A Cornell. Vortices in a Bose-Einstein Condensate. *Phys. Rev. Lett.*, 83(13):2498–2501, sep 1999.

[94] W D McComb. *The Physics of Fluid Turbulence*. Oxford Engineering Science Series. Clarendon Press, 1990.

[95] John H. McLeod. The Axicon: A New Type of Optical Element. *Journal of the Optical Society of America*, 44(8):592, aug 1954.

[96] Vladimir G Minogin, James A Richmond, and Geoffrey I Opat. Time-orbiting-potential quadrupole magnetic trap for cold atoms. *Phys. Rev. A*, 58(4):3138–3145, oct 1998.

[97] Erich J. Mueller. Review of pseudogaps in strongly interacting Fermi gases. *Reports on Progress in Physics*, 80(10):104401, 2017.

[98] B Mukherjee. condensate: Interactive GPU-accelerated numerical solutions of the Gross-Pitaevskii equation., 2020.

[99] Biswaroop Mukherjee. Single Particle BEC1, 2016.

[100] Biswaroop Mukherjee, Parth B. Patel, Zhenjie Yan, Richard J. Fletcher, Julian Struck, and Martin W. Zwierlein. Spectral Response and Contact of the Unitary Fermi Gas. *Phys. Rev. Lett.*, 122(20), 2019.

[101] Biswaroop Mukherjee, Airlia Shaffer, Parth B Patel, Zhenjie Yan, Cedric C Wilson, Valentin Crépel, Richard J Fletcher, and Martin Zwierlein. Crystallization of Bosonic Quantum Hall States. 2021.

[102] Biswaroop Mukherjee, Zhenjie Yan, Parth B. Patel, Zoran Hadzibabic, Tarik Yefsah, Julian Struck, and Martin W. Zwierlein. Homogeneous Atomic Fermi Gases. *Phys. Rev. Lett.*, 118(12):123401, 2017.

[103] P A Murthy, D Kedar, T Lompe, M Neidig, M G Ries, A N Wenz, G Zürn, and S Jochim. Matter-wave Fourier optics with a strongly interacting two-dimensional Fermi gas. *Phys. Rev. A*, 90(4):43611, oct 2014.

[104] M. Naraschewski and D. M. Stamper-Kurn. Analytical description of a trapped semi-ideal Bose gas at finite temperature. *Phys. Rev. A*, 58(3):2423–2426, 1998.

[105] S. Nascimbène, N. Navon, K. J. Jiang, F. Chevy, and C. Salomon. Exploring the thermodynamics of a universal Fermi gas. *Nature*, 463(7284):1057–1060, feb 2010.

[106] N Navon, A L Gaunt, R P Smith, and Z Hadzibabic. Critical dynamics of spontaneous symmetry breaking in a homogeneous Bose gas. *Science*, 347(6218):167–170, 2015.

[107] N Navon, S. Nascimbene, F Chevy, C Salomon, S Nascimbène, F Chevy, C Salomon, S. Nascimbene, F Chevy, C Salomon, S Nascimbène, F Chevy, and C Salomon. The Equation of State of a Low-Temperature Fermi Gas with Tunable Interactions. *Science*, 328(5979):729–732, 2010.

[108] Nir Navon, Alexander L Gaunt, and P Robert. Emergence of a turbulent cascade in a quantum gas. *Nature*, 539(7627):72–75, 2016.

[109] Predrag Nikolic and Subir Sachdev. Renormalization-group fixed points, universal phase diagram, and 1/N expansion for quantum liquids with interactions near the unitarity limit. *Phys. Rev. A*, 75(3):033608, mar 2007.

[110] K. O'Hara, S. Hemmer, M. Gehm, S. Granade, and J. Thomas. Observation of a strongly interacting degenerate Fermi gas of atoms. *Science*, 298:2179, 2002.

[111] F. Palestini, A. Perali, P. Pieri, and G. C. Strinati. Temperature and coupling dependence of the universal contact intensity for an ultracold Fermi gas. *Physical Review A - Atomic, Molecular, and Optical Physics*, 82(2):3–6, 2010.

[112] Maxwell F Parsons, Florian Huber, Anton Mazurenko, Christie S Chiu, Widagdo Setiawan, Katherine Wooley-Brown, Sebastian Blatt, and Markus Greiner. Site-Resolved Imaging of Fermionic ^{6}Li in an Optical Lattice. *Phys. Rev. Lett.*, 114(21):213002, may 2015.

[113] Maxwell F Parsons, Anton Mazurenko, Christie S Chiu, Geoffrey Ji, Daniel Greif, and Markus Greiner. Site-resolved measurement of the spin-correlation function in the Fermi-Hubbard model. *Science*, 353(6305):1253 – 1256, sep 2016.

[114] Parth B Patel, Zhenjie Yan, Biswaroop Mukherjee, Richard J Fletcher, Julian Struck, and Martin W Zwierlein. Universal sound diffusion in a strongly interacting Fermi gas. *Science*, 370(6521):1222–1226, 2020.

[115] W Petrich, M H Anderson, J R Ensher, and E A Cornell. A Stable, Tightly Confining Magnetic Trap for Evaporative Cooling of Neutral Atoms. *Phys. Rev. Lett.*, 74:3352, 1995.

[116] Pierbiagio Pieri, Andrea Perali, and Giancarlo Calvanese Strinati. Enhanced paraconductivity-like fluctuations in the radiofrequency spectra of ultracold Fermi atoms. *Nature Physics*, 5:736, aug 2009.

[117] L Pitaevskii and S Stringari. *Bose–Einstein Condensation*. Oxford University Press, Oxford, 2003.

[118] L.P. Pitaevskii and S. Stringari. *Bose-Einstein Condensation*. International Series of Monographs on Physics. Clarendon Press, 2003.

[119] N. V. Prokof'ev and B. V. Svistunov. Supersolid State of Matter. *Phys. Rev. Lett.*, 94:155302, 2005.

[120] Nikolay Prokof'ev and Boris Svistunov. Bold Diagrammatic Monte Carlo Technique: When the Sign Problem Is Welcome. *Phys. Rev. Lett.*, 99(25):250201, dec 2007.

[121] E L Raab, M Prentiss, Alex Cable, Steven Chu, and D E Pritchard. Trapping of Neutral Sodium Atoms with Radiation Pressure. *Phys. Rev. Lett.*, 59(23):2631–2634, dec 1987.

[122] Mohit Randeria and Edward Taylor. Crossover from Bardeen-Cooper-Schrieffer to Bose-Einstein Condensation and the Unitary Fermi Gas. *Annual Review of Condensed Matter Physics*, 5(1):209–232, 2014.

[123] C A Regal, M Greiner, and D S Jin. Observation of Resonance Condensation of Fermionic Atom Pairs. *Physical Review Letters*, 92(4):40403, jan 2004.

[124] R Rossi, T Ohgoe, E Kozik, N Prokof'ev, B Svistunov, K Van Houcke, and F Werner. Contact and Momentum Distribution of the Unitary Fermi Gas. *Phys. Rev. Lett.*, 121(13):130406, sep 2018.

[125] Yoav Sagi, Tara E. Drake, Rabin Paudel, Roman Chapurin, and Deborah S. Jin. Breakdown of the fermi liquid description for strongly interacting fermions. *Phys. Rev. Lett.*, 114(7), 2015.

[126] Yoav Sagi, Tara E. Drake, Rabin Paudel, and Deborah S. Jin. Measurement of the Homogeneous Contact of a Unitary Fermi Gas. *Physical Review Letters*, 109(22):220402, nov 2012.

[127] C. Sanner. *Fluctuations in Quantum Degenerate Fermi Gases*. PhD thesis, MIT, 2012.

[128] Abraham. Savitzky and M J E Golay. Smoothing and Differentiation of Data by Simplified Least Squares Procedures. *Analytical Chemistry*, 36(8):1627–1639, 1964.

[129] V W Scarola and S Das Sarma. Quantum Phases of the Extended Bose-Hubbard Hamiltonian: Possibility of a Supersolid State of Cold Atoms in Optical Lattices. *Phys. Rev. Lett.*, 95(3):33003, jul 2005.

[130] André Schirotzek, Yong-Il Shin, Christian H. Schunck, and Wolfgang Ketterle. Determination of the superfluid gap in atomic fermi gases by quasiparticle spectroscopy. *Phys. Rev. Lett.*, 101(14), 2008.

[131] Tobias F Schmidutz, Igor Gotlibovych, Alexander L Gaunt, Robert P Smith, Nir Navon, and Zoran Hadzibabic. Quantum Joule-Thomson Effect in a Saturated Homogeneous Bose Gas. *Phys. Rev. Lett.*, 112(4):40403, jan 2014.

[132] V Schweikhard, I Coddington, P Engels, V P Mogendorff, and E A Cornell. Rapidly Rotating Bose-Einstein Condensates in and near the Lowest Landau Level. *Phys. Rev. Lett.*, 92(4):40404, jan 2004.

[133] F Serwane, G Zürn, T Lompe, T B Ottenstein, A N Wenz, and S Jochim. Deterministic Preparation of a Tunable Few-Fermion System. *Science*, 332(6027):336–338, 2011.

[134] Yong-Il Shin, C. H. Schunck, A. Schirotzek, and W. Ketterle. Tomographic rf spectroscopy of a trapped fermi gas at unitarity. *Phys. Rev. Lett.*, 99(9):090403, 2007.

[135] Yong-Il Shin, Christian H Schunck, André Schirotzek, and Wolfgang Ketterle. Phase diagram of a two-component Fermi gas with resonant interactions. *Nature*, 451(7179):689–693, feb 2008.

[136] I Shvarchuck, Ch. Buggle, D S Petrov, K Dieckmann, M Zielonkowski, M Kemmann, T G Tiecke, W von Klitzing, G V Shlyapnikov, and J T M Walraven. Bose-Einstein Condensation into Nonequilibrium States Studied by Condensate Focusing. *Phys. Rev. Lett.*, 89(27):270404, dec 2002.

[137] S Sinha and Y Castin. Dynamic instability of a rotating Bose–Einstein condensate. *Phys. Rev. Lett.*, 87:190402, 2001.

[138] Mingyuan Sun and Xavier Leyronas. High-temperature expansion for interacting fermions. *Phys. Rev. A*, 92(5):53611, nov 2015.

[139] Shina Tan. Energetics of a strongly correlated Fermi gas. *Annals of Physics*, 323(12):2952–2970, 2008.

[140] Shina Tan. Generalized virial theorem and pressure relation for a strongly correlated Fermi gas. *Annals of Physics*, 323(12):2987–2990, 2008.

[141] Shina Tan. Large momentum part of a strongly correlated Fermi gas. *Annals of Physics*, 323(12):2971–2986, 2008.

[142] E Taylor, H Hu, X.-J. Liu, L P Pitaevskii, A Griffin, and S Stringari. First and second sound in a strongly interacting Fermi gas. *Phys. Rev. A*, 80(5):53601, nov 2009.

[143] E Tiesinga, B J Verhaar, and H T C Stoof. Threshold and resonance phenomena in ultracold ground-state collisions. *Phys. Rev. A*, 47:4114, 1993.

[144] D Tong. Lectures on the Quantum Hall Effect. *arXiv:1606.06687*, 2016.

[145] Andrew G Truscott, Kevin E Strecker, William I McAlexander, Guthrie B Partridge, and Randall G Hulet. Observation of Fermi Pressure in a Gas of Trapped Atoms. *Science*, 291(5513):2570 – 2572, mar 2001.

[146] S. Tung, G. Lamporesi, D. Lobser, L. Xia, and E. A. Cornell. Observation of the Presuperfluid Regime in a Two-Dimensional Bose Gas. *Phys. Rev. Lett.*, 105(23):230408, dec 2010.

[147] Haruki Watanabe and Hitoshi Murayama. Redundancies in Nambu-Goldstone Bosons. *Phys. Rev. Lett.*, 110(18):181601, may 2013.

[148] Ronen Weiss, Betzalel Bazak, and Nir Barnea. Nuclear neutron-proton contact and the photoabsorption cross section. *Phys. Rev. Lett.*, 114(1):1–5, 2015.

[149] Kenneth G Wilson. Non-Lagrangian Models of Current Algebra. *Phys. Rev.*, 179(5):1499–1512, mar 1969.

[150] Zhenjie Yan, Parth B. Patel, Biswaroop Mukherjee, Richard J. Fletcher, Julian Struck, and Martin W. Zwierlein. Boiling a Unitary Fermi Liquid. *Physical Review Letters*, 122(9), 2019.

[151] Zong-Chao Yan, James F Babb, A Dalgarno, and G W F Drake. Variational calculations of dispersion coefficients for interactions among H, He, and Li atoms. *Phys. Rev. A*, 54(4):2824–2833, oct 1996.

[152] Shizhong Zhang and Anthony J. Leggett. Sum-rule analysis of radio-frequency spectroscopy of ultracold Fermi gas. *Physical Review A - Atomic, Molecular, and Optical Physics*, 77(3):1–10, 2008.

[153] W. Zwerger. *Proceedings of the International School of Physics "Enrico Fermi" - Course 191 "Quantum Matter at Ultralow Temperatures"*. IOS Press, Amsterdam; SIF Bologna, 2016.

[154] M W Zwierlein, J R Abo-Shaeer, A Schirotzek, C H Schunck, and W Ketterle. Vortices and superfluidity in a strongly interacting Fermi gas. *Nature*, 435(7045):1047–1051, jun 2005.

[155] M W Zwierlein, C A Stan, C H Schunck, S M F Raupach, A J Kerman, and W Ketterle. Condensation of Pairs of Fermionic Atoms near a Feshbach Resonance. *Physical Review Letters*, 92(12):120403, mar 2004.

[156] Martin W. Zwierlein. Superfluidity in ultracold atomic Fermi gases. In *Novel Superfluids*, pages 269–422. Oxford University Press, nov 2014.

[157] M.W. Zwierlein, C.A. Stan, C.H. Schunk, S.M.F. Raupach, S Gupta, Z Hadzibabic, and W Ketterle. Observation of Bose–Einstein Condensation of Molecules. *Phys. Rev. Lett.*, 91:250401, 2003.